UNIVERSITY OF CALIFORNIA,
IRVINE

Single Molecule Coherence with Femtosecond THz-STM

DISSERTATION

submitted in partial satisfaction of the requirements
for the degree of

DOCTOR OF PHILOSOPHY

in Physics

by

Likun Wang

Dissertation Committee:
Professor Wilson Ho, Chair
Professor Shaul Mukamel
Professor Ruqian Wu
Professor Jing Xia

2022

DEDICATION

To

my mother, father, and three sisters

TABLE OF CONTENTS

LIST OF FIGURES AND TABLES

ACKNOWLEDGEMENTS

I am deeply grateful to my advisor and committee chair, Professor Wilson Ho, for all his support and guidance during the long-lasting years of my PhD life. With the endless passion and rigorous attitude in scientific research, he is a true role model as a great scientist whom I will definitely follow in my own academic career. It is a privilege for me to join his outstanding team and get involved in the exciting fs THz-STM project. I have always been inspired by his advice, both on instrumentation and running experiments. He taught me to be focused on the project when I was having a hard time during the pandemic. His requirements on the originality and reproducibility of scientific research set the gold standard for me to abide.

I thank Professor Shaul Mukamel, Professor Ruqian Wu, and Professor Jing Xia for serving my dissertation committee. I also thank Professor Ruqian Wu, Professor William Evans, Professor Jing Xia, and Professor Peter Burke for serving my advancement committee.

I want to express my special thanks to Siyu Chen, Yunpeng Xia, and Dan Bai. Siyu and I collaborated at the early-stage of the fs THz-STM project in STM 2. It was also the time that I got familiar with STM 2 with lots of help from Siyu. Yunpeng joined STM 2 when I was taking the exciting data of the H_2 coherent oscillations. He has a very strong background on the theory part to explain the experimental data, which helped a lot on our understanding of the H_2 two-level system. Dan Bai became a member of STM 2 last year and collaborated with me to run the experiment on the electrical manipulation of the H_2 two-level system. She never made mistakes when taking data, which was very impressive to me.

I also thank Jiang Yao and Wenlu Shi in Ho group. We worked together on the construction and maintenance of the Helium recycling system and many other instrumentations. Jiang has brought lots of innovations to the STM control electronics which I wish I had chance to use.

I am truly grateful to all other group members that I have worked with. Dr. Shaowei Li taught me experimental skills on the STM and the laser system in STM 2. His excellence on academia and daily life has always reminded me that I should do better. Dr. Gregory Czap worked in the mK system but provided me invaluable suggestions. I am impressed by his carefulness when handling a complicated system. I also had overlaps with Dr. Zhumin Han, Dr. Arthur Yu, Dr. Chilun Jiang, Dr. Chen Xu, Dr. Weicai Cao, Dr. Calvin Patel, Dr. Peter Wagner, Andrew Wang, Christian Kim, Dr. Wei Tao, Dr. Tingwei Hu. It is a pleasure to work with all of them in Ho group. Jiawei Zeng joined Ho group during the pandemic and have already shown great potential in research. I wish him the best luck for the next years.

I would also like to thank our collaborators Professor Mona Jarrahi and Dr. Nezih Tolga Yardimci from UCLA. They generously provided us with the plasmonic photoconductive antennas for THz generation. Their antennas have been showing great performance during the past several years.

My three sisters Lihong Wang, Liping Wang, and Liqin Wang have always been my firm support throughout my life. I cannot appreciate more for having them stand behind me. I also thank my friends Qi Yao, Lei Xie, Chi Zhang, and my love Yanxi Chen for their support.

Lastly, I would like to thank National Science Foundation Center for Chemical Innovation on Chemistry at the Space-Time Limit (CaSTL) under Grant No. CHE-1414466 and Office of

Basic Energy Sciences, U.S. Department of Energy, under Grant No. DE-SC0019448 for the funding support in carrying out this research.

VITA

Likun Wang

Education:

- Ph.D. study in Physics, University of California, Irvine, 2015-present

Thesis Advisor: Prof. Wilson Ho

- M.S. in Materials Science and Engineering, Tongji University, 2012-2015

Thesis Advisor: Prof. Wei Xu

- B.S. in Materials Science and Engineering, Shenyang Jianzhu University, 2008-2012

Research Area:

Study of quantum coherence of single molecules and atoms on surfaces with the combination of femtosecond NIR/THz laser and low temperature scanning tunneling microscope (STM).

Research Skills:

Instrumentation skills:

- STM construction and maintenance
- Optical system design and construction based on femtosecond Ti:Sapphire laser
- THz system design and construction
- Helium recycling system construction and maintenance
- Nanofabrication

Coding skills: Labview, Autodesk Inventor, Mathematica, Matlab, Comsol

Honors and Awards:

Graduate Student Award, AVS Nanoscale Science and Technology Division, 2021
Academic Scholarship, Tongji University, 2012-2015
First prize college scholarship, Shenyang Jianzhu University, 2010
First prize in National English Contest for College Students (NECCS), Shenyang Jianzhu University, 2009
Outstanding student leader, Shenyang Jianzhu University, 2009

Memberships:

AVS Platinum membership, 2021-2022

Conferences:

- The 82nd Physical Electronics Conference, 2022.06

Atomic-scale Quantum Sensing Based on the Ultrafast Coherence of an H_2 Molecule in an STM cavity

- APS March meeting, 2022.03

Atomic Scale Quantum Sensing from Ultrafast Coherence Measurement of Single H_2 Molecules in the STM Junction

- AVS meeting, 2021.10

Atomic Scale Quantum Sensing from Ultrafast Coherence Measurement of Single H_2

Molecules in STM Junction

- APS March meeting, 2018.03

Photoinduced Dehydrogenation of a Single Molecule Adsorbed on a Surface

Professional Services:

Graduate Student Researcher, University of California, Irvine, 2015-2021 (12 quarters)
Teaching assistant, University of California, Irvine, 2015-2016, 2021-2022 (9 quarters)
Research assistant, Tongji University, 2012-2015
Teaching assistant, Tongji University, 2013.02-2013.07

Publications:

1. Atomic-scale Quantum Sensing Based on the Ultrafast Coherence of an H_2 Molecule in an STM cavity
   Likun Wang, Yunpeng Xia, and W. Ho*
   Science, **376**, 401-405 (2022)

2. Electrical Manipulation of Quantum Coherence in a Single Molecular Qubit
   Likun Wang, Bai Dan, Yunpeng Xia, and W. Ho*
   in preparation (2022)

3. Pulsed THz Rectification Spectroscopy on Single Molecules and Atoms
   Likun Wang, Yunpeng Xia, and W. Ho*
   in preparation (2022)

4. Optical Tuning of the Kondo State in a Single Atom
   Likun Wang, and W. Ho*
   in preparation (2022)

5. Time Domain THz Coherent Spectroscopy of a Hydrogen Molecule in the STM Junction
   Yunpeng Xia, **Likun Wang**, and W. Ho*
   in preparation (2022)

6. Bond-Selected Photodissociation of Single Molecules Adsorbed on Metal Surfaces
   Shaowei Li, Gregory Czap, Hui Wang, **Likun Wang**, Siyu Chen, Arthur Yu, Ruqian Wu*, and W. Ho*
   Phys. Rev. Lett., **112**, 077401 (2019)

ABSTRACT OF THE DISSERTATION

Single Molecule Coherence with Femtosecond THz-STM

by

Likun Wang

Doctor of Philosophy in Physics

University of California, Irvine, 2022

Professor Wilson Ho, Chair

The main goal of the studies presented in this dissertation is to demonstrate the measurement and manipulation of ultrafast quantum coherence in single molecules. Low temperature scanning tunneling microscopy (STM) with inelastic electron tunneling spectroscopy (IETS) allows determination of molecular fingerprints with atomic-scale spatial resolution. Femtosecond (fs) lasers in the terahertz (THz) range can be used to monitor the quantum coherence of molecules and atoms. Here we combine STM-IETS with fs THz pulses into a fs THz-STM and perform the time-resolved THz rectification spectroscopy (t-TRS) in the STM junction.

When THz pulses are introduced into the STM junction, an effective voltage will be developed by the THz electric field which behaves as a modulation of the static sample bias. A non-zero rectification current can then be monitored due to the nonlinearity originated from the molecular excitation in the STM junction. THz photon absorption can also occur when the energy separation of the ground and excited states in the molecule, such as the hydrogen molecule (H_2), matches the frequency range of the THz pulses. It thus becomes possible to prepare the

superposition state of the H_2 two-level system and track its temporal evolution from time domain pump-probe spectroscopy.

The coherence measurement is successfully demonstrated on a single H_2 molecule by our fs THz-STM. The extreme sensitivity of the H_2 TLS coherent oscillation to the underlying surface chemical environment is discovered by scanning across the Cu_2N surface while performing pump-probe spectroscopy, which shows promising applications in quantum sensing. Both the oscillation frequency and the dephasing time of the initial wave packet fo the H_2 TLS are highly dependent on the applied external electric field under the giant Stark effect. By sweeping the sample bias and the corresponding electric field across the STM junction, we realized the electric manipulation of the quantum coherence of the H_2 TLS. An avoided crossing in the energy levels and a quantum state transition are revealed from fitting the oscillation frequency spectrum to a model Hamiltonian. The surface electrostatic field is then quantified and scanned with sub-Ångström spatial resolution.

We also demonstrate the optical tuning of the Kondo state in a single cobalt (Co) atom in the STM junction by fs near-infrared (NIR) laser illumination. Laser pulses are found to quench the Kondo state completely, and the continuous tuning of the Kondo amplitude is realized by adjusting the laser power. Our study is preliminary to future investigations of the temporal dynamics of Kondo collapse and revival in a single atom.

CHAPTER 1

Introduction

1.1 Background

Quantum coherence describes the non-classical property of the superposition state which is at the heart of quantum mechanics. Originated from the wave nature of quantum states, a linear combination of different quantum states forms the superposition state. Quantum coherence then emerges if there is a well-defined relative phase relationship between these two or more quantum states. Endless efforts have been made to measure and manipulate the quantum coherence in various types of experiments [1–5]. Not only does it deepen our understanding of the quantum phenomena, but also it can benefit the application progress of quantum information science.

The simplest quantum system is a two-level system (TLS) with only two quantum states as the ground state and the excited state, respectively. Due to the interaction (entanglement) with the surrounding environment, the system can lose its coherence, which is called decoherence. The decoherence time is of crucial importance to quantum computation and quantum sensing [6,7]. A quantum computer requires the decoherence time to be as long as possible to allow more quantum operations before it decoheres. Whereas quantum sensing replies more on the weakness of a quantum system, a short decoherence time, for its high sensitivity to the external environment. It then becomes scientists' long-lasting pursuit to measure and manipulate the coherence of quantum systems and find out the most suitable one for industrial application.

Most recently, femtosecond (fs) lasers have been combined with low temperature scanning tunneling microscopes (STM) to measure the quantum coherence of single molecules with both fs temporal and atomic-scale spatial resolutions [4,5,8,9]. The fs laser pulses can excite a molecular

system and prepare the superposition state while its time evolution can be tracked by monitoring the laser induced tunneling current in the STM. With the benefit of localized tunneling current at the atomic scale, the spatial resolution of laser combined STM can easily surpass the diffraction limit of the laser wavelength.

Within several different types of laser-combined STM, fs THz-STM is of particular interest to study the quantum coherence of single molecules. THz sits in between microwave and infrared in the electromagnetic spectrum, the so called 'THz gap'. The THz frequency (0.1 to 10 THz) matches very well with large amounts of molecular vibrations and rotations [10,11]. It then becomes possible to resonantly excite the molecular system under study with THz pulses and monitor its time evolution through pump-probe spectroscopy. In addition, THz irradiation is known to induce negligible thermal effect in the STM junction due to its high reflectivity, which empowers extra advantage of THz over other frequencies such as near-infrared (NIR) in the STM junction.

1.2 fs THz Generation and Characterization

The first thing to consider in implementing THz pulses into the STM system is the THz generation. Previous studies of fs THz-STM have used optical rectification in non-linear crystals to generate THz pulses with a strong electric field around 100 kV/cm, where the THz field is high enough to drive the electrons to tunnel across the junction [4,12,13,8,14]. However, due to the spectral broadening introduced by the strong THz voltage in the junction, it is not possible to demonstrate the THz rectification spectroscopy (TRS) which can give us fingerprints of single molecules and atoms. The THz generation in non-linear crystals also requires a relatively low repetition rate of the NIR laser to have enough generation efficiency, which leads to a low signal to noise ratio of the rectification current in the junction.

With the existing fs NIR laser having a repetition rate of 1 GHz, it is more suitable to use a photoconductive antenna (PCA) for THz generation. The generation efficiency is much higher than the optical rectification in a non-linear crystal, especially with the plasmonic PCA provided by our collaborators [15]. Our signal sampling is benefited a lot from the very high repetition rate of the laser system, where the rectification current is high enough while inducing a low voltage across the junction. TRS over single molecules and atoms were successfully demonstrated with such a fs THz-STM system.

Our THz generation system consists of a femtosecond laser and a large area plasmonic PCA. With center wavelength 820 nm and pulse duration (full width at half-maximum) around 30 fs, the pulses emitted from our Ti: Sapphire laser (repetition rate 1 GHz) are directed to the PCA to generate single-cycle THz transients. We then use electro-optical (E-O) sampling with a 500 um thick ZnTe crystal to characterize the THz waveform. As a result, our generated THz spectrum usually covers from 0 to 3 THz with the center wavelength located at 0.5 THz. The relative THz power is measured with a commercial pyroelectric detector and the THz profile is imaged from a THz camera.

With a large THz box which can be pumped down to vacuum or purged with different gases, we perform E-O sampling to characterize THz in different environments. As shown in Figure 1.1, THz waveforms in Argon gas, Vacuum, Air, and Nitrogen gas are listed. A recurrence of the zero delay signal is found at 10.5 ps, which is from the multireflection of THz in the ZnTe crystal. Note that there was still some residual air when performing the E-O sampling in N_2 gas. The THz waveform in air clearly showed a difference with the other three environments. The wiggles and oscillations are due to the water absorption as further confirmed by the frequency spectra in Figure 1.2 after fast Fourier transform (FFT) of the time domain data.

Figure 1.1 THz waveforms in various environments obtained from the E-O sampling.

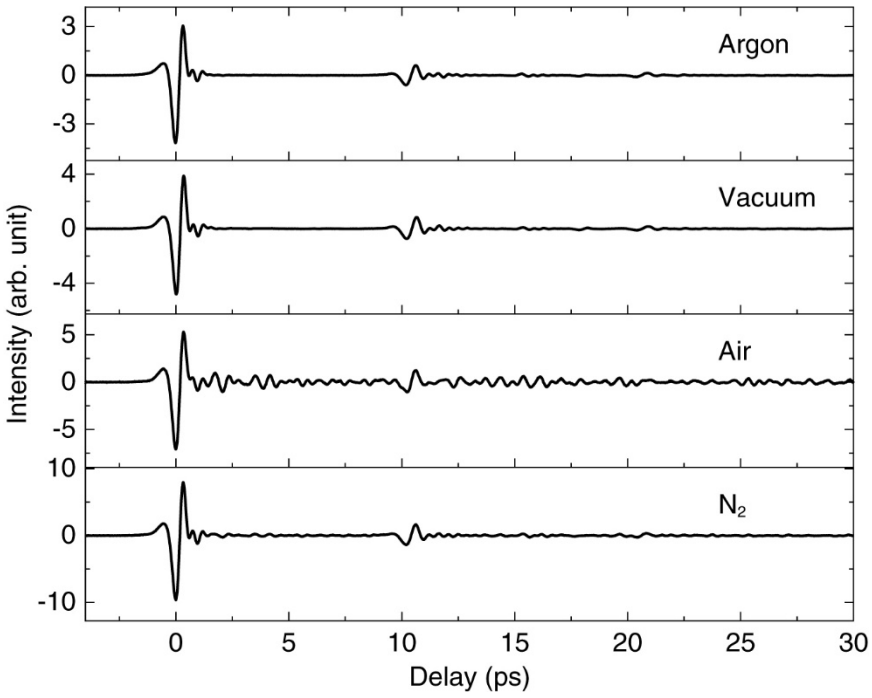
Argon
Vacuum
Air
N2
Intensity (arb. unit)
Delay (ps)
3
0
-3
4
0
-4
5
0
-5
10
0
-10
0
5
10
15
20
25
30

Figure 1.2 FFT results of the time domain data in Figure 1.1.

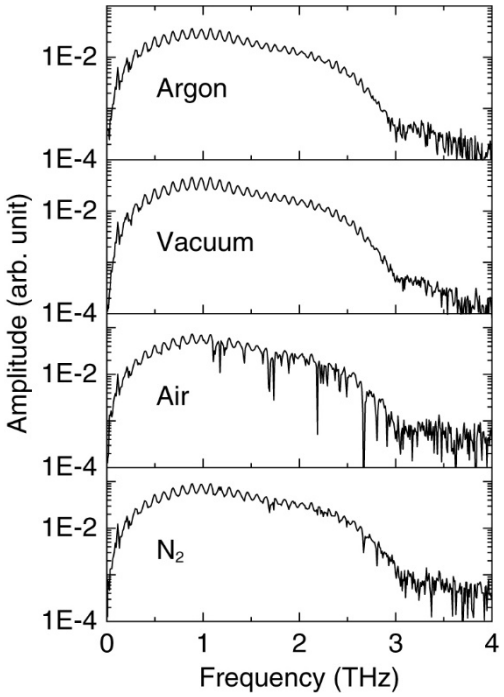
Argon
Vacuum
Air
N2
1E-2
1E-4
Amplitude (arb. unit)
0
1
2
3
4
Frequency (THz)

The background subtracted water absorption spectra in Figure 1.3 matches very well with previous studies [16].

With such a frequency range spanning from 0.1 THz to 3 THz in free space, we will be able to align it to the STM junction through flat silver mirrors and Tsurupica lenses.

Figure 1.3 THz absorption by water vapor.

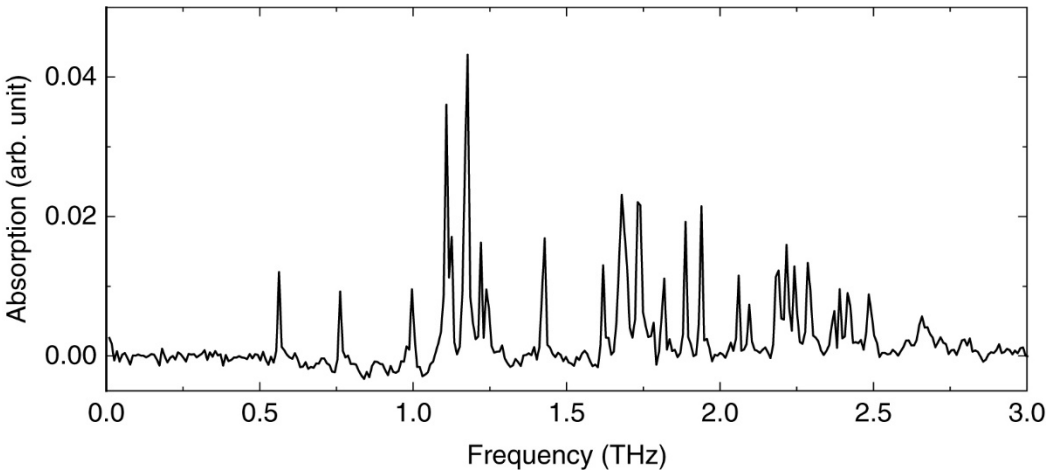
Absorption (arb. unit)
0.04
0.02
0.00
0.0
0.5
1.0
1.5
2.0
2.5
3.0
Frequency (THz)

1.3 fs THz-STM

Over the past several years, the rapid development of THz-STM has enabled various significant studies of molecules and surfaces with sub-picosecond temporal and sub-nanometer spatial resolution. By introducing far field single cycle THz pulses into the STM junction, it becomes possible to pump the system under study into transient excited state and probe the temporal evolution by monitoring the induced rectification current.

In the very first study of THz-STM [4], Repp's group showed that the peak of a terahertz electric-field can facilitate electrons tunneling into the highest occupied molecular orbital (HOMO) of a pentacene molecule. Pump-probe experiment by measuring the rectification current showed periodic oscillations indicating the coherent vertical vibration of the molecule. In a later experiment [8], they applied the near field THz pulse onto a magnesium phthalocyanine molecule (MgPc) to induce the coherent switching between two adsorption states. The oscillation of the switching probabilities under different THz pump power revealed hindered rotation induced by THz electrons tunneling into the lowest unoccupied molecular orbital (LUMO) of MgPc.

Hegmann's group also conducted pioneering THz-STM experiments on semiconductor [12] and metal surfaces [17]. The enhanced THz field in the junction was used to induce band bending in the subsurface depletion layer of Si(111)-(7 × 7) and enable transport between the surface and the bulk. Imaging of the surface at various pump-probe delays verified the sub-picosecond and sub-nanometer resolution of the THz-STM. They also showed THz imaging on Cu(111) and quantified the THz-induced voltage transient at the junction.

Instead of coupling two paired THz pulses to the STM junction, Shigekawa's group presented optical-pump/THz-probe experiments on 2H-MoTe2 to excite the transient electronic state and probe the ultrafast carrier dynamics [13]. Using the same experimental setup, they also

observed the ultrafast electron motion of a C_{60} multilayer structure grown on Au(111) [18]. Taking use of the extremely high voltage driven by intense THz pulses, Takeda's group successfully observed luminescence from the junction of Au tip and Ag(111) surface [14].

In addition to experiments on molecular motions [4,8], surface dynamics [12,13,17], electron motions [18] and luminescence [14], different techniques were also developed to enrich the application of THz-STM. Takeda's group demonstrated a phase shifter to control the carrier-envelope phase of the THz near field [19]. Shigekawa's group presented a method to directly evaluate the enhanced near field in the tunnel junction [13]. With the implementation of a spintronic THz emitter (STE), Wolf's group successfully extended the THz near field up to 15 THz [20], which leads the THz-STM study to ultrabroadband range. To be able to tune between high pulse energy at low repetition rates and high signal fidelity at high repetition rates, Loth's group designed a versatile THz source with adjustable repetition rates between 0.5 and 41 MHz [21].

Despite the significant achievements done by THz-STM, there has been no study on TRS which can distinguish molecular fingerprints similar to IETS but with ultrafast temporal information. Neither did the above studies show the quantum decoherence of molecules, which is a prerequisite for quantum computer and quantum sensing.

1.4 Chapter Summary

The rest parts of this dissertation summarize our efforts in developing a fs THz-STM and the acquired results on the measurement and manipulation of single molecule coherence.

Chapter 2 demonstrates THz rectification spectroscopy (TRS) of various single molecules and atoms. TRS of H_2, Nickelocene ($NiCp_2$), Cobalt (Co), and carbon monoxide (CO) are shown to compare with traditional IETS measurements. TRS exhibits advantage on the capability of

polarization control of the THz field and time-resolved spectral features.

Chapter 3 describes our measurements of the quantum coherence in a single H_2 molecule adsorbed on Cu_2N surface. Coherent oscillations and frequency spectra are shown to reveal the time and energy resolution of our fs THz-STM. The H_2 two-level system (TLS) was found to be extremely sensitive to its surrounding environment, which enables us to treat it as a quantum sensor and map the spatial distribution of the surface chemical environment at the atomic-scale.

Chapter 4 continues with Chapter 3 and demonstrates our manipulation of the quantum coherence of the H_2 TLS with static electric field. Both the coherent oscillation frequency and decoherence time can be controlled by the applied sample bias. By fitting our experimental data to a model Hamiltonian, we also revealed an avoided crossing of the energy levels of the H_2 TLS. We were also able to quantify the surface electrostatic field of the Cu_2N and map its spatial distribution with sub-Angstrom resolution.

Chapter 5 deviates from THz-STM and shows our results on the optical tuning of the Kondo state with a fs NIR-STM. NIR laser illumination was found to quench the Kondo state of a single Co atom. Adjusting the laser power allows us to continuously tune the Kondo amplitude.

Chapter 6 summarizes the above four chapters and proposes future experiments that can be done with our fs THz-STM. STM combined with other laser sources are also suggested.

The appendices describe the instrumentation and testing projects, including the design and machining of a triple cell doser, MIIPS operation to generate frequency combs, preliminary proposal of the spintronic THz emitter, and other parts related to the THz-STM project.

Bibliography

[1] D. Press, T. D. Ladd, B. Zhang, and Y. Yamamoto, *Complete Quantum Control of a Single Quantum Dot Spin Using Ultrafast Optical Pulses*, Nature **456**, 7219 (2008).

[2] V. V. Dobrovitski, G. D. Fuchs, A. L. Falk, C. Santori, and D. D. Awschalom, *Quantum Control over Single Spins in Diamond*, Annual Review of Condensed Matter Physics **4**, 23 (2013).

[3] S. Baumann, W. Paul, T. Choi, C. P. Lutz, A. Ardavan, and A. J. Heinrich, *Electron Paramagnetic Resonance of Individual Atoms on a Surface*, Science **350**, 417 (2015).

[4] T. L. Cocker, D. Peller, P. Yu, J. Repp, and R. Huber, *Tracking the Ultrafast Motion of a Single Molecule by Femtosecond Orbital Imaging*, Nature **539**, 7628 (2016).

[5] S. Li, S. Chen, J. Li, R. Wu, and W. Ho, *Joint Space-Time Coherent Vibration Driven Conformational Transitions in a Single Molecule*, Phys. Rev. Lett. **119**, 176002 (2017).

[6] C. L. Degen, F. Reinhard, and P. Cappellaro, *Quantum Sensing*, Rev. Mod. Phys. **89**, 035002 (2017).

[7] F. Troiani, A. Ghirri, M. G. A. Paris, C. Bonizzoni, and M. Affronte, *Towards Quantum Sensing with Molecular Spins*, Journal of Magnetism and Magnetic Materials **491**, 165534 (2019).

[8] D. Peller, L. Z. Kastner, T. Buchner, C. Roelcke, F. Albrecht, N. Moll, R. Huber, and J. Repp, *Sub-Cycle Atomic-Scale Forces Coherently Control a Single-Molecule Switch*, Nature **585**, 7823 (2020).

[9] L. Wang, Y. Xia, and W. Ho, *Atomic-Scale Quantum Sensing Based on the Ultrafast Coherence of an H_2 Molecule in an STM Cavity*, Science **376**, 401 (2022).

[10] C. A. Schmuttenmaer, *Exploring Dynamics in the Far-Infrared with Terahertz Spectroscopy*, Chem. Rev. **104**, 1759 (2004).

[11] T. Kampfrath, K. Tanaka, and K. A. Nelson, *Resonant and Nonresonant Control over Matter and Light by Intense Terahertz Transients*, Nature Photon **7**, 9 (2013).

[12] V. Jelic, K. Iwaszczuk, P. H. Nguyen, C. Rathje, G. J. Hornig, H. M. Sharum, J. R. Hoffman, M. R. Freeman, and F. A. Hegmann, *Ultrafast Terahertz Control of Extreme Tunnel Currents through Single Atoms on a Silicon Surface*, Nature Phys **13**, 6 (2017).

[13] S. Yoshida, H. Hirori, T. Tachizaki, K. Yoshioka, Y. Arashida, Z.-H. Wang, Y. Sanari, O. Takeuchi, Y. Kanemitsu, and H. Shigekawa, *Subcycle Transient Scanning Tunneling Spectroscopy with Visualization of Enhanced Terahertz near Field*, ACS Photonics **6**, 1356 (2019).

[14] K. Kimura, Y. Morinaga, H. Imada, I. Katayama, K. Asakawa, K. Yoshioka, Y. Kim, and J. Takeda, *Terahertz-Field-Driven Scanning Tunneling Luminescence Spectroscopy*, ACS Photonics **8**, 982 (2021).

[15] N. T. Yardimci, S.-H. Yang, C. W. Berry, and M. Jarrahi, *High-Power Terahertz Generation Using Large-Area Plasmonic Photoconductive Emitters*, IEEE Transactions on Terahertz Science and Technology **5**, 223 (2015).

[16] Z. Dai, Q. Su, D. Lu, L. Sun, and W. Liu, *A Combined Experimental and Theoretical Study on the Terahertz Vibrations of Water Vapors*, Spectrochimica Acta Part A: Molecular and Biomolecular Spectroscopy **214**, 277 (2019).

[17] Y. Luo, V. Jelic, G. Chen, P. H. Nguyen, Y.-J. R. Liu, J. A. M. Calzada, D. J. Mildenberger, and F. A. Hegmann, *Nanoscale Terahertz STM Imaging of a Metal Surface*, Phys. Rev. B **102**, 205417 (2020).

[18] S. Yoshida, Y. Arashida, H. Hirori, T. Tachizaki, A. Taninaka, H. Ueno, O. Takeuchi, and H. Shigekawa, *Terahertz Scanning Tunneling Microscopy for Visualizing Ultrafast Electron Motion in Nanoscale Potential Variations*, ACS Photonics **8**, 315 (2021).

[19] K. Yoshioka, I. Katayama, Y. Arashida, A. Ban, Y. Kawada, K. Konishi, H. Takahashi, and J. Takeda, *Tailoring Single-Cycle Near Field in a Tunnel Junction with Carrier-Envelope Phase-Controlled Terahertz Electric Fields*, Nano Lett. **18**, 5198 (2018).

[20] M. Müller, N. Martín Sabanés, T. Kampfrath, and M. Wolf, *Phase-Resolved Detection of Ultrabroadband THz Pulses inside a Scanning Tunneling Microscope Junction*, ACS Photonics **7**, 2046 (2020).

[21] M. Abdo, S. Sheng, S. Rolf-Pissarczyk, L. Arnhold, J. A. J. Burgess, M. Isobe, L. Malavolti, and S. Loth, *Variable Repetition Rate THz Source for Ultrafast Scanning Tunneling Microscopy*, ACS Photonics **8**, 702 (2021).

CHAPTER 2

Pulsed THz Rectification Spectroscopy on Single Molecules and Atoms[†]

2.1 Abstract

We report pulsed THz rectification spectroscopy (TRS) on various single molecules and atoms by the combination of a femtosecond THz laser with a scanning tunneling microscope (STM). In pulsed-TRS, THz induced rectification current is monitored as a function of sample bias. While chemical sensitivity is obtained similarly to inelastic electron tunneling spectroscopy (IETS), laser polarization control in TRS reveals the distinctive role of the electric and magnetic field components of THz radiation. Furthermore, THz induced population change in single two-level systems further enables measurement with simultaneous spatial and temporal resolutions.

[†] This chapter by Likun Wang, Yunpeng Xia, and W. Ho is prepared for submission.

2.2 Article

It has been more than twenty years since the demonstration of single molecule IETS measurements with STM [1]. Based on the nonlinearity of the junction, originating from inelastic tunneling associated with excitations of the adsorbed molecule, IETS was widely employed to fingerprint atoms and molecules [2,3]. To extract the small inelastic tunneling current, a sinusoidal wave modulation is applied to the sample bias through a lock-in amplifier, as schematically shown in Figure 2.1(a). A Taylor series expansion provides an approximation of the total tunneling current with the second harmonic signal proportion to the IETS intensity. Similar to the sinusoidal wave modulation in IETS measurement, microwave radiation has been introduced into the STM junction to perform the microwave rectification spectroscopy (MRS) [4,5]. Here, the high frequency microwave is further chopped by a low frequency square wave to extract the microwave induced rectification current. Despite showing similar chemical sensitivity and atomic-scale spatial resolution, the polarization control of the external radiation is still lacking, prohibiting a full study of the rectification spectroscopy. On the other hand, the sub-picosecond coherent excitation in single atoms and molecules has yet to be demonstrated in either IETS or MRS. Such time dependent studies would advance quantum information processing.

Recent experiments have introduced femtosecond pulses into the STM junction to probe the ultrafast coherence of single molecules with atomic-scale spatial resolution far below the diffraction limit [6–9]. Depending on the specific molecular system under study, THz electric field assisted tunneling electron or THz photon absorption triggers the ultrafast dynamics, which can be monitored by the time resolved THz induced rectification current. Pulsed-TRS has been demonstrated on single H_2 molecules, showing a significant difference with IETS [9]. It is thus desirable to apply pulsed-TRS and explore a broad range of single atoms and molecules. In pulsed-

TRS, the power of optical techniques, such as polarization and time resolution, is combined with the STM to advance precision measurements of nanoscale systems.

In this letter, we demonstrate the pulsed-TRS on various types of single atoms and molecules by combining femtosecond THz laser pulses with a home built STM. By monitoring the THz induced rectification current as a function of the sample bias, distinctive spectroscopic features are revealed over individual atoms and molecules. Compared to IETS, the extra control on the polarization of the incident THz electromagnetic waves discloses effects of both the electric and magnetic field components on the measured TRS. Time resolved TRS with pump-probe THz pulses further provides ultrafast time evolution of the spectroscopic features in single molecules.

Experiments on various types of atoms and molecules were performed in a home built STM at a base temperature of 9.0 K and with silver (Ag) tips. The experimental setups for IETS, single beam TRS, and time resolved double beam TRS measurements are shown in Figure 2.1(a)-(c). The THz pulses with a repetition rate of 1 GHz were generated from a plasmonic photoconductive antenna [10] and aligned through flat silver mirrors and focused into the STM junction by a convex Tsurupica lens of 4 in. focal length. Additional details of the fs THz-STM experimental setup and the THz power measurement are described in the Supplemental Materials and Figure S2.1. Throughout the measurements, the sinusoidal wave bias modulation for IETS and square wave intensity modulation of THz pulses for TRS are both set at a frequency of 263.03 Hz.

Figure 2.1 Experimental setups for three different modulation techniques. (a) Schematic diagram of the experimental setup for IETS with STM. The black curve at the bottom illustrates the sine-wave modulation for IETS with a frequency of 263.03 Hz. (b) Schematic diagram of the experimental setup for single beam TRS with STM. A beam of THz pulses with 1 GHz repetition rate is focused into the junction. The THz beam is further square wave modulated at 263.03 Hz with ~ 1.9 million THz pulses in each modulation period, as illustrated schematically by the green curve at the bottom. (c) Schematic diagram of the experimental setup for time resolved double beam TRS with STM. A combination of two beams of THz pulses with a variable delay time between them is focused into the junction. The combined THz beam is further square wave modulated at 263.03 Hz with ~ 3.8 million THz pulses in each modulation period, as illustrated schematically by the green curve at the bottom.

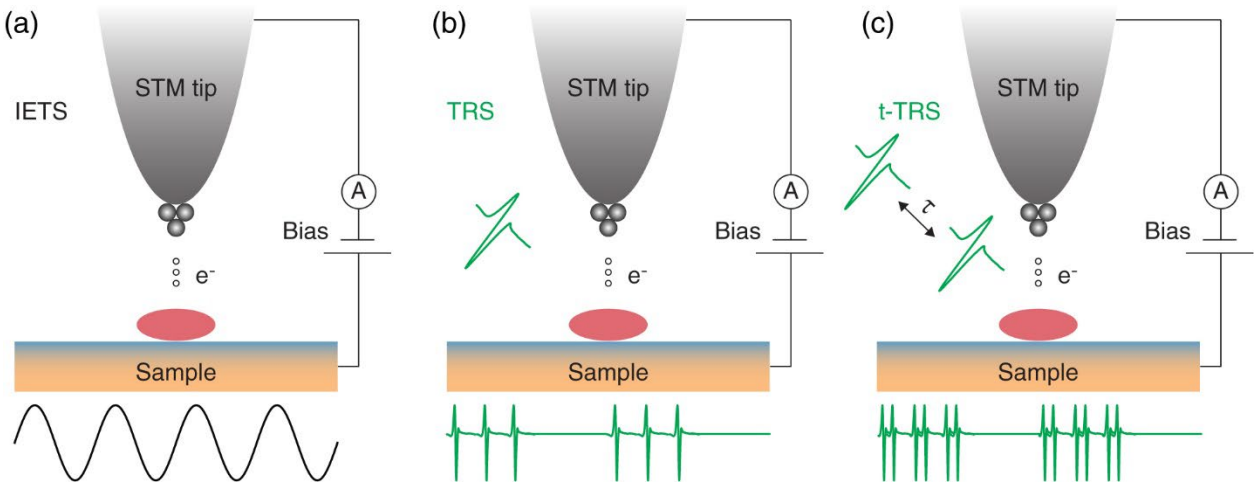
(a)
IETS
STM tip
Bias
A
e⁻
Sample
(b)
TRS
STM tip
Bias
A
e⁻
Sample
(c)
t-TRS
STM tip
τ
Bias
A
e⁻
Sample

To demonstrate the universality of the pulsed TRS with STM, we studied four distinct molecular and atomic species adsorbed on different surfaces, namely H_2 on copper nitride (Cu_2N), nickelocene ($NiCp_2$) on Cu(001), cobalt (Co) on NiAl(110), carbon monoxide (CO) on Cu(001), as shown in Figure 2.2. The STM topography of Cu_2N surface is shown in Figure 2.2(a) with the image contrast greatly enhanced by the existence of H_2 molecule trapped in the junction [11]. In Figure 2.2(b), the IETS measurement of H_2 shows the hindered vibration mode at ±18 mV and hindered rotation mode at ±44 mV. By introducing a single THz beam into the junction, we performed the pulsed TRS of H_2 as shown in Figure 2.2(c) with the same condition as IETS. Comparing to the IETS in Figure 2.2(b), single beam TRS shows similar vibrational and rotational excitation energies but with different spectral line shapes. For example, the peak-dip feature of the rotational mode at -44 mV in IETS changes to a pure peak in TRS, which can be explained by the molecular response to bias modulation at different frequencies. It is worth noting that the peak and dip features in H_2 TRS are closely related to the STM tip structure. Previous studies have proved H_2 in the STM junction as a two-level system (TLS) in a double well potential [12–14,9] which can be greatly affected by modifying the tip, resulting in a low energy separation in the THz frequency range between the two levels. Resonant absorption of THz photons becomes possible and the population of H_2 molecule can be considerably altered. In this case, not only the line shape but also the peak position and the number of peaks in TRS will appear differently from IETS.

In contrast to the H_2 molecule, the TRS of $NiCp_2$, Co, and CO share the same spectra line shape as the corresponding IETS, as shown in Figure 2.2(d)-(l). A direct comparison of the peak width of TRS with IETS allows us to estimate the effective THz voltage developed in the junction [9]. With an increased THz power, a broadening effect can be seen in TRS of all three molecules as shown in Figure S2.2. The peak intensity of H_2 TRS increases linearly with THz

power, whereas the $NiCp_2$ and Co TRS tend to saturate at high THz power. Due to the limited THz power generated from the PCA and the low signal intensity, we were not able to perform power dependence of TRS over the CO molecule.

Figure 2.2 Comparison of IETS with single beam TRS over single molecules and atom. (a) Constant current STM topography of the Cu_2N surface. Image size 16.7 Å × 16.7 Å. Scanning condition: –20 mV/0.3 nA. (b) STM-IETS measurement of H_2 with root-mean-square (RMS) bias modulation of 3 mV. Tip is placed at the position marked in (a) with –20 mV/0.3 nA setpoint. (c) Single beam TRS measurement of H_2 over the same position and setpoint as in (b). (d)-(f) STM topography, IETS, and TRS of a single nickelocene ($NiCp_2$) molecule adsorbed on Cu(001) surface. Image size 25.1 Å × 25.1 Å. Scanning condition: 50 mV/50 pA. Tip is placed at the position marked in (d) with –20 mV/0.8 nA setpoint for IETS and TRS measurements. A bias modulation of 3 mV is applied for the IETS measurement. (g)-(i) STM topography, IETS, and TRS of single Co atoms adsorbed on NiAl(110) surface. Image size 50.2 Å × 50.2 Å. Scanning condition: 100 mV/40 pA. Tip is placed at the position marked in (g) with 25 mV/0.9 nA setpoint for IETS and TRS measurements. A bias modulation of 1 mV is applied for the IETS measurement. (j)-(l) STM topography, IETS, and TRS of a single carbon monoxide (CO) molecule adsorbed on Cu(001) surface. Image size 25.1 Å × 25.1 Å. Scanning condition: 100 mV/0.1 nA. Tip is placed at the position marked in (g) with 25 mV/1 nA setpoint for IETS and 50 mV/10 nA setpoint for TRS measurements. A bias modulation of 1 mV is applied for the IETS measurement.

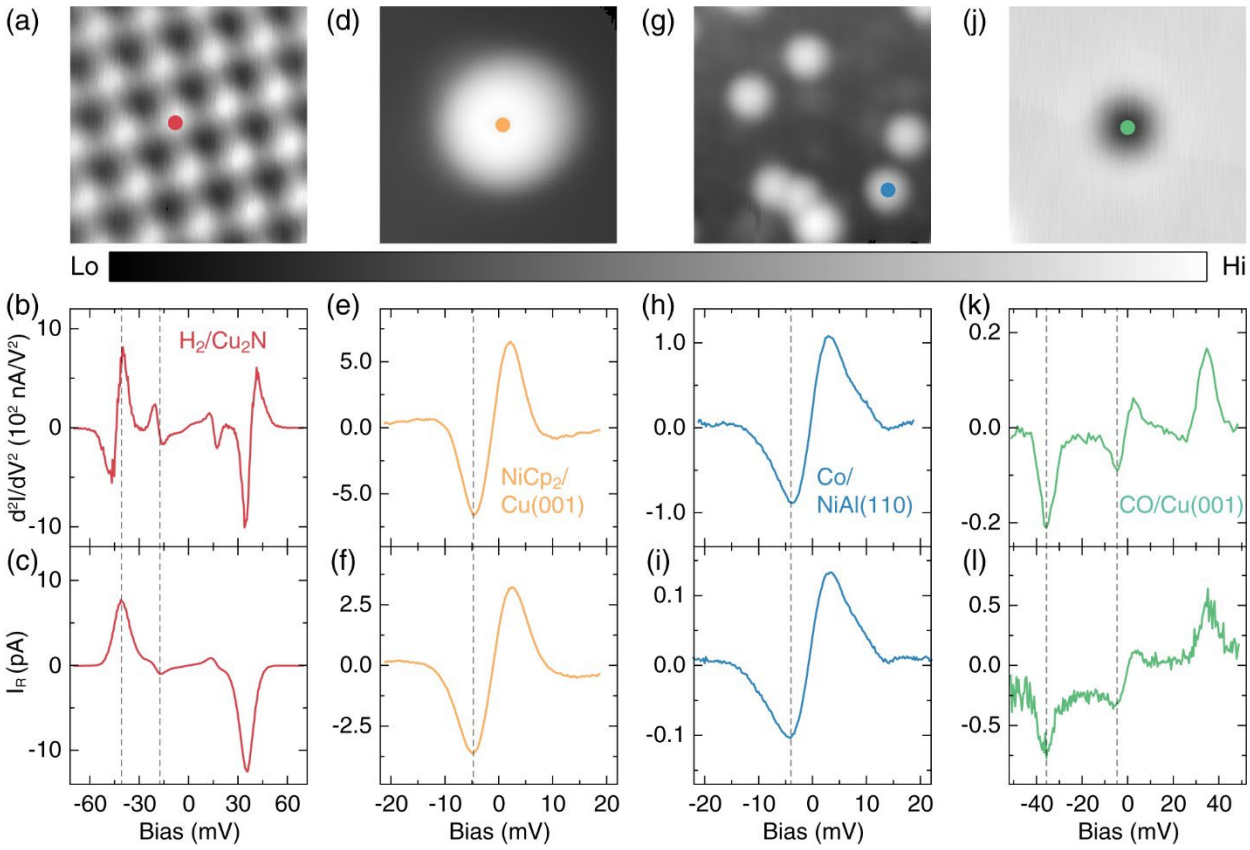
(a)
(d)
(g)
(j)
Lo
Hi
(b)
(e)
(h)
(k)
H2/Cu2N
NiCp2/
Cu(001)
Co/
NiAl(110)
CO/Cu(001)
d²I/dV² (10² nA/V²)
(c)
(f)
(i)
(l)
IR (pA)
Bias (mV)
Bias (mV)
Bias (mV)
Bias (mV)

A great advantage of using external THz pulses as a modulation to the sample bias is the ability to control the polarization of the THz electromagnetic waves. The polarization angle of the linearly polarized THz pulses can be easily varied by rotating the PCA while keeping the same applied voltage. It was found that the emitted THz power remained almost constant throughout the rotation from 0° to 360°. Here, the electric field of THz is parallel to the tip axis when the rotation angle is 0° and 180°, whereas 90° and 270° correspond to the THz electric field perpendicular to the tip axis. A large enhancement of the THz electric field at the junction is expected [15–17] when it is aligned with the tip axis, thus an increase on the THz rectification current. Indeed, the polarization dependence of the H_2 TRS shows a clear anisotropy on the peak intensity as shown in Figure 2.3(a). The peak intensity of TRS at 0° can be ~13 times as large as 90°. The detailed TRS at various polarization angles is shown in Figure S2.3.

The two states of the H_2 TLS originate from different adsorption configurations of H_2 in the STM junction. The ground and excited states can be dipole coupled by the THz electric field. The transition moment matrix element is thus proportional to the dipole matrix element and the peak THz electric field. When the THz electric field is enhanced the most at 0°, the light-matter interaction reaches the maximum. As a result, the rectification current is maximized at 0°, giving rise to the anisotropic polarization dependence of the TRS. The striking difference of the TRS between 0° and 90° can be seen in Figure 2.3(b) where the TRS at 90° almost disappeared.

An obvious difference is found between the polarization dependence of $NiCp_2$ and H_2. As shown in Figure 2.3(c) and (d), the polarization dependence of $NiCp_2$ is more isotropic with the rectification current at 0° only ~1.9 times as large as 90°. The TRS in Figure 2.3(d) is still prominent when the THz electric field is perpendicular to the tip axis. Considering the negligible voltage induced by the perpendicular THz electric field at the junction, it is unlikely that the

rectification current arises from the THz electric field induced voltage modulation. Instead, this strong signal at 90° can be explained by the magnetic field contribution from the irradiated THz electromagnetic wave [18–20]. The magnetic field is orthogonal to the electric field, thus becomes aligned with the tip axis when the polarization angle is 90°. $NiCp_2$ is known to possess an in-plane magnetic moment at the ground state (m=0) and an out-of-plane magnetic moment at the excited state (m=1) [21,22]. The spin-flip probability can be potentially increased when the THz magnetic field is in parallel with the out-of-plane magnetic moment [23]. As a result, the rectification current at 90° is still prominent even with a minimized THz electric field induced voltage modulation, as shown in Figure 2.3(d). The magnetic field contribution to the rectification current is further confirmed by the power dependence of TRS over $NiCp_2$ in Figure S2.2(c) and (d) with the THz polarization angle at 0°. The peak intensity deviates from the linear relationship and approaches saturated at high THz power. When the THz electric field is in parallel with the tip axis, the magnetic field is in-plane with the magnetic moment of the ground state of $NiCp_2$ (m=0). The rectification current increases with an increased THz electric field induced voltage modulation, whereas it can be decreased as the spin-flip process is suppressed by the THz magnetic field. As a result of this competing effect, the observed THz rectification current becomes less compared to the situation without the THz magnetic field. Similar to the $NiCp_2$ molecule, the isotropic polarization dependence is also observed on the Co atom adsorbed on NiAl(110) surface, as shown in Figure 2.3(e) and (f).

Figure 2.3 Polarization dependence of TRS measurements with 45° angle of incidence. (a) Peak intensity of single beam TRS measurements of H_2 adsorbed on Cu_2N surface with a series of polarization angles of the linearly polarized THz. The polarization angle is controlled by the rotation of the PCA. P-polarization with 0° corresponding to the THz electric field in the plane of incidence, 45° from the STM tip axis. Polarization rotation is in the plane perpendicular to the incidence direction (90° is s-polarized, perpendicular to the tip axis). All the measurements were performed with the same set point of -20 mV/0.3 nA. (b) TRS of H_2 at 0° and 90°. (c)-(d) Polarization dependence of TRS measurements over a single $NiCp_2$ molecule. All the measurements were performed with the same set point of -20 mV/0.8 nA. (e)-(f) Polarization dependence of TRS measurements over a Co atom. All the measurements were performed with the same set point of 25 mV/0.9 nA.

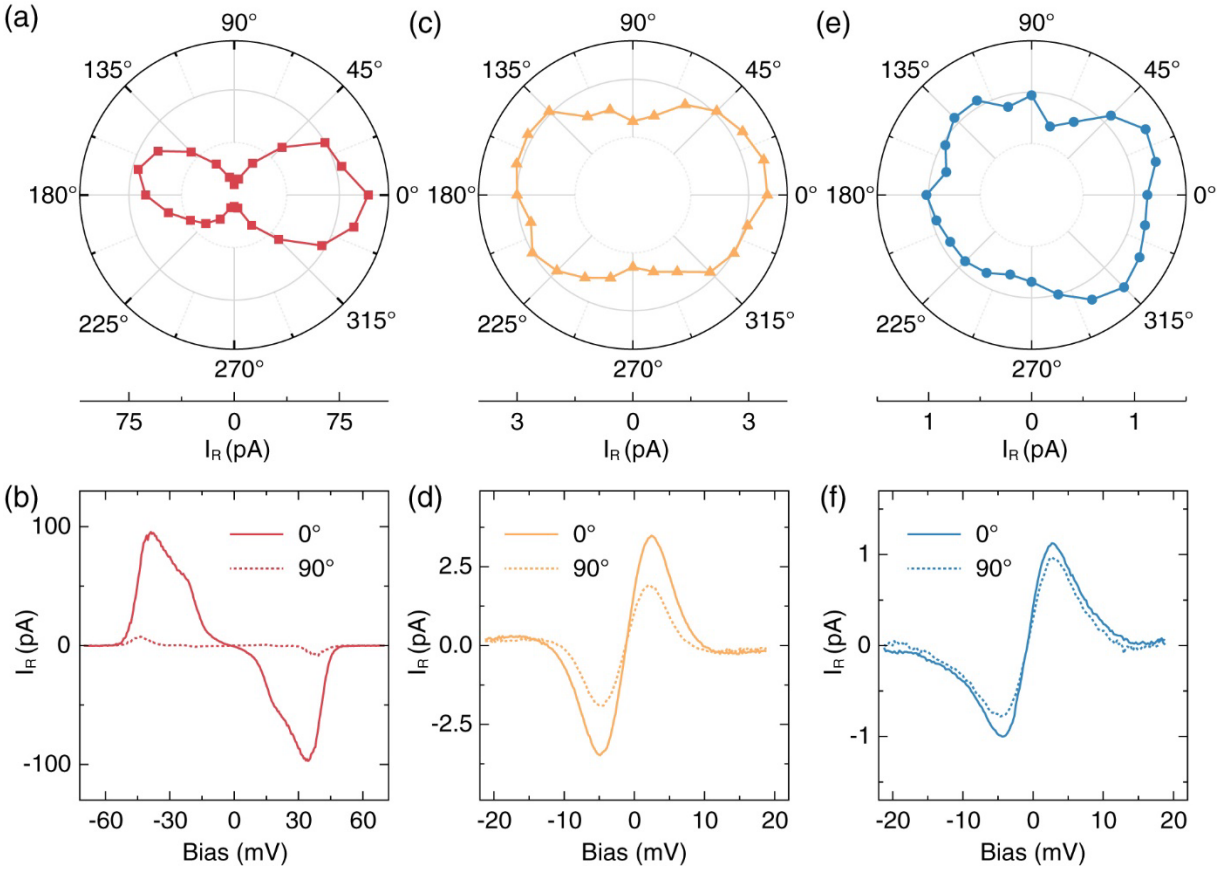
(a)
90°
135°
45°
180°
0°
225°
315°
270°
75
0
75
I_R (pA)
(c)
90°
135°
45°
180°
0°
225°
315°
270°
3
0
3
I_R (pA)
(e)
90°
135°
45°
180°
0°
225°
315°
270°
1
0
1
I_R (pA)
(b)
100
0
-100
I_R (pA)
0°
90°
-60
-30
0
30
60
Bias (mV)
(d)
2.5
0.0
-2.5
I_R (pA)
0°
90°
-20
-10
0
10
20
Bias (mV)
(f)
1
0
-1
I_R (pA)
0°
90°
-20
-10
0
10
20
Bias (mV)

In addition to the single beam TRS discussed above, a great advantage of introducing pulsed THz into the junction is its capability of performing pump-probe measurements. The time resolved TRS (t-TRS) allows us to track the spectra change as a function of the time delay between the two THz pulses and monitor the ultrafast coherence of a molecular system. In Figure 2.4(a)-(c), we compared the t-TRS at two different delays with the traditional IETS over the H_2 molecule adsorbed on Cu_2N surface. As the THz pulse width is ~0.5 ps, the t-TRS at 0.35 ps in Figure 2.4(b) can be effectively treated as a single beam TRS. A clear difference is observed in t-TRS compared to the IETS, including the peak width, peak position, and the peak number. Obviously, there is population change induced by THz irradiation. When the time delay is varied between the pump and probe THz pulses, the measured H_2 TLS population also varies. To monitor the time evolution of the TRS spectral change, we recorded the TRS over the same Cu_2N position while continuously changing the time delay, as shown in Figure 2.4(d). The peaks in TRS are clearly resolved in the negative bias range. While the peak position keeps fixed as the time delay is varied, the peak intensity oscillates periodically. This rectification current oscillation indicates a coherent oscillation on the observed population of the H_2 TLS. The oscillation period around 2.5 ps (0.4 THz in frequency) corresponds to the energy separation of the H_2 TLS. A gradual decrease on the oscillation period can be seen as the sample bias is swept from the negative to positive bias, which originated from the Stark effect of the energy levels of H_2 under the external electric field [9]. The THz rectification imaging based on the pump-probe measurements is further shown in Figure S2.4. In contrast to featureless IETS and single beam TRS imaging, time-resolved rectification imaging displays a much higher contrast of the Cu_2N surface, which enables us to probe the two dimensional electrostatic distribution of the underlying surface [9].

Figure 2.4 Time resolved TRS measurements of H_2. (a) IETS measurement of H_2 over Cu_2N with a bias modulation of 3 mV. Setpoint: –20 mV/40 pA. (b) Time resolved TRS measurement with a time delay of 0.35 ps between the two THz beams. Setpoint: -20 mV/40 pA. (b) Time resolved TRS measurement with a time delay of 2.10 ps between the two THz beams. Setpoint: -20 mV/40 pA. The dashed lines in (a)-(c) mark the excitation energies of the external vibration and rotation of adsorbed H_2 at –18 mV and –43 mV, respectively. (d) Color map of time resolved TRS measurement with a series of time delays between the two THz beams. All spectra were performed over the same position and with the same setpoint of -20 mV/40 pA

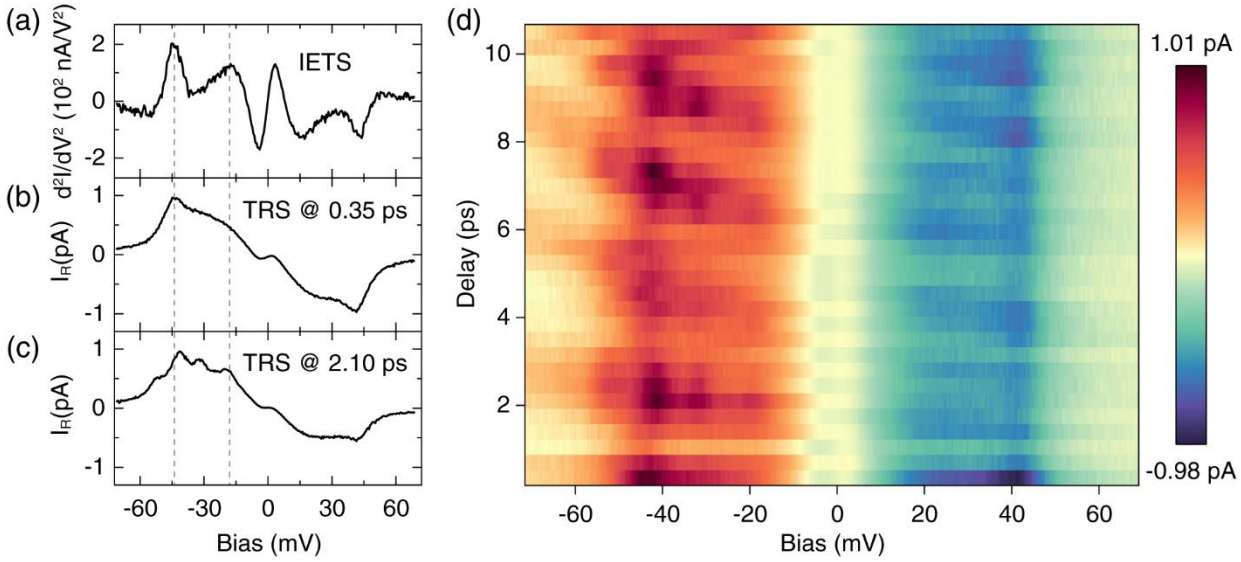
(a)
IETS
d²I/dV² (10² nA/V²)
(b)
TRS @ 0.35 ps
I_R(pA)
(c)
TRS @ 2.10 ps
I_R(pA)
Bias (mV)
(d)
Delay (ps)
Bias (mV)
1.01 pA
-0.98 pA

In summary, we have demonstrated pulsed TRS on single molecules and atoms by coupling femtosecond THz pulses with a low temperature STM. The pulsed TRS was shown to be not only comparable to the traditional IETS which exhibits the vibrational, rotational, or spin excitations of single molecules or atoms, but also greatly advantageous on the polarization control of the irradiating THz pulses. Both the electric field and magnetic field components of the THz were found to be involved in the TRS measurement, depending on the specific excitation processes. Furthermore, the time resolved TRS on single H_2 molecule tracks the ultrafast coherence of the H_2 TLS, which can be demonstrated by the time evolution of its spectroscopic features. Finally, the time resolved THz rectification imaging proclaimed the achievement of ultrafast coherence measurement with both femtosecond temporal and atomic-scale spatial resolutions. Our approach of pulsed THz rectification measurements can be applied to study the ultrafast dynamics of various systems including the proton transfer [24] and structural transformation [25] in molecules, and inter- and intralayer excitons in two dimensional materials [26,27].

2.3 Supplementary Information

Materials and Methods

Sample and Tip Preparation

All three experiments were performed in a home-built ultrahigh vacuum (UHV) scanning tunneling microscope (STM) operating at 9 K.

The same Cu(001) sample was used for H_2 and Nickelocene ($NiCp_2$) experiments. The Cu(001) surface was first cleaned by repeated cycles of Ne sputtering and annealing to 800 K. Clean N_2 gas was then introduced into the chamber to prepare Cu_2N islands by N_2 sputtering of the clean Cu(001) surface and annealing to 630 K. Hydrogen molecules from the UHV chamber background were adsorbed spontaneously onto the polar Cu_2N surface. $NiCp_2$ molecules were sublimed at room temperature onto the Cu(001) surface with prepared Cu_2N islands at 9 K via a variable leak valve. The $NiCp_2$ under study was adsorbed on the clean copper surface area.

For the Cobalt (Co) experiment, NiAl(110) surface was cleaned by repeated cycles of Ne sputtering and annealing to 1120 K. The clean NiAl(110) surface was exposed to clean O_2 gas at 780 K and annealed to 1070 K to form a thin Al_2O_3 film with a coverage of ~50%. Co atoms were evaporated onto the surface from a Knudsen cell doser. A current of 16.2 A was applied to the Tungsten filament (0.03” diameter) around the ceramic cell to evaporate the Co for 1 min. The Co under study was adsorbed on the clean NiAl(110) surface area.

THz Power Measurement

The THz power measurement in the THz-STM system is shown schematically in **Figure S2.1**(a). The power meter is a pyroelectric detector (Gentec-EO) operating in the THz range. The

lock-in technique was used for the THz power measurement by chopping the voltage applied onto the PCA at a frequency of 20 Hz. The THz power can be controlled by the applied voltage or the NIR power. The applied voltage was controlled by a home-made tunable voltage amplifier synchronized with the lock-in amplifier. The NIR power was controlled by a continuous neutral density filter. The THz power as a function of NIR power is shown in **Figure S2.1**(b), whereas it scales linearly with the applied voltage.

Figure S2.1 Schematic diagram of the fs THz-STM system and free space THz power measurement. (a) A pair of fs NIR pulses with equal power from a Mach–Zehnder interferometer is focused onto the plasmonic PCA to generate a pair of THz pulses. The time delay, τ, between the two pulses is controlled by a step motor with 1 nm resolution. THz pulses are then directed to the STM junction by flat silver mirrors and Tsurupica lenses. The THz generation and propagation to the crystal quartz window of the UHV chamber occur inside a homebuilt dry N_2 purged aluminum box to eliminate water absorption. A flat mirror (dashed) is placed in the THz propagation path when measuring the THz power with a pyroelectric power meter. The purge box is exposed to air during power measurement. (b) Single beam THz power as a function of the single beam NIR power received by the PCA. The red line is a second order polynomial fit of the data. The power is measured with a pyroelectric power meter as illustrated in (a).

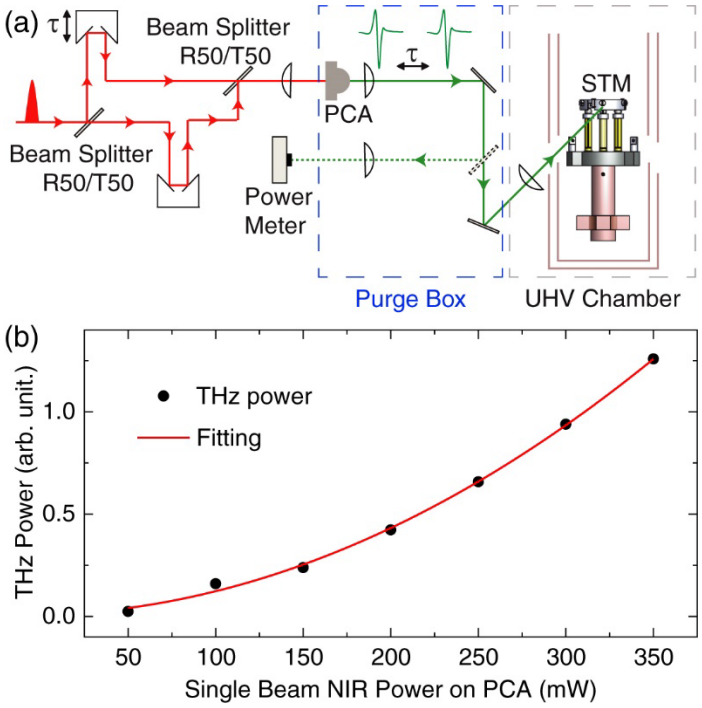
(a)
τ
Beam Splitter
R50/T50
Beam Splitter
R50/T50
PCA
τ
Power
Meter
STM
Purge Box
UHV Chamber
(b)
THz Power (arb. unit.)
0.0
0.5
1.0
THz power
Fitting
50
100
150
200
250
300
350
Single Beam NIR Power on PCA (mW)

Figure S2.2 THz power dependent single beam TRS of H_2, $NiCp_2$, and Co. (a) TRS of H_2 with various THz power. The THz power is controlled by changing the NIR laser power received by the plasmonic PCA. All the measurements were performed with the same setpoint of -20 mV/0.3 nA over the same position of Cu_2N. (b) Peak intensity of the measurements in (a). The red line is a linear fit of the data. (c) TRS of $NiCp_2$ with various THz power. The THz power is controlled by changing the voltage applied onto the plasmonic PCA. All the measurements were performed with the same setpoint of -20 mV/0.8 nA over the center of $NiCp_2$. (d) Peak intensity of the measurements in (c). The yellow line is a second order polynomial fit of the data. (e) TRS of Co with various THz power. The THz power is controlled by changing the voltage applied onto the plasmonic PCA. All the measurements were performed with the same setpoint of -20 mV/0.9 nA over the center of Co. (f) Peak intensity of the measurements in (e). The blue line is a second order polynomial fit of the data.

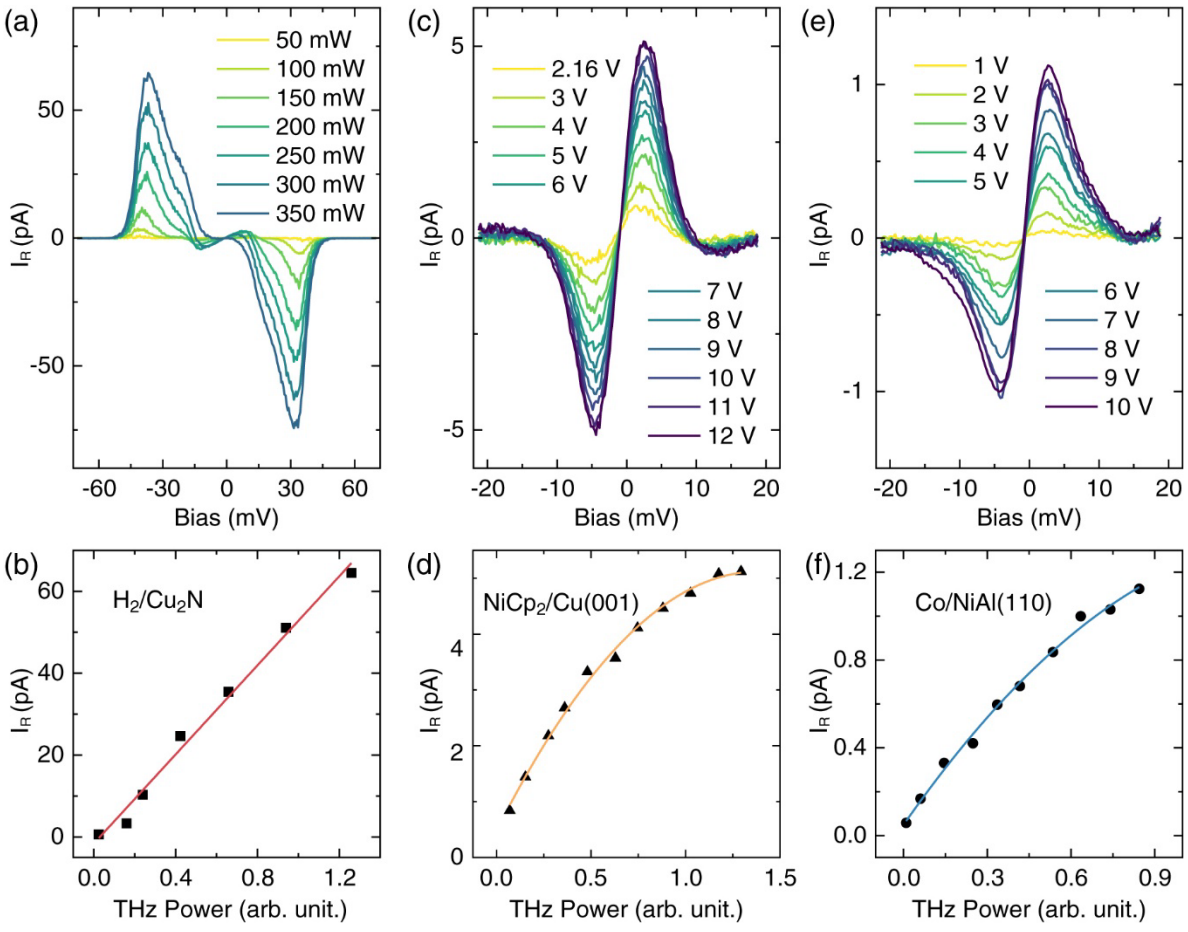
(a)
50 mW
100 mW
150 mW
200 mW
250 mW
300 mW
350 mW
I_R (pA)
Bias (mV)
(c)
2.16 V
3 V
4 V
5 V
6 V
7 V
8 V
9 V
10 V
11 V
12 V
I_R (pA)
Bias (mV)
(e)
1 V
2 V
3 V
4 V
5 V
6 V
7 V
8 V
9 V
10 V
I_R (pA)
Bias (mV)
(b)
H2/Cu2N
I_R (pA)
THz Power (arb. unit.)
(d)
NiCp2/Cu(001)
I_R (pA)
THz Power (arb. unit.)
(f)
Co/NiAl(110)
I_R (pA)
THz Power (arb. unit.)

Figure S2.3 Polarization dependent single beam TRS of H_2, $NiCp_2$, and Co. (a) TRS of H_2 at seven polarization angles from 0° to 90°. All the measurements were performed with the same setpoint of -20 mV/0.3 nA over the same position of Cu_2N. (b) TRS of $NiCp_2$ at seven polarization angles from 0° to 90°. All the measurements were performed with the same setpoint of -20 mV/0.8 nA over the center of $NiCp_2$. (c) TRS of Co at seven polarization angles from 0° to 90°. All the measurements were performed with the same setpoint of -20 mV/0.9 nA over the center of Co.

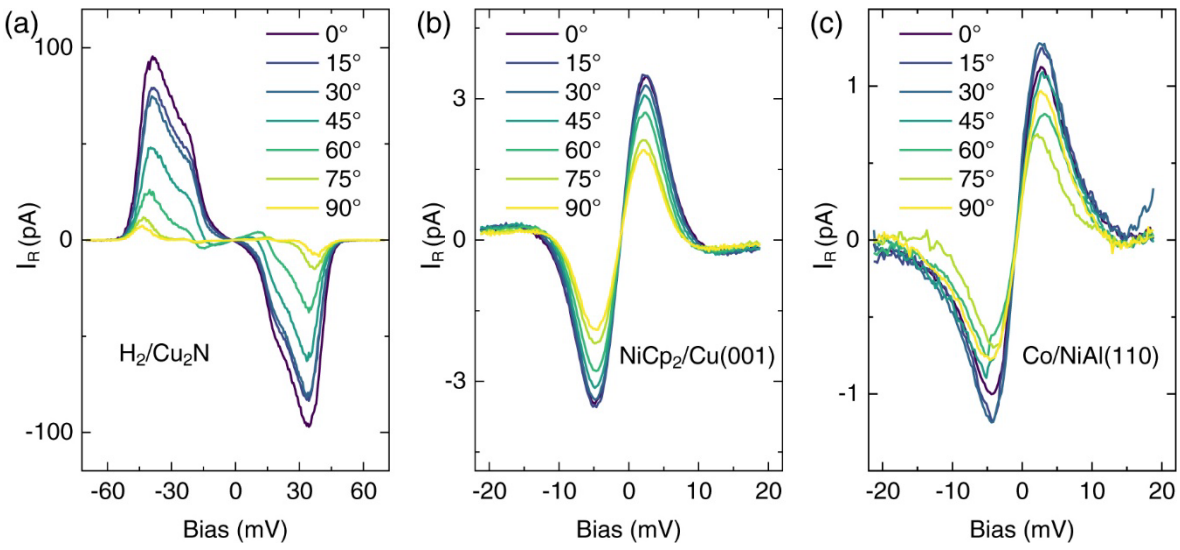
(a)
100
0
-100
I_R (pA)
0°
15°
30°
45°
60°
75°
90°
H_2/Cu_2N
-60
-30
0
30
60
Bias (mV)
(b)
3
0
-3
I_R (pA)
0°
15°
30°
45°
60°
75°
90°
$NiCp_2/Cu(001)$
-20
-10
0
10
20
Bias (mV)
(c)
1
0
-1
I_R (pA)
0°
15°
30°
45°
60°
75°
90°
Co/NiAl(110)
-20
-10
0
10
20
Bias (mV)

Figure S2.4 Comparison of IETS imaging with rectification imaging. (a) Constant current STM topography of the Cu_2N surface. Image size 12.6 Å × 12.6 Å. Scanning condition: –20 mV/40 pA. (b) STM topography same as (a) with the Cu_2N lattice structure superimposed. (c) IETS imaging of the Cu_2N surface. (d) Single beam THz rectification imaging of the Cu_2N surface. (e) Time-resolved THz rectification imaging of the Cu_2N surface at 8.6 ps after the pump pulse. (f) Time-resolved THz rectification imaging of the Cu_2N surface at 74.6 ps after the pump pulse. (c-f) were obtained at the same Cu_2N area as in (a). For each pixel in the images of (c-f), tip is positioned at setpoint –20 mV/40 pA, and then feedback is turned off and bias is ramped to –30 mV. Feedback is turned on before and during the tip movement to the next pixel.

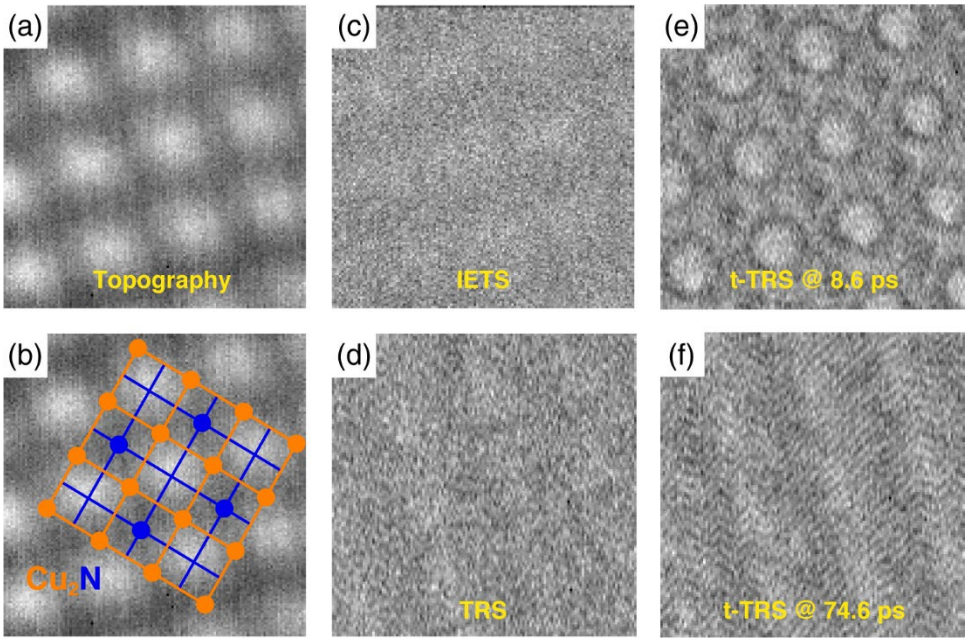
(a)
Topography
(c)
IETS
(e)
t-TRS @ 8.6 ps
(b)
Cu_2N
(d)
TRS
(f)
t-TRS @ 74.6 ps

Bibliography

[1] B. C. Stipe, M. A. Rezaei, and W. Ho, *Single-Molecule Vibrational Spectroscopy and Microscopy*, Science **280**, 1732 (1998).

[2] W. Ho, *Single-Molecule Chemistry*, J. Chem. Phys. **117**, 11033 (2002).

[3] A. J. Heinrich, J. A. Gupta, C. P. Lutz, and D. M. Eigler, *Single-Atom Spin-Flip Spectroscopy*, Science **306**, 466 (2004).

[4] J. Lee, X. Tu, and W. Ho, *Spectroscopy and Microscopy of Spin-Sensitive Rectification Current Induced by Microwave Radiation*, Nano Lett. **5**, 2613 (2005).

[5] X. W. Tu, J. H. Lee, and W. Ho, *Atomic-Scale Rectification at Microwave Frequency*, J. Chem. Phys. **124**, 021105 (2006).

[6] T. L. Cocker, D. Peller, P. Yu, J. Repp, and R. Huber, *Tracking the Ultrafast Motion of a Single Molecule by Femtosecond Orbital Imaging*, Nature **539**, 7628 (2016).

[7] S. Li, S. Chen, J. Li, R. Wu, and W. Ho, *Joint Space-Time Coherent Vibration Driven Conformational Transitions in a Single Molecule*, Phys. Rev. Lett. **119**, 176002 (2017).

[8] D. Peller, L. Z. Kastner, T. Buchner, C. Roelcke, F. Albrecht, N. Moll, R. Huber, and J. Repp, *Sub-Cycle Atomic-Scale Forces Coherently Control a Single-Molecule Switch*, Nature **585**, 7823 (2020).

[9] L. Wang, Y. Xia, and W. Ho, *Atomic-Scale Quantum Sensing Based on the Ultrafast Coherence of an H_2 Molecule in an STM Cavity*, Science **376**, 401 (2022).

[10] N. T. Yardimci, S.-H. Yang, C. W. Berry, and M. Jarrahi, *High-Power Terahertz Generation Using Large-Area Plasmonic Photoconductive Emitters*, IEEE Transactions on Terahertz Science and Technology **5**, 223 (2015).

[11] S. Liu, A. Shiotari, D. Baugh, M. Wolf, and T. Kumagai, *Enhanced Resolution Imaging of Ultrathin ZnO Layers on Ag(111) by Multiple Hydrogen Molecules in a Scanning Tunneling Microscope Junction*, Phys. Rev. B **97**, 195417 (2018).

[12] J. A. Gupta, C. P. Lutz, A. J. Heinrich, and D. M. Eigler, *Strongly Coverage-Dependent Excitations of Adsorbed Molecular Hydrogen*, Phys. Rev. B **71**, 115416 (2005).

[13] W. H. A. Thijssen, D. Djukic, A. F. Otte, R. H. Bremmer, and J. M. van Ruitenbeek, *Vibrationally Induced Two-Level Systems in Single-Molecule Junctions*, Phys. Rev. Lett. **97**, 226806 (2006).

[14] A. Halbritter, P. Makk, Sz. Csonka, and G. Mihály, *Huge Negative Differential Conductance in Au-H_2 Molecular Nanojunctions*, Phys. Rev. B **77**, 075402 (2008).

[15] T. L. Cocker, V. Jelic, M. Gupta, S. J. Molesky, J. A. J. Burgess, G. D. L. Reyes, L. V. Titova, Y. Y. Tsui, M. R. Freeman, and F. A. Hegmann, *An Ultrafast Terahertz Scanning Tunnelling Microscope*, Nat. Photon. **7**, 8 (2013).

[16] V. Jelic, K. Iwaszczuk, P. H. Nguyen, C. Rathje, G. J. Hornig, H. M. Sharum, J. R. Hoffman, M. R. Freeman, and F. A. Hegmann, *Ultrafast Terahertz Control of Extreme Tunnel Currents through Single Atoms on a Silicon Surface*, Nat. Phys. **13**, 6 (2017).

[17] M. Garg and K. Kern, *Attosecond Coherent Manipulation of Electrons in Tunneling Microscopy*, Science **367**, 411 (2020).

[18] T. Kampfrath, A. Sell, G. Klatt, A. Pashkin, S. Mährlein, T. Dekorsy, M. Wolf, M. Fiebig, A. Leitenstorfer, and R. Huber, *Coherent Terahertz Control of Antiferromagnetic Spin Waves*, Nat. Photon. **5**, 1 (2011).

[19] R. Zhou, Z. Jin, G. Li, G. Ma, Z. Cheng, and X. Wang, *Terahertz Magnetic Field Induced Coherent Spin Precession in $YFeO_3$*, Appl. Phys. Lett. **100**, 061102 (2012).

[20] V. Balos, G. Bierhance, M. Wolf, and M. Sajadi, *Terahertz-Magnetic-Field Induced Ultrafast Faraday Rotation of Molecular Liquids*, Phys. Rev. Lett. **124**, 093201 (2020).

[21] M. Ormaza et al., *Efficient Spin-Flip Excitation of a Nickelocene Molecule*, Nano Lett. **17**, 1877 (2017).

[22] G. Czap, P. J. Wagner, F. Xue, L. Gu, J. Li, J. Yao, R. Wu, and W. Ho, *Probing and Imaging Spin Interactions with a Magnetic Single-Molecule Sensor*, Science **364**, 670 (2019).

[23] R. T. Hammond, *Spin Flip Probability of Electron in a Uniform Magnetic Field*, Appl. Phys. Lett. **100**, 121112 (2012).

[24] T. Kumagai, F. Hanke, S. Gawinkowski, J. Sharp, K. Kotsis, J. Waluk, M. Persson, and L. Grill, *Controlling Intramolecular Hydrogen Transfer in a Porphycene Molecule with Single Atoms or Molecules Located Nearby*, Nat. Chem. **6**, 1 (2014).

[25] J. Gaudioso and W. Ho, *Steric Turnoff of Vibrationally Mediated Negative Differential Resistance in a Single Molecule*, Angewandte Chemie International Edition **40**, 4080 (2001).

[26] P. Steinleitner, P. Merkl, P. Nagler, J. Mornhinweg, C. Schüller, T. Korn, A. Chernikov, and R. Huber, *Direct Observation of Ultrafast Exciton Formation in a Monolayer of WSe_2*, Nano Lett. **17**, 1455 (2017).

[27] M. Plankl et al., *Subcycle Contact-Free Nanoscopy of Ultrafast Interlayer Transport in Atomically Thin Heterostructures*, Nat. Photon. **15**, 8 (2021).

CHAPTER 3

Atomic-scale Quantum Sensing Based on the Ultrafast Coherence of an H_2 Molecule in an STM Cavity[†]

3.1 Abstract

Scanning tunneling microscope (STM) combined with pump-probe femtosecond terahertz (THz) laser can provide the capability of coherence measurement of single molecules. We report THz pump-probe measurements that demonstrate quantum sensing based on a hydrogen molecule in the cavity created with an STM tip near a surface. Atomic-scale spatial and femtosecond temporal resolutions were obtained from this quantum coherence. The H_2 acts as a two-level system with its coherent superposition exhibiting extreme sensitivity to the applied electric field and the underlying atomic composition of the Cu_2N monolayer islands grown on a Cu(100) surface. We further acquire time resolved images of THz rectification of H_2 over Cu_2N islands for variable pump-probe delay times to visualize the sub-Ångström scale heterogeneity of the chemical environment.

[†] This chapter by Likun Wang, Yunpeng Xia, and W. Ho is reprinted with permission from Science, Volume 376, Issue 6591, pages 401-405, 2022.

3.2 Article

Quantum sensing and quantum computing, together with other quantum processes, have shown advantages over their classical counterparts [1,2]. Unlike quantum computing, which pursues the long decoherence time in a robust quantum system such as an isolated qubit, quantum sensing capitalizes on the weakness of a quantum system for its high sensitivity to the external environment. Although nitrogen-vacancy (NV) centers [3–6], trapped ions [7], and single electron transistors [8,9] have been used as quantum sensors, the large size of existing sensors or the limited experimental technique have not achieved atomic-scale spatial resolution.

Scanning tunneling microscope (STM) offers atomic-scale measurement and control of molecular systems in a surrounding environment that can be characterized by imaging [10]. A molecular quantum dot has been attached to the STM tip to measure the surface electric potential [11]. Electron spin resonance (ESR) sensors based on single magnetic atom functionalized tips have probed local magnetic field from atomic and molecular spins [12–16]. The combination of STM and femtosecond lasers has probed the temporal dynamics of molecular motions in the STM cavity with atomic-scale spatial resolution far below the diffraction limit [17–19].

Here, we study single H_2 molecules in the cavity defined by the Ag tip and a Cu_2N island grown on the Cu(100) surface using the combination of a femtosecond laser, corresponding to terahertz (THz) frequencies, with a low-temperature STM. By performing THz rectification spectroscopy (TRS) and THz pump-probe measurements, we demonstrate the sensitivity of the coherence of a single H_2 molecule to its immediate environment. The THz pulses in the STM cavity can couple two low-lying states of H_2 in a double-well potential and create a superposition that oscillates periodically with a frequency corresponding to the energy separation of the two

states. The damping of this coherent oscillation provides a measure of the decoherence time from the interaction of the two-level system (TLS) with its surrounding environment.

Experiments were performed in a home-built ultrahigh-vacuum (UHV) STM at a base temperature of 9.0 K and with silver (Ag) tips. A femtosecond Ti:Sapphire laser with 1-GHz repetition rate was used to generate THz pulses from a plasmonic photoconductive antenna (PCA) [20]. The THz pulses were aligned and focused into the cavity through flat silver mirrors and aspheric Tsurupica lenses. The experimental approach is shown schematically in Figure 3.1A, and additional details are described in the Supplementary Materials (Figure S3.1 and Figure S3.2).

Hydrogen molecules adsorb on a variety of materials, including metal surfaces [21], insulating layers [22–26], and single molecules [27,28]. To describe a H_2 molecule in the tunnel junction, a TLS in a double-well potential has been widely adopted [29,30], where the H_2 molecule switches between two different adsorption configurations [31] (Figure 3.1B). The population change from the predominant lower state $|a\rangle$ to upper state $|b\rangle$ can be greatly enhanced when the tunneling electrons have sufficient energy to excite H_2 external vibrational or rotational states [30] lying above the central barrier of the double-well potential.

With a H_2 molecule weakly trapped inside the STM cavity, the spatial resolution in constant current topography can be greatly enhanced [22]. A topographic image of an incommensurate Cu_2N island grown on Cu(100) [32] is shown in Figure 3.1C, with zoom in image in Figure 3.1D. By performing inelastic electron tunneling spectroscopy (IETS) measurements over different sites of the Cu_2N island (Figure 3.1E), we confirmed the presence of an H_2 molecule in the cavity [25–27]. The ν=0→1 excitation of the external-vibration at ±20 mV and j=0→2 (para-hydrogen) rotational excitation at ±43 mV did not show resolvable differences for the three high symmetry positions over Cu_2N.

The spatial variations of the charge distribution on the heteroatomic Cu_2N surface [33] were expected to induce a dipole moment in the adsorbed H_2 molecules. Femtosecond THz laser pulses irradiating the STM cavity can excite the TLS, change its population, and facilitate tunneling of H_2 between the two states. To extract the population change from the tunneling current induced by THz irradiation, we implemented atomic-scale rectification spectroscopy, initially demonstrated in the microwave frequency range [34,35]. The calibration of the absolute rectification current is shown in Figure S3. A peak voltage of 4.2 mV was derived from THz irradiation by comparing the peak width of IETS and TRS measurements. Further discussion on this weak THz field is given in the Supplementary Materials (Figure S3.4). Single-beam TRS shows unchanged vibrational and rotational excitation energies (Figure 3.1F) for the same tip-substrate separation and substrate positions as IETS in Figure 3.1E. However, the spectral line shapes in Figure 3.1, E and F, substantially differ because of population change in the H_2 TLS induced by the THz pulses.

Figure 3.1 IETS and TRS of H_2 over different sites of Cu_2N. (**A**) Schematic diagram of the THz-STM experimental setup. τ is the temporal delay between the pump-probe THz pulses. (**B**) Asymmetric double well potential of a H_2 molecule in the STM cavity. (**C**) Constant current topography of a Cu_2N island acquired with a Ag tip; image size 62.0 Å by 62.0 Å. Scanning condition: −20 mV/0.3 nA. (**D**) Zoom in topographic image of the Cu_2N island, 7.4 Å by 7.4 Å, with red (1), yellow (2), and blue (3) dots over the hollow, bridge, and top sites of the Cu_2N lattice, respectively. (**E**) STM-IETS measurements of H_2 molecule acquired with 3 mV root-mean-square (rms) bias modulation at 263.03 Hz. Tip is positioned at the three different positions labelled in (D) with −20 mV/40 pA set point. The black curve in the upper schematic illustrates the sine wave modulation for IETS. (**F**) TRS measurements of H_2 molecule over the three high-symmetry positions. Single beam of THz pulses is aligned into the junction with the same setpoint and chopped at the same frequency as the STM-IETS for acquiring the spectra. The green curve in the upper schematic illustrates modulation of the single THz beam for TRS. Within half of each square wave modulation period, a pulse train of ~1.9 million THz pulses are directed into the STM cavity. Dashed lines in (E) and (F) mark the excitation energies of the external-vibration and rotation at −20 mV and −43 mV, respectively. All of the spectra in (E) and (F) are offset vertically for clarity.

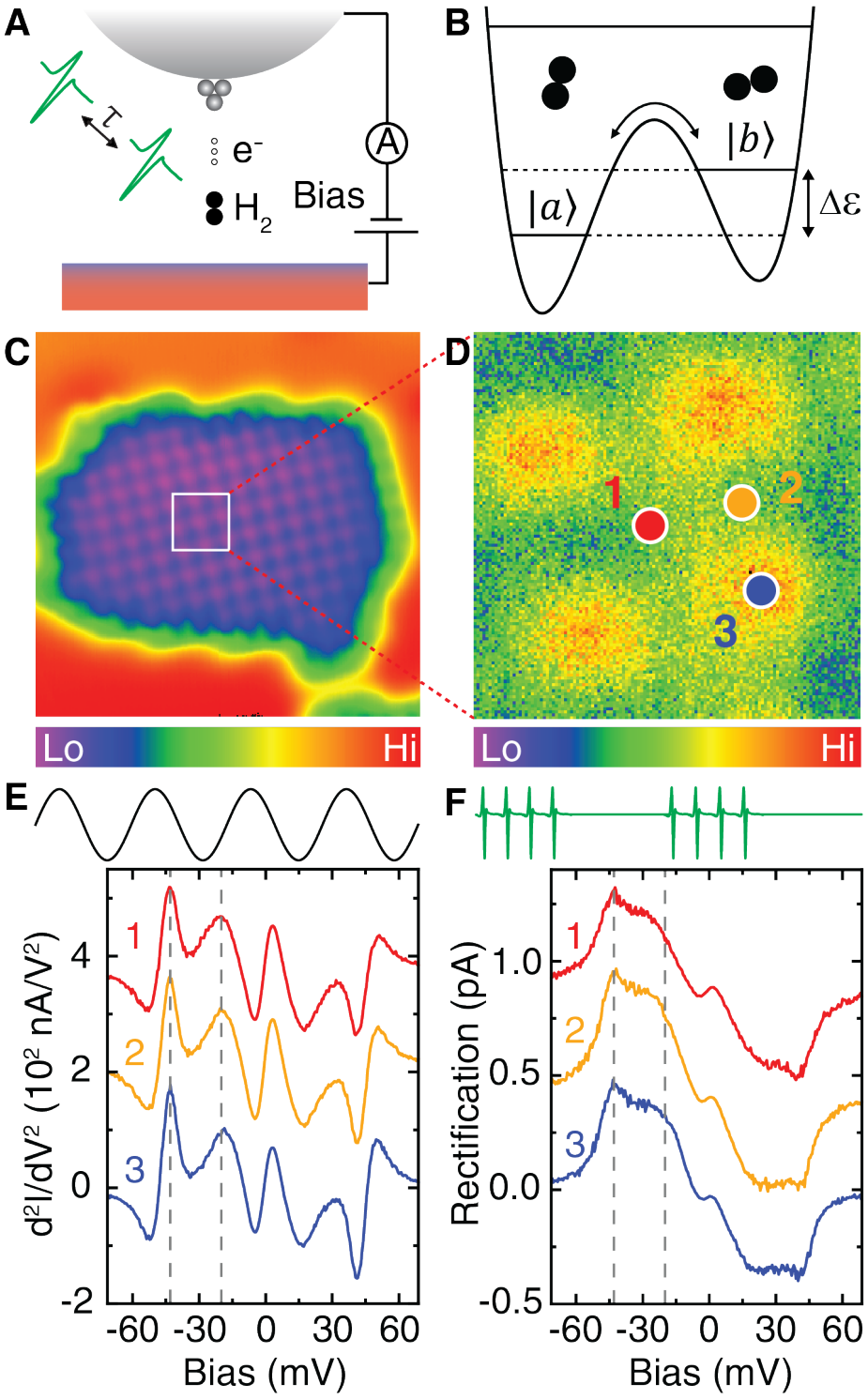
A
τ
e⁻
H2
Bias
A
B
|b⟩
|a⟩
Δε
C
D
Lo
Hi
Lo
Hi
1
2
3
E
F
d²I/dV² (10² nA/V²)
4
2
0
-2
-60 -30 0 30 60
Bias (mV)
Rectification (pA)
1.0
0.5
0.0
-0.5
-60 -30 0 30 60
Bias (mV)

To monitor the temporal evolution of the THz induced population change, THz pump-probe measurements were conducted over H_2 trapped between the STM tip and the Cu_2N surface. The rectification current was recorded as a function of the time delay, τ, between two nearly identical THz beams (Figure 3.2A). Coherent oscillations with temporal decay and beating were clearly resolved with the tip positioned over different positions of the Cu_2N island. At each of the three high-symmetry positions, a strong peak appeared in the fast Fourier transform (FFT) that corresponded to the main oscillation in the time domain. Additionally, the beating in each delay scan led to satellite peaks in the frequency domain. Similar oscillation was also seen in the spectral intensity of TRS for different delay times, as shown in Figure S3.5. Additional details and analyses are described in the Supplementary Materials.

The coherent oscillations of H_2 were sensitive to the position of the tip over the Cu_2N island (Figure 3.2A). The description of the Cu_2N lattice is given in Figure S3.6. No substantial difference in the vibrational and rotational excitation energies could be resolved by IETS and single-beam TRS for the STM tip over the three lateral positions of the Cu_2N layer. In contrast, the THz pump-probe measurements revealed largely distinct frequencies for the three positions (Figure 3.2B). For example, an oscillation frequency shift of 0.11 THz was recorded from position 2 (0.26 THz) to position 3 (0.37 THz), which corresponded to a sensitivity of 58 GHz/Å in the surface plane. The frequency difference was well resolved in the FFT spectrum even though the lateral distance between positions 2 and 3 was only 1.9 Å.

The lattice mismatch between Cu_2N and Cu(100) [32] and the asymmetry of the STM tip could induce multiple closely related configurations of H_2 and lift the degeneracy of the TLS energy levels, which led to satellite peaks in the FFT spectrum (Figure 3.2B). By fitting multiple sinusoidal functions with an exponential decay term to the coherent oscillations over each position

(Figure S3.7), we could also extract the decoherence time T_2, as shown in the inset of Figure 3.2B. Positions 1 and 3 showed similar T_2 around 45 ps, whereas position 2 exhibited a longer time of 80 ps. A set of THz pump-probe measurements with the STM tip over a series of the protrusion sites across the Cu_2N island is shown in Figure S3.8, illustrating the high spatial sensitivity of the coherent oscillations and surface heterogeneity. In addition, the coherent oscillation over position 1 of Figure S3.8A exhibited negligible beating and revealed a single peak located at 0.444 THz in the FFT spectrum as shown in Figure S3.9. The full-width at half-maximum (FWHM) of the peak was 4.3 GHz by fitting with a Gaussian peak. Taking the resolving power to be the separation of two peaks by the FWHM, the THz pump-probe measurements could resolve frequency shift of 4.3 GHz or energy resolution of 18 μeV.

The periodic arrangement of non-neutral Cu and N atoms determines the surface chemical environment distribution of Cu_2N [36,37]. When the tip was placed over the three high-symmetry positions with the same setpoint, the H_2 molecule trapped inside the cavity exhibited different dipole moments caused by the heterogeneous atomic composition of the underlying surface. As a result, the energy separation of the two levels changes, making the H_2 molecule a sensitive probe of the surface chemical environment.

The effect of intermolecular interactions from other adsorbed H_2 molecules was ruled out with the observation of a constant oscillation frequency at various H_2 concentrations (Figure S3.10). Unlike the IETS and single-beam TRS which showed no resolvable position-dependent differences on the excitation energies, THz pump-probe measurements probing the TLS coherence showed an advantage in sensing changes in the molecular environment. In addition to the frequency shift, the decoherence time of the oscillations also exhibited spatial dependence at the atomic scale.

Figure 3.2 THz pump-probe measurements of H_2 over different positions of Cu_2N. (**A**) Time domain measurements of the THz rectification current through H_2 over three lateral positions. The tip is positioned over the correspondingly colored spots with the feedback setpoint –20 mV/40 pA. The feedback is then turned off and sample bias is ramped to −30 mV for the measurements. All of the spectra are offset vertically for clarity. The green curve in the upper schematic illustrates modulation of THz pump-probe beams for TRS. Within half of each square wave modulation period, a pulse train including ~1.9 million THz pulse pairs is directed into the STM cavity. Inset: Constant-current STM topography of Cu_2N surface, 7.4 Å by 7.4 Å, showing the tip positions (1, 2, and 3) and lines connecting the Cu and N atoms in the two sub-lattices. (**B**) FFT results of the corresponding measurements in (A). Inset: Decoherence times extracted from fitting of the data shown in (A).

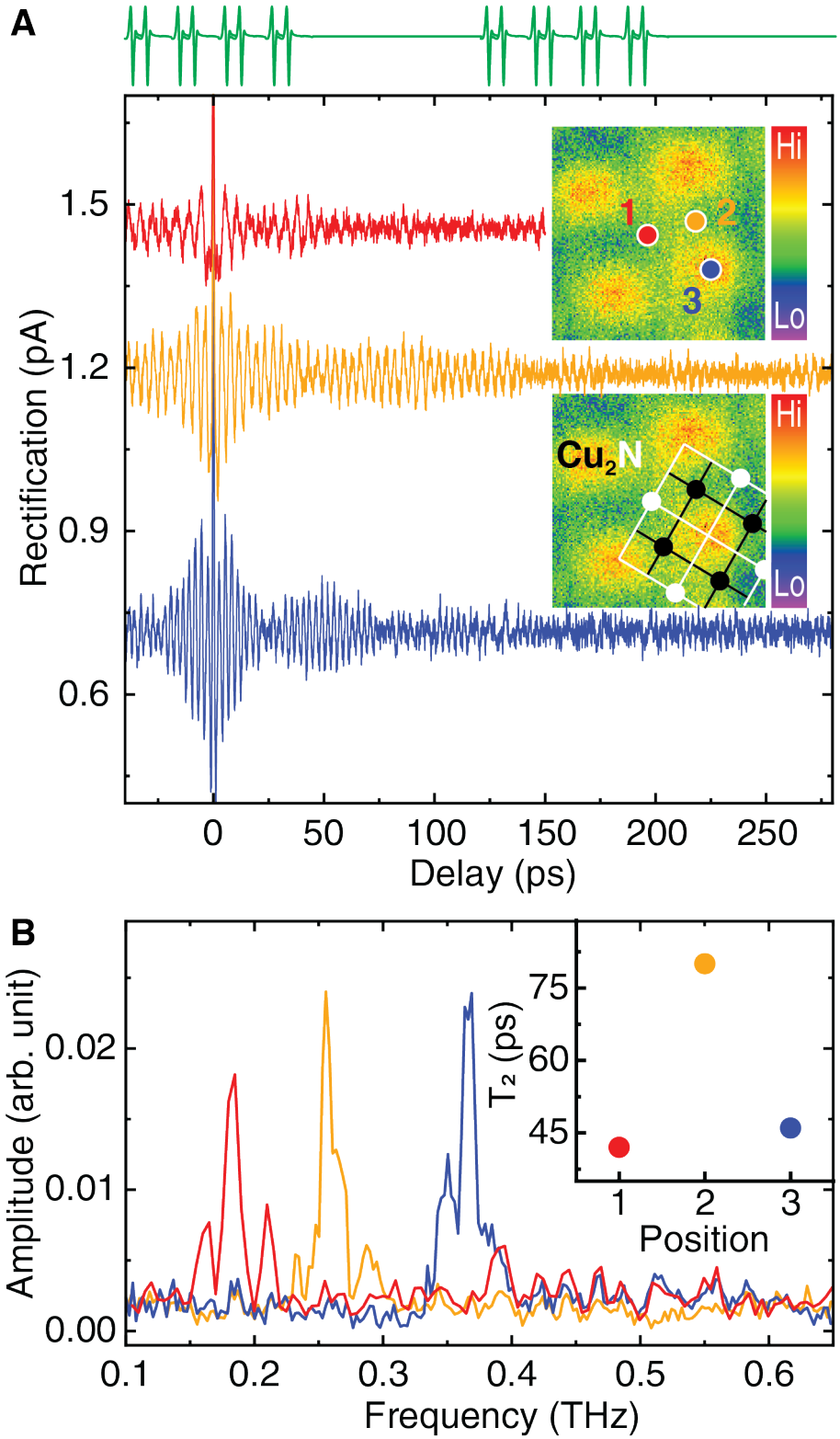
A
Rectification (pA)
1.5
1.2
0.9
0.6
0
50
100
150
200
250
Delay (ps)
Hi
Lo
1
2
3
Cu2N
B
Amplitude (arb. unit)
0.02
0.01
0.00
0.1
0.2
0.3
0.4
0.5
0.6
Frequency (THz)
T2 (ps)
75
60
45
1
2
3
Position

The energy difference of the TLS could also be tuned by varying the tip-substrate separation which was controlled by adjusting the tunneling current at constant sample bias. As the tunneling current increased from 0.02 to 0.2 nA, the tip moved toward the surface by ~1 Å. A series of THz pump-probe measurements at different tip-substrate separations (Figure 3.3A) showed that as the tip approached the substrate, the coherent oscillation gradually became weaker. The color map of the measurements in Figure S3.11B showed changes in the oscillation period and amplitude as a function of tip-substrate separation.

The frequency from the FFT exponentially increased as the tip-substrate separation decreased in Figure 3.3B. A frequency sensitivity of 0.19 THz/Å in the normal direction (tunneling gap) was determined. Both the oscillation amplitude and decoherence time decreased when the tip-substrate separation decreased in Figure 3.3A, suggesting a stronger coupling of the H_2 molecule with the junction environment. The variation in the tip-substrate separation across the Cu_2N lattice was only ~0.03 Å, as measured from the line cut in Figure S3.6F. This height variation contributed ~0.006 THz to the frequency shift observed in Figure 3.2B.

To provide further insight into the change in the energy separation of the TLS, we varied the sample bias while monitoring the coherent oscillations (Figure 3.3, C and D). The oscillation frequency increased by ~0.2 THz upon changing the sample bias from −50 mV to 40 mV (Figure 3.3E). The total electric field experienced by the H_2 molecule trapped in the STM cavity was a combination of the surface electrostatic field and the DC field from the sample bias. As we altered the sample bias without changing the tip position or tip-substrate separation, the DC field varied while the surface electrostatic field remained the same. Because the energy levels shifted under external field through the Stark effect, the energy separation of the TLS changed. Analysis and fitting of the data in Figure 3.3E yielded a surface electrostatic field of 43 mV/Å pointing toward

the surface. In addition, the dipole moment difference of the two states along this field was extracted and found to be ~0.6 Debye. Details of the fitting are described in the Supplementary Materials. Besides varying the sample bias, the coherent oscillation frequency could also be shifted for different tips under the same sample bias (Figure S3.12). Effectively, the DC fields varied with tip structure from different tips, which modified the total electric field acting on the H_2 and thus changed its oscillation frequency.

Figure 3.3 Coherent oscillation dependency on tip-substrate separation and sample bias. (**A**) THz pump-probe measurements at various tip-substrate separations. The separation is controlled by ramping the tunneling current before turning the feedback off at –20 mV. The bias is then ramped to –30 mV to take the measurements. The colored texts label the corresponding change of tip-substrate separation. (**B**) Oscillation frequency at each change of tip-surface separation from FFT of the time domain measurements in (A); the red line is an exponential fit. (**C**) THz pump-probe measurements at various sample biases. The sample bias is controlled by ramping the bias after turning the feedback off at –20mV/40pA. The colored texts label the corresponding sample bias. (**D**) Color map of a series of THz pump-probe measurements, some of which are displayed in (C); the change of the coherent oscillation as a function of sample bias can be visualized. For clarity, the intensity of all of the spectra is normalized positively to the color palette with range (0,1). (**E**) Oscillation frequency at each bias from FFT of the time domain measurements in (C); the red line is a fitting of the data with function described in the Supplementary Materials.

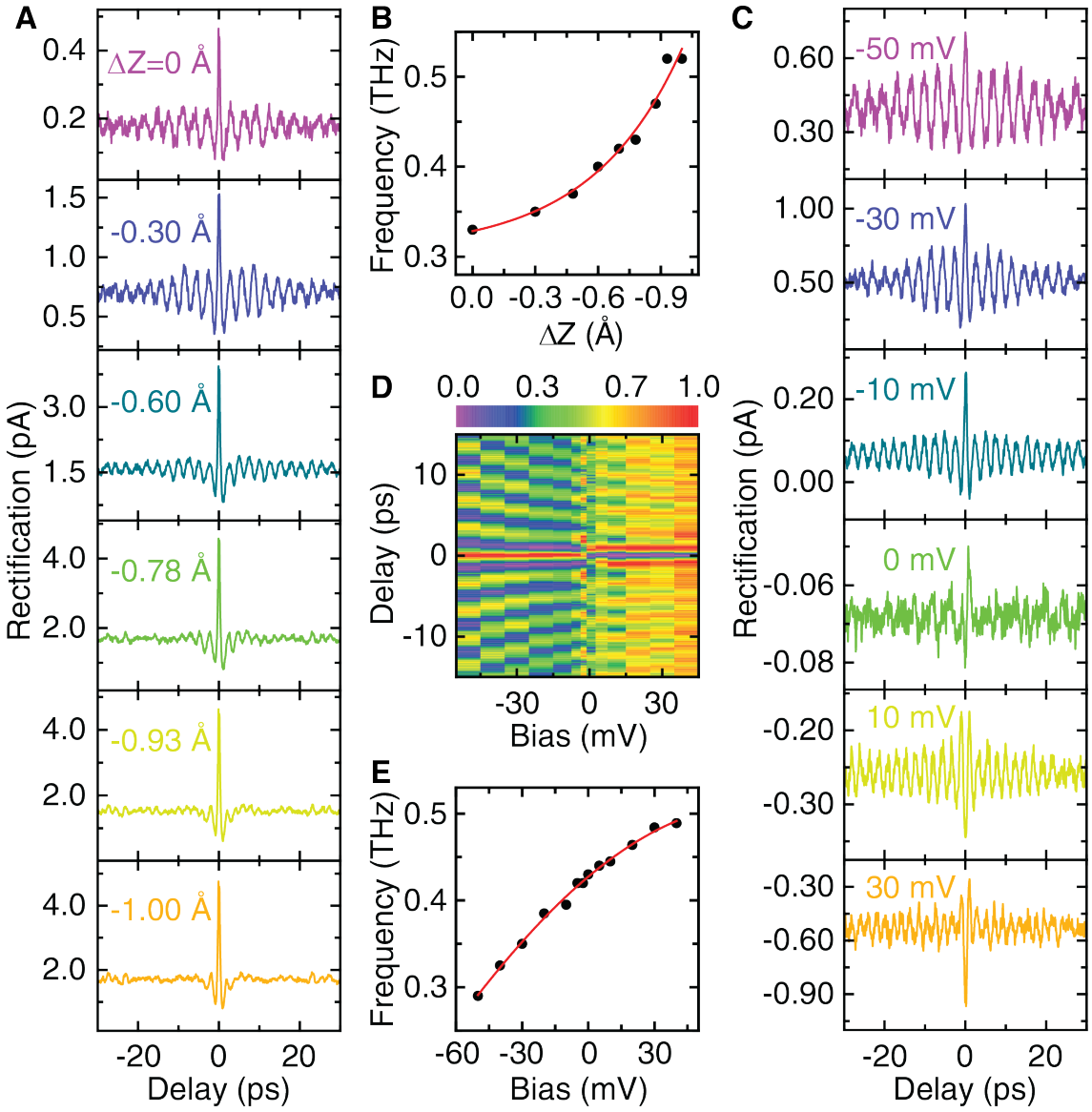
A
ΔZ=0 Å
-0.30 Å
-0.60 Å
-0.78 Å
-0.93 Å
-1.00 Å
Rectification (pA)
Delay (ps)
B
Frequency (THz)
ΔZ (Å)
C
-50 mV
-30 mV
-10 mV
0 mV
10 mV
30 mV
Rectification (pA)
Delay (ps)
D
Delay (ps)
Bias (mV)
E
Frequency (THz)
Bias (mV)

We acquired THz rectification images in real space with atomic-scale spatial and femtosecond-scale temporal resolutions. The spectroscopic features of the TLS exhibited temporal evolution that sensitively depended on the molecule's surrounding environment in the surface plane. As shown in Figure 3.4, a series of constant-height THz rectification imaging was recorded at different time delays between pump-probe pulses. These images provided temporal snapshots of the spatial variations of the H_2 TLS coherence caused by the heterogeneity of the surface. Four successive images of the whole Cu_2N island (Figure 3.4, A to D) revealed the wave-like evolution of the 'ripples' from the upper left to the bottom right of the island.

A series of images (Figure 3.4, E to P), zooming in the yellow square window in Figure 3.4A, revealed the alternation of the ripple features between bright and dark, or high and low rectification current, as a function of the time delay. Two sequences of temporal snapshots were composed and viewed as Movie S3.1 and Movie S3.2. The properties of the coherent oscillations were highly sensitive to the lateral position of STM tip, as shown in Figure 3.2 and Figure S3.8. In rectification imaging at a chosen delay, the tip was located over different positions of the surface. The oscillation frequency shifted spatially because the surface chemical environment experienced by the H_2 TLS varies over different positions of the surface. The decoherence time also changed as a response to the local environment sensed by the H_2. As a result, the spatially resolved rectification imaging at different delay times effectively revealed the surface chemical environment distribution of the Cu_2N island.

Figure 3.4 Temporal snapshots of THz rectification imaging of Cu_2N surface at various delay times. (**A** to **D**) Rectification imaging of the entire Cu_2N island at four different delays. For each pixel in the images, tip is positioned at setpoint –20 mV/40 pA, and then feedback is turned off and bias is ramped to –30 mV. Feedback is turned on prior to and during the tip movement to the next pixel. All images are 53.2 Å by 44.9 Å and 266 by 224 pixels. (**E** to **P**) Series of zoom in rectification images at various delays. All images are 13.8 Å by 13.8 Å and 137 by 137 pixels.

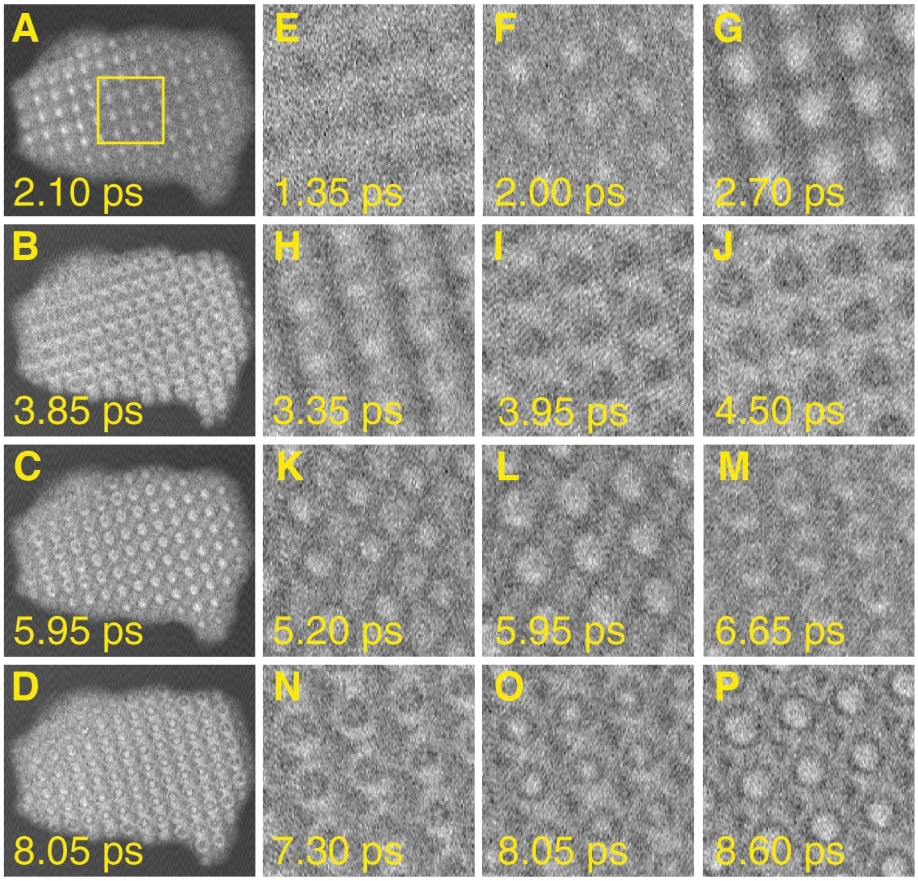
A
2.10 ps
E
1.35 ps
F
2.00 ps
G
2.70 ps
B
3.85 ps
H
3.35 ps
I
3.95 ps
J
4.50 ps
C
5.95 ps
K
5.20 ps
L
5.95 ps
M
6.65 ps
D
8.05 ps
N
7.30 ps
O
8.05 ps
P
8.60 ps

The extreme sensitivity of the H_2 TLS coherent oscillation to the applied electric field and the underlying surface chemical environment heralds the application of H_2 molecule in the STM cavity for extreme quantum sensing. Compared to other quantum sensors like NV centers in diamond, the H_2 coherent sensor in the STM cavity provides simultaneous atomic-scale spatial and femtosecond temporal resolutions with GHz energy discrimination. H_2 molecules have been found to be trapped over a variety of surfaces, atoms and molecules [22,24,27]. THz pump-probe measurements with H_2 molecule in the STM cavity can be used to probe the electrostatic field and potential energy surface of the sample. The ability to measure and control coherent oscillations of the H_2 TLS in different environments opens a route for quantum sensing of a broad range of systems from single atoms to heteroatomic molecules and solid surfaces.

3.3 Supplementary Information

Materials and Methods

Sample and Tip Preparation

The experiment was conducted in a home-built ultrahigh vacuum scanning tunneling microscope operating at 9 K. Electrochemically etched Ag tips were prepared in vacuo by three cycles of Ne sputtering and annealing. The Cu(100) surface was cleaned by repeated cycles of Ne sputtering and annealing to 800 K. The Cu_2N islands with various sizes and shapes were prepared by N_2 sputtering of the clean Cu(100) surface and annealing to 630 K. Hydrogen molecules from the background in the ultrahigh vacuum chamber were adsorbed spontaneously onto the polar Cu_2N surface. A stable H_2 concentration was reached in a month. We also desorbed the H_2 molecules by the NIR (820 nm) laser and dosed H_2 molecules onto the surface through a variable leak valve, giving no observable difference in the spectra and delay scan oscillations from the background H_2 in the ultrahigh vacuum chamber.

THz Generation and Characterization

Figure S3.1A shows the schematic diagram of the optical layout for THz generation and characterization using electro-optical sampling. The femtosecond near infrared (NIR) pulses were emitted from a Ti:Sapphire laser (Taccor ultra 8, Laser Quantum) with 1GHz repetition rate and 30 nm FWHM bandwidth centered at 820 nm. The laser output was split with 90% of the full power (1.6 W) used for THz generation and 10% for THz characterization. A stepping motor (Newport UTM100PP) was placed in the THz generation path to vary the delay between the NIR and THz pulses. THz pulses were generated by focusing the NIR pulses into a plasmonic photoconductive antenna (PCA) fabricated by Mona Jarrahi's group at UCLA. An indium tin oxide (ITO) coated glass was used to combine the THz pulses and NIR pulses. The two beams were then

focused onto a 500 um thick ZnTe crystal by a Tsurupica lens. The THz electric field induced a polarization change of the NIR beam which was detected by a pair of balanced photodiodes. The THz waveform in the time domain and spectrum in the frequency domain are shown in Figure S3.1B and C. THz generation and characterization were carried out inside an aluminum box sealed with o-rings and purged with dry N_2 gas to eliminate water absorption of the THz radiation.

Figure S3.1 Free space THz generation and characterization. (**A**) The single NIR laser beam is split into two beams by a R90/T10 beam splitter. A majority (90%) of the full power (1.6 W) is directed to the PCA for THz generation. The generated THz and the remaining 10% of the NIR laser beams are combined through an ITO glass with a time delay between the two laser pulses set by the step motor. (**B**) Electric field of the generated THz pulses from time domain measurement with the setup in (A). (**C**) Frequency domain spectrum showing the bandwidth of the generated THz pulses, obtained from FFT of the time domain spectrum in (B). (**D**) THz power as a function of the voltage applied to the PCA. The power is measured with a pyroelectric detector using the lock-in technique. The PCA voltage is chopped into a square wave of 20 Hz frequency from a voltage amplifier driven with the TTL output from the lock-in amplifier for internal referencing. The THz power is extracted from the first harmonic output of the lock-in amplifier.

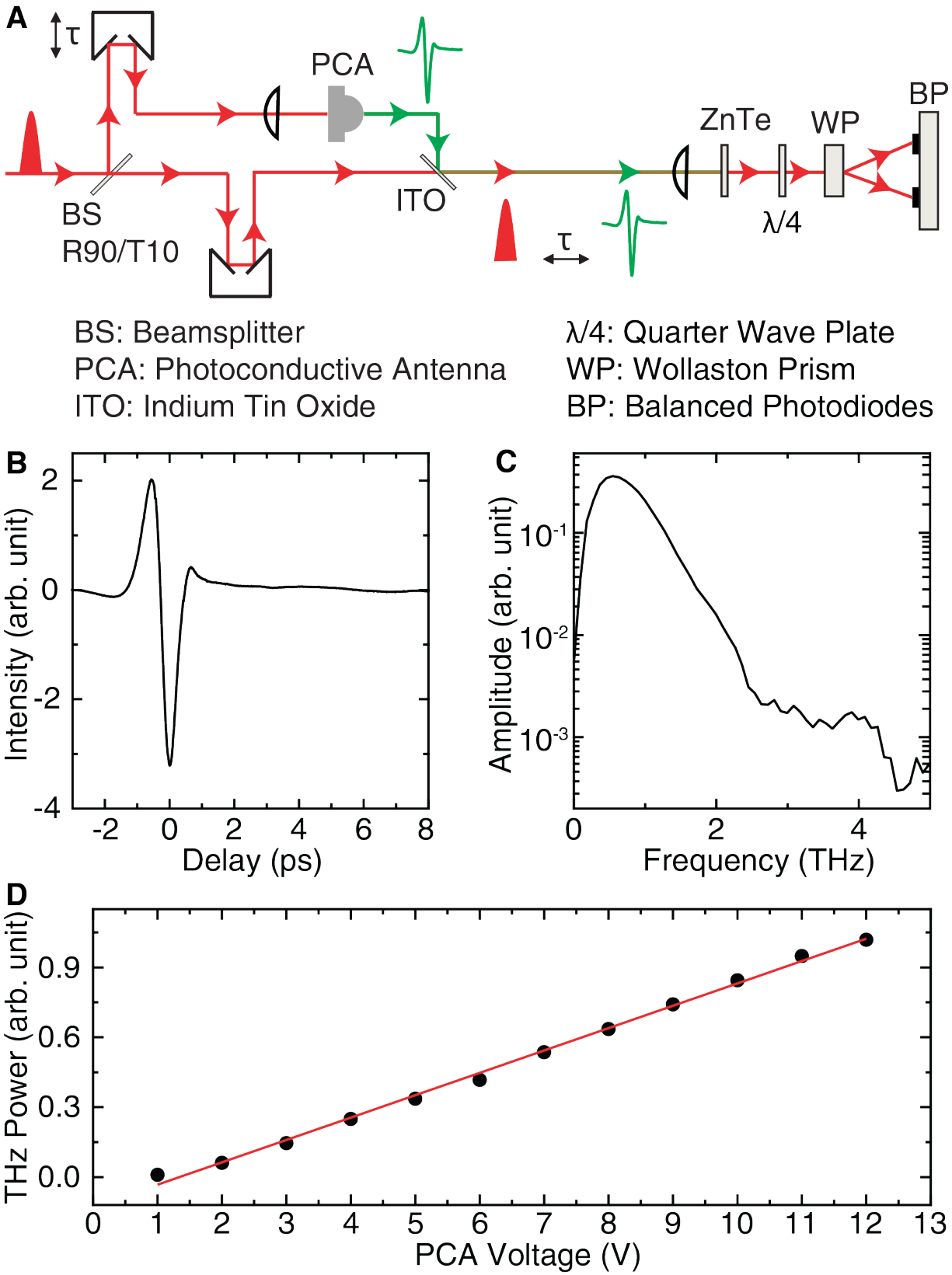
A
τ
PCA
ZnTe
WP
BP
BS
R90/T10
ITO
τ
λ/4
BS: Beamsplitter
PCA: Photoconductive Antenna
ITO: Indium Tin Oxide
λ/4: Quarter Wave Plate
WP: Wollaston Prism
BP: Balanced Photodiodes
B
Intensity (arb. unit)
Delay (ps)
C
Amplitude (arb. unit)
Frequency (THz)
D
THz Power (arb. unit)
PCA Voltage (V)

fs THz-STM Setup

The schematic diagram of our fs THz-STM setup is shown in Figure S3.2. To generate two THz beams with equal power, a laser beam from the Ti:Sapphire laser was split equally and recombined by a Mach-Zehnder interferometer. A translational stage was inserted into the path of one of the beams to impose the variable delay time τ. The generated THz pulse pairs with linear polarization were focused through a Tsurupica lens and aligned into the STM junction with the THz electric field component along the STM tip axis (p-polarization). The THz laser had a bandwidth of 0.1THz to 4 THz in free space and was narrowed down to about 0.1THz to 1THz in the STM junction. Due to the weak field of our THz source, there was negligible temperature increase and change of tip-substrate separation when the THz laser was focused and aligned into the junction.

Figure S3.2 Schematic diagram of the fs THz-STM setup. One single beam from the Ti:Sapphire laser is split equally into two beams by a 50%-50% beam splitter. The time delay between two beams is controlled by a step motor with 1nm resolution. The two beams are recombined by the second beam splitter and focused onto the plasmonic PCA to generate THz radiation. A 0 to 10 V square wave is applied to the PCA and modulates the THz beams to alternate between equal intervals of the on and off states at a frequency of 263.03 Hz. This amplitude modulation allows lock-in detection of the small THz induced rectification current (pA) as a function of the sample bias in THz rectification spectroscopy. The generated THz pulses are directed by two Ag mirrors and focused into the STM junction by a plano-convex Tsurupica lens (effective focal length of 4 in). The THz generation and propagation to the crystal quartz window of the UHV chamber occur inside a homebuilt THz box purged with dry N_2 to eliminate effects due to ambient water absorption.

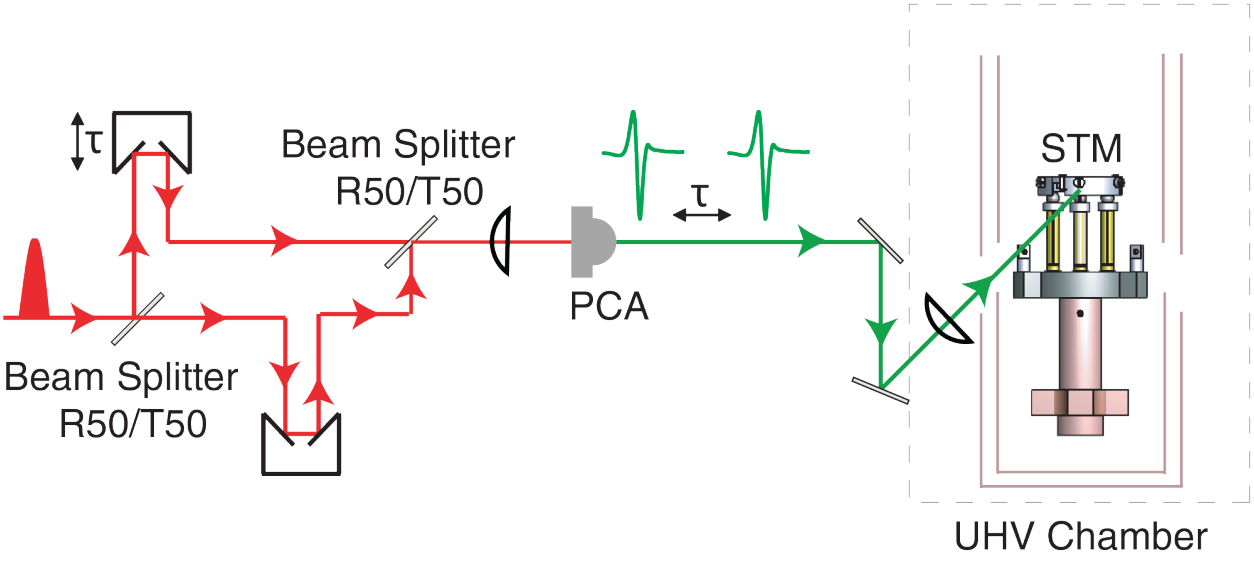
τ
Beam Splitter
R50/T50
τ
STM
Beam Splitter
R50/T50
PCA
UHV Chamber

STM-IETS and THz Rectification Spectroscopy

To perform STM-IETS measurements, a sine wave modulation of 3 mV root mean square (RMS) amplitude and 263.03 Hz frequency from the lock-in amplifier was applied to the DC sample bias. We turned off the feedback at a set point of −20 mV/40 pA, followed by linear ramping of the DC bias to acquire the STM-IETS spectra. The procedure was the same when the non-chopped THz radiation was additionally present in the junction.

For the THz rectification spectroscopy with either single THz beam or pump and probe beams, amplitude modulation was imposed from chopping the THz radiation by applying a 0 to 10 V square wave at 263.03 Hz to the PCA. The chopping frequency was set by the lock-in amplifier to implement internal referencing.

All the data presented in the main figures and Figure S3.4, S3.5, S3.6, S3.7, S3.8, S3.9, and S3.11 (S3.1 and S3.2 are schematic diagrams) were obtained with the same tip and over the same Cu_2N island. Figure S3. was obtained from a different tip over a nickelocene molecule adsorbed on Cu(100). Different tips over different Cu_2N islands showed variations on the oscillation frequency and decoherence time as shown in Figure S3.10 and S3.12.

Data Processing

All the STM topographies and THz rectification imaging snapshots were plane fit without further processing. The plane fit was to correct the slight sample slope. A 0.1 THz high-pass FFT filter was applied to all the THz pump-probe measurements to remove the long-range rectification current variations due to laser misalignment from increasingly large motions of the stepping motor for long pump-probe delays.

Supplementary Text

THz Field Calibration

As THz absorption induces population change of the TLS and modifies the nonlinearity in the conductance, the spectral lineshapes in IETS and TRS are quite different. It is thus difficult to calibrate the THz field amplitude at the junction through the comparison of the TRS with IETS over the H_2 molecule. Instead, we performed IETS and TRS over a nickelocene molecule which did not absorb THz radiation. As shown in Figure S3.A, TRS over nickelocene reproduced the spectrum from IETS taken with a V_{rms}=3 mV sine wave modulation at the same temperature. The matching peak width indicated a peak voltage of 4.2 mV developed at the junction from THz irradiation.

To calibrate the rectification current read from the lock-in amplifier, we subtracted the I-V curve without THz irradiation from the I-V curve with THz irradiation. The difference gave the absolute rectification current induced by THz irradiation. As can be seen in Figure S3.C, the I-V subtraction reproduced the TRS spectrum.

Figure S3.3 THz field calibration. (**A**) Comparison of STM-IETS and TRS over a nickelocene molecule adsorbed on Cu(001). Black curve is the IETS spectrum, which is acquired with 3 mV root mean square (rms) bias modulation at 263.03 Hz. Red curve is the TRS spectrum acquired with single beam THz irradiation chopped at the same frequency as the STM-IETS. The spectra are taken at the same –20 mV/0.8 nA setpoint and the same tip position over the molecule. The peak at 3.8 mV corresponds to the spin excitation in nickelocene (*10*). (**B**) Calibration of the rectification current from subtraction of I-V spectra. Black curve is obtained by subtracting the I-V curve without THz irradiation from the I-V curve with square wave modulated THz irradiation. Red curve is the TRS spectra acquired simultaneously with the square wave modulated THz irradiated I-V curve. (**C**) The slanted baseline of the black curve shown in (B) has been subtracted to get a more accurate value of the rectification current. The slant is due to subtraction of two curves to extract the small magnitude THz induced DC (rectification) current.

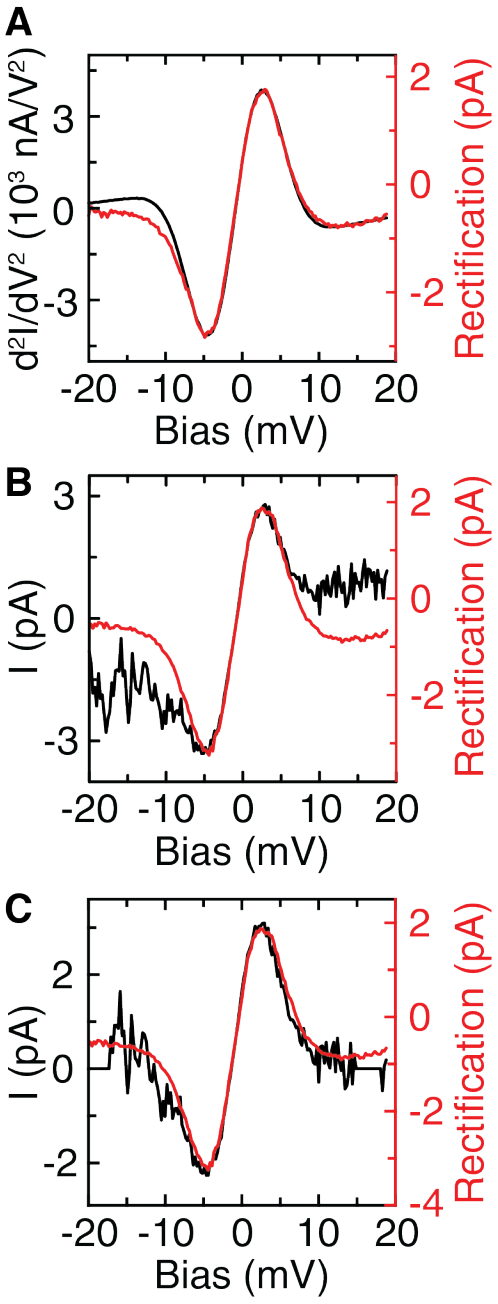
A
d²I/dV² (10³ nA/V²)
3
0
-3
2
0
-2
Rectification (pA)
-20 -10 0 10 20
Bias (mV)
B
I (pA)
3
0
-3
2
0
-2
Rectification (pA)
-20 -10 0 10 20
Bias (mV)
C
I (pA)
2
0
-2
2
0
-2
-4
Rectification (pA)
-20 -10 0 10 20
Bias (mV)

To confirm the weak field of our THz pulses, we also performed THz pump-probe measurements under a different THz power and by flipping the THz field direction. As shown in Figure S3.4A, the oscillation period remained the same for a weaker THz irradiation by reducing the voltage supplied to the PCA from 0 ~ +10 V to 0 ~ +5 V. As we flipped the THz field direction in Figure S3.4C by reversing the voltage applied to the PCA, both the oscillation period and the phase at zero delay remained unchanged.

Figure S3.4 Coherent oscillations showing the weak field of the THz pulses. (**A**) THz pump-probe measurements for different THz powers by adjusting the voltage applied onto the PCA. Both measurements are performed with the same −20 mV/40 pA setpoint. The bias is then ramped to −30 mV after feedback is turned off. (**B**) FFT of the corresponding measurements in (A) with both peaks at 0.35 THz. (**C**) Measurements performed with opposite THz field directions. By flipping the voltage applied to the PCA, the radiated THz field direction is reversed. Both measurements are performed under the same −20 mV/40 pA setpoint. The bias is then ramped to −42 mV after turning off the feedback. (**D**) FFT of the corresponding measurements in (C) with both peaks at 0.37 THz. Curves in (A) and (C) are offset vertically for clarity.

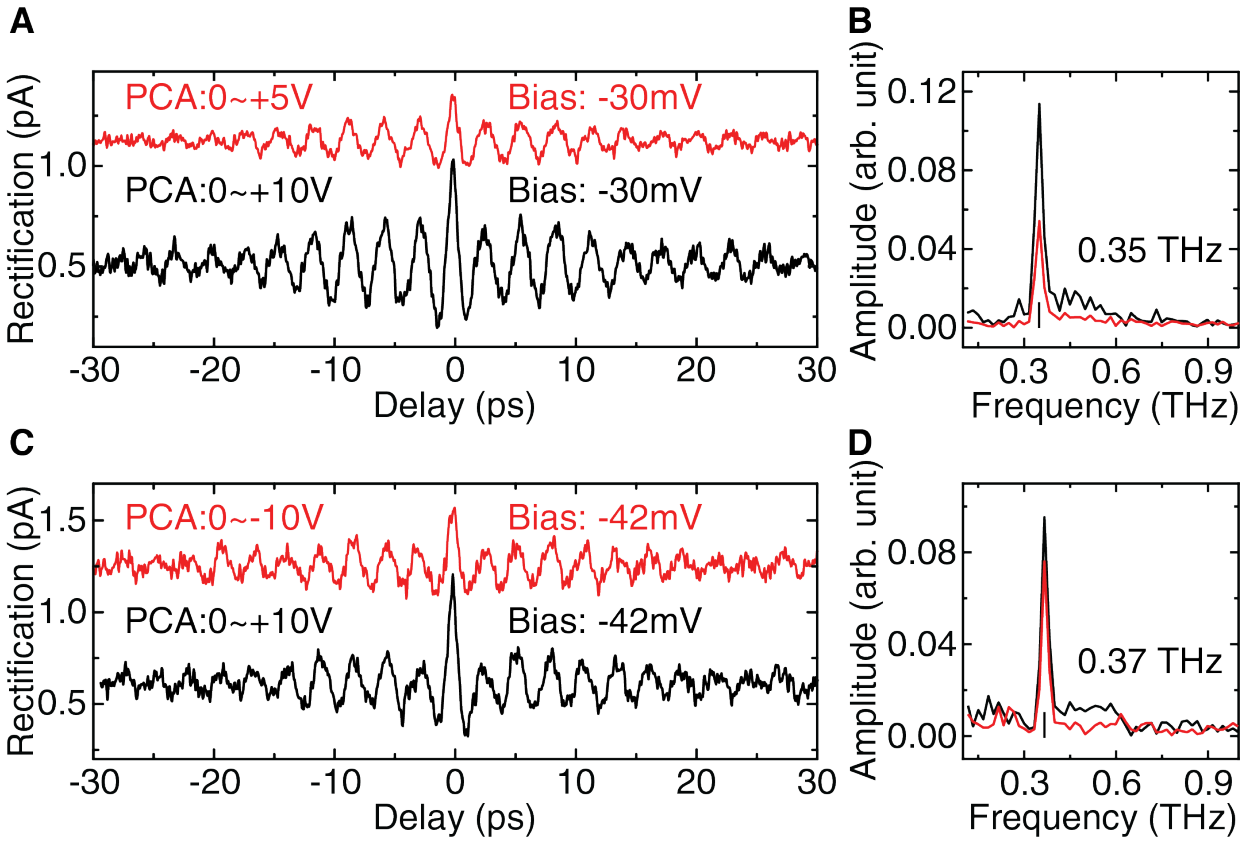
A
B
C
D
PCA:0~+5V
Bias: -30mV
PCA:0~+10V
Bias: -30mV
Rectification (pA)
Delay (ps)
Amplitude (arb. unit)
Frequency (THz)
0.35 THz
PCA:0~-10V
Bias: -42mV
PCA:0~+10V
Bias: -42mV
0.37 THz

Model Used for Bias Dependence Data Fitting

The interpretation of the bias-dependent frequency shift can be obtained from the Hamiltonian described below:

$$H = \begin{pmatrix} \varepsilon_0 - [\mu_1 \cdot (E_{surface} + E_{DC}) + \frac{1}{2}\alpha_1 \cdot (E_{surface} + E_{DC})^2] & -A \\ -A & \varepsilon_0 - [\mu_2 \cdot (E_{surface} + E_{DC}) + \frac{1}{2}\alpha_2 \cdot (E_{surface} + E_{DC})^2] \end{pmatrix}$$

Here, $E_{surface}$ and E_{DC} represent the surface electrostatic field and DC field from the sample bias, respectively. μ_1, μ_2 denote the induced dipole moment of the two states of H_2 for the TLS, and α_1, α_2 denote the corresponding polarizability. The coupling associated with tunneling between the two states is represented by A, and the field-free energy level is ε_0.

The energy separation between the two levels from the Stark-shift Hamiltonian is given by:

$$\Delta\varepsilon = \sqrt{[\Delta\mu \cdot (E_{surface} + E_{DC}) + \frac{1}{2}\Delta\alpha \cdot (E_{surface} + E_{DC})^2]^2 + 4A^2}$$

where $\Delta\mu = \mu_2 - \mu_1$, and $\Delta\alpha = \alpha_2 - \alpha_1$.

By fitting the bias dependence data in Figure 3.3E with the equation of $\Delta\varepsilon$, we were able to extract $E_{surface}$. The surface electrostatic field in units of mV/Å could then be calculated from the sample bias by approximating the tip-substrate separation as 6 Å.

The fitting parameters with errors next to the values were found to be:

$E_{surface}$ (mV/Å)	$\Delta\mu$ (Debye)	$\Delta\alpha$ (Å^3)	A (meV)
-43 (±15)	0.6 (±0.1)	64 (±36)	0.3 (±0.5)

Time Domain TRS

Spectroscopic insights into the coherent oscillations of the TLS have been further obtained by contrasting STM-IETS and TRS, as an example over position 3, for different THz pump-probe delays. Spectral features by STM-IETS, without chopping the two THz beams, showed insensitivity to the time delay between the THz pump-probe pulses (Figure S3.5A). Whereas in TRS, measured while both THz beams were chopped periodically by a low frequency square wave for lock-in detection, the intensity of the rectification current at a selected bias varied periodically with THz pump-probe delay (Figure S3.5B). By fitting the THz rectification spectra with three Gaussian functions, we were able to accurately rebuild the spectra for all pump-probe delays as shown in Figure S3.5C. As shown in Figure S3.5D-F, the STM-IETS measurements at –43 mV, –30mV, and –20 mV showed random fluctuations on the signal intensity as time delay varied. In contrast, the TRS measurements at the same sample biases in Figure S3.5G-I showed clear coherent oscillations.

Similar to STM-IETS, TRS also measures the I-V nonlinearity of the STM junction. As the amplitude modulated THz electric field developed a modulated bias voltage across the junction, we would expect spectra from TRS and IETS to share similar lineshape. However, the absorption of THz photons by the TLS of H_2 in the STM cavity changed the populations of the two states and modified the junction nonlinearity. The minute THz induced change on the junction nonlinearity can be effectively extracted from the lock-in amplifier as the THz beams were amplitude modulated at a low frequency limited by the small bandwidth at high gain of the current pre-amplifier. In addition to changes in the spectral lineshape and intensity at the vibrational and rotational peaks, a new peak at –30 mV emerged. Changes in the intensity of the spectral features in TRS at different biases, including the new peak at –30 mV, were measured as a function of THz

pump-probe delay. In contrast to TRS, the sample bias and not the THz beams were modulated in the IETS measurements in Figure S3.5A, which prevented clear extraction of the weak THz induced rectification current hidden in the stronger DC tunneling current. As a result, the −30 mV peak and its temporal intensity oscillation could not be resolved by IETS even with THz radiation in the junction. Both IETS and TRS detected I-V nonlinearity associated with excitations between two states by tunneling electrons, e.g. vibration and rotation. In addition to the field property that led to a bias oscillation for spectroscopy, THz photons could be absorbed by the TLS and alter the I-V nonlinearity over a broad range of biases. The absorption changed the properties of the H_2 in the STM cavity and consequently the rectification spectra. Both the wave-like (TRS) and particle-like (TLS absorption) properties of THz radiation enabled the spectroscopic measurement of the absorption induced coherent superposition of H_2 states in the STM cavity.

Figure S3.5 IETS and TRS at different pump-probe delay times. (**A**) STM-IETS of H_2 molecule with non-chopped THz pump-probe pulses. The top panel shows the schematic diagram of the two modulation techniques. Within each sine wave modulation period (263.03 Hz), there are ~3.8 million THz pulse pairs (1 GHz repetition rate) irradiating the cavity. Tip is placed over position 3 as labeled in Figure 3.1D. Before taking each spectrum, the probe THz pulse is set at a specific delay after the pump pulse by moving the delay stage. From bottom to top, the pump-probe delays are 0.50 ps, 1.20 ps, 2.00 ps, 2.70 ps, 3.65 ps, 4.25 ps, 4.85 ps, 5.60 ps, 6.30 ps, 7.00 ps, 7.70 ps, 8.40 ps, 9.00 ps, and 9.90 ps. Set point: –20 mV/40 pA. (**B**) Time domain TRS of H_2 molecule with chopped THz pump-probe pulses. The top panel shows the schematic diagram of the THz modulation. Within half of each square wave chopping period (263.03 Hz), there are ~1.9 million THz pulse pairs irradiating the cavity. Tip position, tunneling gap setpoint, and delay times are the same as in (A). (**C**) Peak fitting of the negative bias range superimposed on the experimental data in (B). All the spectra are fitted with a function composed of three Gaussian peak functions $y = y_0 + \sum_{i=1}^{3} \sqrt{\frac{4\ln 2}{\pi}} \cdot w_i^{-1} \cdot A_i \cdot e^{-4(\ln 2)(x-x_i)^2 w_i^{-2}}$, with x_i representing the peak positions, w_i the full width at half maximum (FWHM), and A_i the peak area. The bottom spectrum shows an example of the fit by three Gaussian peaks and the sum is indicated by the solid red line following closely the data points. Dashed lines in (A), (B) and (C) mark the energy positions at –43 mV, –30 mV, and –20 mV. All the spectra are offset vertically for clarity. (**D-F**) Plot of the STM-IETS measurements in (A) at –43 mV, –30 mV and –20 mV, respectively, as a function of time delay between the THz pump-probe pulses. (**G-I**) Plot of the TRS measurements in (B) at –43 mV, –30 mV and –20 mV, respectively, as a function of time delay between the THz pump-probe pulses.

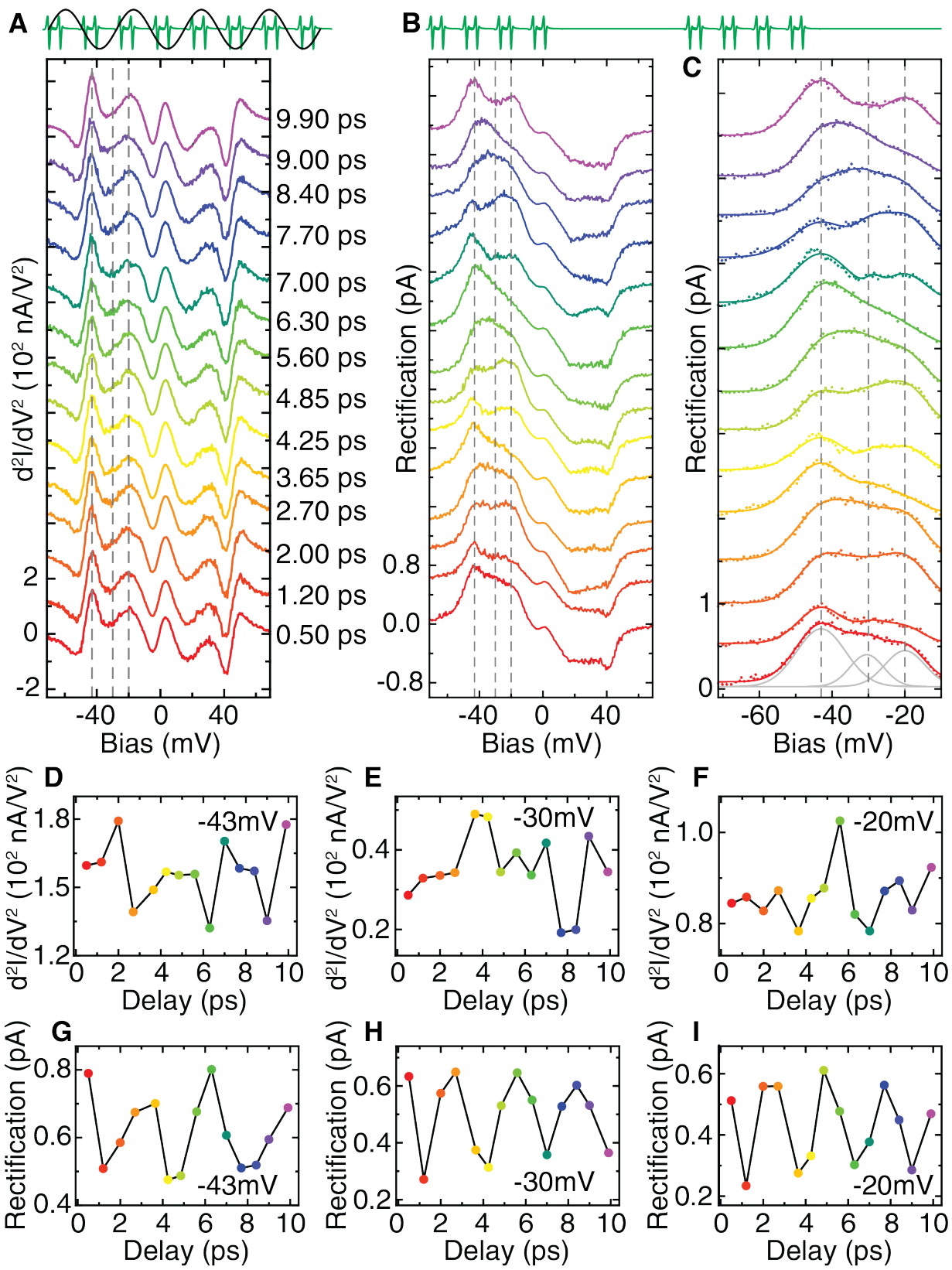
A
B
C
9.90 ps
9.00 ps
8.40 ps
7.70 ps
7.00 ps
6.30 ps
5.60 ps
4.85 ps
4.25 ps
3.65 ps
2.70 ps
2.00 ps
1.20 ps
0.50 ps
d²I/dV² (10² nA/V²)
Rectification (pA)
Bias (mV)
D
E
F
-43mV
-30mV
-20mV
Delay (ps)
G
H
I

Coherent Oscillations at Different H_2 Concentrations

Surface adsorbed H_2 molecules can be desorbed by femtosecond NIR laser pulses. After confirming the complete desorption of H_2 on Cu_2N, we blocked the NIR laser and continuously performed the THz pump-probe measurements as the H_2 concentration recovered, as shown in Figure S3.10. The coherent oscillation period and frequency showed no change with increasing H_2 concentrations even though the absolute rectification current increased by over 5 times. This constant coherent oscillation clearly ruled out any intermolecular interaction contribution to the energy separation of the TLS.

It should be noted that the tip-substrate separation could change under different H_2 concentrations when the sample bias was set within a range of ±70 mV in Figure S3.4. The existence of H_2 largely modified the junction nonlinearity which increased with a higher H_2 concentration. For the THz pump-probe measurements at different H_2 concentrations, we chose a setpoint of 100 mV/80 pA to eliminate the tip-substrate separation variation. For other THz pump-probe measurements, except for Figure S3.4C, we waited long enough (more than 15 days) to reach an equilibrium H_2 concentration before taking data. Measurements in Figure S3.4C were performed 9 days after cooling down the sample to 9 K, and the H_2 concentration was still increasing slowly. Consequently, the tip-substrate separation was smaller than the separation at equilibrium concentration and the oscillation frequency in Figure S3.4D was higher than Figure S3.4B. Nevertheless, the long term H_2 concentration change barely affected the two consecutive measurements with opposite THz field directions in Figure S3.4C.

Coherent Oscillations with Different Tips

Figure S3.12 shows the coherent oscillations acquired with different STM tips. The oscillation frequency and the decoherence time varied from tip to tip. Different tip structures could modify the electric field applied across the tunneling gap, leading to a change on the energy separation of the TLS.

Figure S3.6 Cu_2N lattice assignment. (**A**) Large area STM constant current topography showing three Cu_2N islands. Image size: 105.4 Å by 105.4 Å. Scanning condition: –20 mV/0.3 nA. (**B**) Cu_2N lattice assignment deduced from the single Cu atom wide boundary between the two Cu_2N islands. Black dots represent the Cu atoms and white dots the N atoms. Image size: 62.0 Å by 62.0 Å. Scanning condition: –20 mV/0.3 nA. (**C**) Zoom in on the topography. Lines connect the Cu and N atoms in the two sub-lattices of Cu_2N. Image size: 16.4 Å by 16.4 Å. Scanning condition: –20 mV/0.3 nA. (**D**) STM topography of the same area as (C) with scanning condition: –20 mV/40 pA. (**E**) Zoom in topographic image of the Cu_2N island, 7.4 Å by 7.4 Å, with red (1), yellow (2), and blue (3) dots over the hollow, bridge, and top sites of the Cu_2N lattice, respectively. Scanning condition: –20 mV/40 pA. (**F**) Linecut along the black lines marked in (E) to show the Z variation. Position 3 is chosen to be the reference point.

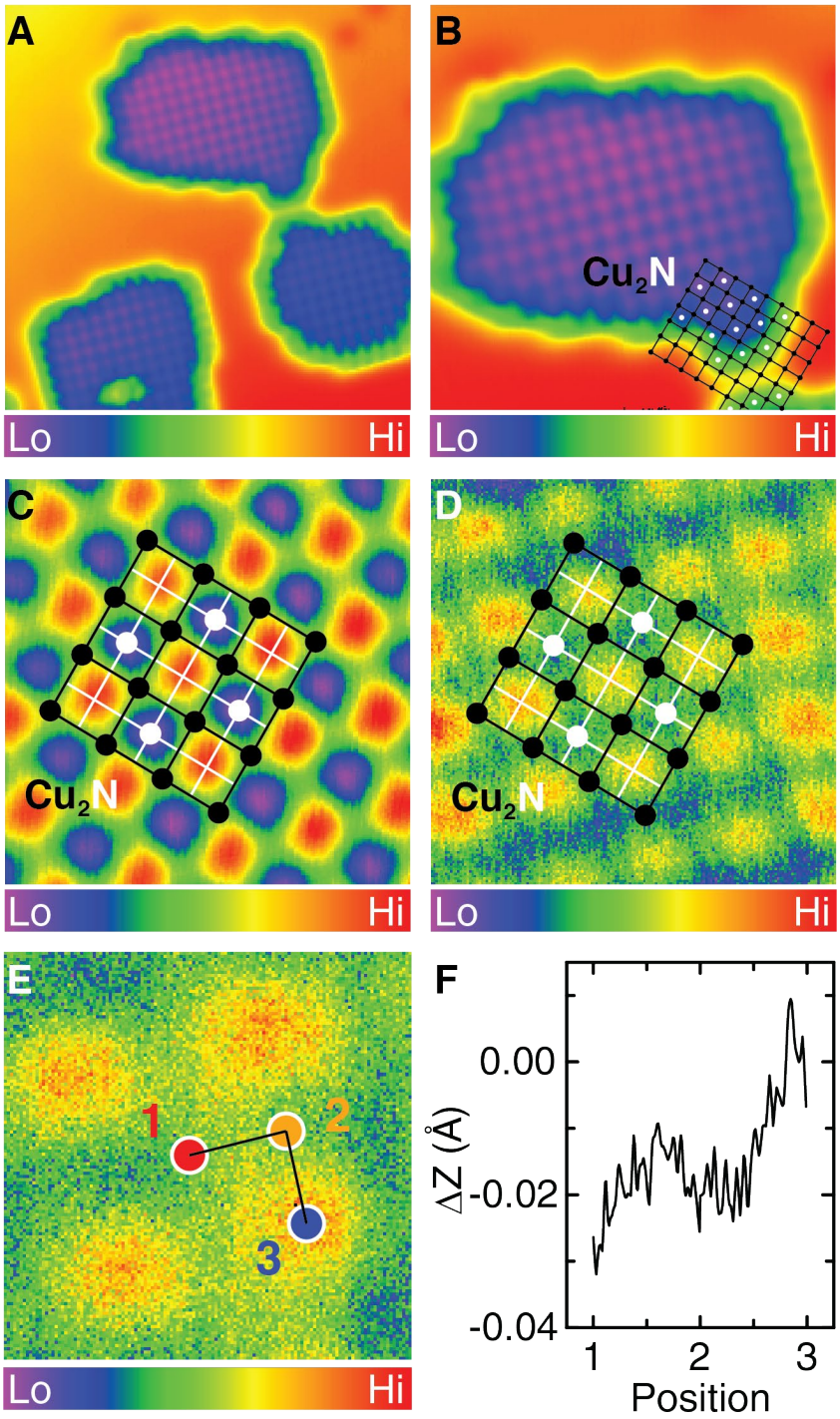
A
B
Cu2N
Lo
Hi
C
Cu2N
D
Cu2N
E
1
2
3
F
0.00
-0.02
-0.04
ΔZ (Å)
1
2
3
Position

Figure S3.7 Fitting of the coherent oscillations over three positions. (**A**) Position 1. (**B**) Position 2. (**C**) Position 3. The frequencies and relative amplitudes are obtained from the main and satellite peaks in the FFT spectra. The fitting function is a sum of three parts: a constant incoherent background signal (R_0), a Gaussian function for the THz pulse interference near zero delay $A \cdot e^{\frac{-(\tau-\tau_0)^2}{2\sigma^2}}$, and multiple sinusoidal functions with an exponential decay for the decoherence: $\sum_{i=1}^{4}[A_i \cdot \sin(2\pi \cdot f_i \cdot |\tau-\tau_0| + \phi)] \cdot e^{\frac{-|\tau-\tau_0|}{T_2}}$.

The fitting function is given by:

$$R(\tau) = R_0 + A \cdot e^{\frac{-(\tau-\tau_0)^2}{2\sigma^2}} + \sum_{i=1}^{4}[A_i \cdot \sin(2\pi \cdot f_i \cdot |\tau-\tau_0| + \phi)] \cdot e^{\frac{-|\tau-\tau_0|}{T_2}},$$

where τ is the time delay between pump and probe pulses, τ_0 represents the zero delay offset, A_i the oscillation amplitude for each sinusoidal oscillation, f_i the oscillation frequency, and T_2 the decoherence time. We assume the same phase ($\phi = 90°$) and T_2 for all the coherent oscillations.

The fitting parameters are found to be:

Position	f_1 (THz)	f_2 (THz)	f_3 (THz)	f_4 (THz)	T_2 (ps)
1	0.163	0.183	0.210		46
2	0.234	0.256	0.268	0.289	80
3	0.343	0.350	0.362	0.368	42
Position	A_1 (pA)	A_2 (pA)	A_3 (pA)	A_4 (pA)	
1	0.028	0.096	0.029		
2	0.025	0.192	0.080	0.044	
3	0.100	0.100	0.140	0.150	

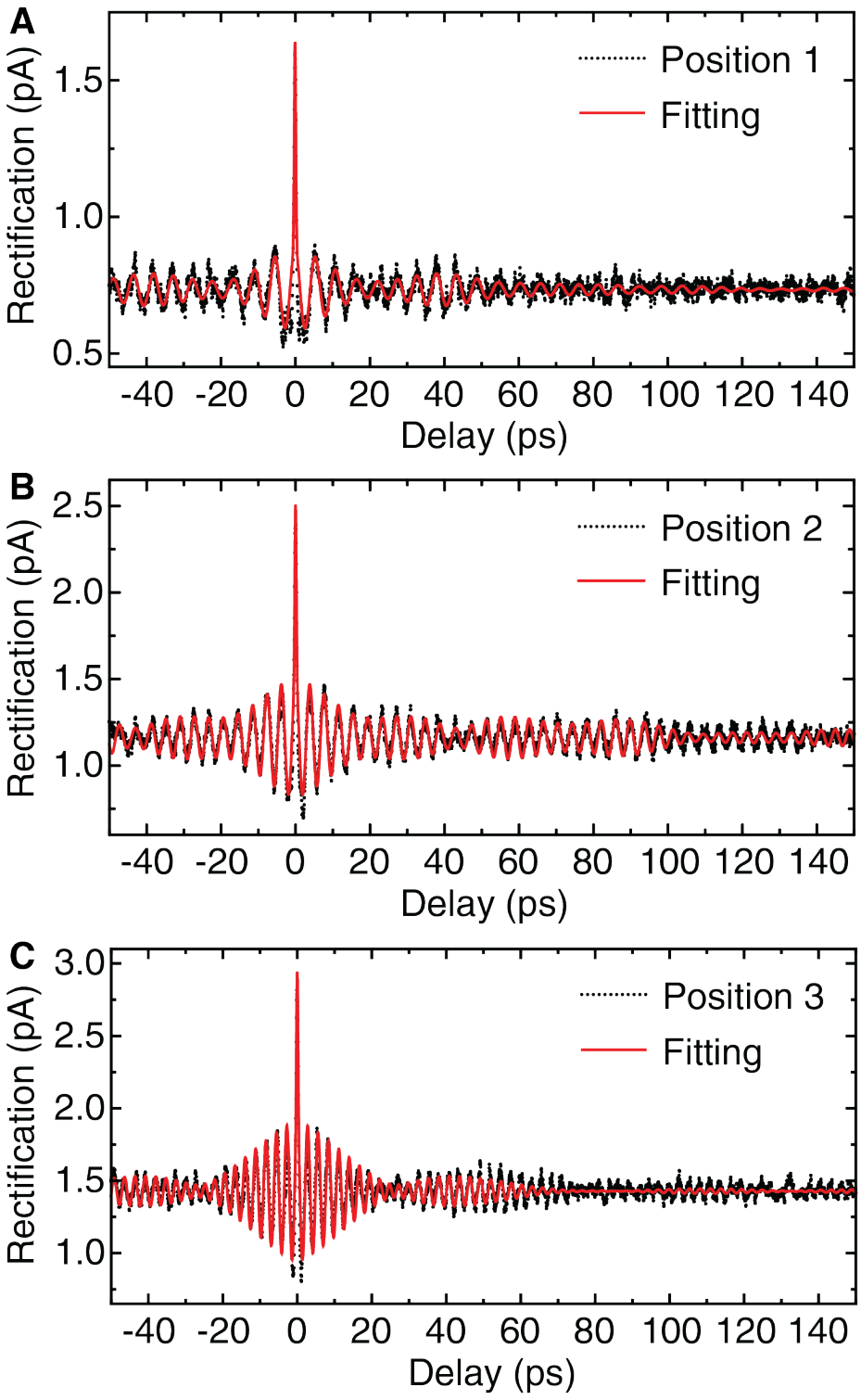
A
Rectification (pA)
1.5
1.0
0.5
Position 1
Fitting
-40 -20 0 20 40 60 80 100 120 140
Delay (ps)
B
Rectification (pA)
2.5
2.0
1.5
1.0
Position 2
Fitting
-40 -20 0 20 40 60 80 100 120 140
Delay (ps)
C
Rectification (pA)
3.0
2.5
2.0
1.5
1.0
Position 3
Fitting
-40 -20 0 20 40 60 80 100 120 140
Delay (ps)

Figure S3.8 THz pump-probe measurements across the whole Cu_2N island. (**A**) THz rectification imaging at 2.10 ps delay. The colored dots indicate the tip parked over 8 bright (high rectification current) positions across the Cu_2N island. Image size: 53.2 Å by 44.9 Å. (**B**) THz pump-probe measurements over 8 positions across the whole Cu_2N island with colors and numbers corresponding to the marked positions in (A). (**C**) FFT of the corresponding measurements in (B). The black vertical lines mark the central frequency position. (**D**) Main frequencies of the corresponding peak in (C) at different positions. (**E**) Fitting of the corresponding measurements in (B). The fitting function is the same as used in Figure S3.7. (**F**) Decoherence times of the corresponding measurements extracted from the fitting in (E).

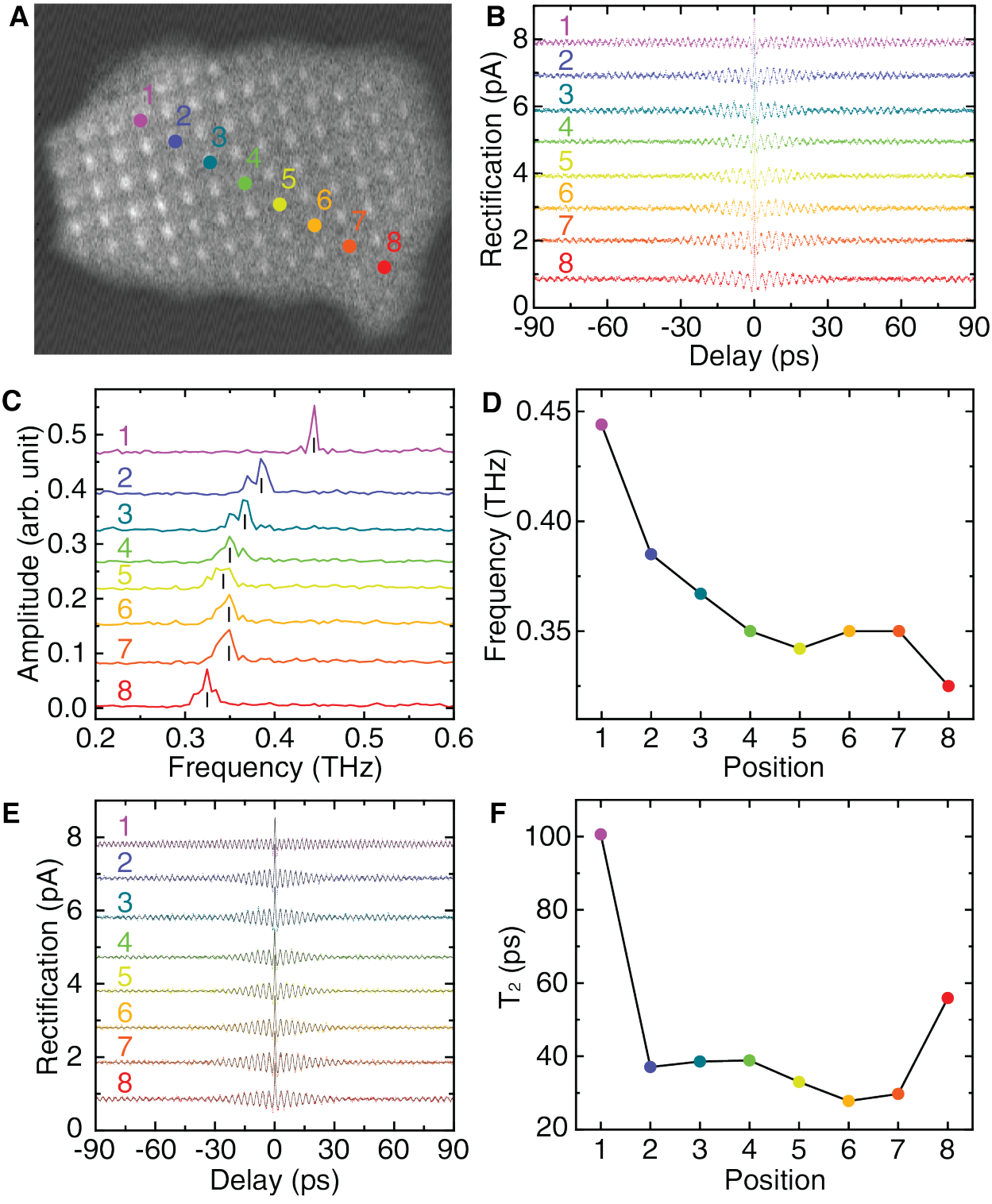
A
1
2
3
4
5
6
7
8
B
Rectification (pA)
Delay (ps)
C
Amplitude (arb. unit)
Frequency (THz)
D
Frequency (THz)
Position
E
Rectification (pA)
Delay (ps)
F
T2 (ps)
Position

Figure S3.9 Energy resolution of the THz pump-probe measurement. (**A**) The whole range of THz pump-probe measurement of position 1 in Figure S3.8. Left inset: THz rectification imaging at 2.10 ps delay. The purple dot marks the tip position. Image size: 53.2 Å by 44.9 Å. Right inset: FFT of the THz pump-probe measurement. The zoom in peak is also shown, with the vertical line marking the central frequency position. The central frequency and the FWHM extracted from a Gaussian peak fitting. (**B**) Zoom in THz pump-probe measurement of the position in (A). (**C**) Further zoom in measurement with its fitting. The fitting function is the same as used in Figure S3.7.

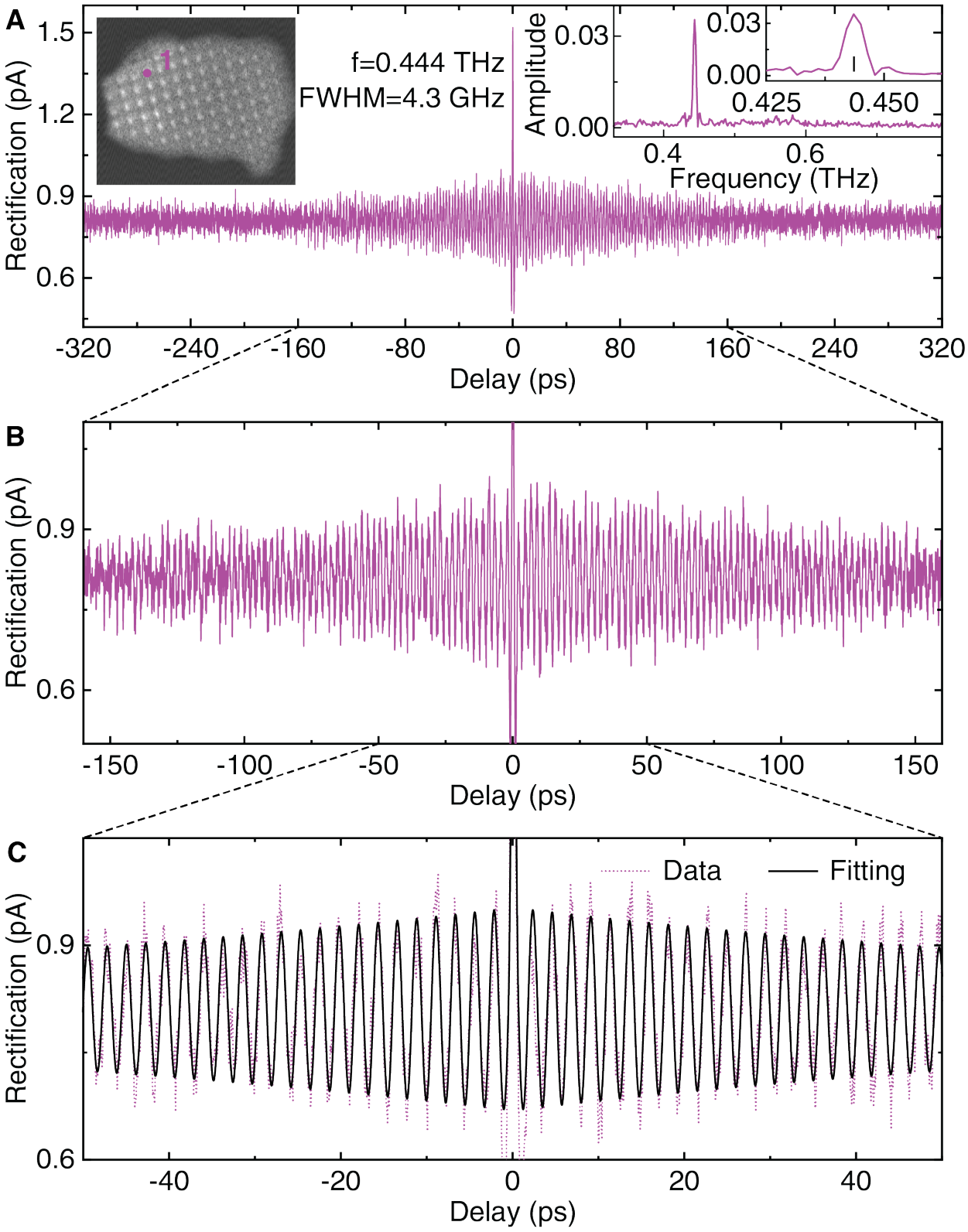
A
1.5
1.2
0.9
0.6
Rectification (pA)
1
f=0.444 THz
FWHM=4.3 GHz
Amplitude
0.03
0.00
0.4
0.6
Frequency (THz)
0.03
0.00
0.425
0.450
-320
-240
-160
-80
0
80
160
240
320
Delay (ps)
B
0.9
0.6
Rectification (pA)
-150
-100
-50
0
50
100
150
Delay (ps)
C
Data
Fitting
0.9
0.6
Rectification (pA)
-40
-20
0
20
40
Delay (ps)

Figure S3.10 Monitoring the coherent oscillations at increasing H_2 concentrations. (**A**) THz pump-probe measurements as a function of H_2 exposure time. Adsorbed H_2 molecules are desorbed by NIR (820 nm), 200 μW, femtosecond laser irradiation prior to measurements. As the H_2 concentration recovers as a function of the exopsure time with background H_2 in the ultrahigh vacuum chamber, THz pump-probe measurements are performed continuously. For each measurement, the sample bias is ramped to −30 mV after turning off the feedback at 100 mV/80 pA. It is found that the tip-substrate separation keeps constant under 100mV/80pA setpoint at different H_2 concentrations. (**B**) FFT colormap of the measurements in (A). For clarity, the amplitude of each spectrum is normalized positively to the color palette with range (0,1). (**C**) Examples of THz pump-probe measurement are selected from (A) to show the coherent oscillations at different H_2 exposure times. The colored texts label the corresponding exposure times. All spectra are offset vertically for clarity. (**D**) FFT of the corresponding measurements in (C). The dashed vertical line marks the unchanged peak frequency. All the FFT spectra are offset vertically for clarity.

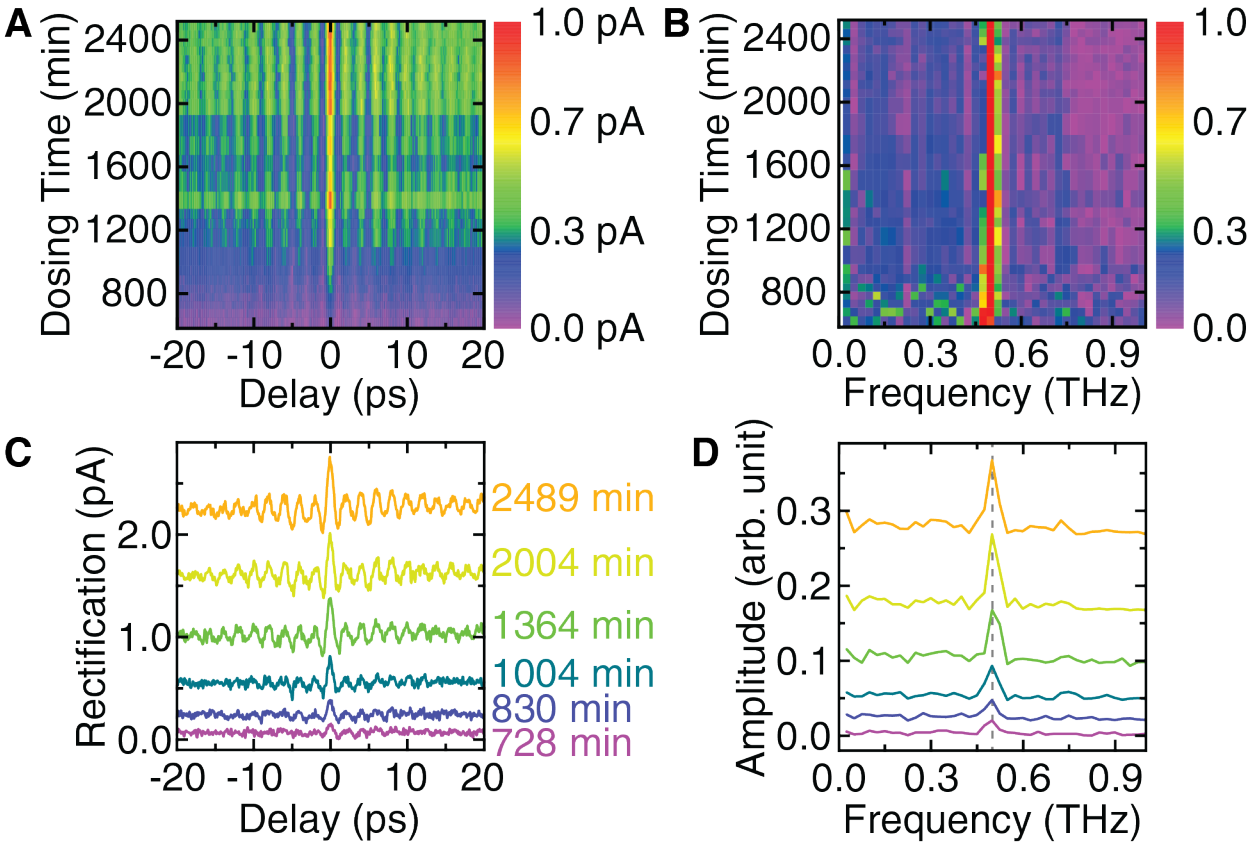
A
Dosing Time (min)
2400
2000
1600
1200
800
-20 -10 0 10 20
Delay (ps)
1.0 pA
0.7 pA
0.3 pA
0.0 pA
B
Dosing Time (min)
2400
2000
1600
1200
800
0.0 0.3 0.6 0.9
Frequency (THz)
1.0
0.7
0.3
0.0
C
Rectification (pA)
2.0
1.0
0.0
-20 -10 0 10 20
Delay (ps)
2489 min
2004 min
1364 min
1004 min
830 min
728 min
D
Amplitude (arb. unit)
0.3
0.2
0.1
0.0
0.0 0.3 0.6 0.9
Frequency (THz)

Figure S3.11 Tip separation and sample bias dependence of the coherent oscillation. (**A**) FFT of the THz pump-probe measurements in Figure 3.3A. The colored texts label the corresponding change of tip-substrate separation. The vertical line under each FFT peak mark the central frequency plotted in Figure 3.3B. (**B**) Colormap of the series of THz pump-probe measurements, some of which are displayed in Figure 3.3A; the change of the coherent oscillation as a function of the tip-substrate separation can be visualized. For clarity, the intensity of all the spectra is normalized positively to the color palette with range (0,1) and the peaks near 0 delay are masked. (**C**) FFT of the THz pump-probe measurements in Figure 3.3C. The colored texts label the corresponding sample bias. The vertical line under each FFT peak mark the central frequency plotted in Figure 3.3E. (**D**) Colormap of the series of FFT results, some of which are displayed in (A); the change of the oscillation frequency as a function of the tip-substrate separation can be visualized. The black curve is an exponential fit shown the same as in Figure 3.3B. For clarity, the intensity of all the spectra is normalized positively to the color palette with range (0,1). (**E**) Colormap of the series of FFT results, some of which are displayed in (C); the change of the oscillation frequency as a function of the sample bias can be visualized. The black curve is the fitting of the same data shown in Figure 3.3E. For clarity, the intensity of all the spectra is normalized positively to the color palette with range (0,1).

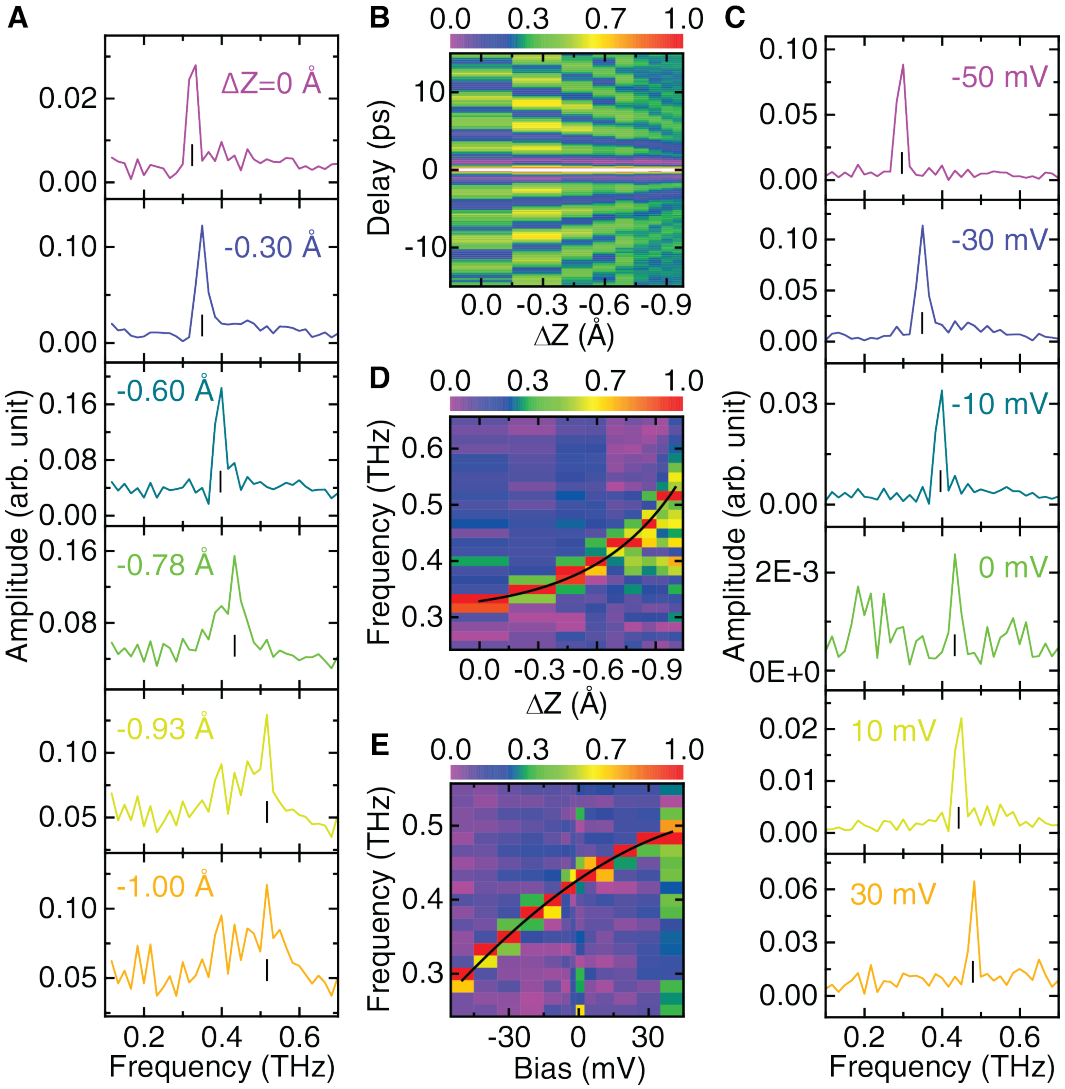
A
ΔZ=0 Å
-0.30 Å
-0.60 Å
-0.78 Å
-0.93 Å
-1.00 Å
Amplitude (arb. unit)
Frequency (THz)
B
Delay (ps)
ΔZ (Å)
D
Frequency (THz)
ΔZ (Å)
E
Frequency (THz)
Bias (mV)
C
-50 mV
-30 mV
-10 mV
0 mV
10 mV
30 mV
Amplitude (arb. unit)
Frequency (THz)

Figure S3.12 Measured coherent oscillations with different tips. (**A**) THz pump-probe measurements with four different tips. All the measurements are performed over the protrusion sites (as Position 3) of the Cu_2N island. Sample bias is ramped to −30 mV after turning off the feedback at −20 mV/40 pA for all measurements. All spectra are offset vertically for clarity. (**B**) FFT of the corresponding measurements in (A). The colored texts label the center position of the corresponding peak. All the FFT spectra are offset vertically for clarity.

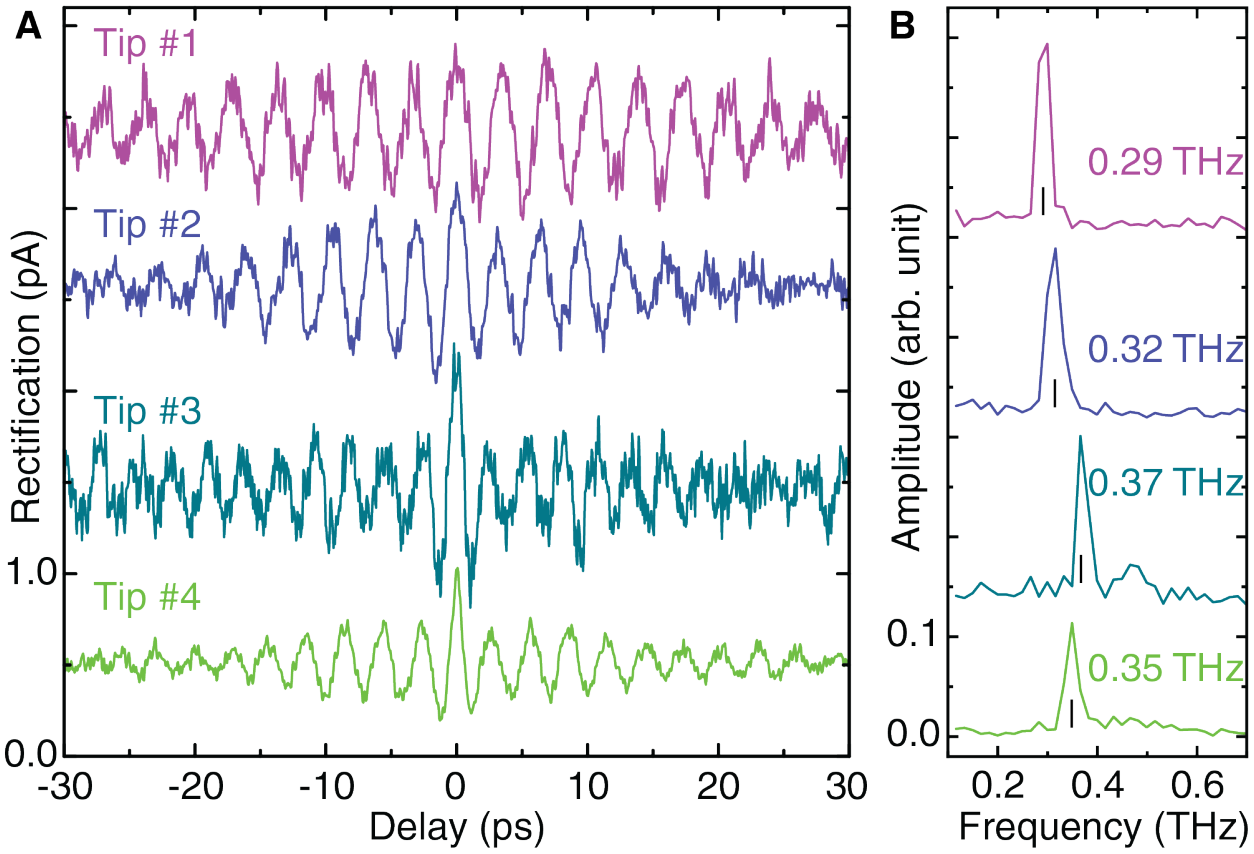
A
Tip #1
Tip #2
Tip #3
Tip #4
Rectification (pA)
1.0
0.0
-30
-20
-10
0
10
20
30
Delay (ps)
B
0.29 THz
0.32 THz
0.37 THz
0.35 THz
Amplitude (arb. unit)
0.1
0.0
0.2
0.4
0.6
Frequency (THz)

Bibliography

[1] C. L. Degen, F. Reinhard, and P. Cappellaro, *Quantum Sensing*, Rev. Mod. Phys. **89**, 035002 (2017).

[2] F. Troiani, A. Ghirri, M. G. A. Paris, C. Bonizzoni, and M. Affronte, *Towards Quantum Sensing with Molecular Spins*, J. Magn. Magn. Mater. **491**, 165534 (2019).

[3] M. S. Grinolds, P. Maletinsky, S. Hong, M. D. Lukin, R. L. Walsworth, and A. Yacoby, *Quantum Control of Proximal Spins Using Nanoscale Magnetic Resonance Imaging*, Nat. Phys. **7**, 687 (2011).

[4] N. Aslam et al., *Nanoscale Nuclear Magnetic Resonance with Chemical Resolution*, Science **357**, 67 (2017).

[5] P. Maletinsky, S. Hong, M. S. Grinolds, B. Hausmann, M. D. Lukin, R. L. Walsworth, M. Loncar, and A. Yacoby, *A Robust Scanning Diamond Sensor for Nanoscale Imaging with Single Nitrogen-Vacancy Centres*, Nat. Nanotechnol. **7**, 320 (2012).

[6] K. Bian, W. Zheng, X. Zeng, X. Chen, R. Stöhr, A. Denisenko, S. Yang, J. Wrachtrup, and Y. Jiang, *Nanoscale Electric-Field Imaging Based on a Quantum Sensor and Its Charge-State Control under Ambient Condition*, Nat. Commun. **12**, 2457 (2021).

[7] M. J. Biercuk, H. Uys, J. W. Britton, A. P. Vandevender, and J. J. Bollinger, *Ultrasensitive Detection of Force and Displacement Using Trapped Ions*, Nat. Nanotechnol. **5**, 646 (2010).

[8] M. J. Yoo, T. A. Fulton, H. F. Hess, R. L. Willett, L. N. Dunkleberger, R. J. Chichester, L. N. Pfeiffer, and K. W. West, *Scanning Single-Electron Transistor Microscopy: Imaging Individual Charges*, Science **276**, 579 (1997).

[9] J. Martin, N. Akerman, G. Ulbricht, T. Lohmann, J. H. Smet, K. Von Klitzing, and A. Yacoby, *Observation of Electron-Hole Puddles in Graphene Using a Scanning Single-*

Electron Transistor, Nat. Phys. **4**, 144 (2008).

[10] G. Czap, P. J. Wagner, F. Xue, L. Gu, J. Li, J. Yao, R. Wu, and W. Ho, *Probing and Imaging Spin Interactions with a Magnetic Single-Molecule Sensor*, Science **364**, 670 (2019).

[11] C. Wagner et al., *Quantitative Imaging of Electric Surface Potentials with Single-Atom Sensitivity*, Nat. Mater. **18**, 853 (2019).

[12] X. Zhang, C. Wolf, Y. Wang, H. Aubin, T. Bilgeri, P. Willke, A. J. Heinrich, and T. Choi, *Electron Spin Resonance of Single Iron Phthalocyanine Molecules and Role of Their Non-Localized Spins in Magnetic Interactions*, Nat. Chem. **14**, 59 (2022).

[13] P. Willke, W. Paul, F. D. Natterer, K. Yang, Y. Bae, T. Choi, J. Fernández-Rossier, A. J. Heinrich, and C. P. Lutz, *Probing Quantum Coherence in Single-Atom Electron Spin Resonance*, Sci. Adv. **4**, 1 (2018).

[14] T. Choi, W. Paul, S. Rolf-Pissarczyk, A. J. Macdonald, F. D. Natterer, K. Yang, P. Willke, C. P. Lutz, and A. J. Heinrich, *Atomic-Scale Sensing of the Magnetic Dipolar Field from Single Atoms*, Nat. Nanotechnol. **12**, 420 (2017).

[15] K. Yang, W. Paul, S.-H. Phark, P. Willke, Y. Bae, T. Choi, T. Esat, A. Ardavan, A. J. Heinrich, and C. P. Lutz, *Coherent Spin Manipulation of Individual Atoms on a Surface*, Science **366**, 509 (2019).

[16] S. Baumann, W. Paul, T. Choi, C. P. Lutz, A. Ardavan, and A. J. Heinrich, *Electron Paramagnetic Resonance of Individual Atoms on a Surface*, Science **350**, 417 (2015).

[17] T. L. Cocker, D. Peller, P. Yu, J. Repp, and R. Huber, *Tracking the Ultrafast Motion of a Single Molecule by Femtosecond Orbital Imaging*, Nature **539**, 263 (2016).

[18] S. Li, S. Chen, J. Li, R. Wu, and W. Ho, *Joint Space-Time Coherent Vibration Driven Conformational Transitions in a Single Molecule.*, Phys. Rev. Lett. **119**, 176002 (2017).

[19] D. Peller, L. Z. Kastner, T. Buchner, C. Roelcke, F. Albrecht, N. Moll, R. Huber, and J. Repp, *Sub-Cycle Atomic-Scale Forces Coherently Control a Single-Molecule Switch*, Nature **585**, 58 (2020).

[20] N. T. Yardimci, S. H. Yang, C. W. Berry, and M. Jarrahi, *High-Power Terahertz Generation Using Large-Area Plasmonic Photoconductive Emitters*, IEEE Trans. Terahertz Sci. Technol. **5**, 223 (2015).

[21] J. A. Gupta, C. P. Lutz, A. J. Heinrich, and D. M. Eigler, *Strongly Coverage-Dependent Excitations of Adsorbed Molecular Hydrogen*, Phys. Rev. B **71**, 115416 (2005).

[22] S. Liu, A. Shiotari, D. Baugh, M. Wolf, and T. Kumagai, *Enhanced Resolution Imaging of Ultrathin ZnO Layers on Ag(111) by Multiple Hydrogen Molecules in a Scanning Tunneling Microscope Junction*, Phys. Rev. B **97**, 195417 (2018).

[23] C. Ping, X. Zhitao, L. Jizhong, L. Jianyi, and T. Kuang Lee, *Interaction of Hydrogen with Metal Nitrides and Imides*, Nature **420**, 20 (2002).

[24] F. D. Natterer, F. Patthey, and H. Brune, *Resonant-Enhanced Spectroscopy of Molecular Rotations with a Scanning Tunneling Microscope*, ACS Nano **8**, 7099 (2014).

[25] F. D. Natterer, F. Patthey, and H. Brune, *Distinction of Nuclear Spin States with the Scanning Tunneling Microscope*, Phys. Rev. Lett. **111**, 175303 (2013).

[26] S. Li, A. Yu, F. Toledo, Z. Han, H. Wang, H. Y. He, R. Wu, and W. Ho, *Rotational and Vibrational Excitations of a Hydrogen Molecule Trapped within a Nanocavity of Tunable Dimension*, Phys. Rev. Lett. **111**, 146102 (2013).

[27] S. Li, D. Yuan, A. Yu, G. Czap, R. Wu, and W. Ho, *Rotational Spectromicroscopy: Imaging the Orbital Interaction between Molecular Hydrogen and an Adsorbed Molecule.*, Phys. Rev. Lett. **114**, 206101 (2015).

[28] J. Jung, S. Nam, C. Wolf, A. J. Heinrich, and J. Chae, *Atomic-Scale Intermolecular Interaction of Hydrogen with a Single VOPc Molecule on the Au(111) Surface*, RSC Adv. **11**, 6240 (2021).

[29] A. Halbritter, P. Makk, S. Csonka, and G. Mihály, *Huge Negative Differential Conductance in Au-H_2 Molecular Nanojunctions*, Phys. Rev. B **77**, 075402 (2008).

[30] W. H. A. Thijssen, D. Djukic, A. F. Otte, R. H. Bremmer, and J. M. van Ruitenbeek, *Vibrationally Induced Two-Level Systems in Single-Molecule Junctions*, Phys. Rev. Lett. **97**, 226806 (2006).

[31] H. Wang, S. Li, H. He, A. Yu, F. Toledo, Z. Han, W. Ho, and R. Wu, *Trapping and Characterization of a Single Hydrogen Molecule in a Continuously Tunable Nanocavity*, J. Phys. Chem. Lett. **6**, 3453 (2015).

[32] T. Choi, C. D. Ruggiero, and J. A. Gupta, *Incommensurability and Atomic Structure of c(2×2)N/Cu(100): A Scanning Tunneling Microscopy Study*, Phys. Rev. B **78**, 035430 (2008).

[33] C. F. Hirjibehedin, C. Lin, A. F. Otte, M. Ternes, C. P. Lutz, B. A. Jones, and A. J. Heinrich, *Large Magnetic Anisotropy of a Single Atomic Spin Embedded in a Surface Molecular Network*, Science **317**, 1199 (2007).

[34] J. Lee, X. Tu, and W. Ho, *Spectroscopy and Microscopy of Spin-Sensitive Rectification Current Induced by Microwave Radiation*, Nano Lett. **5**, 2613 (2005).

[35] X. W. Tu, J. H. Lee, and W. Ho, *Atomic-Scale Rectification at Microwave Frequency*, J. Chem. Phys. **124**, 021105 (2006).

[36] M. Schneiderbauer, M. Emmrich, A. J. Weymouth, and F. J. Giessibl, *CO Tip Functionalization Inverts Atomic Force Microscopy Contrast via Short-Range Electrostatic*

Forces, Phys. Rev. Lett. **112**, 166102 (2014).

[37] K. T. Crampton, J. Lee, and V. A. Apkarian, *Ion-Selective, Atom-Resolved Imaging of a 2D Cu_2N Insulator: Field and Current Driven Tip-Enhanced Raman Spectromicroscopy Using a Molecule-Terminated Tip*, ACS Nano **13**, 6363 (2019).

CHAPTER 4

Electrical Manipulation of Quantum Coherence in a Single Molecular Qubit[†]

4.1 Abstract

The ability to manipulate a quantum system is central for the advancement of quantum information science [1–4]. Superposition of quantum states in a qubit implicates quantum coherence which conveys information such as the resonant frequency and the decoherence time of the qubit [5–12]. The quantum coherence at the ultrafast time scale allows operation of quantum computer and quantum sensing with ultrahigh precision and efficiency [13–15]. However, it remains challenging and appealing to manipulate the coherence of a single qubit using the easily generated electric field. Here we demonstrate the manipulation of ultrafast quantum coherence of a single hydrogen molecular qubit by employing static electric field from the sample bias in a femtosecond terahertz scanning tunneling microscope. A H_2 molecule adsorbed on the polar Cu_2N surface develops an electric dipole and exhibits a giant Stark effect. An avoided crossing [16–18] of the quantum state energy levels is derived from the resonant frequency of the single H_2 qubit. The dephasing time of the initial wave packet can also be changed by applying the electric field. Furthermore, the electrical manipulation for different tunneling gaps in three-dimensions allows quantification of the surface electrostatic fields at the atomic scale. Our work demonstrated the potential application of molecules as controllable qubits.

[†] This chapter by Likun Wang, Dan Bai, Yunpeng Xia, and W. Ho is prepared for submission.

4.2 Article

Quantum coherence at the ultrafast time scale is invaluable to quantum information processing [13,19–21]. The femtosecond (fs) to picosecond coherent oscillations of superposition states in a quantum bit (qubit) enable ultrafast operations to store and process information tha outperform the most powerful classical systems. It is thus paramount to be able to locally manipulate the resonant frequency and decoherence time of the ultrafast quantum coherence of an individual qubit [13,14,20]. The facile method of electrical manipulation of ultrafast coherence at the atomic scale with known qubit's environment has yet to be demonstrated.

Scanning tunneling microscope (STM) combined with time-domain techniques provides an effective platform to study the quantum coherence with unprecedented spatial resolution in a variety of systems. With a magnetic atom functionalized tip, pulsed electron spin resonance (ESR) has been performed on single atoms and molecules to measure and manipulate the spin coherence at the nanosecond time scale [12,22]. The free coherent evolution of a coupled spin-1/2 system was also demonstrated by direct current (DC) pump-probe spectroscopy in the STM [23]. On the other hand, laser combined STM [24–26] has been employed to probe the ultrafast electron [27,28], spin [29], or polaron [30] dynamics with nanoscale spatial resolution. The successful detection of ultrafast quantum coherence in single molecules proclaimed the remarkable accomplishments by terahertz (THz) [31,32,15] and optical-STM [33–36].

In this work, we demonstrated the electrical manipulation of the ultrafast quantum coherence as exemplified by a single H_2 molecule trapped inside the STM junction. Our femtosecond THz-STM enabled us to monitor variations of the coherent oscillations while changing the applied sample bias to impose the DC electric field on the molecule in the STM junction. The oscillation frequency varied along an asymmetric parabola as a function of the

sample bias. The dephasing time T_2^* was greatly extended by increasing the total electric field experienced by the H_2. An avoided crossing between the ground and excited state energy levels of H_2 can be determined from the close agreement between the experimental results and the fittings from the proposed Hamiltonian. With the ability to operate the STM tip in three-dimensional space, we systematically investigated the influence of the tip-substrate separation and the underlying surface atomic composition on our electrical manipulation method. A quantification of the surface electrostatic field was further obtained with sub-angstrom distribution. This is a major step forward from previous efforts, in which the coherence measurement over a single molecular qubit was demonstrated [15]. In this work, a complete manipulation of the quantum coherence is realized by changing the DC electric field.

Our fs THz-STM scheme employed pairs of delayed fs THz pulses focused into the STM junction, as illustrated in Figure 4.1a (see Methods for the THz generation and Sample and tip preparation details). The H_2 molecules were adsorbed on the monolayer Cu_2N islands grown on the Cu(001) surface. A charge transfer took place between the polar Cu_2N surface [37] and H_2 molecule, giving rise to a non-zero charge displacement and an electric dipole in the H_2 [38–40]. The total electric field $\mathbf{F_{tot}}$ experienced by the H_2 molecule was a combination of the underlying surface electrostatic field $\mathbf{F_{surface}}$ and the DC field $\mathbf{F_{DC}}$ from the externally applied sample bias [41]. By exclusively tuning the sample bias, the magnitude and direction of $\mathbf{F_{tot}}$ could be controlled precisely with a fixed $\mathbf{F_{surface}}$. Three situations are shown in Figure 4.1b-d where $\mathbf{F_{tot}}$ was set to be negative, zero, and positive, respectively.

A H_2 molecule trapped with two different adsorption configurations in the STM junction can be described as a two-level system (TLS) in a double-well potential [42,15], similar to the well-known TLS of gaseous ammonia molecule. The tunnel-coupling between the original basis

states leads to two eigenstates delocalized in the double-well potential, as shown schematically in Figure 4.1e-g. In accordance with the setting of $\mathbf{F_{tot}}$ in Figure 4.1b-d, the asymmetry of the double-well potential and the two eigenstate energy levels can be tuned (Figure 4.1e-g) [43]. The tunnel-coupled ground and excited state wavefunctions are also redistributed in the double-well potential. The highly localized wavefunctions in Figure 4.1e become delocalized and distributed equally in the two wells when the total electric field is zero and the double well potential becomes symmetric in Figure 4.1f.

Figure 4.1 Experimental setup and electrical manipulation of the quantum states. **a**, Schematic of the fs THz-STM experimental setup. A pair of THz pulses with variable temporal delay τ is aligned into the junction. H_2 molecules are adsorbed on a monolayer Cu_2N island grown on the Cu(001) surface. **b-d**, Schematics of the total electric field experienced by the H_2 molecule in the STM junction: **b**, The total electric field points toward the Cu_2N surface ($\mathbf{F_{tot}} < 0$). **c**, The total electric field is zero ($\mathbf{F_{tot}} = 0$). **d**, The total electric field points toward the tip ($\mathbf{F_{tot}} > 0$). The blue and red dashed arrows represent the electrostatic field from the Cu_2N surface and DC field from the applied sample bias, respectively. The thicker arrows in (**d)** represent stronger DC field due to the higher sample bias. **e-g**, Schematics of the ground and excited eigenstate wavefunction distribution of the two-level system in the double well potential: **e**, When $\mathbf{F_{tot}} < 0$, the ground state locates primarily in the right well, whereas the excited state locates primarily in the left well. **f**, When $\mathbf{F_{tot}} = 0$, the ground and excited states locate evenly in the symmetric double well. **g**, When $\mathbf{F_{tot}} > 0$, the ground state locates primarily in the left well, whereas the excited state locates primarily in the right well. Blue and red shaded curves represent the ground and excited state wavefunctions, respectively.

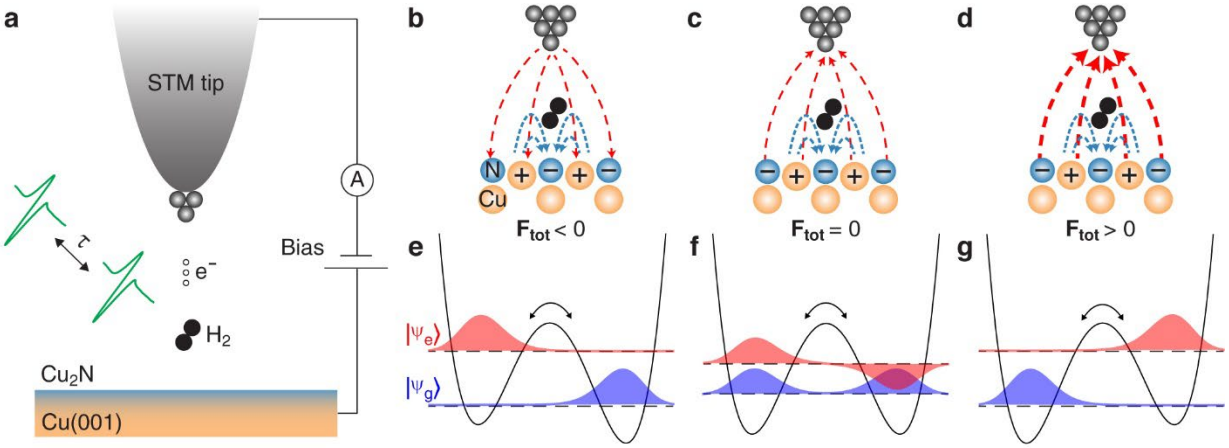
a
STM tip
A
Bias
e⁻
H2
Cu2N
Cu(001)
b
N
Cu
Ftot < 0
c
Ftot = 0
d
Ftot > 0
e
|ψe⟩
|ψg⟩
f
g

The energy separation of the H_2 TLS falls in the THz range, thus making it possible to prepare a superposition of the eigenstates using THz pulse excitation and monitor its ultrafast coherent evolution through time domain pump-probe measurements in our fs THz-STM [15]. The ultrafast coherence varied with the sample bias while maintaining the same tip-substrate separation and tip position as marked in the topographic image in Figure 4.2a. A series of bias dependent delay scans of the coherent oscillations were acquired in Figure 4.2b. The oscillation period gradually changed with sample bias, showing the largest period near 45 mV. In the corresponding fast Fourier transform (FFT) spectra to extract the oscillation frequency, a parabola with the minimum at 0.28 THz was revealed at the sample bias of 45 mV (Figure 4.2c). In addition, the parabola appeared asymmetric on the two sides of 45 mV with the slope higher on the left side.

Unlike previous studies of Stark shift showing symmetric parabolas [41,44], the asymmetry here cannot be explained by considering only the linear and quadratic components in the Stark effect. The non-zero minimum frequency of 0.28 THz also indicates an interaction which lifts the degeneracy of the ground and excited state when the $\mathbf{F_{tot}}$ is zero. For a TLS in the double-well potential, the observed energy separation 2Ω has contributions from the energy splitting 2Δ of the two basis states under Stark effect and the tunnel coupling A between them, as shown in Figure 4.2d. By applying the second-order Stark effect on the basis states and including the tunnel-coupling, we obtain the Hamiltonian of the TLS in a double well potential:

$$\mathbf{H} = \begin{pmatrix} E_0 - (\boldsymbol{\mu_a} \cdot \mathbf{F_{tot}} + \frac{1}{2}\boldsymbol{\alpha_a} \cdot \mathbf{F_{tot}}^2) & -A \\ -A & E_0 - (\boldsymbol{\mu_b} \cdot \mathbf{F_{tot}} + \frac{1}{2}\boldsymbol{\alpha_b} \cdot \mathbf{F_{tot}}^2) \end{pmatrix}$$

The energy separation between the two eigenstates of this Hamiltonian is given by:

$$\Delta E = 2\Omega = \sqrt{(\boldsymbol{\Delta\mu}\cdot\mathbf{F_{tot}} + \frac{1}{2}\boldsymbol{\Delta\alpha}\cdot\mathbf{F_{tot}}^2)^2 + 4A^2}$$

where $\mathbf{F_{tot}} = \mathbf{F_{surface}} + \mathbf{F_{DC}}$, $\boldsymbol{\Delta\mu} = \boldsymbol{\mu_b} - \boldsymbol{\mu_a}$, and $\boldsymbol{\Delta\alpha} = \boldsymbol{\alpha_b} - \boldsymbol{\alpha_a}$ are the total electric field, the change in dipole moment and in polarizability between the two basis states, respectively.

A comparison in Figure 4.2e shows the energy level shift calculated from the model Hamiltonian for the basis states and eigenstates as a function of the sample bias. Under the Stark effect, the energy levels of the basis states cross. An avoided level crossing emerges by incorporating the tunnel-coupling term in calculating the eigenstates. The ground and excited eigenstates are linear combinations of the basis states, $|g\rangle = \cos\left(\frac{\theta}{2}\right)|a\rangle + \sin\left(\frac{\theta}{2}\right)|b\rangle$ and $|e\rangle = -\sin\left(\frac{\theta}{2}\right)|a\rangle + \cos\left(\frac{\theta}{2}\right)|b\rangle$, with the mixing angle θ defined by the ratio of the tunnel-coupling to half of the energy splitting of the two basis states, $\tan\theta = \frac{A}{\Delta}$. At a negative sample bias far away from the avoided crossing region, the mixing angle approaches a minimum value of zero and the eigenstate $|g\rangle(|e\rangle)$ is mostly composed of the basis state $|a\rangle(|b\rangle)$. The mixing angle has the maximum value of $\pi/2$ at the tuning point in the avoided crossing region, where $|g\rangle = \frac{\sqrt{2}}{2}(|a\rangle + |b\rangle)$ and $|e\rangle = \frac{\sqrt{2}}{2}(-|a\rangle + |b\rangle)$ and the symmetric and antisymmetric eigenfunctions are delocalized equally in the two potential wells (Figure 4.1f). As illustrated by the color palette in Figure 4.2e, the majority component of the eigenstate $|g\rangle(|e\rangle)$undergoes a transition from the basis state $|a\rangle(|b\rangle)$ on the left side of the avoided crossing region to the basis state $|b\rangle(|a\rangle)$ on the right side, as manipulated by the sample bias. The energy separation ΔE of the TLS can be employed to closely fit the observed resonant frequency, as shown in Figure 4.2c.

We also performed numerical fitting to the time domain results in Figure 4.2b to extract the coherent properties of the H_2 TLS system under the external DC electric field, as shown in Figure 4.2f-h. Previous studies have shown that interferences among multiple closely related excited states in the H_2 TLS led to a fast dephasing of the initial wave packet, shown in Figure S4.1, which is closely related to the decoherence time [15]. This dephasing time T_2^* shows a strong dependence on the sample bias (Figure 4.2f), reaching a minimum of around 5 ps at the tuning point of 45 mV where the total electric field is 0. Upon increasing the magnitude of the total electric field, T_2^* is extended, reaching a maximum of 20 ps at -150 mV. As the total electric field increases, the electric dipole of the H_2 molecule increasingly aligns with the field, leading to a smaller difference between multiple closely related excited states and thus a longer T_2^*. In Figure 4.2g, the coherent oscillation amplitude reaches two local maxima at around ±45 mV, which matches the $j = 0 \rightarrow 2$ rotational excitation of a para-hydrogen [45–47,38,15], as shown in the inelastic electron tunneling spectroscopy (IETS) measurement in Figure S4.2. The fitted oscillation frequency in Figure 4.2h shows consistent agreement with the FFT results in Figure 4.2e.

Figure 4.2 Electrical manipulation of quantum states from the ultrafast coherence measurement. **a,** Constant-current topography of Cu_2N; image size 13.0 Å × 13.0 Å. Scanning condition: –20 mV/0.1 nA. The Cu_2N lattice structure is superimposed on the topography with lines connecting the Cu (black) and N (white) atoms in the two sub-lattices. **b**, Color map of a series of THz pump-probe measurements as a function of sample bias. The sample bias is controlled by ramping the bias after turning the feedback off at –30 mV/40 pA. The dashed lines serve as a guide to show the change of the oscillation period. **c**, Color map of FFT results from the time domain measurements in (**b**). The superimposed orange curve is the fitting of the data. For clarity, the intensity of all the spectra is normalized positively to the color palette with range (0,1). **d**, Energy level diagram of the basis states ($|a\rangle$, $|b\rangle$) and eigenstates ($|g\rangle$, $|e\rangle$) of the two-level system in a double well potential. The energy separation 2Ω of the eigenstates has contributions from the energy separation 2Δ and the tunnel-coupling A between the two basis states, $2\Omega = \sqrt{(2\Delta)^2 + 4A^2}$. **e**, The propagation of the avoided level crossing under the influence of the sample bias. The energy levels of the basis states (dashed lines) cross at 45 meV, whereas an avoided crossing develops for the eigenstates (solid lines) due to the tunnel-coupling. Colors represent the calculated mixing angle θ which indicates the relative magnitude of A to Δ with $\tan\theta = A/\Delta$. **f-h**, The bias dependent dephasing time T_2^*, coherent oscillation amplitude, and oscillation frequency extracted from the fitting of the oscillations in the time-domain results in (**b**). The blue and red lines in (**f**) and (**g**) are guides to the eye. The orange line in (**h**) is the same fitted curve as in (**c**).

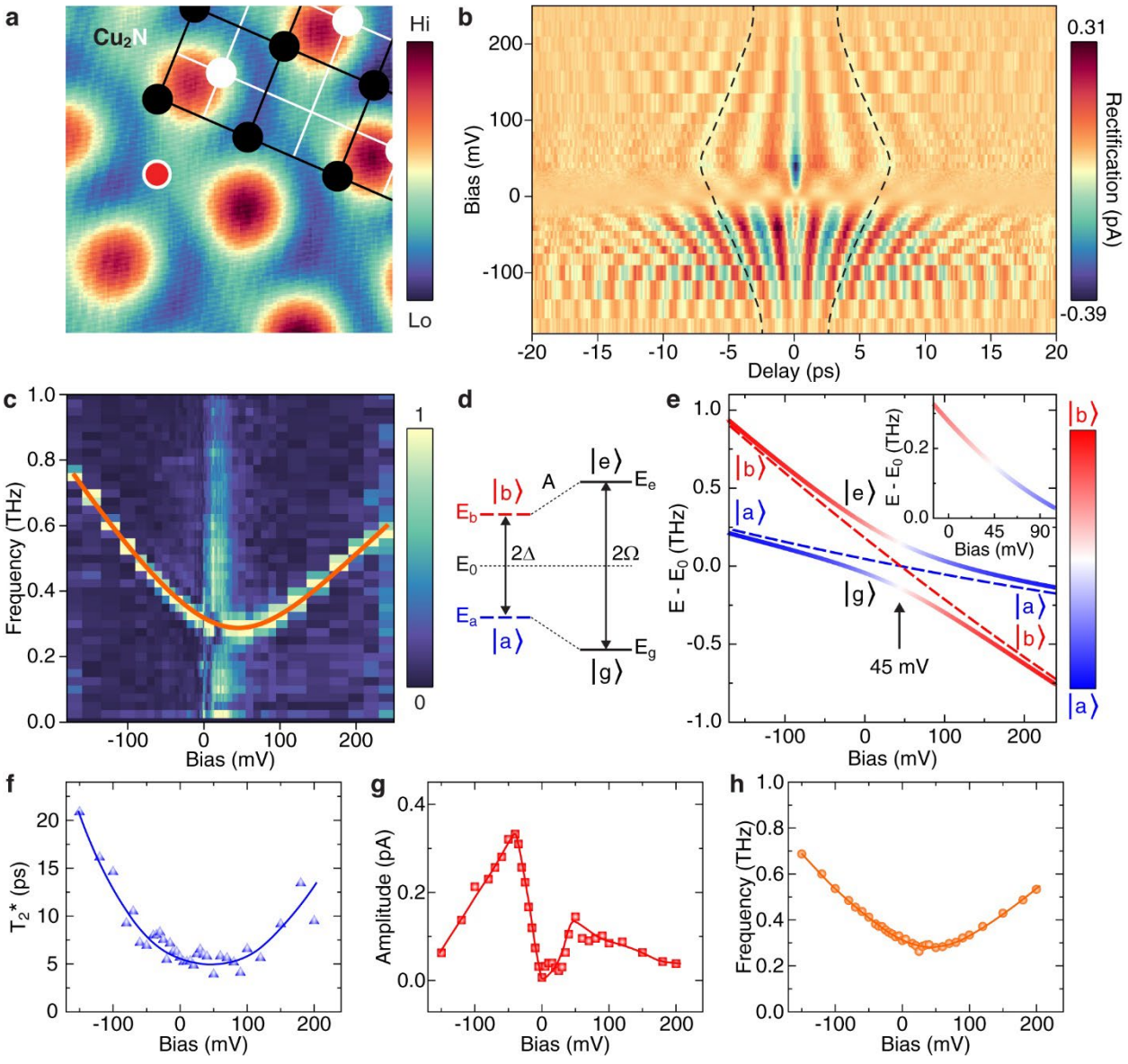
a
Cu2N
Hi
Lo
b
Bias (mV)
Delay (ps)
Rectification (pA)
0.31
-0.39
c
Frequency (THz)
Bias (mV)
1
0
d
|e⟩
|b⟩
|a⟩
|g⟩
A
Ee
Eb
Ea
Eg
E0
2Δ
2Ω
e
E - E0 (THz)
Bias (mV)
45 mV
f
T2* (ps)
Bias (mV)
g
Amplitude (pA)
Bias (mV)
h
Frequency (THz)
Bias (mV)

The tunnel-coupling strongly depends on the tip-substrate separation. As shown in Figure 4.3a-d and Figure S4.3, an obvious blue shift is observed on the overall shape of the parabola as the tip approaches the surface. For each parabola, the minimum resonant frequency at the tuning point represents the tunnel-coupling energy in THz unit. As the tip-substrate separation is decreased, the central barrier of the double-well potential can be lowered, thus increasing the tunnel-coupling and the corresponding resonant frequency. The parabola shape also shows an increased asymmetry for decreasing tip-substrate separation, which indicates a change of the dipole moment and the polarizability of the H_2 molecule. In addition, the corresponding sample bias of the minimum resonant frequency shows a slight increase from Figure 4.3a to d, which can be explained by a larger surface electrostatic field experienced by the H_2 molecule as it is likely pushed closer to the surface.

Figure 4.3e-h and j-l show variations of the parabola at position 2 and position 3 as labelled in Figure 4.3i. The sample bias differs for the minimum resonant frequency at each position and the same setpoint for the tip-substrate separation. When the tip is placed over these three different positions with the same setpoint, the applied DC field from the sample bias does not exhibit consequential differences. However, the underlying surface electrostatic field varies due to the different elemental composition of the Cu_2N lattice. As a result, the total electric field experienced by the H_2 changes and is reflected in the different parabolas shown for the three positions in Figure 4.3.

Figure 4.3 Panorama of the quantum state manipulation. a-d, e-h, and j-l, Color maps of the sample bias-controlled oscillation frequency with various tip-substrate separations over position 1, 2, and 3 marked in (**i**). The tip-substrate separation is controlled by ramping the tunneling current to the value labelled in each panel before turning off the feedback. Orange curves are the fittings of the data. For clarity, the intensity of all the spectra is normalized positively to the color palette with range (0,1). **i**, Constant current topography of the Cu_2N surface; image size 7.4 Å by 7.4 Å. Scanning condition: –20 mV/0.1 nA.

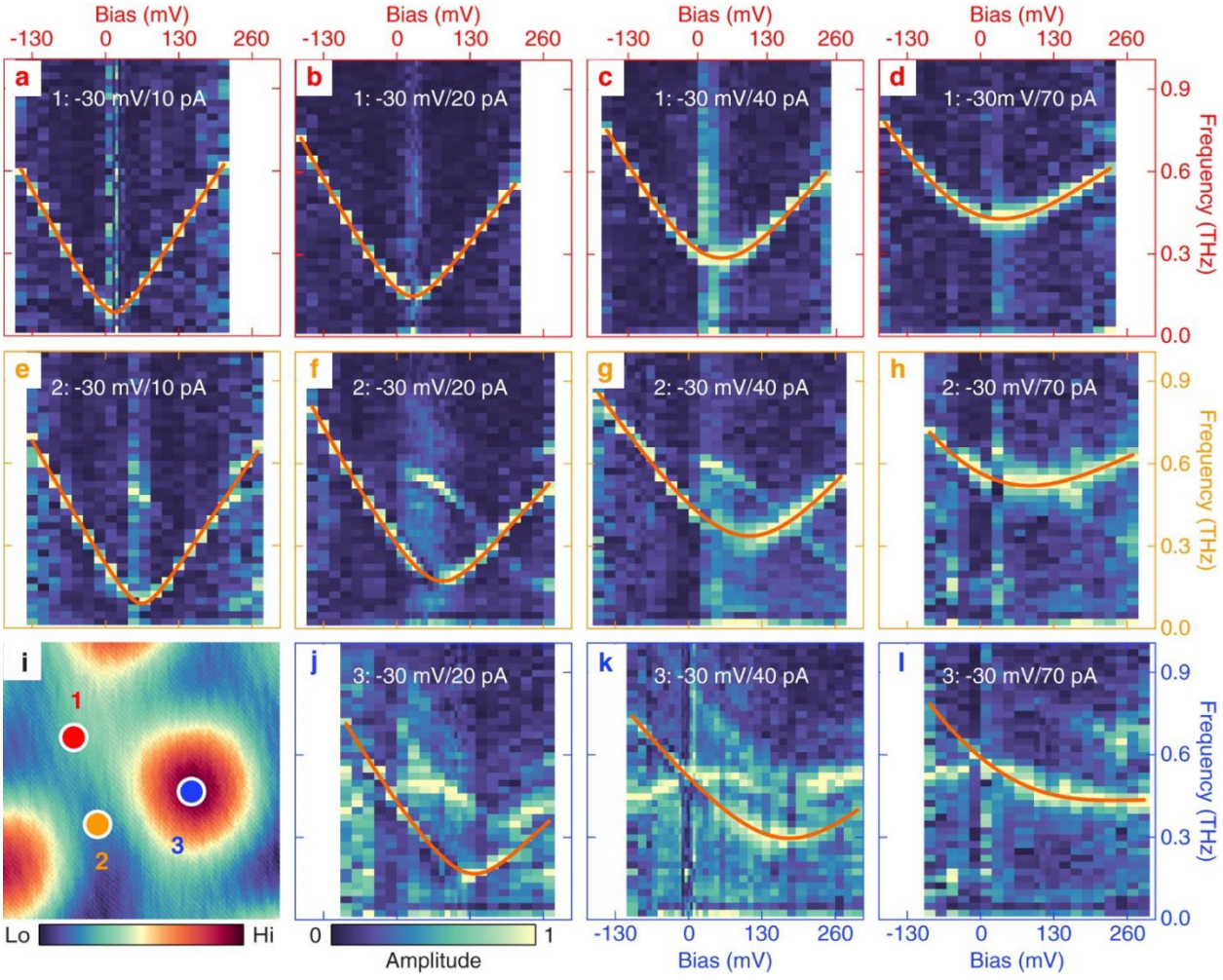
Bias (mV)
-130
0
130
260
a
1: -30 mV/10 pA
b
1: -30 mV/20 pA
c
1: -30 mV/40 pA
d
1: -30m V/70 pA
Frequency (THz)
0.9
0.6
0.3
0.0
e
2: -30 mV/10 pA
f
2: -30 mV/20 pA
g
2: -30 mV/40 pA
h
2: -30 mV/70 pA
i
1
2
3
Lo
Hi
j
3: -30 mV/20 pA
k
3: -30 mV/40 pA
l
3: -30 mV/70 pA
0
1
Amplitude
Bias (mV)

By fitting each parabola in Figure 4.3 to the eigenstate energy separation $\Delta E = 2\Omega$, we can quantify the parameters in the Hamiltonian. An analysis of the tip-substrate separation (Figure S4.4) was performed to convert the sample bias to electric field. As shown in Figure 4.4a, the tunnel-coupling A increases exponentially as the tip approaches the surface, in accordance with the lowering of the central barrier in the double-well potential. No obvious difference in A is observed by comparing the three different lateral positions indicated in Figure 4.3i, which is consistent with negligible variations in the tip-substrate separation when the tip is scanned in the constant current mode. The surface electrostatic field $\mathbf{F_{surface}}$ experienced by the H_2 shows a linear increase upon decreasing the tip-substrate separation (Figure 4.4b). Unlike the tunnel-coupling, $\mathbf{F_{surface}}$ varies significantly over these three positions, consistent with the different elemental composition of the underlying Cu_2N lattice. The dipole moment and polarizability differences for the two basis states can also be extracted from the fitting in Figure 4.3, as shown in Figure 4.4c and d.

A series of pump-probe measurements over 63 positions along the line in Figure 4.4e provided a semi-quantitative description of the surface electrostatic distribution, in contrast to the near constancy of the tunnel-coupling at different positions (Figure 4.4a). The hourglass shape of the time domain map (Figure 4.4f) clearly reveals the spatial variation and symmetry of the oscillation period along the line. The corresponding FFT results shown in Figure 4.4g display the oscillation frequency distribution, which essentially points to the sub-angstrom scale electrostatic environment experienced by the H_2 molecule. A series of images showing the THz induced rectification snapshots at selected time delays in the Figure S4.5 demonstrate the spatial distribution of the surface electrostatic field.

Figure 4.4 Quantitative description of the H_2 two-level system (TLS). **a-d**, Fitting parameters of the tunnel-coupling, surface electrostatic field, dipole moment difference, and polarizability difference of the TLS, respectively. All parameters are extracted from the corresponding fitting curves in Figure 4.3 and Figure S4.3. **e**, Linecut showing the positions 1 to 63 superimposed on top of the topography. **f**, Color map of a series of THz pump-probe measurements for the 63 tip positions along the line in (**e**). The tip is positioned with the feedback set point –30 mV/40 pA. The feedback is then turned off for measurements. **g**, Color map of the series of FFT results from the time domain measurements in (**f**). The superimposed dashed orange curve is a guide to show the change of the oscillation frequency as a function of tip position.

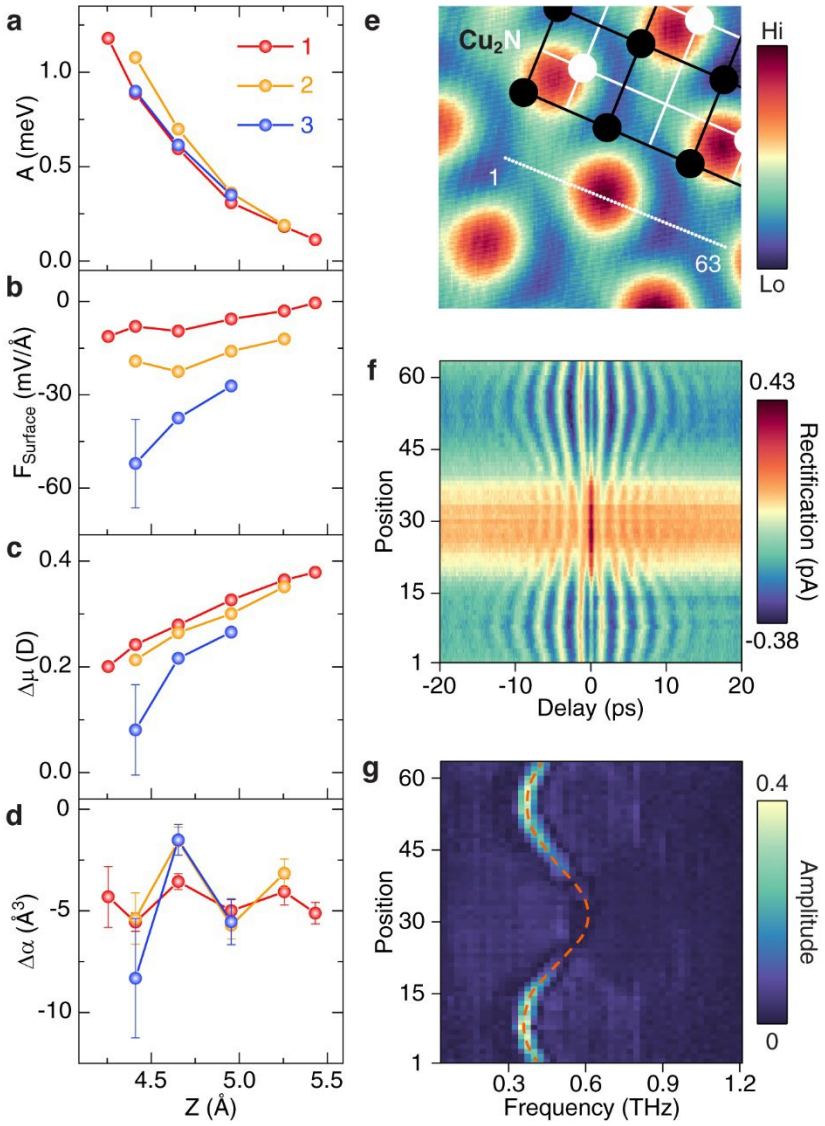
a
A (meV)
1.0
0.5
0.0
1
2
3
b
$F_{Surface}$ (mV/Å)
0
-30
-60
c
Δμ (D)
0.4
0.2
0.0
d
Δα (Å^3)
0
-5
-10
4.5
5.0
5.5
Z (Å)
e
Cu_2N
1
63
Hi
Lo
f
Position
60
45
30
15
1
-20
-10
0
10
20
Delay (ps)
0.43
-0.38
Rectification (pA)
g
Position
60
45
30
15
1
0.3
0.6
0.9
1.2
Frequency (THz)
0.4
0
Amplitude

In summary, we have established an electrical method to locally manipulate the ultrafast quantum coherence in a single molecular qubit with atomic scale spatial resolution. Both the coherent oscillation frequency and the dephasing time T2* can be precisely manipulated by simply varying the sample bias. The combination of shorter oscillation period and longer T2* under the electric field allows larger number of ultrafast quantum operations within the decoherence time. The atomic scale environment is also quantified by our simple but effective model Hamiltonian. This paradigm of electrical manipulation should be readily applicable to other molecular qubits [48,49]. Furthermore, electrical manipulation of the coherent evolution can be extended to molecular qubit systems that can be coupled and to establish protocols for creating and manipulating entangled states. This work points to the possibility of quantum information processing based on molecules with the distinct advantages of having widely tunable properties through chemical synthesis.

4.3 Supplementary Information

Sample and tip preparation

STM measurements were performed using Ag tips. The entire microscope and the sample were at 9 K±1.5 mK and pressure 6 $\times 10^{-11}$ torr. The electrochemically etched tips were prepared in vacuo by three cycles of Ne^+ sputtering and annealing. The Cu(001) surface was cleaned by repeated cycles of Ne^+ sputtering and annealing to 800 K. The monolayer Cu_2N islands were prepared by sputtering the clean Cu(001) surface with ionized N_2 gas and annealing to 670 K for 5 min. Hydrogen molecules adsorbed spontaneously onto the polar Cu_2N surface from the ultrahigh vacuum chamber background. The experimental data were taken more than one month after the initial cool down of the STM system, reaching a stable H_2 concentration on the Cu_2N surface. The desorption of the H_2 molecules were performed by illuminating the STM junction with the NIR (820 nm) laser of 100 uW power for 30 min.

Femtosecond (fs) THz-STM setup

Pairs of fs THz pulses were aligned into the STM junction to setup the fs THz-STM [15]. The THz pulses were generated by focusing femtosecond near infrared (NIR) pulses on a voltage controlled plasmonic photoconductive antenna (PCA). The NIR pulses were emitted from a Ti:Sapphire laser (Taccor ultra 8, Laser Quantum) with 1GHz repetition rate and 30 nm FWHM bandwidth centered at 820 nm. A beam from the Ti:Sapphire laser was split equally and recombined by a Mach-Zehnder interferometer to generate a pair of equal THz beams. The variable delay time between pulses in the two beams was controlled by a translational stage inserted into the path of one of the beams. The generated THz pulse pairs with linear polarization were focused through a Tsurupica lens and aligned into the STM junction with the THz electric field component 45^o from the STM tip axis and in the plane of incidence (p-polarization). The THz laser had a

bandwidth of 0.1 THz to 4 THz in free space and was narrowed down to about 0.1 THz to 1 THz in the STM junction. Due to the weak field of our THz source, there was negligible temperature increase and change of tip-substrate separation when the THz laser was focused and aligned into the junction.

Inelastic Electron Tunneling Spectroscopy (IETS) and THz Rectification Spectroscopy (TRS) with the STM

The STM-IETS measurements in Figure S4.2b were performed with a sine wave modulation of 3 mV root mean square (RMS) amplitude and 263.03 Hz frequency from the lock-in amplifier added to the DC sample bias. The STM feedback was turned off at −30 mV/40 pA set point before the DC bias was linearly ramped to acquire the STM-IETS spectra. For the TRS measurements, amplitude modulation was imposed by chopping the THz radiation with 0 to 10 V square wave of 263.03 Hz applied to the PCA. The chopping frequency was set by the lock-in amplifier to implement internal referencing. All the data presented in the main figures, and those in the Supplementary Information were obtained with the same tip.

Data Processing

All the STM topographies and the temporal snapshots of THz rectification imaging were plane fit without further processing. The plane fit was to correct the slight sample slope. A 0.1 THz high-pass FFT filter was applied to all the time domain measurements to remove the long-range delay variations in the rectification current due to laser misalignment.

Lattice assignment of the Cu_2N surface.

The contrast of Cu_2N topographic image depends on various parameters, including the tip structure, sample bias, and the adsorbed H_2 concentration [48,49]. Under high sample bias of 500 mV, most of the H_2 molecules near the STM tip will be ‘kicked’ away from the junction by the

high energy tunneling electrons [49]. The STM topography obtained at 500 mV in Figure S4.1c reveals the intrinsic contrast of the Cu_2N lattice image. The protrusions in Figure S4.1c can be assigned to the four-fold hollow sites, in consistency with previous studies [50]. Similarly, by desorbing all the adsorbed H_2 molecules with near-infrared 820 nm laser illumination [15], the STM topography at low sample bias also reveals the intrinsic Cu_2N surface (Figure S4.1e). Indeed, the same contrast is found for Figure S4.1c and Figure S4.1e with the protrusion to be the four-fold hollow site. The higher resolution in Figure S4.1c is probably due to residual H_2 molecules that remained in the junction. By comparing the topographic images under different sample biases and different H_2 coverages, we can conclude a contrast inversion and lateral offset in the topographic images taken at -20 mV/0.1 nA (Figure S4.1b, d, f).

Fitting the time domain data.

As shown in Figure S4.1a, the main coherent oscillation near zero delay is an interference of multiple closely related excited states, leading to a faster decay in the initial wave packet compared to the decoherence time. The dephasing time T_2^*, closely relates to but shorter than the decoherence time, characterizes the decay of the initial wave packet. The FFT result in Figure S4.1b also shows a broad peak composed of multiple frequencies that interfere to produce revivals in Figure S4.1a. A sinusoidal decay fitting function can be employed to obtain a good approximation of T_2^*.

The fitting function is a sum of three parts: a constant incoherent background signal (R_0), a Gaussian function for the THz pulse interference near zero delay $Be^{\frac{-(\tau-\tau_0)^2}{2\sigma^2}}$, and a sinusoidal function with an exponential decay for the dephasing: $A\,[\sin(2\pi f|\tau-\tau_0|+\varphi)]e^{\frac{-|\tau-\tau_0|}{T_2^*}}$.

The fitting function is given by:

$$R(\tau) = R_0 + Be^{\frac{-(\tau-\tau_0)^2}{2\sigma^2}} + A\,[\sin(2\pi f|\tau-\tau_0| + \varphi)]e^{\frac{-|\tau-\tau_0|}{T_2^*}},$$

where τ is the time delay between pump and probe pulses, τ_0 represents the zero-delay offset, A the oscillation amplitude, f the central frequency, and T_2^* the dephasing time. Figure S4.2a shows six examples of the fitting results.

Figure S4.1 Decay of the initial wave packet. **a**, Large range THz pump-probe measurement to show the decay of the initial wave packet at a short delay (about 15 ps) and 'revivals' at longer delays as indicated by the vertical arrows. The measurement in the range of 20 ps to 300 ps is magnified three times to highlight the multiple 'revivals'. **b**, FFT of the time domain results in (**a**). The central peak frequency is indicated by the vertical arrow.

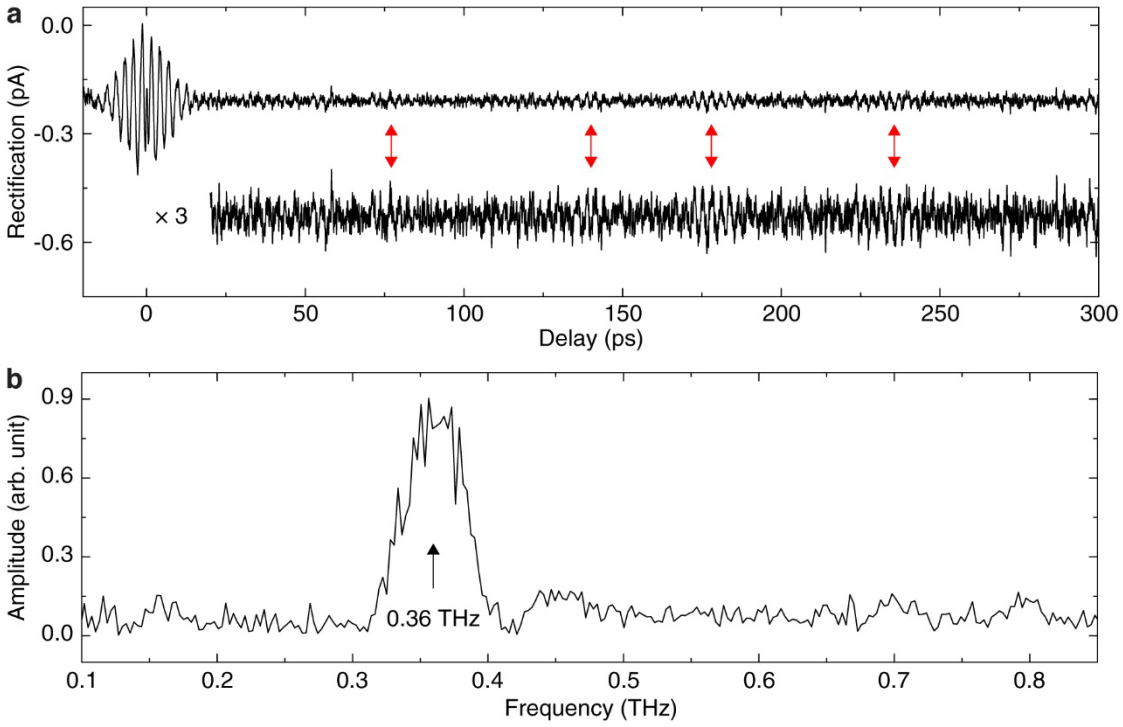
a
0.0
-0.3
-0.6
Rectification (pA)
× 3
0
50
100
150
200
250
300
Delay (ps)
b
0.9
0.6
0.3
0.0
Amplitude (arb. unit)
0.36 THz
0.1
0.2
0.3
0.4
0.5
0.6
0.7
0.8
Frequency (THz)

Figure S4.2 IETS and THz rectification spectroscopy (TRS) of H_2 over three different sites of Cu_2N. **a**, Constant current topography of the Cu_2N surface; image size 7.4 Å by 7.4 Å. Scanning condition: –20 mV/0.1 nA. **b**, STM-IETS measurements of the H_2 molecule. Tip is positioned at the three different positions labeled in (**a**) with –30 mV/40 pA set point. **c**, Large bias range TRS measurements of H_2 molecule over the three positions. **d**, Zoom-in TRS measurements to show the same sample bias range as in (**b**). All the spectra in (**b**), (**c**) and (**d**) are offset vertically for clarity.

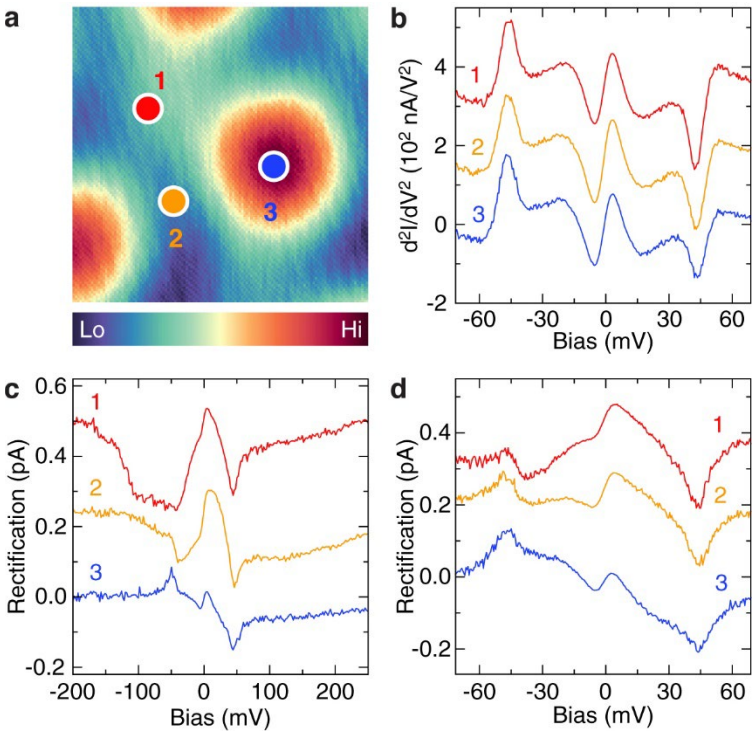
a
1
2
3
Lo
Hi
b
1
2
3
d²I/dV² (10² nA/V²)
4
2
0
-2
-60
-30
0
30
60
Bias (mV)
c
1
2
3
Rectification (pA)
0.6
0.4
0.2
0.0
-0.2
-200
-100
0
100
200
Bias (mV)
d
1
2
3
Rectification (pA)
0.4
0.2
0.0
-0.2
-60
-30
0
30
60
Bias (mV)

Figure S4.3 Complementary parabolas to Figure 4.3. Color maps of the sample bias-manipulated oscillation frequency with the other two additional tip-substrate separations over position 1 are shown in (**a**) and (**b**). Orange curves are the fittings of the data. For clarity, the intensity of all the spectra is normalized positively to the color palette with range (0, 1).

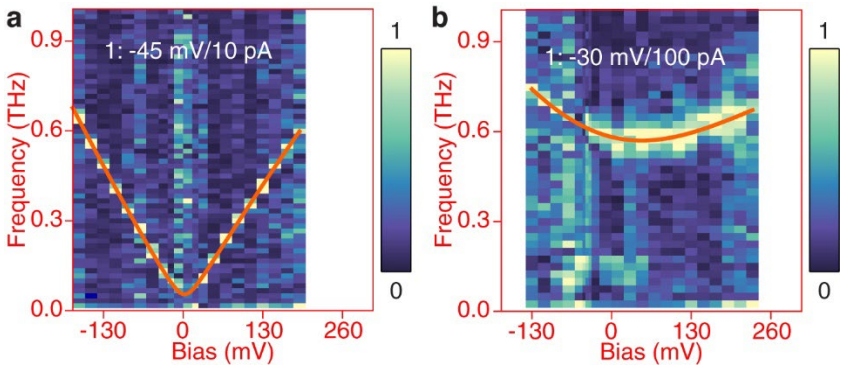
a
1: -45 mV/10 pA
Frequency (THz)
0.9
0.6
0.3
0.0
-130
0
130
260
Bias (mV)
1
0
b
1: -30 mV/100 pA
Frequency (THz)
0.9
0.6
0.3
0.0
-130
0
130
260
Bias (mV)
1
0

Figure S4.4 Determination of the tip-substrate separation. The scattered data points (black square) are the measured conductance G over the Cu_2N surface, Normalized to the conductance quantum G_0. A point contact is reached when $G = G_0$. The red line is a linear fitting of the data in the semi-log plot. The tip-substrate separation Z refers to the absolute tip height over the surface.

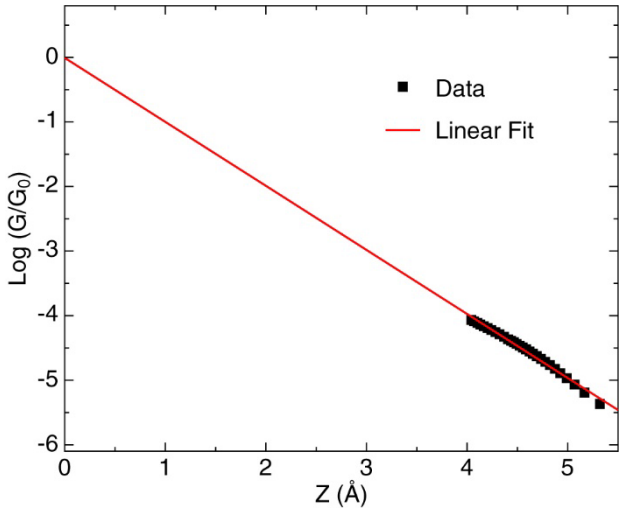
Data
Linear Fit
Log (G/G0)
Z (Å)
0
-1
-2
-3
-4
-5
-6
0
1
2
3
4
5

Figure S4.5 Evolution of the THz rectification images with increased delay times. **a**-**t**, A series of rectification imaging of the Cu_2N surface at delay times labelled in each image. All twenty images are measured in the same region. For each pixel in the images, tip is positioned at –30 mV/20 pA, and then feedback is turned off to sample 997 times of the rectification current. Feedback is turned on before and during the tip movement to the next pixel. All images are 14.8 Å × 14.8 Å (128 × 128 pixels) and 57 min acquisition time for each image. The orange dot marks the same position in all the images, which is also position 3 in Figure 4.3**i**.

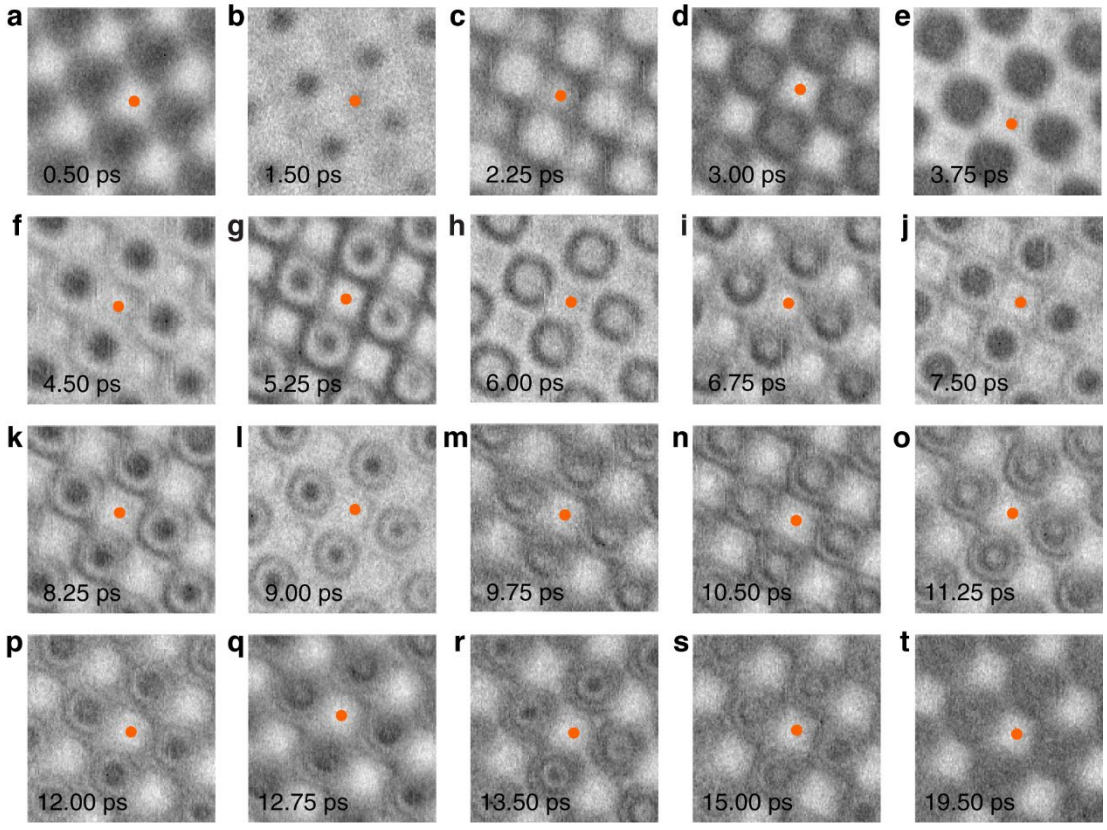
a
0.50 ps
b
1.50 ps
c
2.25 ps
d
3.00 ps
e
3.75 ps
f
4.50 ps
g
5.25 ps
h
6.00 ps
i
6.75 ps
j
7.50 ps
k
8.25 ps
l
9.00 ps
m
9.75 ps
n
10.50 ps
o
11.25 ps
p
12.00 ps
q
12.75 ps
r
13.50 ps
s
15.00 ps
t
19.50 ps

Figure S4.6 Cu_2N lattice assignment. **a**, STM constant current topography of a Cu_2N island. Scanning condition: -20 mV/0.1 nA. Image size: 88.5 Å by 75.4 Å. **b**, Zoom-in topography of the Cu_2N island in (**a**). Black dots represent the Cu atoms and white dots the N atoms. Scanning condition: -20 mV/0.1 nA. Image size: 13.0 Å by 13.0 Å. **c** and **d**, Consecutive STM topography of the same Cu_2N area at 500 mV/1 nA (**c**) and -20 mV/0.1 nA (**d**). High sample bias tends to excite the H_2 molecule out of the junction, revealing the bare Cu_2N surface under the STM tip. The image contrast inversion and lateral offset are observed from the comparison of (**c**) and (**d**). **e** and **f**, Consecutive STM topography of the same Cu_2N area after desorbing all the H_2 molecules by near-infrared laser illumination (**e**) and after the H_2 coverage recovers partially (**f**). A similar image contrast inversion and lateral offset are observed from the comparison of (**e**) and (**f**) as in (**c**) and (**d**). Image size for **c**-**f**: 14.8 Å by 14.8 Å.

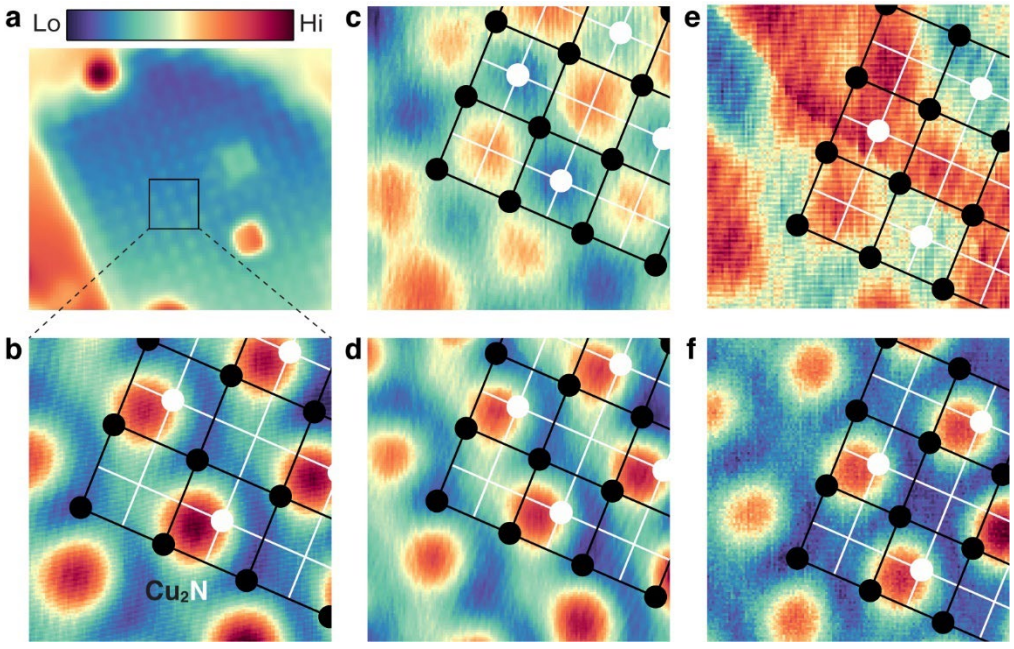
a
Lo
Hi
b
c
d
e
f
Cu2N

Figure S4.7 Fitting of the coherent oscillations. **a**, THz pump-probe measurements at six different sample biases (black) and their corresponding fitting (red). **b**, FFT of the time domain results in (**a**). The vertical line under each FFT peak marks the central frequency.

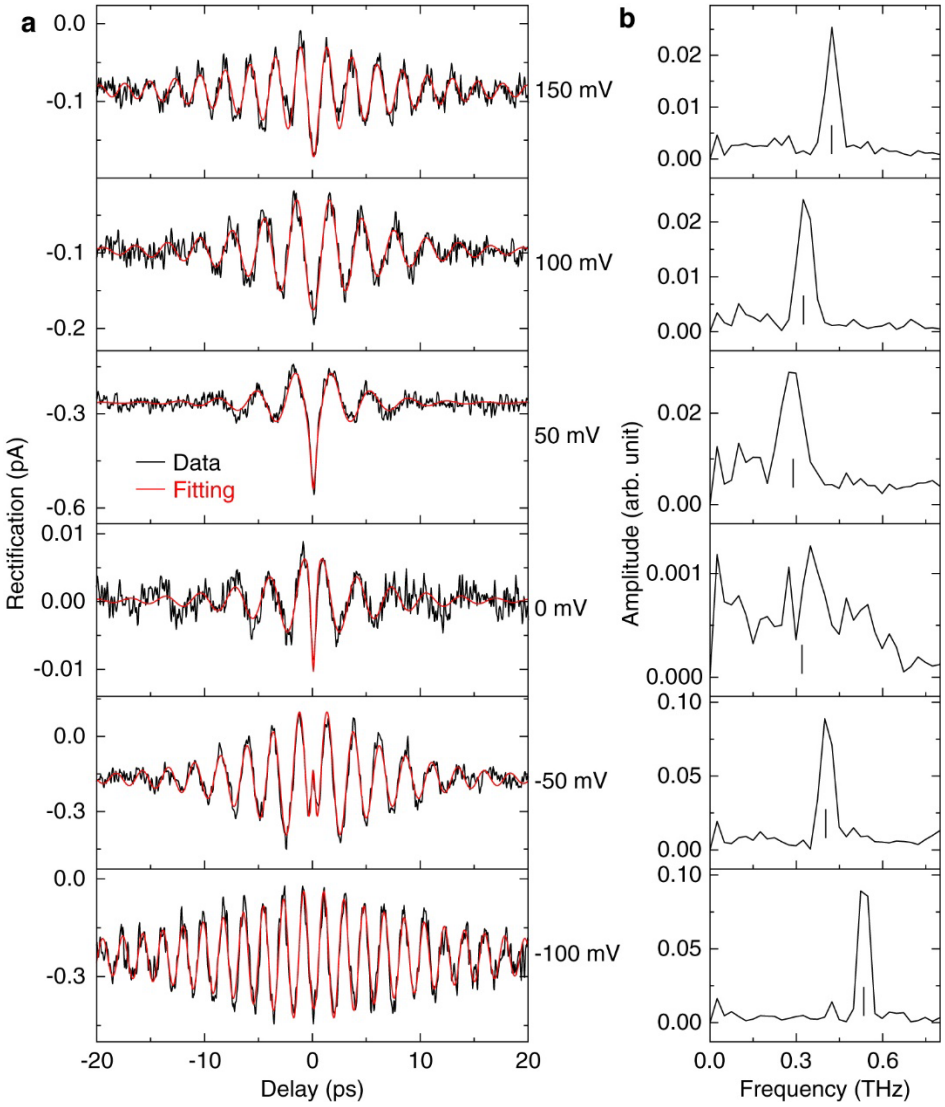
a
b
Rectification (pA)
Data
Fitting
150 mV
100 mV
50 mV
0 mV
-50 mV
-100 mV
Delay (ps)
Amplitude (arb. unit)
Frequency (THz)

Bibliography

[1] C. H. Bennett and D. P. DiVincenzo, *Quantum Information and Computation*, Nature **404**, 6775 (2000).

[2] Y. Makhlin, G. Schön, and A. Shnirman, *Quantum-State Engineering with Josephson-Junction Devices*, Rev. Mod. Phys. **73**, 357 (2001).

[3] L. M. K. Vandersypen and I. L. Chuang, *NMR Techniques for Quantum Control and Computation*, Rev. Mod. Phys. **76**, 1037 (2005).

[4] T. D. Ladd, F. Jelezko, R. Laflamme, Y. Nakamura, C. Monroe, and J. L. O'Brien, *Quantum Computers*, Nature **464**, 7285 (2010).

[5] K. C. Nowack, F. H. L. Koppens, Yu. V. Nazarov, and L. M. K. Vandersypen, *Coherent Control of a Single Electron Spin with Electric Fields*, Science **318**, 1430 (2007).

[6] R. Hanson and D. D. Awschalom, *Coherent Manipulation of Single Spins in Semiconductors*, Nature **453**, 7198 (2008).

[7] J. J. Pla, K. Y. Tan, J. P. Dehollain, W. H. Lim, J. J. L. Morton, D. N. Jamieson, A. S. Dzurak, and A. Morello, *A Single-Atom Electron Spin Qubit in Silicon*, Nature **489**, 7417 (2012).

[8] S. Thiele, F. Balestro, R. Ballou, S. Klyatskaya, M. Ruben, and W. Wernsdorfer, *Electrically Driven Nuclear Spin Resonance in Single-Molecule Magnets*, Science **344**, 1135 (2014).

[9] A. Laucht et al., *Electrically Controlling Single-Spin Qubits in a Continuous Microwave Field*, Science Advances **1**, e1500022 (2015).

[10] C. L. Degen, F. Reinhard, and P. Cappellaro, *Quantum Sensing*, Rev. Mod. Phys. **89**, 035002 (2017).

[11] P. Willke, W. Paul, F. D. Natterer, K. Yang, Y. Bae, T. Choi, J. Fernández-Rossier, A. J. Heinrich, and C. P. Lutz, *Probing Quantum Coherence in Single-Atom Electron Spin Resonance*, Science Advances **4**, eaaq1543 (2018).

[12] K. Yang, W. Paul, S.-H. Phark, P. Willke, Y. Bae, T. Choi, T. Esat, A. Ardavan, A. J. Heinrich, and C. P. Lutz, *Coherent Spin Manipulation of Individual Atoms on a Surface*, Science **366**, 509 (2019).

[13] S. M. Clark, K.-M. C. Fu, T. D. Ladd, and Y. Yamamoto, *Quantum Computers Based on Electron Spins Controlled by Ultrafast Off-Resonant Single Optical Pulses*, Phys. Rev. Lett. **99**, 040501 (2007).

[14] D. Press, T. D. Ladd, B. Zhang, and Y. Yamamoto, *Complete Quantum Control of a Single Quantum Dot Spin Using Ultrafast Optical Pulses*, Nature **456**, 7219 (2008).

[15] L. Wang, Y. Xia, and W. Ho, *Atomic-Scale Quantum Sensing Based on the Ultrafast Coherence of an H_2 Molecule in an STM Cavity*, Science **376**, 401 (2022).

[16] M. Grifoni and P. Hänggi, *Driven Quantum Tunneling*, Physics Reports **304**, 229 (1998).

[17] G. E. Santoro and E. Tosatti, *Optimization Using Quantum Mechanics: Quantum Annealing through Adiabatic Evolution*, J. Phys. A: Math. Gen. **39**, R393 (2006).

[18] J. Clarke and F. K. Wilhelm, *Superconducting Quantum Bits*, Nature **453**, 7198 (2008).

[19] J. Berezovsky, M. H. Mikkelsen, N. G. Stoltz, L. A. Coldren, and D. D. Awschalom, *Picosecond Coherent Optical Manipulation of a Single Electron Spin in a Quantum Dot*, Science **320**, 349 (2008).

[20] D. Press, K. De Greve, P. L. McMahon, T. D. Ladd, B. Friess, C. Schneider, M. Kamp, S. Höfling, A. Forchel, and Y. Yamamoto, *Ultrafast Optical Spin Echo in a Single Quantum Dot*, Nature Photon **4**, 6 (2010).

[21] R. Hildner, D. Brinks, and N. F. van Hulst, *Femtosecond Coherence and Quantum Control of Single Molecules at Room Temperature*, Nature Phys **7**, 2 (2011).

[22] P. Willke, T. Bilgeri, X. Zhang, Y. Wang, C. Wolf, H. Aubin, A. Heinrich, and T. Choi, *Coherent Spin Control of Single Molecules on a Surface*, ACS Nano **15**, 17959 (2021).

[23] L. M. Veldman, L. Farinacci, R. Rejali, R. Broekhoven, J. Gobeil, D. Coffey, M. Ternes, and A. F. Otte, *Free Coherent Evolution of a Coupled Atomic Spin System Initialized by Electron Scattering*, Science **372**, 964 (2021).

[24] Y. Terada, S. Yoshida, O. Takeuchi, and H. Shigekawa, *Real-Space Imaging of Transient Carrier Dynamics by Nanoscale Pump–Probe Microscopy*, Nature Photon **4**, 12 (2010).

[25] T. L. Cocker, V. Jelic, M. Gupta, S. J. Molesky, J. A. J. Burgess, G. D. L. Reyes, L. V. Titova, Y. Y. Tsui, M. R. Freeman, and F. A. Hegmann, *An Ultrafast Terahertz Scanning Tunnelling Microscope*, Nature Photon **7**, 8 (2013).

[26] S. Yoshida, H. Hirori, T. Tachizaki, K. Yoshioka, Y. Arashida, Z.-H. Wang, Y. Sanari, O. Takeuchi, Y. Kanemitsu, and H. Shigekawa, *Subcycle Transient Scanning Tunneling Spectroscopy with Visualization of Enhanced Terahertz near Field*, ACS Photonics **6**, 1356 (2019).

[27] S. Yoshida, Y. Arashida, H. Hirori, T. Tachizaki, A. Taninaka, H. Ueno, O. Takeuchi, and H. Shigekawa, *Terahertz Scanning Tunneling Microscopy for Visualizing Ultrafast Electron Motion in Nanoscale Potential Variations*, ACS Photonics **8**, 315 (2021).

[28] M. Abdo, S. Sheng, S. Rolf-Pissarczyk, L. Arnhold, J. A. J. Burgess, M. Isobe, L. Malavolti, and S. Loth, *Variable Repetition Rate THz Source for Ultrafast Scanning Tunneling Microscopy*, ACS Photonics **8**, 702 (2021).

[29] S. Yoshida, Y. Aizawa, Z. Wang, R. Oshima, Y. Mera, E. Matsuyama, H. Oigawa, O. Takeuchi, and H. Shigekawa, *Probing Ultrafast Spin Dynamics with Optical Pump–Probe Scanning Tunnelling Microscopy*, Nature Nanotech **9**, 8 (2014).

[30] C. Guo et al., *Probing Nonequilibrium Dynamics of Photoexcited Polarons on a Metal-Oxide Surface with Atomic Precision*, Phys. Rev. Lett. **124**, 206801 (2020).

[31] T. L. Cocker, D. Peller, P. Yu, J. Repp, and R. Huber, *Tracking the Ultrafast Motion of a Single Molecule by Femtosecond Orbital Imaging*, Nature **539**, 7628 (2016).

[32] D. Peller, L. Z. Kastner, T. Buchner, C. Roelcke, F. Albrecht, N. Moll, R. Huber, and J. Repp, *Sub-Cycle Atomic-Scale Forces Coherently Control a Single-Molecule Switch*, Nature **585**, 7823 (2020).

[33] S. Li, S. Chen, J. Li, R. Wu, and W. Ho, *Joint Space-Time Coherent Vibration Driven Conformational Transitions in a Single Molecule*, Phys. Rev. Lett. **119**, 176002 (2017).

[34] M. Garg and K. Kern, *Attosecond Coherent Manipulation of Electrons in Tunneling Microscopy*, Science **367**, 411 (2020).

[35] M. Garg, A. Martin-Jimenez, Y. Luo, and K. Kern, *Ultrafast Photon-Induced Tunneling Microscopy*, ACS Nano **15**, 18071 (2021).

[36] M. Garg, A. Martin-Jimenez, M. Pisarra, Y. Luo, F. Martín, and K. Kern, *Real-Space Subfemtosecond Imaging of Quantum Electronic Coherences in Molecules*, Nat. Photon. **16**, 3 (2022).

[37] M. Schneiderbauer, M. Emmrich, A. J. Weymouth, and F. J. Giessibl, *CO Tip Functionalization Inverts Atomic Force Microscopy Contrast via Short-Range Electrostatic Forces*, Phys. Rev. Lett. **112**, 166102 (2014).

[38] S. Li, D. Yuan, A. Yu, G. Czap, R. Wu, and W. Ho, *Rotational Spectromicroscopy: Imaging the Orbital Interaction between Molecular Hydrogen and an Adsorbed Molecule*, Phys. Rev. Lett. **114**, 206101 (2015).

[39] H. Wang, S. Li, H. He, A. Yu, F. Toledo, Z. Han, W. Ho, and R. Wu, *Trapping and Characterization of a Single Hydrogen Molecule in a Continuously Tunable Nanocavity*, J. Phys. Chem. Lett. **6**, 3453 (2015).

[40] S. Li, G. Czap, J. Li, Y. Zhang, A. Yu, D. Yuan, H. Kimura, R. Wu, and W. Ho, *Confinement-Induced Catalytic Dissociation of Hydrogen Molecules in a Scanning Tunneling Microscope*, J. Am. Chem. Soc. **144**, 9618 (2022).

[41] S. A. Empedocles and M. G. Bawendi, *Quantum-Confined Stark Effect in Single CdSe Nanocrystallite Quantum Dots*, Science **278**, 2114 (1997).

[42] J. A. Gupta, C. P. Lutz, A. J. Heinrich, and D. M. Eigler, *Strongly Coverage-Dependent Excitations of Adsorbed Molecular Hydrogen*, Phys. Rev. B **71**, 115416 (2005).

[43] C. Lotze, M. Corso, K. J. Franke, F. von Oppen, and J. I. Pascual, *Driving a Macroscopic Oscillator with the Stochastic Motion of a Hydrogen Molecule*, Science **338**, 779 (2012).

[44] Ph. Tamarat et al., *Stark Shift Control of Single Optical Centers in Diamond*, Phys. Rev. Lett. **97**, 083002 (2006).

[45] F. D. Natterer, F. Patthey, and H. Brune, *Distinction of Nuclear Spin States with the Scanning Tunneling Microscope*, Phys. Rev. Lett. **111**, 175303 (2013).

[46] S. Li, A. Yu, F. Toledo, Z. Han, H. Wang, H. Y. He, R. Wu, and W. Ho, *Rotational and Vibrational Excitations of a Hydrogen Molecule Trapped within a Nanocavity of Tunable Dimension*, Phys. Rev. Lett. **111**, 146102 (2013).

[47] F. D. Natterer, F. Patthey, and H. Brune, *Resonant-Enhanced Spectroscopy of Molecular Rotations with a Scanning Tunneling Microscope*, ACS Nano **8**, 7099 (2014).

[48] R. Temirov, S. Soubatch, O. Neucheva, A. C. Lassise, and F. S. Tautz, *A Novel Method Achieving Ultra-High Geometrical Resolution in Scanning Tunnelling Microscopy*, New J. Phys. **10**, 053012 (2008).

[49] C. Weiss, C. Wagner, C. Kleimann, M. Rohlfing, F. S. Tautz, and R. Temirov, *Imaging Pauli Repulsion in Scanning Tunneling Microscopy*, Phys. Rev. Lett. **105**, 086103 (2010).

[50] T. Choi, C. D. Ruggiero, and J. A. Gupta, *Incommensurability and Atomic Structure of* c*(2×2)N/Cu(100): A Scanning Tunneling Microscopy Study*, Phys. Rev. B **78**, 035430 (2008).

CHAPTER 5

Optical Tuning of the Kondo State in a Single Atom[†]

5.1 Abstract

We report the optical tuning of the Kondo state in a single cobalt atom adsorbed on the NiAl(110) surface by employing a femtosecond near-infrared laser in a scanning tunneling microscope. The Kondo state of a cobalt atom can be completely quenched by laser illumination, whereas it recovers after blocking the laser. Laser power adjustment allows continuous tuning of the Kondo amplitude. An exponential decay of the Kondo amplitude is found upon increasing the laser power. The spatial distribution and quenching of the Kondo resonance is demonstrated by Kondo imaging with and without laser illumination.

[†] This chapter by Likun Wang, and W. Ho is prepared for submission.

5.2 Introduction

Since its first prediction in the 1960s [1], Kondo effect has attracted tremendous attention due to the rich physics in this many-body behavior [2]. When magnetic impurities are hosted in a non-magnetic metal, the localized magnetic moment is screened by the surrounding conduction electrons in the host [3]. The exchange interaction between the impurity spin and the host spin forms a correlated impurity-host singlet which acts as a local scattering potential for electrons in the host metal. The experimental measurement of Kondo effect has been realized with various methods, such as transport-based studies [4–7] and optical spectroscopy [8–11]. Furthermore, the quantum quench of the Kondo state has been demonstrated in the quantum dot experiments [9]. Photon absorption in the quantum dot created an electron-hole pair and induced a sudden change in the local charge configuration, which quenched the Kondo resonance of the quantum dot. However, these experiments offered no spatial resolution of the Kondo state.

The spatial resolution can be naturally provided by scanning tunneling microscopy (STM) and spectroscopy (STS) [12]. Since the first demonstration of Kondo state in a single cobalt (Co) atom studied by STM and STS [13,14], various types of atoms and molecules have been investigated to show the Kondo states. The Kondo effect has been proven to exist in single neutral atoms [15–18], magnetic molecules [19–23], charged molecules [24], or even two-dimensional molecular gas [25]. With the unique capability of STM to modify the single molecule [19] or the assembly of molecules [20], the Kondo state can be controlled correspondingly. Nevertheless, a reversible and continuous tuning of the Kondo state is still lacking, especially using optical lasers.

In this letter, we studied the Kondo state of single Co atoms adsorbed on the NiAl(110) surface using a femtosecond (fs) near-infrared (NIR) laser together with a home-built low-temperature STM. By performing scanning tunneling spectroscopy, we confirmed the existence of

Kondo state of the Co atom (Figure 5.1). The Kondo state can be completely quenched by laser illumination while the sample temperature only increased by ~1.9 K. Adjusting the laser power allowed continuous tuning of the Kondo amplitude, whereas the spectral width kept constant. An exponential decay of the Kondo amplitude was found upon increasing the power of laser illumination. Kondo imaging was then performed to demonstrate the spatial distribution of the Kondo state and its quenching by femtosecond lasers with atomic-scale resolution.

5.3 Experimental Details

The experiment was performed in a home-built ultrahigh vacuum (UHV, 8×10^{-11} torr) scanning tunneling microscope (STM) operating at a base temperature of 9 K in the absence of laser illumination. The NiAl(110) surface was cleaned by repeated cycles of Ne sputtering and subsequent annealing to 1120 K. The clean NiAl(110) surface was exposed to clean O_2 gas at 780 K and annealed to 1070 K to form a thin Al_2O_3 film with a coverage of ~50%. Silver tips were electrochemically etched in air before further repeated cycles of Ne sputtering and anneal in the UHV chamber. Co atoms were evaporated onto the surface at the 9 K from a Knudsen cell doser. A current of 16.2 A was applied to the Tungsten filament (0.03" diameter) around the ceramic cell to evaporate the Co for 1 min. The Co atoms under study were adsorbed on the clean NiAl(110) surface area.

fs NIR pulses from a Ti:Sapphire oscillator (Taccor ultra 8, Laser Quantum) were focused into the STM junction [Figure 5.2(a)] using a 4" focal length plano-convex Tsurupica lens. The incident angle is 45°from the surface normal with the laser polarization angle parallel with the tip axis. The laser is centered at 820 nm with 1 GHz repetition rate and 30 nm full width half maximum bandwidth. A continuously variable neutral density filter from Thorlabs was employed to adjust the laser power.

The surface temperature measured by silicon diodes increases linearly with the laser power illuminated into the STM junction. It takes ~30 mins for the STM to reach a thermal equilibrium after laser illumination. All the measurements were obtained after the both the sample temperature and the tip-substrate separation stabilized. The fluctuation on the tip-substrate separation induced by laser illumination is negligible in our operation range of the laser power.

5.4 Results and Discussions

A. Kondo state of a single Co atom

Single Co atoms appear as protrusions when adsorbed on the NiAl(110) surface, as shown in Figure 5.1(a). Two types of single Co atoms with different sizes and heights can be easily distinguished. We label the smaller and lower Co atom as 'Type A' and the larger and higher Co atom as 'Type B'. A zoom in topography of the 'Type A' Co atom is shown in Figure 5.1(b). A series of STM spectroscopy were then performed over the six lateral positions marked in Figure 5.1(b) by measuring the differential conductance (dI/dV). The tip-substrate separation was fixed during the measurements and a 1 mV (root mean square value) sinusoidal wave modulation with a frequency of 263.03 Hz was applied on the sample bias for lock-in detection. As shown in Figure 5.1(c), the dI/dV spectra over position 1 shows an asymmetric Fano-like dip around the Fermi level, which can be described as the Kondo resonance [13,14]. Previous studies have also shown Kondo effect of Co adsorbed on other different metal surfaces, such as copper [15], gold [13], and silver [26]. When the tip was moved away from the top site of the Co atom, the intensity of the dip gradually decreased. The dip almost disappeared over position 6 which is about 12 Å from the top site of the Co atom. A small change on the symmetry of the dip shape can also be seen from position 1 to position 6 [13]. The asymmetry of the Kondo resonance is determined by the

interference between electrons from the STM tip tunneling into the conduction band of the substrate and into the Kondo state of the adsorbed Co atom.

The Kondo state shown in the dI/dV spectra can be expressed by the Fano equation [27,28,12,25]:

$$\frac{dI(V)}{dV} = A\frac{(\varepsilon + q)^2}{1+\varepsilon^2} + B$$

with $\varepsilon = \frac{eV-\varepsilon_0}{\Gamma}$,

and $\Gamma = \frac{1}{2}\sqrt{\left(3.2k_B T_{tip}\right)^2 + \left(5.4k_B T_{sample}\right)^2 + \left(2\sqrt{2}V_{ac}\right)^2 + (2k_B T_k)^2}$

Here A is the Kondo amplitude, B is the background signal, q is the Fano parameter, and ε is the energy parameter with ε_0 representing the energy position of the Kondo resonance. Γ is the half-width at half-minimum of the Kondo dip, which is related to the sample (T_{sample}) and tip (T_{tip}) temperature, the bias modulation (V_{ac}), and the Kondo temperature (T_k).

The Fano parameter q of only -0.07 ±0.0029 extracted from the fitting of the dI/dV spectra over position 1 indicates that almost all electrons tunnel into the conduction band of NiAl(110) surface modified by the Kondo resonance. The extracted Kondo temperature $T_k = 38$ K is similar to previous studies of Co atoms on other surfaces [26].

B. Optical tuning of the Kondo state

The Kondo state can be quenched efficiently by femtosecond NIR illumination, as shown in Figure 5.2. The dI/dV spectra of the 'Type A' Co atom in Figure 5.2(c) appeared similarly to the one in Figure 5.1(c). A striking decrease of the dI/dV signal was found upon introducing laser illumination into the STM junction. In Figure 5.2(c), an illumination of 15 mW NIR pulses almost

quenched the Kondo state completely. The residual feature in the dI/dV spectra with laser illumination can be ascribed to the surface state, as also shown in Figure 5.2(c). The optical suppression of the Kondo state is further confirmed by the d^2I/dV^2 signal [Figure 5.2(d)] obtained simultaneously with the dI/dV spectra in Figure 5.2(c). The Kondo state recovers once we block the laser illumination.

We also performed dI/dV measurements over the 'Type B' Co atom in Figure 5.2(b). As shown in Figure 5.2(e), it exhibited a similar Kondo resonance but with a broader dip. A Kondo temperature of 152 K can be extracted from the fitting of the Fano equation to the dI/dV spectra. Comparing to the 'Type A' Co atom, 'Type B' Co possessed a much higher temperature which can be possibly explained by a stronger overlap of the d orbital of the 'Type B' Co with the conduction band states of the NiAl(110) surface. Apart from the higher Kondo temperature, a surprising difference was found between the light effect of the Kondo state over the two types of Co atoms. The Kondo signal of 'Type B' Co remained strong with the same laser illumination, as shown in Figure 5.2(e) and (f).

To demonstrate the optical tuning of the Kondo state with our fs NIR laser pulses, we performed the laser power dependence of the Kondo amplitude over the 'Type A' Co atom marked in Figure 5.3(a). The laser power was adjusted from 0 mW to 16 mW by a continuously variable neutral density (ND) filter. As shown in Figure 5.3(b), the Kondo dip gradually disappeared upon increasing the laser power. The d^2I/dV^2 spectra in Figure 5.3(c) further confirmed the tuning of the Kondo state by laser power. The Kondo amplitude can be defined as the peak-dip intensity difference in the d^2I/dV^2 spectra [25], which minimized the background signal in the dI/dV spectra. An exponential decay of the Kondo amplitude as a function of the laser power is shown in Figure 5.3(d).

Similar measurements over the 'Type B' Co atom are also shown in Figure 5.4. In contrast to the 'Type A' Co atom, the laser power dependence of the Kondo state in Figure 5.4(b) and Figure 5.4(c) shows a much smaller change on the Kondo state. A linear decrease on the Kondo amplitude was found over the 'Type B' Co atom, as shown in Figure 5.4(d). It should be noted that, in either case, the dI/dV spectral width did not show any change under laser illumination, which ruled out the possibility of an obvious contribution to the Kondo signal from the temperature increase indued by the laser. The constant dI/dV spectral width can be further confirmed by the fixed peak position in the d^2I/dV^2 spectra.

C. Kondo imaging

A major advantage of STM on the study of Kondo effect is the ability to image the spatial distribution of the Kondo state with atomic-scale resolution, in addition to the spectroscopy. To demonstrate the optical quench of the Kondo state, we performed d^2I/dV^2 imaging over the 'Type A' Co atom. The peak and dip positions in the d^2I/dV^2 spectra were found to be unchanged upon changing the lateral position, tip-substrate separation, and the laser power. By fixing the sample bias at the peak (2.2 mV) and dip (-5 mV) positions over the 'Type A' Co atom, we can acquire the constant height d^2I/dV^2 images across the atom. A subtraction of these two images allows us to display the imaging of the Kondo amplitude, as shown in Figure 5.5(a). The Kondo imaging of the 'Type A' Co atom without laser illumination appeared as a protrusion following its constant current topography in Figure 5.2(b). As a power of 15 mW laser pulses are irradiated into the STM junction, the spatial distribution of the Kondo state was smeared out almost completely, as shown in Figure 5.5(b). The Kondo imaging under laser illumination with spatial resolution further confirmed the optical quench of the Kondo state.

The optical tuning of the Kondo state of the Co atom in the STM junction involves the coupling of photon with tunneling electrons [29]. Previous studies have shown light induced suppression of Kondo effect in a quantum dot, where an electron-hole pair was generated by the photon absorption, leading to the destruction of the correlated dot-reservoir singlet [9]. The above theory should also be applicable to our study. The unpaired electron in the Co atom responsible for the Kondo state is combined with the extra electron in the generated electron-hole pair from laser illumination. Due to the stronger coupling of the 'Type B' Co atom with the substrate, higher laser power would be necessary to completely quench its Kondo state. However, the exponential decay of the Kondo amplitude over the 'Type A' Co atom upon increasing the laser power remains elusive and requires further experimental evidence and theoretical simulations.

5.5 Conclusion

In summary, we have demonstrated the continuous tuning of the Kondo effect in a single Co atom by fs NIR laser pulses combined with a low temperature STM. The ability to tune and completely quench the Kondo amplitude of a single Co atom by laser illumination allows the optical tuning of Kondo state with atomic-scale spatial resolution. With fs NIR laser pulses, it becomes even possible to track the time evolution of the Kondo state collapse and revival by pump-probe techniques [11]. Our study provides a new platform for investigating Kondo related physics with both spatial and temporal resolutions.

Figure 5.1 Detection of the Kondo state in a single Co atom. (a) Large area constant current STM topography of the Co atoms adsorbed on the NiAl(110) surface. Two types of single Co atoms with different sizes and heights can be clearly distinguished and are labelled as 'Type A' (star) and 'Type B' (triangle), respectively. Image size 100.4 Å × 100.4 Å. Scanning condition: 100 mV/40 pA. (b) Constant current STM topography of a 'Type A' Co atom adsorbed on the NiAl(110) surface. Image size 25.1 Å × 25.1 Å. Scanning condition: 100 mV/40 pA. (c) A series of dI/dV spectra over six different lateral positions. Tip is placed at the correspondingly colored positions marked in (b) with 20 mV/0.9 nA setpoint for dI/dV measurements. A sinusoidal wave modulation of 1 mV at 263.03 Hz is applied on the sample bias for all the dI/dV measurements. The red curve is a fitting of the measurement over position 1 using the model described in the text. All spectra are offset vertically for clarity.

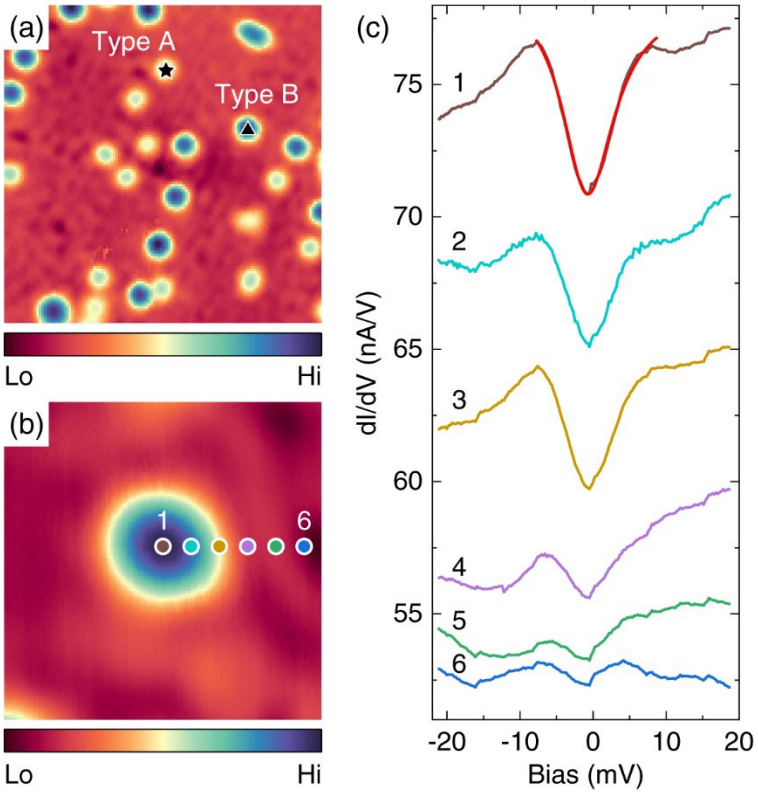
(a)
Type A
Type B
Lo
Hi
(b)
1
6
Lo
Hi
(c)
75
70
65
60
55
dI/dV (nA/V)
1
2
3
4
5
6
-20
-10
0
10
20
Bias (mV)

Figure 5.2 Optical quenching of the Kondo state. (a) Schematic diagram of the experimental setup for the NIR-STM. A beam of fs NIR laser pulses is coupled into the STM junction. (b) Constant current STM topography of two Co atoms adsorbed on the NiAl(110) surface. Image size 25.1 Å × 25.1 Å. Scanning condition: 100 mV/40 pA. The two types of Co are labelled as 'Type A' (star) and 'Type B' (triangle), respectively. (c) dI/dV spectra taken with the tip positioned over the 'Type A' Co atom with (red) or without (black) pulsed laser illumination. (d) d^2I/dV^2 spectra acquired simultaneously with the dI/dV spectra in (c). (e) dI/dV spectra taken with the tip positioned over the 'Type B' Co atom with (red) or without (black) pulsed laser illumination. (f) d^2I/dV^2 spectra acquired simultaneously with the dI/dV spectra in (e). The laser power is 15 mW for 'Light ON' measurements. Tip is set at 20 mV/0.7 nA over the corresponding Co atom before turning off the feedback to take all the spectra in (c) to (f).

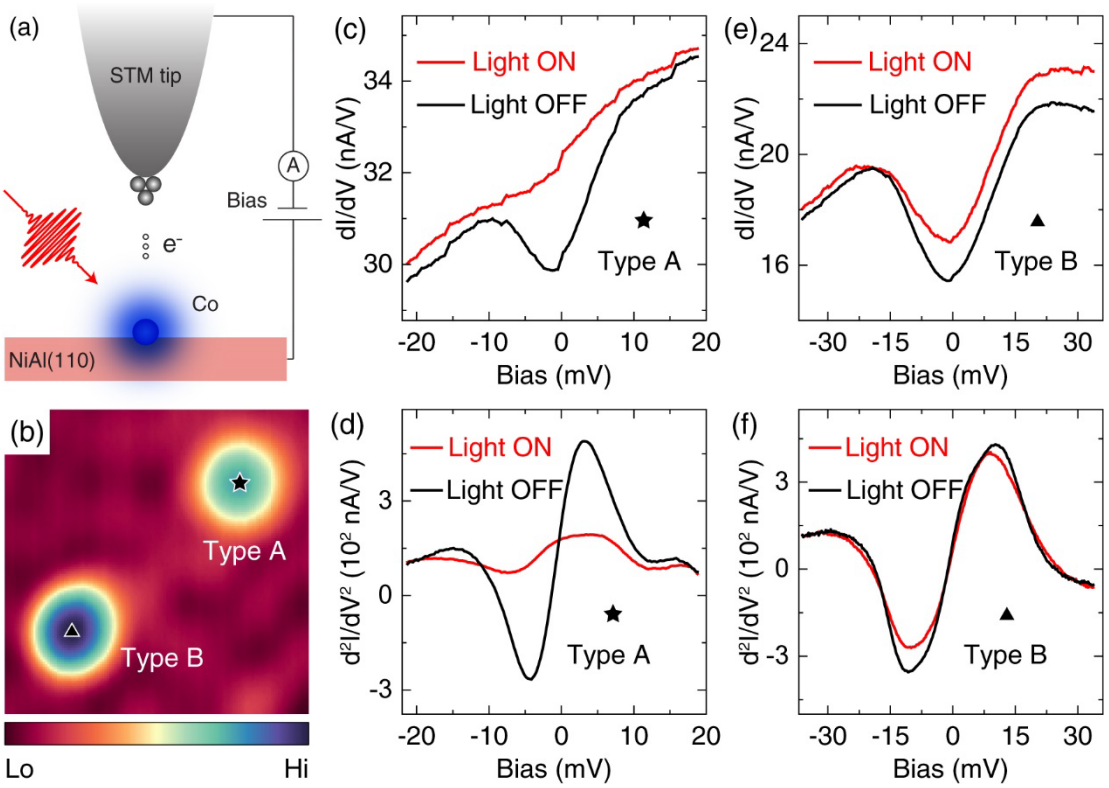
(a)
STM tip
A
Bias
e⁻
Co
NiAl(110)
(b)
Type A
Type B
Lo
Hi
(c)
Light ON
Light OFF
dI/dV (nA/V)
34
32
30
Type A
-20
-10
0
10
20
Bias (mV)
(e)
24
20
16
Light ON
Light OFF
dI/dV (nA/V)
Type B
-30
-15
0
15
30
Bias (mV)
(d)
Light ON
Light OFF
d²I/dV² (10² nA/V)
3
0
-3
Type A
-20
-10
0
10
20
Bias (mV)
(f)
Light ON
Light OFF
d²I/dV² (10² nA/V)
3
0
-3
Type B
-30
-15
0
15
30
Bias (mV)

Figure 5.3 Optical tuning of the Kondo amplitude. (a) Constant current STM topography of Co atoms adsorbed on the NiAl(110) surface. Image size 50.2 Å × 50.2 Å. Scanning condition: 100 mV/40 pA. (b) A series of laser power dependent dI/dV spectra taken with the tip positioned over the 'Type A' Co atom marked in (a). The laser power is adjusted from 0 mW (bottom) to 16 mW (top). All the measurements were performed with the same setpoint of 25 mV/0.9 nA. (c) d^2I/dV^2 spectra acquired simultaneously with the dI/dV spectra in (b). The dashed line indicates a fixed peak position upon increasing the laser power. (d) The laser power dependence of the Kondo amplitude. The Kondo amplitude is extracted from the peak intensity of the d^2I/dV^2 spectra in (c). The red line is a linear fitting to the data in the semi-log plot.

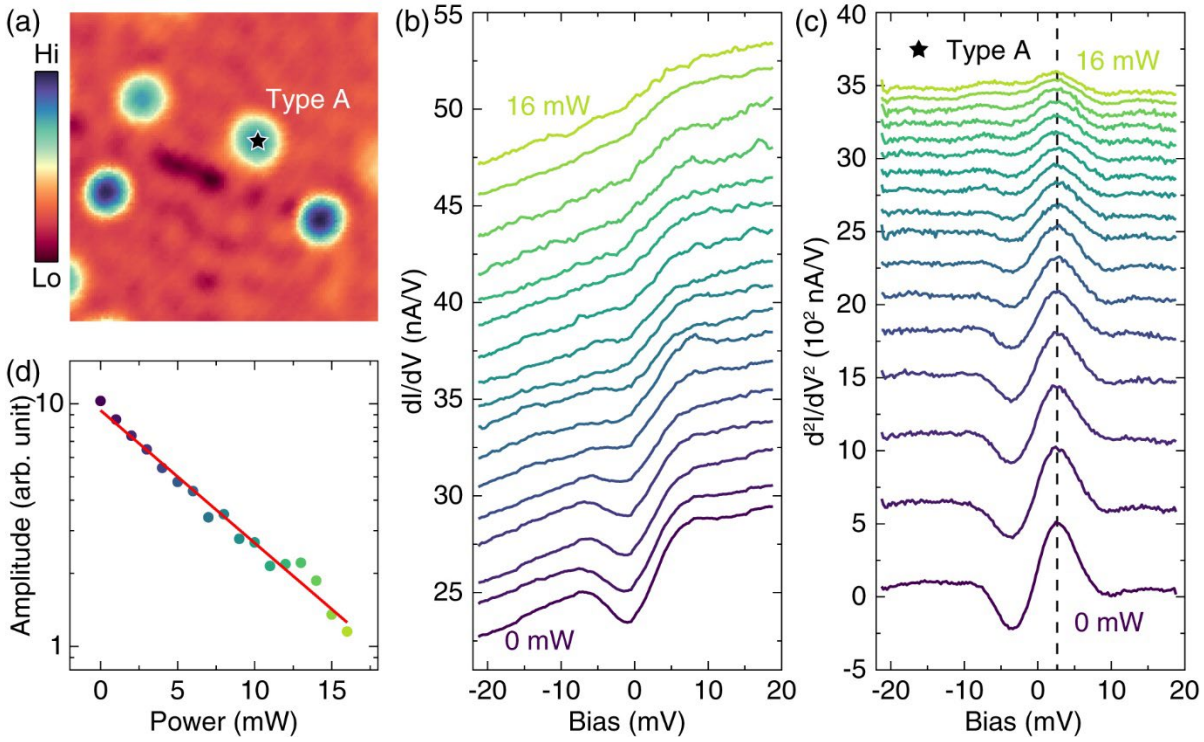
(a)
Hi
Lo
Type A
(b)
16 mW
0 mW
dI/dV (nA/V)
Bias (mV)
(c)
Type A
16 mW
0 mW
d²I/dV² (10² nA/V)
Bias (mV)
(d)
Amplitude (arb. unit)
Power (mW)

Figure 5.4 Laser power dependence of the 'Type B' Co atom. (a) Constant current STM topography same as Figure 5.2(b). (b) A series of laser power dependent dI/dV spectra taken with the tip positioned over the 'Type B' Co atom marked in (a). The laser power is adjusted from 0 mW (bottom) to 12 mW (top). All the measurements were performed with the same setpoint of 35 mV/0.7 nA. (c) d^2I/dV^2 spectra acquired simultaneously with the dI/dV spectra in (b). The dashed line indicates a fixed peak position upon increasing the laser power. (d) The laser power dependence of the Kondo amplitude. The Kondo amplitude is extracted from the peak intensity of the d^2I/dV^2 spectra in (c). The red line is a linear fitting to the data.

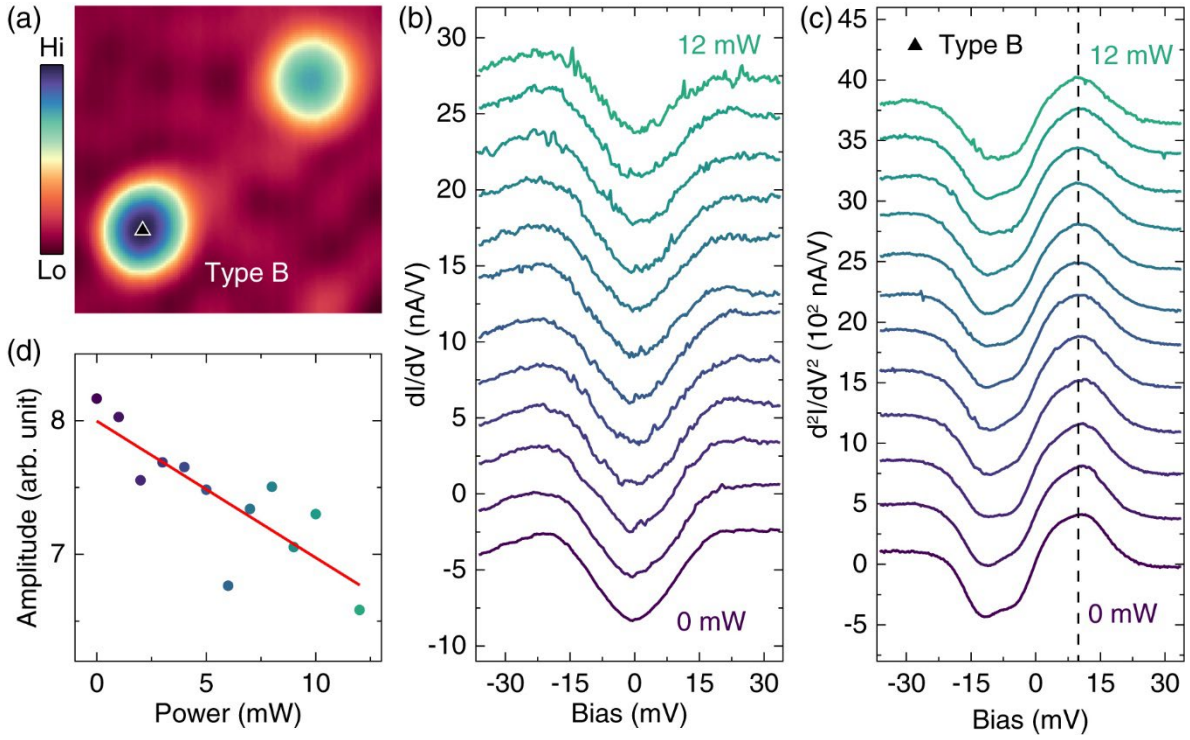
(a)
Hi
Lo
Type B
(b)
12 mW
0 mW
dI/dV (nA/V)
Bias (mV)
(c)
Type B
12 mW
0 mW
d²I/dV² (10² nA/V)
Bias (mV)
(d)
Amplitude (arb. unit)
Power (mW)

Figure 5.5 Kondo imaging of the 'Type A' Co atom in Figure 5.2(a) without (a) and with (b) pulsed laser illumination. The image is a subtraction of the d^2I/dV^2 imaging at -5 mV (dip) from the concurrent d^2I/dV^2 imaging at 2.2 mV (peak). The tip is placed over the 'Type B' Co atom in Figure 5.2(a) with a setpoint of 35 mV/0.7 nA, then feedback is turned off and bias is ramped to -5 mV and 2.2 mV to take the corresponding d^2I/dV^2 images. Feedback is turned off throughout the measurement. Laser power is 15 mW for measurements in (b). Image size 11.2 Å × 11.2 Å.

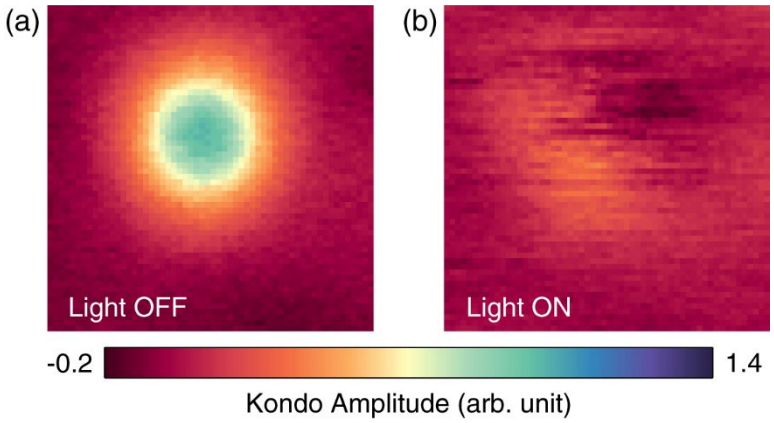
(a)
Light OFF
(b)
Light ON
-0.2
1.4
Kondo Amplitude (arb. unit)

Bibliography

[1] J. Kondo, *Resistance Minimum in Dilute Magnetic Alloys*, Progress of Theoretical Physics **32**, 37 (1964).

[2] L. Kouwenhoven and L. Glazman, *Revival of the Kondo Effect*, Phys. World **14**, 33 (2001).

[3] G. Gruner and A. Zawadowski, *Magnetic Impurities in Non-Magnetic Metals*, Rep. Prog. Phys. **37**, 1497 (1974).

[4] D. Goldhaber-Gordon, H. Shtrikman, D. Mahalu, D. Abusch-Magder, U. Meirav, and M. A. Kastner, *Kondo Effect in a Single-Electron Transistor*, Nature **391**, 6663 (1998).

[5] S. M. Cronenwett, T. H. Oosterkamp, and L. P. Kouwenhoven, *A Tunable Kondo Effect in Quantum Dots*, Science **281**, 540 (1998).

[6] W. G. van der Wiel, S. D. Franceschi, T. Fujisawa, J. M. Elzerman, S. Tarucha, and L. P. Kouwenhoven, *The Kondo Effect in the Unitary Limit*, Science **289**, 2105 (2000).

[7] P. Jarillo-Herrero, J. Kong, H. S. J. van der Zant, C. Dekker, L. P. Kouwenhoven, and S. De Franceschi, *Orbital Kondo Effect in Carbon Nanotubes*, Nature **434**, 7032 (2005).

[8] Y. S. Kwon, T. Suzuki, and T. Kasuya, *Influence of the Kondo Effect in Optical Excitation Spectra and the Band Structure in Rare-Earth Monopnictides*, Journal of Magnetism and Magnetic Materials **116**, 73 (1992).

[9] C. Latta et al., *Quantum Quench of Kondo Correlations in Optical Absorption*, Nature **474**, 7353 (2011).

[10] H. E. Türeci, M. Hanl, M. Claassen, A. Weichselbaum, T. Hecht, B. Braunecker, A. Govorov, L. Glazman, A. Imamoglu, and J. von Delft, *Many-Body Dynamics of Exciton Creation in a Quantum Dot by Optical Absorption: A Quantum Quench towards Kondo Correlations*, Phys. Rev. Lett. **106**, 107402 (2011).

[11] C. Wetli, S. Pal, J. Kroha, K. Kliemt, C. Krellner, O. Stockert, H. v. Löhneysen, and M. Fiebig, *Time-Resolved Collapse and Revival of the Kondo State near a Quantum Phase Transition*, Nat. Phys. **14**, 11 (2018).

[12] M. Ternes, A. J. Heinrich, and W.-D. Schneider, *Spectroscopic Manifestations of the Kondo Effect on Single Adatoms*, J. Phys.: Condens. Matter **21**, 053001 (2008).

[13] V. Madhavan, W. Chen, T. Jamneala, M. F. Crommie, and N. S. Wingreen, *Tunneling into a Single Magnetic Atom: Spectroscopic Evidence of the Kondo Resonance*, Science **280**, 567 (1998).

[14] J. Li, W.-D. Schneider, R. Berndt, and B. Delley, *Kondo Scattering Observed at a Single Magnetic Impurity*, Phys. Rev. Lett. **80**, 2893 (1998).

[15] N. Knorr, M. A. Schneider, L. Diekhöner, P. Wahl, and K. Kern, *Kondo Effect of Single Co Adatoms on Cu Surfaces*, Phys. Rev. Lett. **88**, 096804 (2002).

[16] N. Néel, J. Kröger, L. Limot, K. Palotas, W. A. Hofer, and R. Berndt, *Conductance and Kondo Effect in a Controlled Single-Atom Contact*, Phys. Rev. Lett. **98**, 016801 (2007).

[17] A. F. Otte, M. Ternes, K. von Bergmann, S. Loth, H. Brune, C. P. Lutz, C. F. Hirjibehedin, and A. J. Heinrich, *The Role of Magnetic Anisotropy in the Kondo Effect*, Nat. Phys. **4**, 11 (2008).

[18] J. Bork, Y. Zhang, L. Diekhöner, L. Borda, P. Simon, J. Kroha, P. Wahl, and K. Kern, *A Tunable Two-Impurity Kondo System in an Atomic Point Contact*, Nat. Phys. **7**, 11 (2011).

[19] A. Zhao et al., *Controlling the Kondo Effect of an Adsorbed Magnetic Ion Through Its Chemical Bonding*, Science **309**, 1542 (2005).

[20] V. Iancu, A. Deshpande, and S.-W. Hla, *Manipulation of the Kondo Effect via Two-Dimensional Molecular Assembly*, Phys. Rev. Lett. **97**, 266603 (2006).

[21] Y. Zhang, S. Kahle, T. Herden, C. Stroh, M. Mayor, U. Schlickum, M. Ternes, P. Wahl, and K. Kern, *Temperature and Magnetic Field Dependence of a Kondo System in the Weak Coupling Regime*, Nat. Commun. **4**, 1 (2013).

[22] L. Liu et al., *Revealing the Atomic Site-Dependent g Factor within a Single Magnetic Molecule via the Extended Kondo Effect*, Phys. Rev. Lett. **114**, 126601 (2015).

[23] R. Hiraoka, E. Minamitani, R. Arafune, N. Tsukahara, S. Watanabe, M. Kawai, and N. Takagi, *Single-Molecule Quantum Dot as a Kondo Simulator*, Nat. Commun. **8**, 1 (2017).

[24] U. Ham and W. Ho, *Imaging Single Electron Spin in a Molecule Trapped within a Nanocavity of Tunable Dimension*, J. Chem. Phys. **138**, 074703 (2013).

[25] Y. Jiang, Y. N. Zhang, J. X. Cao, R. Q. Wu, and W. Ho, *Real-Space Imaging of Kondo Screening in a Two-Dimensional O_2 Lattice*, Science **333**, 324 (2011).

[26] P. Wahl, L. Diekhöner, M. A. Schneider, L. Vitali, G. Wittich, and K. Kern, *Kondo Temperature of Magnetic Impurities at Surfaces*, Phys. Rev. Lett. **93**, 176603 (2004).

[27] U. Fano, *Effects of Configuration Interaction on Intensities and Phase Shifts*, Phys. Rev. **124**, 1866 (1961).

[28] M. Plihal and J. W. Gadzuk, *Nonequilibrium Theory of Scanning Tunneling Spectroscopy via Adsorbate Resonances: Nonmagnetic and Kondo Impurities*, Phys. Rev. B **63**, 085404 (2001).

[29] S. Li, S. Chen, J. Li, R. Wu, and W. Ho, *Joint Space-Time Coherent Vibration Driven Conformational Transitions in a Single Molecule*, Phys. Rev. Lett. **119**, 176002 (2017).

CHAPTER 6

Conclusions and Prospects

6.1 Concluding Remarks

The combination of low temperature STM with fs lasers allows us to measure and manipulate quantum coherence in single molecules and atoms with both atomic-scale spatial and femtosecond temporal resolutions. Not only can we get deeper understanding of the fundamental two-level system, but also it has promising implications on the potential applications in quantum information science.

Treating THz electric field as a low bias modulation, we successfully demonstrated pulsed THz rectification spectroscopy (TRS) over various types of single molecules and atoms. Comparing to traditional inelastic electron tunneling spectroscopy (IETS), the pulsed TRS exhibited similar fingerprints of single molecules and atoms, such as the vibrational, rotational, or spin excitations. On the other hand, TRS also showed great advantage on the polarization control of the irradiating THz pulses, which reveals the contribution of both the electric field and magnetic field components of THz in TRS. In addition to the field effect, THz photon absorption can occur in the H_2 TLS. The time resolved TRS on single H_2 molecule allows monitoring the ultrafast coherence of the H_2 TLS, which can be demonstrated by the time evolution of its spectroscopic features.

Time domain THz pump-probe spectroscopy was performed on single H_2 molecules in the STM junction to continuously measure the ultrafast quantum coherence of the H_2 TLS. The coherent oscillations in the time domain and peaks in the frequency domain demonstrated extreme sensitivity of the H_2 TLS to the applied electric field and the underlying surface chemical

environment. Time resolved THz rectification image of H_2 over Cu_2N islands for variable pump-probe delay times allows us to visualize the sub-Ångström scale heterogeneity of the chemical environment. The application of the H_2 TLS in quantum sensing heralds a new type of quantum sensor with simultaneous atomic-scale spatial and femtosecond temporal resolutions with GHz energy discrimination.

We further employed the DC electric field from the sample bias across the junction to manipulate the ultrafast coherence of the H_2 TLS. A giant Stark effect was found in the H_2 TLS as the H_2 molecule behaves as an electric dipole when adsorbed on the polar Cu_2N surface. By fitting the sample bias dependent frequency spectrum to a simple but effective model Hamiltonian, we were able to reveal an avoided crossing of the quantum state energy levels of the H_2 TLS. The dephasing time of the initial wave packet can be greatly extended by the applied electric field. Furthermore, the electrical manipulation for different tunneling gaps in three-dimensions allows quantification of the surface electrostatic fields at the atomic scale.

Lastly, we also discovered the optical tuning of the Kondo state on a single Co atom by introducing fs near-infrared (NIR) laser illumination into the STM junction. The Kondo state can be completely quenched by NIR laser illumination without an obvious sample temperature increase. Adjusting the laser power with a neutral density filter allows continuous tuning of the Kondo amplitude of the same Co atom. Kondo imaging was further acquired to contrast the difference of the spatial distribution of the Kondo state with and without laser illumination.

6.2 Future Prospects

fs laser combined STM provides an ideal platform to investigate the quantum coherence of single molecules and atoms [1–4]. On the laser side, the amplitude, frequency, phase, and polarization of the laser pulse can be controlled with existing techniques [5–8]. By increasing the number of laser beams, it is even possible to perform photon echo [9,10] or two-dimensional spectroscopy [11,12] in the STM junction. On the STM side, the tunneling current and the movement of the piezo in three dimensions allow us to measure and manipulate the quantum states of single molecules and atoms. The combination of fs lasers with low temperature STM is just at its very early stage which requires decades to enrich this research field [13].

There are several other potential molecules that are suitable for the fs THz-STM, such as the magnetic $NiCp_2$ molecule [14]. It is very promising to detect the coherence in the spin excitation of $NiCp_2$ by a careful design of a spin polarized tip and the polarization angle of the laser. Other two-level systems such as the intramolecular tautomerization of porphycene [15] is of great importance to single molecule chemistry, which is also waiting for the first experimental demonstration of its ultrafast coherence. Apart from single molecules, the intermolecular interactions are also very exciting, which has been implicated in our results.

The time domain pump-probe spectroscopy can also be combined with frequency domain absorption spectroscopy to show the simultaneous time and energy resolutions. Our energy resolution in the study of the H_2 TLS was essentially limited by the repetition rate the Ti:Sapphire laser (1 GHz). By choosing a laser with lower repetition rate, the frequency spacing can be deceased efficiently. The application of a continuous wave laser with high tuning resolution on the same system would allow unprecedented energy resolution not limited by the temperature and bias modulation.

Another prospect of laser combined STM is the direct excitation of molecular vibrations or rotations resonantly from a laser. Most vibrations and rotations sit in the range of 1 THz to 100 THz, it is thus important to extend the operation frequency of the laser. A mid-infrared laser in pulsed or continuous wave mode can be combined with the STM to excite molecular vibrations and rotations directly [16,17].

Our experimental technique can also be applied in various other systems such as the 2D materials. Laser pulses can generate electron-hole pairs (excitons) either in one layer or between two layers [18,19]. By measuring the tunneling current, it becomes possible to monitor the ultrafast dynamics of excitons with atomic-scale spatial resolution, which has not been demonstrated so far.

Bibliography

[1] T. L. Cocker, D. Peller, P. Yu, J. Repp, and R. Huber, *Tracking the Ultrafast Motion of a Single Molecule by Femtosecond Orbital Imaging*, Nature **539**, 7628 (2016).

[2] S. Li, S. Chen, J. Li, R. Wu, and W. Ho, *Joint Space-Time Coherent Vibration Driven Conformational Transitions in a Single Molecule*, Phys. Rev. Lett. **119**, 176002 (2017).

[3] D. Peller, L. Z. Kastner, T. Buchner, C. Roelcke, F. Albrecht, N. Moll, R. Huber, and J. Repp, *Sub-Cycle Atomic-Scale Forces Coherently Control a Single-Molecule Switch*, Nature **585**, 7823 (2020).

[4] L. Wang, Y. Xia, and W. Ho, *Atomic-Scale Quantum Sensing Based on the Ultrafast Coherence of an H_2 Molecule in an STM Cavity*, Science **376**, 401 (2022).

[5] K. Yoshioka, I. Katayama, Y. Arashida, A. Ban, Y. Kawada, K. Konishi, H. Takahashi, and J. Takeda, *Tailoring Single-Cycle Near Field in a Tunnel Junction with Carrier-Envelope Phase-Controlled Terahertz Electric Fields*, Nano Lett. **18**, 5198 (2018).

[6] M. Müller, N. Martín Sabanés, T. Kampfrath, and M. Wolf, *Phase-Resolved Detection of Ultrabroadband THz Pulses inside a Scanning Tunneling Microscope Junction*, ACS Photonics **7**, 2046 (2020).

[7] K. Kimura, Y. Morinaga, H. Imada, I. Katayama, K. Asakawa, K. Yoshioka, Y. Kim, and J. Takeda, *Terahertz-Field-Driven Scanning Tunneling Luminescence Spectroscopy*, ACS Photonics **8**, 982 (2021).

[8] M. Abdo, S. Sheng, S. Rolf-Pissarczyk, L. Arnhold, J. A. J. Burgess, M. Isobe, L. Malavolti, and S. Loth, *Variable Repetition Rate THz Source for Ultrafast Scanning Tunneling Microscopy*, ACS Photonics **8**, 702 (2021).

[9] W. P. de Boeij, M. S. Pshenichnikov, and D. A. Wiersma, *ULTRAFAST SOLVATION DYNAMICS EXPLORED BY FEMTOSECOND PHOTON ECHO SPECTROSCOPIES*, Annu. Rev. Phys. Chem. **49**, 99 (1998).

[10] D. Press, K. De Greve, P. L. McMahon, T. D. Ladd, B. Friess, C. Schneider, M. Kamp, S. Höfling, A. Forchel, and Y. Yamamoto, *Ultrafast Optical Spin Echo in a Single Quantum Dot*, Nat. Photon. **4**, 6 (2010).

[11] D. M. Jonas, *Two-Dimensional Femtosecond Spectroscopy*, Annual Review of Physical Chemistry **54**, 425 (2003).

[12] F. Perakis, L. De Marco, A. Shalit, F. Tang, Z. R. Kann, T. D. Kühne, R. Torre, M. Bonn, and Y. Nagata, *Vibrational Spectroscopy and Dynamics of Water*, Chem. Rev. **116**, 7590 (2016).

[13] J. Lloyd-Hughes et al., *The 2021 Ultrafast Spectroscopic Probes of Condensed Matter Roadmap*, J. Phys.: Condens. Matter **33**, 353001 (2021).

[14] G. Czap, P. J. Wagner, F. Xue, L. Gu, J. Li, J. Yao, R. Wu, and W. Ho, *Probing and Imaging Spin Interactions with a Magnetic Single-Molecule Sensor*, Science **364**, 670 (2019).

[15] T. Kumagai, J. N. Ladenthin, Y. Litman, M. Rossi, L. Grill, S. Gawinkowski, J. Waluk, and M. Persson, *Quantum Tunneling in Real Space: Tautomerization of Single Porphycene Molecules on the (111) Surface of Cu, Ag, and Au*, J. Chem. Phys. **148**, 102330 (2018).

[16] S. Woutersen, U. Emmerichs, and H. J. Bakker, *Femtosecond Mid-IR Pump-Probe Spectroscopy of Liquid Water: Evidence for a Two-Component Structure*, Science **278**, 658 (1997).

[17] S. Duval, M. Bernier, V. Fortin, J. Genest, M. Piché, and R. Vallée, *Femtosecond Fiber Lasers Reach the Mid-Infrared*, Optica, OPTICA **2**, 623 (2015).

[18] M. Plankl et al., *Subcycle Contact-Free Nanoscopy of Ultrafast Interlayer Transport in Atomically Thin Heterostructures*, Nat. Photon. **15**, 8 (2021).

[19] T. Siday et al., *Ultrafast Nanoscopy of High-Density Exciton Phases in WSe2*, Nano Lett. **22**, 2561 (2022).

APPENDIX A

Triple Cell Doser

Knudsen cell dosers are often used in the STM community to thermally evaporate different types of molecules and atoms onto surfaces for further STM study [1]. In the past, Ho group used to design and fabricate single cell dosers which were usually fitted to the 2.75" CF flange. Due to limited number of vacuum ports to mount molecular dosers in the STM chamber, it is always desirable to make a multi-cell doser which can evaporate different molecules separately or concurrently. With more than one type of molecules in the Knudsen cell doser, the operation of the STM system under the UHV environment will be elongated without venting and baking. It is also beneficial to dose two or three molecules at the same time to study specific molecular systems, such as the DNA base pairs [2].

The triple cell doser designed by the author is shown in Figure A.1. The doser has water cooling for all three crucibles to maintain a low temperature for the other two crucibles while the third is working. In this way, pure molecules from the third crucible will be evaporated onto the substrate with contaminations from the other two crucibles. Controlled by the manual rotary feedthrough, the shutter can be operated under one molecule dosing mode or concurrent two molecules dosing mode. Three pairs of K type thermocouples were also designed to measure the temperature of each crucible.

A heat reservoir made of oxygen free high thermal conductivity (OFHC) copper shown in Figure A.2 was designed to dissipate the heat during outgassing the doser and dosing molecules. The copper reservoir was machined from a whole piece of copper with some efforts, which was feasible after some practices in the machine shop.

Figure A.1 3D drawing of the triple cell doser.

Figure A.2 Copper reservoir.

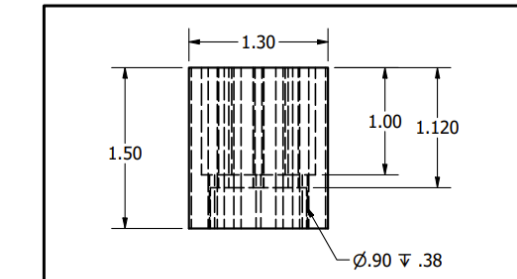

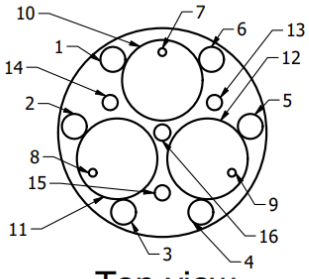

Top view

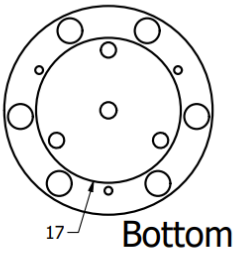

Bottom view

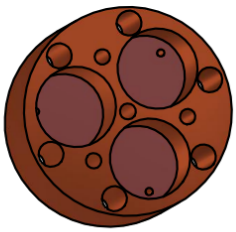

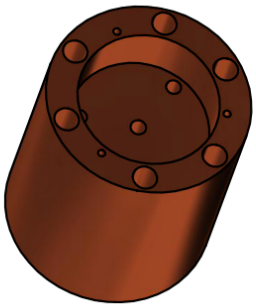

PARTS LIST				
Label	X	Y	DEPTH	DIAMETER
1	-0.308	-0.456	THRU	0.188"
2	-0.549	-0.038	THRU	0.188"
3	-0.241	0.494	THRU	0.188"
4	0.241	0.494	THRU	0.188"
5	0.549	-0.038	THRU	0.188"
6	0.308	-0.456	THRU	0.188"
7	0	-0.500	THRU	0.047"
8	-0.433	0.250	THRU	0.047"
9	0.433	0.250	THRU	0.047"
10	0	-0.338	1"	0.5"
11	-0.281	0.163	1"	0.5"
12	0.281	0.163	1"	0.5"
13	0.188	-0.188	THRU	0.1"
14	-0.188	-0.188	THRU	0.1"
15	0	0.375	THRU	0.1"
16	0	0	THRU	0.1"
17	0	0	0.38"	0.9"

DRAWN	STM2-data collector	10/29/2019	
CHECKED			
QA			TITLE
MFG			
APPROVED			
		SIZE A4	DWG NO Copper Resevior-02 REV
		SCALE 1 : 1	SHEET 1 OF 2

As shown in Figure A.3, the crucible shared the same design and dimensions as the old ones in the Ho group with external threading for Tungsten filament to increase the heating efficiency [3]. The current filament has a diameter of 0.02” but can be changed to 0.03” with no difficulties. The crucible with a diameter of 0.313” and length of 1.1” is wound with 13 turns of the filament. A photo of the machined crucibles with wound filaments are shown in Figure A.4. It is thus easy to interchange the crucibles with old dosers. A ceramic tube sits in between the crucible and the copper reservoir to behave as both electrical and thermal insulators. The heating efficiency can be increased by the thermal insulating provided by this ceramic tube. Another six thin ceramic tubes were used to insulate the six Tantalum electrodes from the copper reservoir, respectively.

The tantalum shutter 1 with formed thin film during outgassing the molecule is shown in Figure A.5. Since the three crucibles are angularly distributed by 120° in the plane, a specific shutter 2 shown in Figure A.6 was also designed for this triple cell doser to allow dosing only one type of molecule or two types of molecules at the same time. When the two holes for co-dosing are aligned with two crucibles, the third crucible will be blocked since the third hole is not aligned with it. In this way, any pair of the three crucibles can be used for dosing two molecules at the same time. When the single dosing hole is aligned with one crucible, the other two crucibles will be blocked. In this way, only one molecule is dosed onto the surface.

Only four copper electrodes were used to provide electric power to the three filaments, as shown in Figure A.7 and Figure A.8. Note that the three filaments share one same electrode but can be heated separately by applying power to only one filament. Figure A.7 illustrates the three configures where the tungsten filament #1, #2, or #3 is heated, respectively. The blue dots in the figure represent the four electrodes on the electrical feedthrough. One of them was labelled as ‘ground’ (should be corrected to ‘common’) by a paper tag and all other three electrodes were

labelled as 1, 2, and 3 respectively together with dosing conditions. The photo in Figure A.8 shows how the ‘common’ electrode is split into three to connect with the three filaments.

Due to the limited access to purchasing parts from outside during the pandemic, some compromises on the design had to be made to minimize the machine and assembly time. Instead of a thick rotatable blank flange, two separate flanges were bolted together to support the copper reservoir and water-cooling system. A double sided 2.75” CF flange with a big through hole was designed to mount the three 1.33” mini flanges on the side for rotary feedthrough, electrodes, and thermal couples. The bottom flange was designed to support the water-cooling system for the triple cell doser, as shown in Figure A.8 and Figure A.9. The water tank is in close contact with the copper reservoir to ensure efficient cooling power. The water tank must be welded with vacuum seal.

Figure A.3 3D drawing of the copper reservoir with crucibles and electrodes.

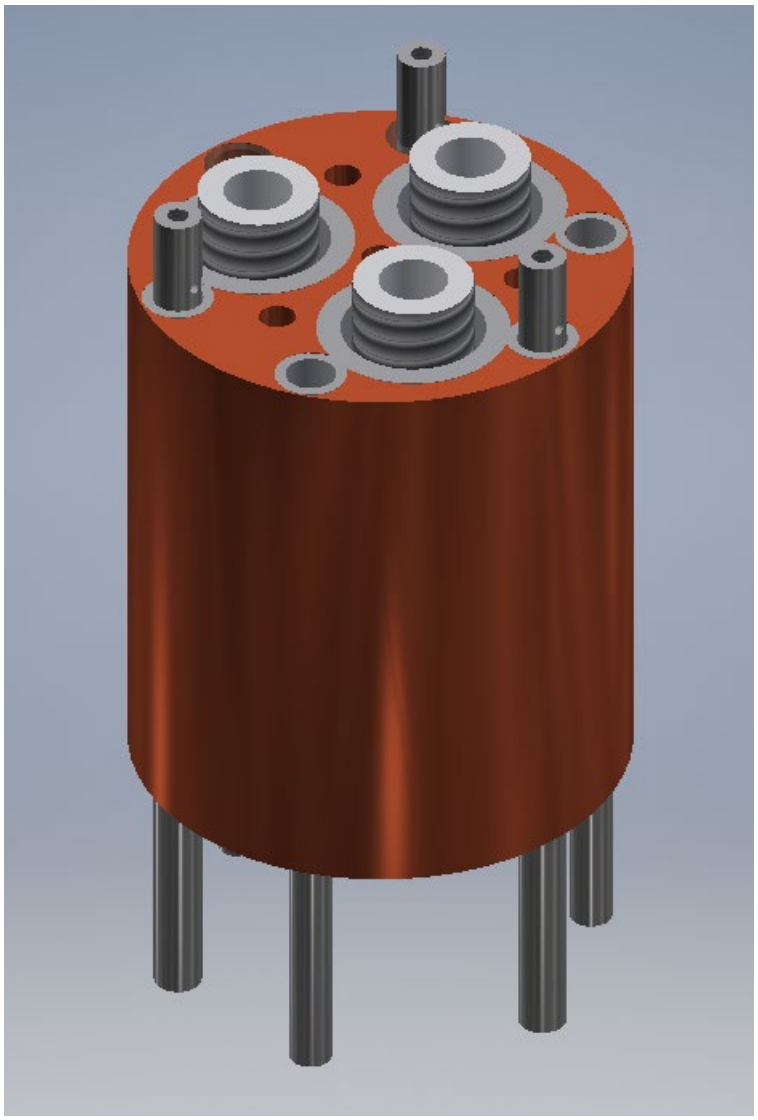

Figure A.4 Photo of the crucibles with filaments.

Figure A.5 Photo of the shutter 1. Below is a table listing dosing details of three different molecules with this shutter.

Molecule	Label	Angle (°)	Chiller temperature (°C)	Dosing current (A)
C_{60}	#1	270	15	3.80
Porphycene	#2	30	10	2.40
C_{70}	#3	150	15	3.90

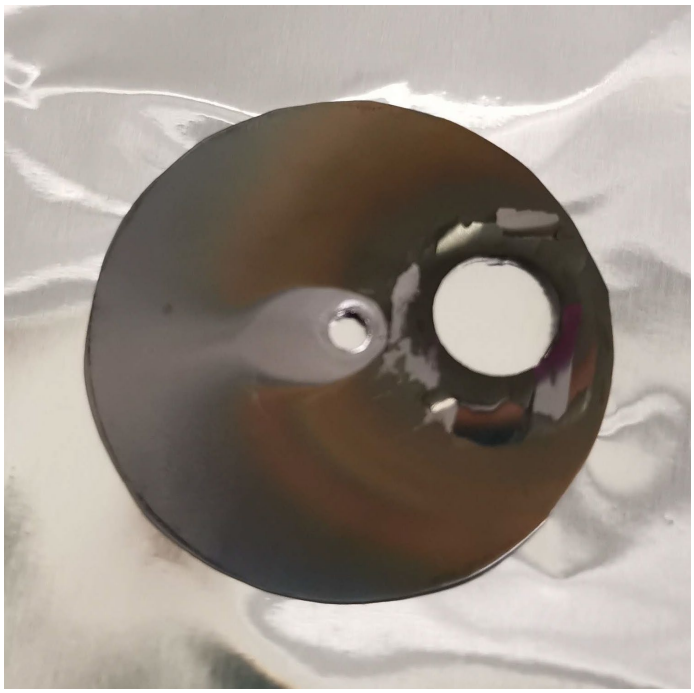

Figure A.6 3D drawing of the shutter 2.

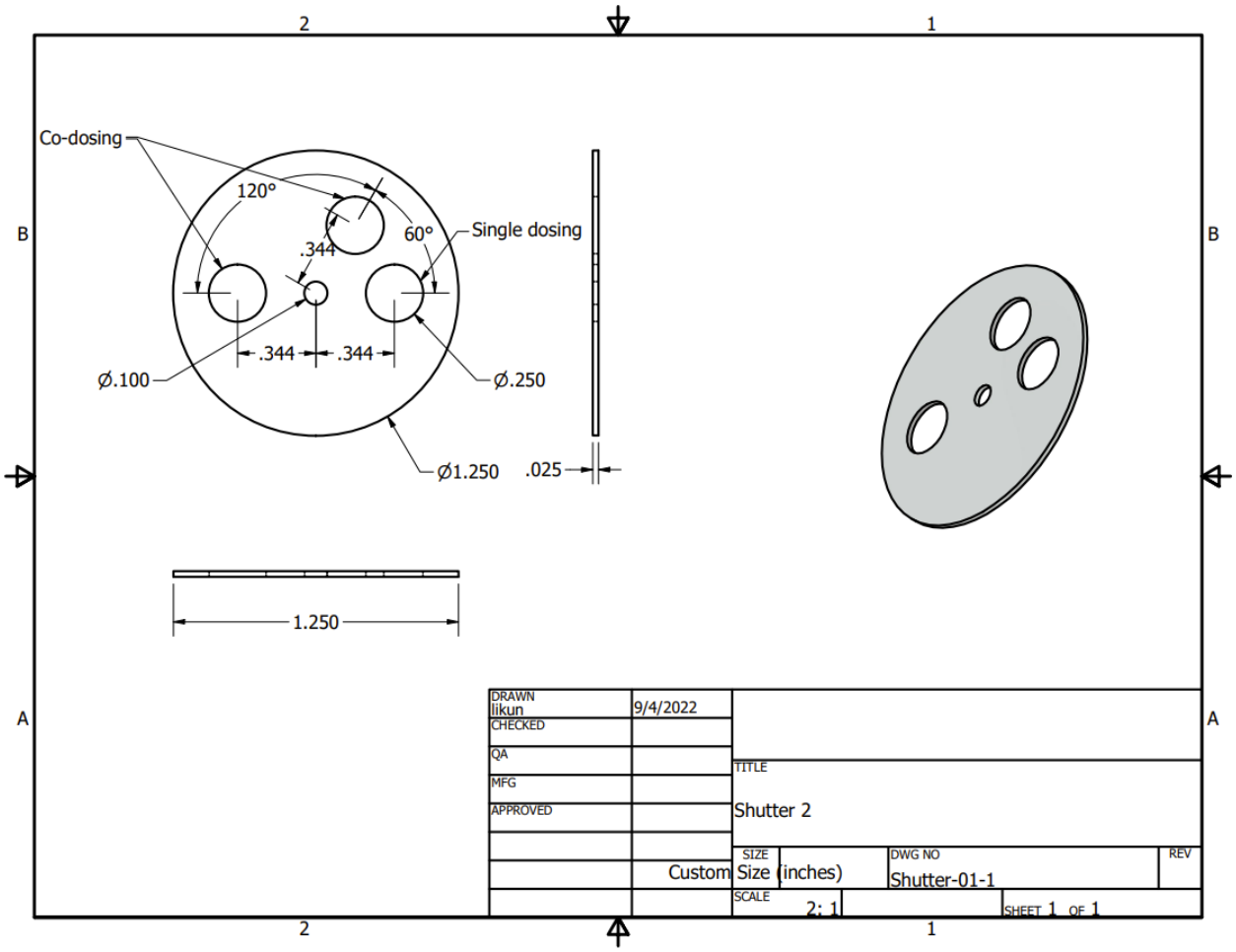
Co-dosing
120°
60°
Single dosing
.344
.344
.344
Ø.100
Ø.250
Ø1.250
.025
1.250
DRAWN
likun
9/4/2022
CHECKED
QA
MFG
APPROVED
Custom
TITLE
Shutter 2
SIZE
Size (inches)
DWG NO
Shutter-01-1
REV
SCALE
2: 1
SHEET 1 OF 1

Figure A.7 Schematic diagram of the electric connections.

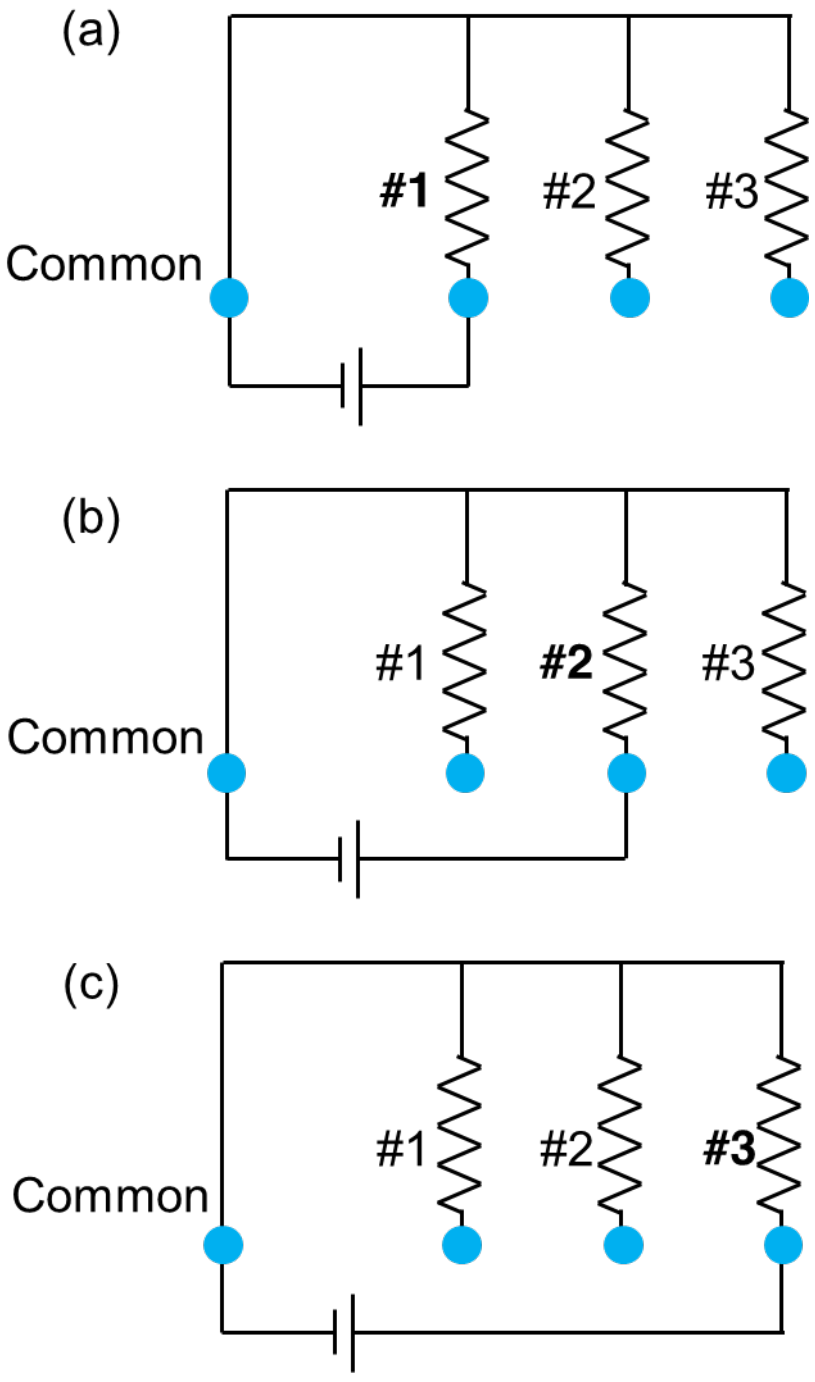
(a)
Common
#1
#2
#3
(b)
Common
#1
#2
#3
(c)
Common
#1
#2
#3

Figure A.8 Picture of the electric connections.

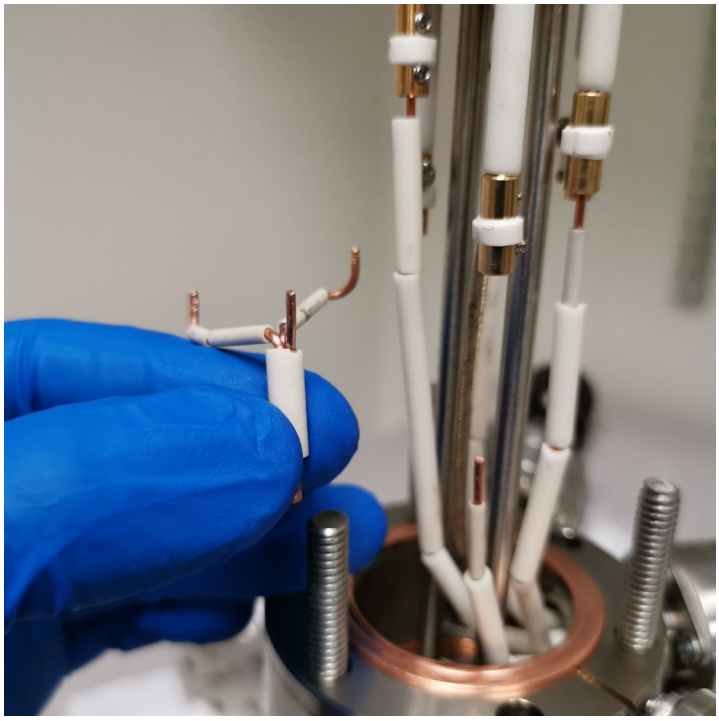

Figure A.9 3D drawing and annotations of the water-cooling system.

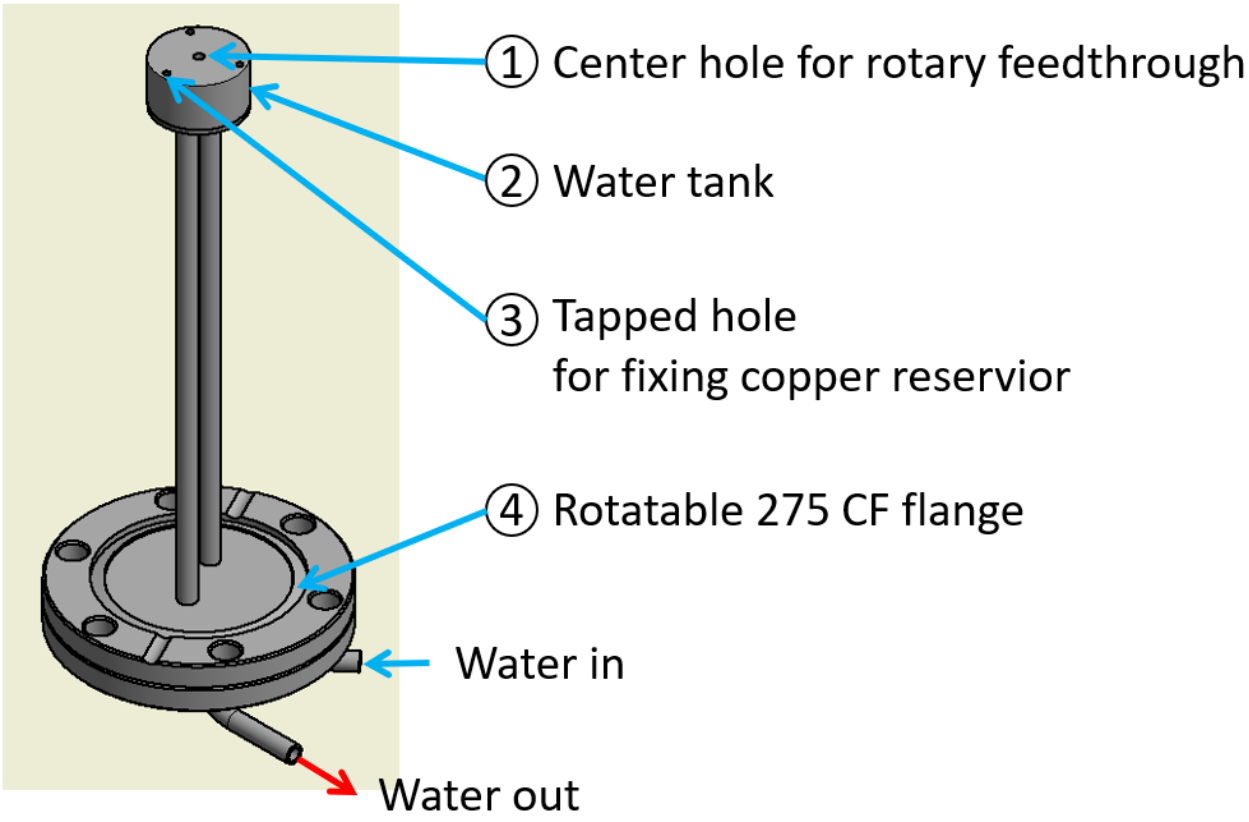
① Center hole for rotary feedthrough
② Water tank
③ Tapped hole
for fixing copper reservior
④ Rotatable 275 CF flange
Water in
Water out

Figure A.10 2D drawing of the water-cooling system.

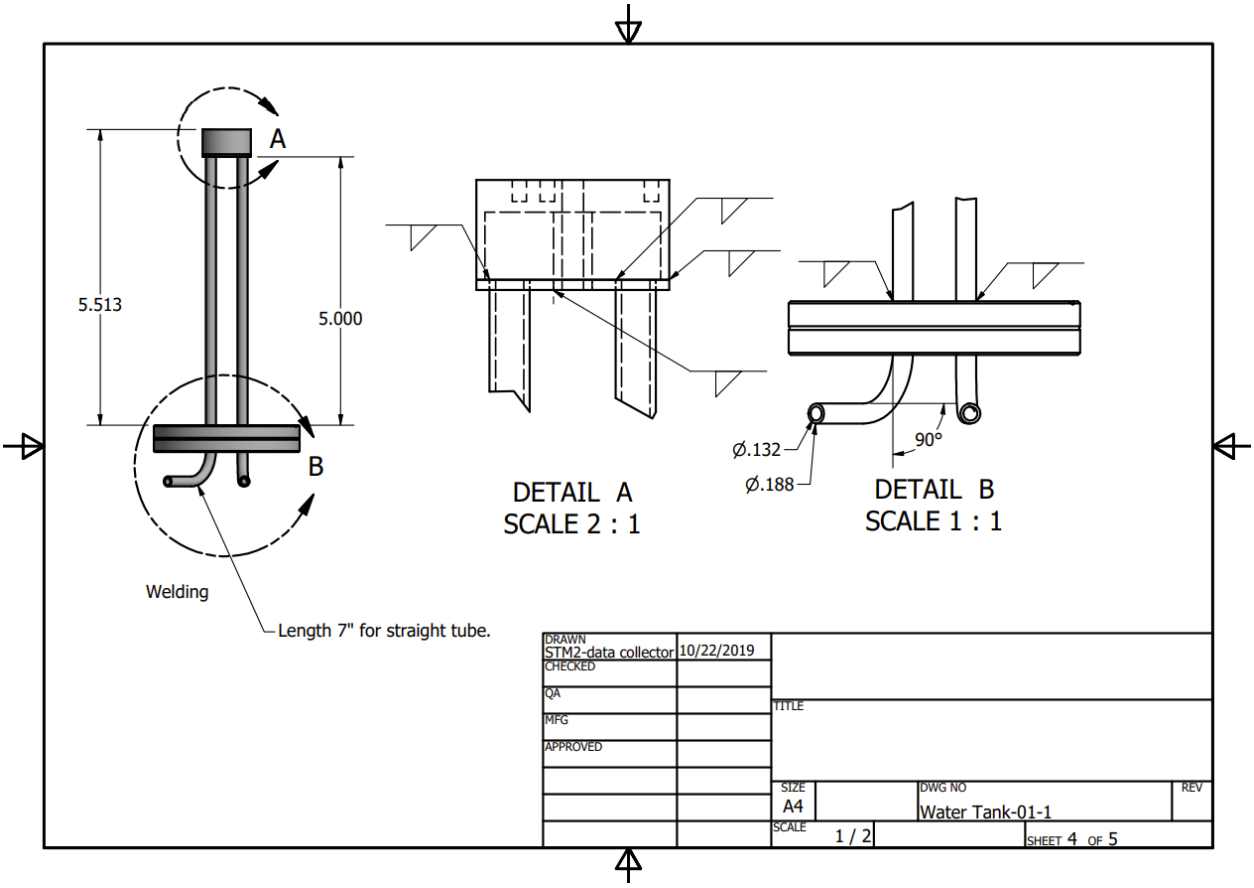
A
B
5.513
5.000
Welding
Length 7" for straight tube.
DETAIL A
SCALE 2 : 1
Ø.132
Ø.188
90°
DETAIL B
SCALE 1 : 1
DRAWN
STM2-data collector
10/22/2019
CHECKED
QA
MFG
APPROVED
TITLE
SIZE
A4
DWG NO
Water Tank-01-1
REV
SCALE
1 / 2
SHEET 4 OF 5

A picture of the assembled triple cell doser is shown in Figure A.11. The blank mini flange on the side can be replaced with a feedthrough with three pairs of thermocouples to measure the temperature separately at the bottom of each crucible. But following the tradition of only measuring the electrical current during dosing, it is workable for the triple cell doser to function very well.

This assembled triple cell doser was later used to test the dosing conditions of three different organic molecules, namely C_{70}, C_{60}, and porphycene, as shown in Figure A.12. The three glass slides on the top panel showed the resulting thin film when the dosing conditions were found on the leak station. The dosing conditions for C_{70} and C_{60} were found to be very accurate with the successful dosing onto the NiAl(110) surface in the STM 2 chamber. The porphycene was not used to dose in the chamber so far, but the dosing condition was very similar to the single cell doser assembled previously.

In the future, several improvements can be made for the next version of the triple cell doser. Firstly, a heat transfer analysis should be performed with Comsol simulation to ensure a more efficient heat dissipation. Secondly, it is beneficial to make a power supply box with feedback control while monitoring the temperatures of all three crucibles. The dosing condition can then be narrow down to a very precise value without looking for it during dosing in the STM chamber. Thirdly, the bottom flange welding assembly should be replaced with a single flange for a more convenient assembly. The copper gasket between the two bottom flanges in the current design has to be replaced with a new one when a disassembly is needed for the triple cell doser.

Figure A.11 Picture of the assembled triple cell doser.

Figure A.12 Dosing conditions of three different molecules in the triple cell doser.

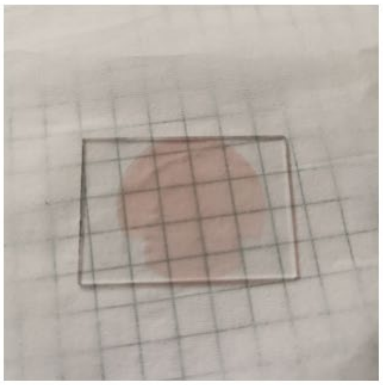

C70@3.90A

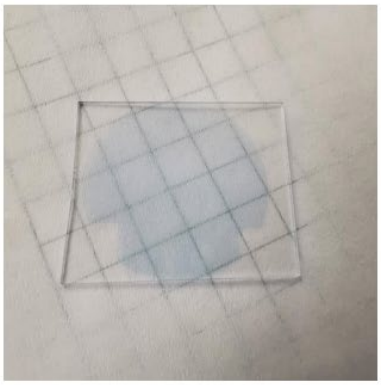

C60@3.80A

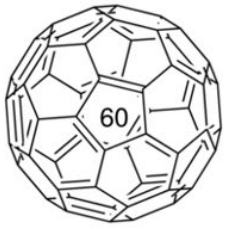

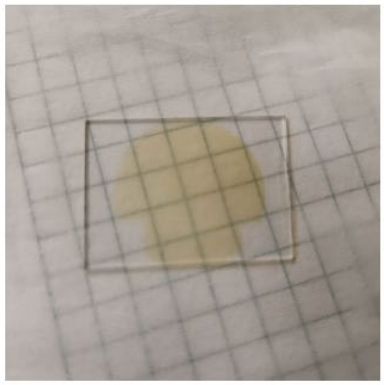

Porphycene@2.40A

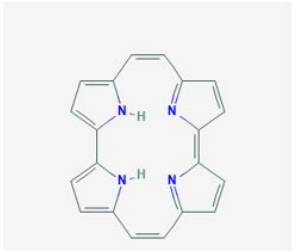

Bibliography

[1] A. K. Shukla, S. Banik, R. S. Dhaka, C. Biswas, S. R. Barman, and H. Haak, *Versatile UHV Compatible Knudsen Type Effusion Cell*, Review of Scientific Instruments **75**, 4467 (2004).

[2] R. Otero, W. Xu, M. Lukas, R. E. A. Kelly, E. Lægsgaard, I. Stensgaard, J. Kjems, L. N. Kantorovich, and F. Besenbacher, *Specificity of Watson–Crick Base Pairing on a Solid Surface Studied at the Atomic Scale*, Angewandte Chemie International Edition **47**, 9673 (2008).

[3] K. A. Brown and W. Ho, *A Threading Tool for Hard Materials*, Review of Scientific Instruments **66**, 5371 (1995).

APPENDIX B

THz Boxes

The electromagnetic waves in the THz range were known to show water absorption at some frequencies. It is thus necessary to put the THz system in a vacuum sealed box or a box purged with dry nitrogen gas. In this way, water absorption can be removed from the THz and the THz power introduced into the STM junction will also be increased.

There were two types of boxes designed and machined for the THz system. Both boxes have the capability of being pump down to 10^{-6} torr with leak check passed. The vacuum was sealed by O-rings with the KF flanges. But one drawback of pumping the box into vacuum was the alignment change induced by the deformation of the box with a large pressure difference with the outside. On the other hand, no difference was found on the emitted THz spectrum between the pumped and the dry N_2 purged box. It is thus good enough to operate the THz box with clean and dry N_2 gas. Both boxes can be purged down to 0% humidity measured by the humidity and temperature monitor placed in the box.

As shown in Figure B.1 and Figure B.2, the first THz box (24”×24”×12”) was a large box made of stainless-steel frames and aluminum side and bottom plates, and the top cover was machined from acrylic plate for transparency and strength. The stainless-steel frame in Figure B.3 was a welded structure from six machined plates. O-ring groves were also designed on the outside of the frame. The four side plates provided different sizes of ports to mount KF flanges such as the fused silica view port, the electric feedthrough and vacuum gauge, as shown in Figure B.4. The bottom aluminum plate (Figure B.5) had the same ¼-20 threaded holes as the optical table, which

can be aligned pretty well for the ease of laser alignment. The top cover (Figure B.6) is made of transparent acrylic to have a good view of the optics inside the large THz box. The detailed drawing of the O-ring grove is shown in Figure B.7. Due to the large size of the box, there was no standard O-ring that met our requirements. Instead, a Viton O-ring with 6.99 mm cross section and 670 mm inside diameter was custom made from Macro Rubber & Plastics. The part number was SVV1000-6.99X670. Figure B.8 shows a photo of the assembled THz box. All the ports had passed the leak check after further polishing with sandpapers.

The initial optical and THz paths are shown in Figure B.9. The box was large enough to have both THz generation and characterization by EO sampling inside it. Two PCAs from Batop were used instead of only one PCA to take use of the most NIR power. The generated THz was further shrunk by a telescope made of two gold off-axis parabolic mirrors. The THz beams can be combined with the NIR beam by a glass coated with ITO thin films which transmits NIR but reflects THz. This combined beam can either be directed to the STM junction or to the balanced photodiode for EO sampling.

As listed in the right panel of Figure B.9, the above setup allows various combinations of NIR and THz beams to perform different types of experiments. Both NIR and THz can be the pump or the probe beam, depending on the specific system under study. It is also possible to design 2D spectroscopy experiments provided that at least three delay stages can be used to control the delays between each two pulses.

The gas absorption experiments in Chapter 1 were also done in this large THz box. The experimental setup is shown in Figure B.10. A 2.75” CF flange tee was employed as the gas cell. With a THz path of 5” in this gas cell, the absorption was strong enough for us to see in the data.

Figure B.1 3D drawing of the first THz box.

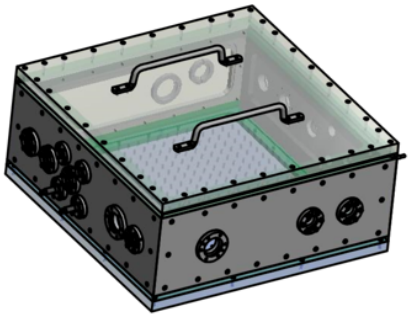

THz
vacuum box

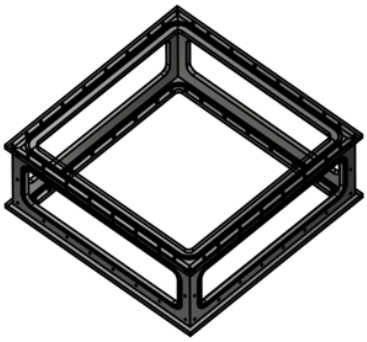

Stainless steel frame

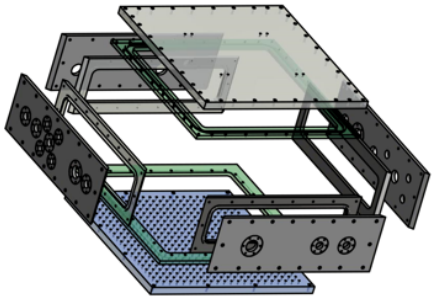

Aluminum side plates
with flange ports

Figure B.2 Dimensions of the first THz box.

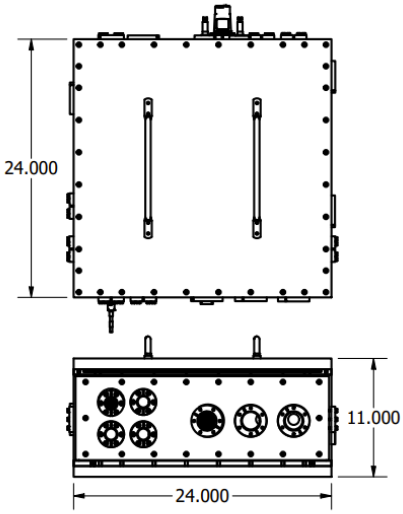

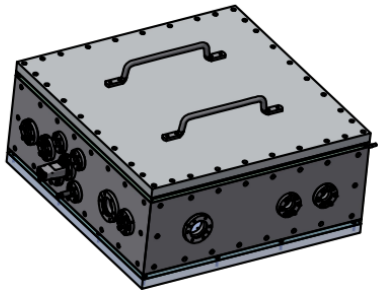

This project is to build a vacuum box with six detachable sides by O-ring seal.
There are five O-ring grooves on the outside of the welded stainless steel frame and another one on the bottom aluminum plate.

Materials:
6061 Aluminum
304 stainless steel
Acrylic

Unit: Inch

DRAWN Likun Wang	10/1/2018	UC Irvine
CHECKED		TITLE: Vacuum box
QA		
MFG		
APPROVED		
SIZE A4	DWG NO THz Box v3_012819	REV
SCALE 1 / 10		SHEET 1 OF 15

Figure B.3 Dimensions of the stainless-steel frame.

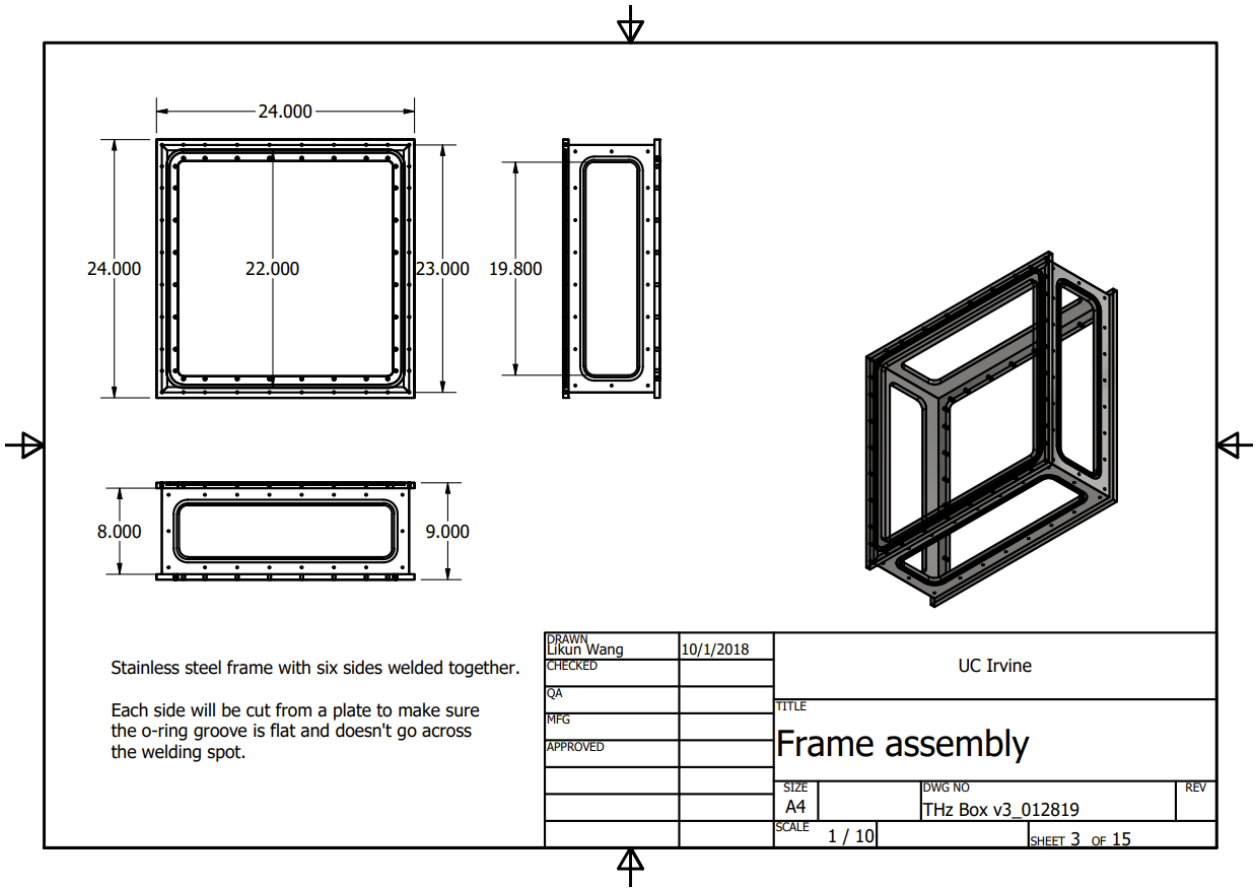
24.000
24.000
22.000
23.000
19.800
8.000
9.000
Stainless steel frame with six sides welded together.
Each side will be cut from a plate to make sure the o-ring groove is flat and doesn't go across the welding spot.
DRAWN Likun Wang 10/1/2018
CHECKED
QA
MFG
APPROVED
UC Irvine
TITLE
Frame assembly
SIZE A4
DWG NO THz Box v3_012819
REV
SCALE 1 / 10
SHEET 3 OF 15

Figure B.4 Dimensions of the aluminum side plates.

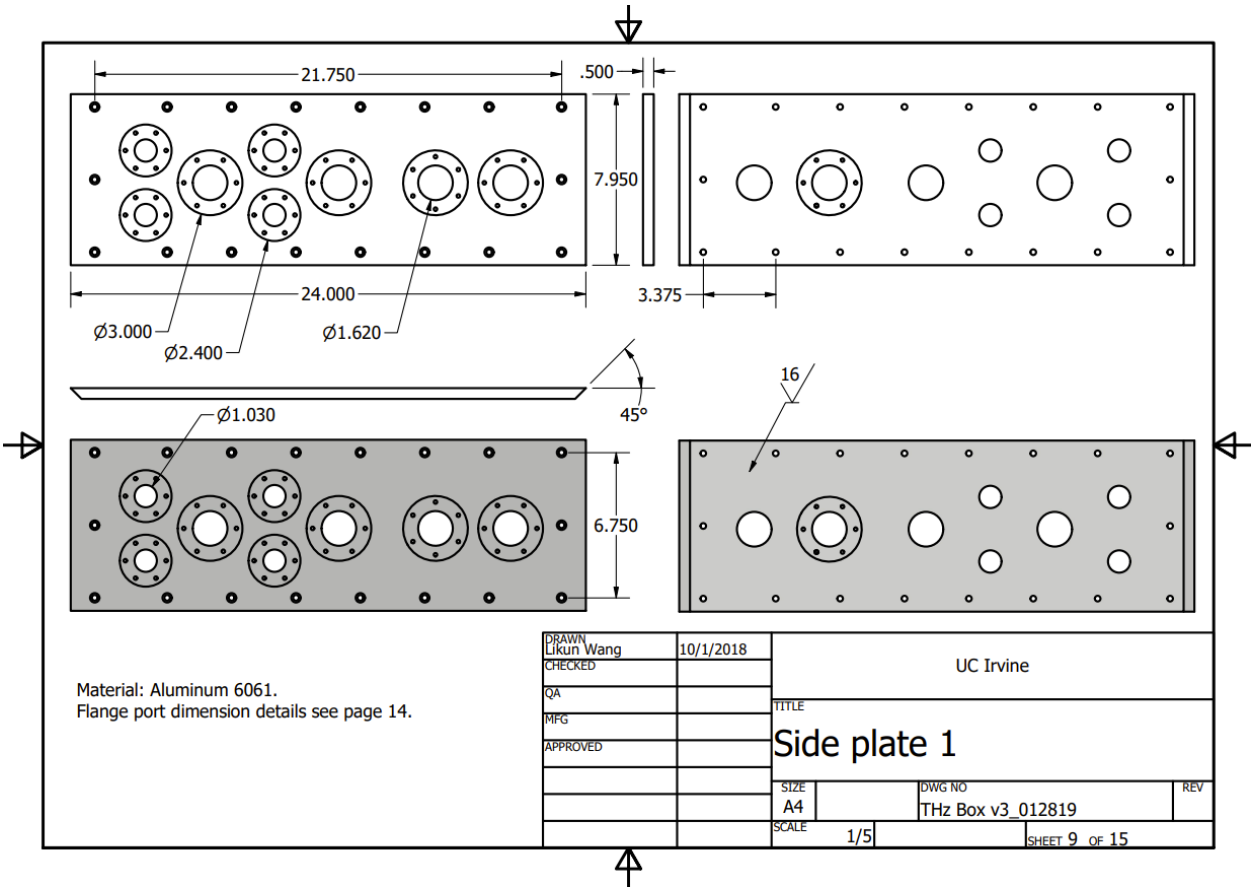
21.750
.500
7.950
24.000
3.375
Ø3.000
Ø2.400
Ø1.620
45°
16
Ø1.030
6.750
Material: Aluminum 6061.
Flange port dimension details see page 14.
DRAWN Likun Wang
10/1/2018
CHECKED
QA
MFG
APPROVED
UC Irvine
TITLE
Side plate 1
SIZE A4
DWG NO THz Box v3_012819
REV
SCALE 1/5
SHEET 9 OF 15

Figure B.5 Dimensions of the bottom aluminum plate.

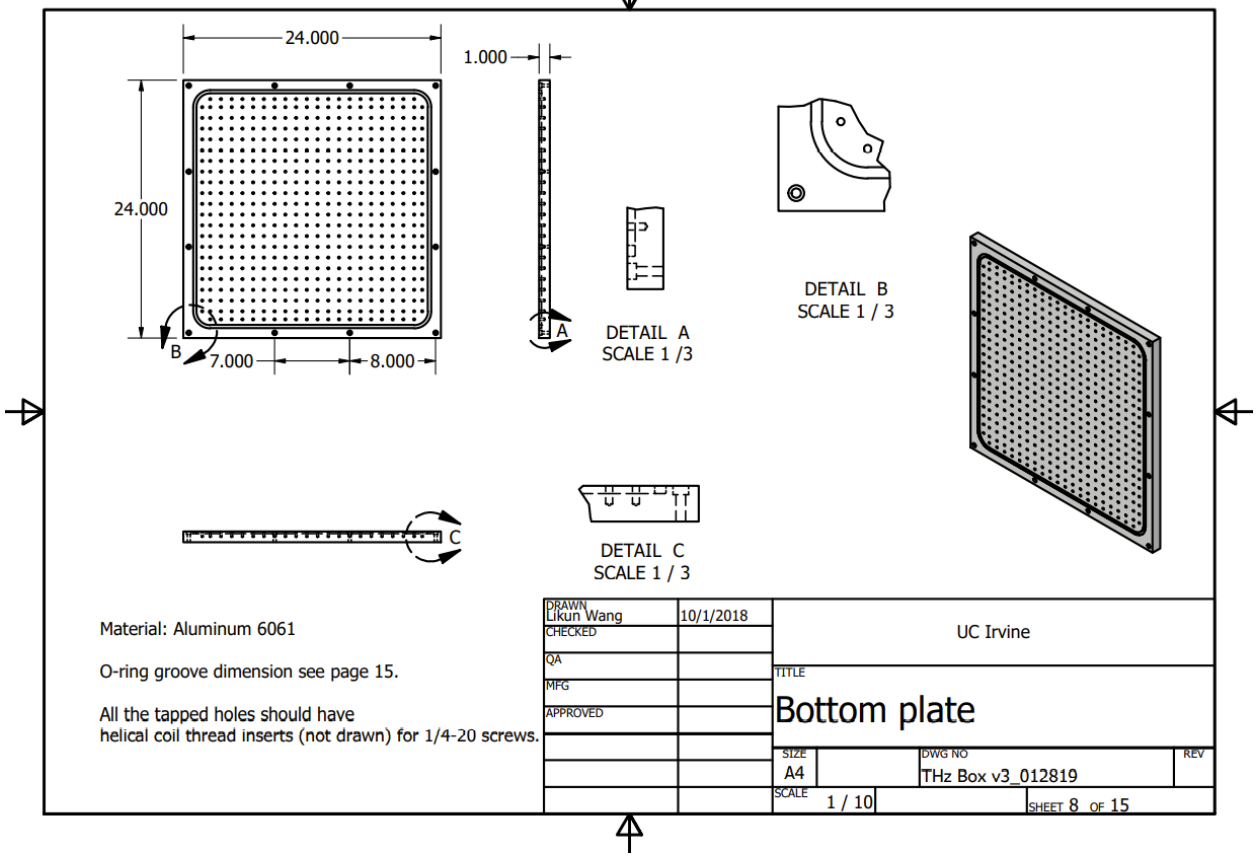
24.000
1.000
24.000
B
7.000
8.000
A
DETAIL A
SCALE 1 /3
DETAIL B
SCALE 1 / 3
C
DETAIL C
SCALE 1 / 3
Material: Aluminum 6061
O-ring groove dimension see page 15.
All the tapped holes should have
helical coil thread inserts (not drawn) for 1/4-20 screws.
DRAWN Likun Wang 10/1/2018
CHECKED
QA
MFG
APPROVED
UC Irvine
TITLE
Bottom plate
SIZE A4
DWG NO THz Box v3_012819
REV
SCALE 1 / 10
SHEET 8 OF 15

Figure B.6 Dimensions of the acrylic top cover.

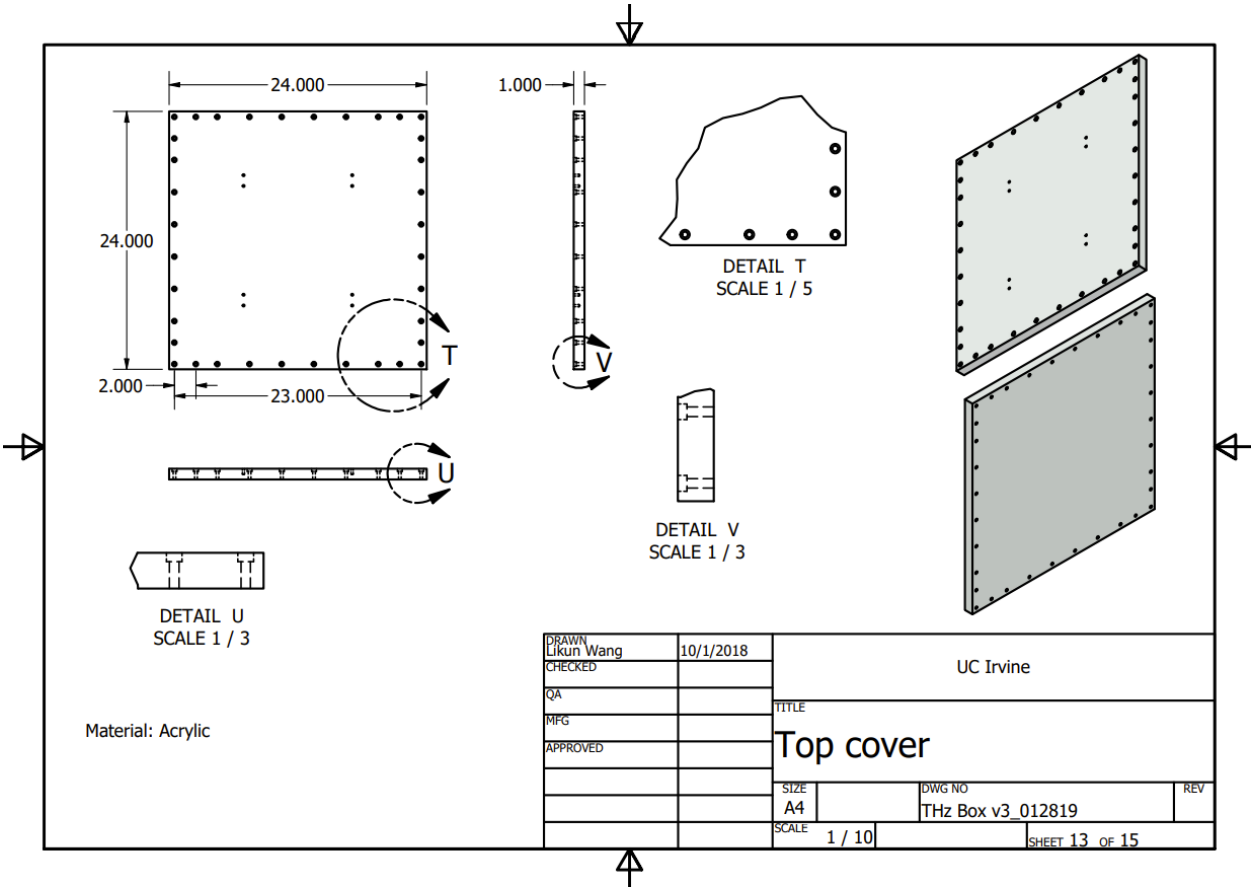
24.000
24.000
2.000
23.000
T
U
1.000
V
DETAIL T
SCALE 1 / 5
DETAIL V
SCALE 1 / 3
DETAIL U
SCALE 1 / 3
Material: Acrylic
DRAWN Likun Wang 10/1/2018
CHECKED
QA
MFG
APPROVED
UC Irvine
TITLE
Top cover
SIZE A4
DWG NO THz Box v3_012819
REV
SCALE 1 / 10
SHEET 13 OF 15

Figure B.7 Dimensions of the O-ring grove.

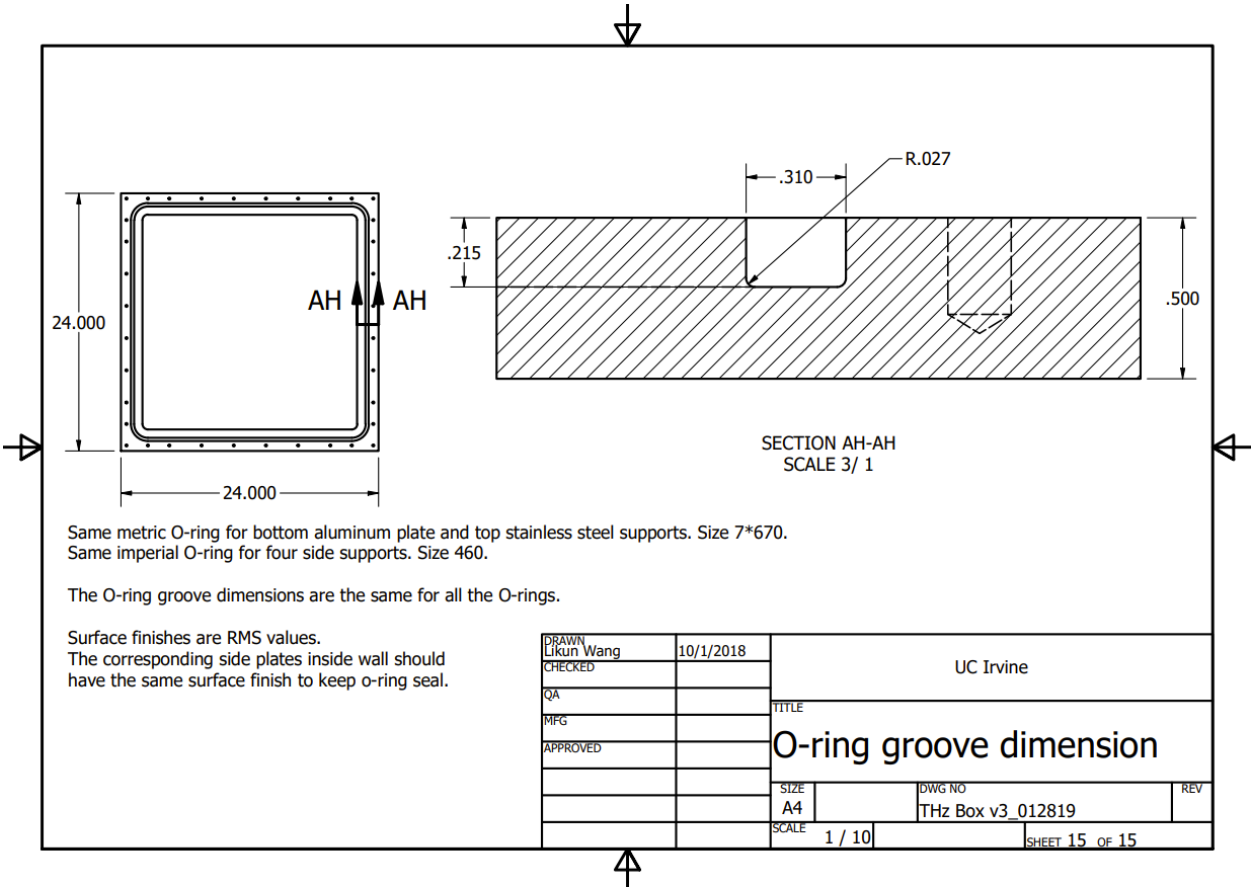

Same metric O-ring for bottom aluminum plate and top stainless steel supports. Size 7*670.
Same imperial O-ring for four side supports. Size 460.

The O-ring groove dimensions are the same for all the O-rings.

Surface finishes are RMS values.
The corresponding side plates inside wall should have the same surface finish to keep o-ring seal.

DRAWN Likun Wang	10/1/2018	UC Irvine
CHECKED		TITLE: O-ring groove dimension
QA		
MFG		
APPROVED		
SIZE A4	DWG NO THz Box v3_012819	REV
SCALE 1 / 10		SHEET 15 OF 15

Figure B.8 Picture of the first THz box.

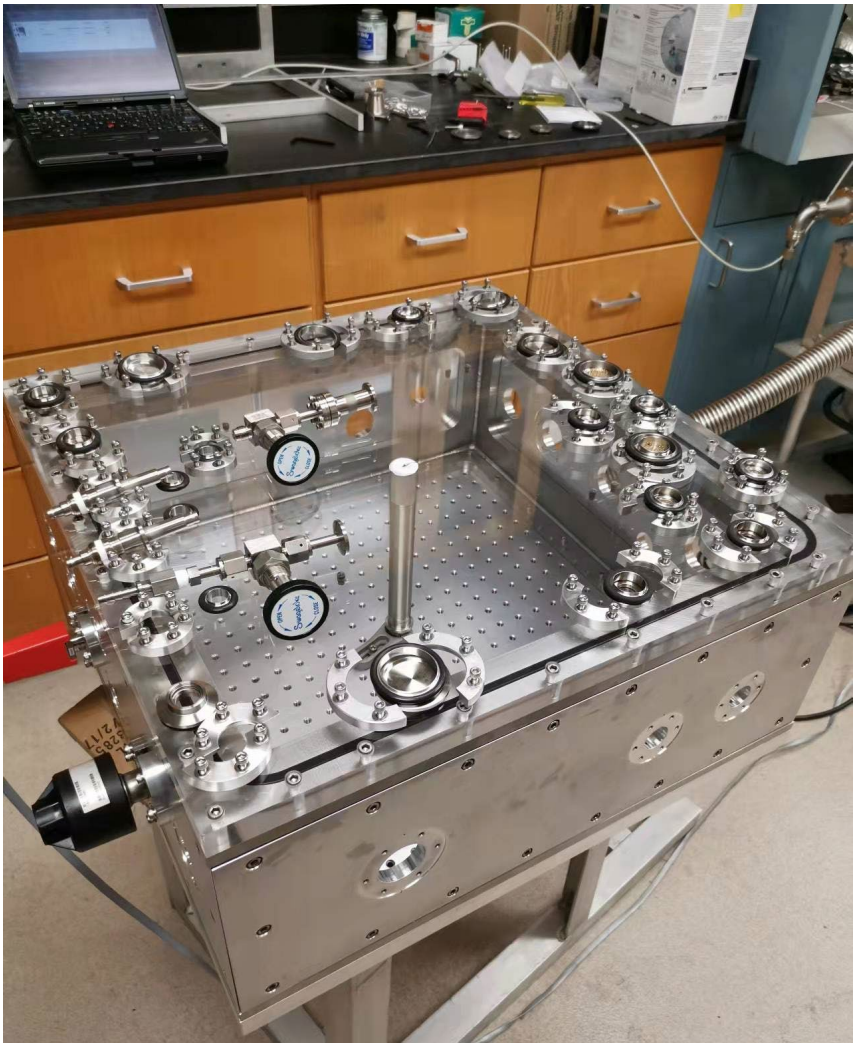

Figure B.9 Optical and THz system in the THz box.

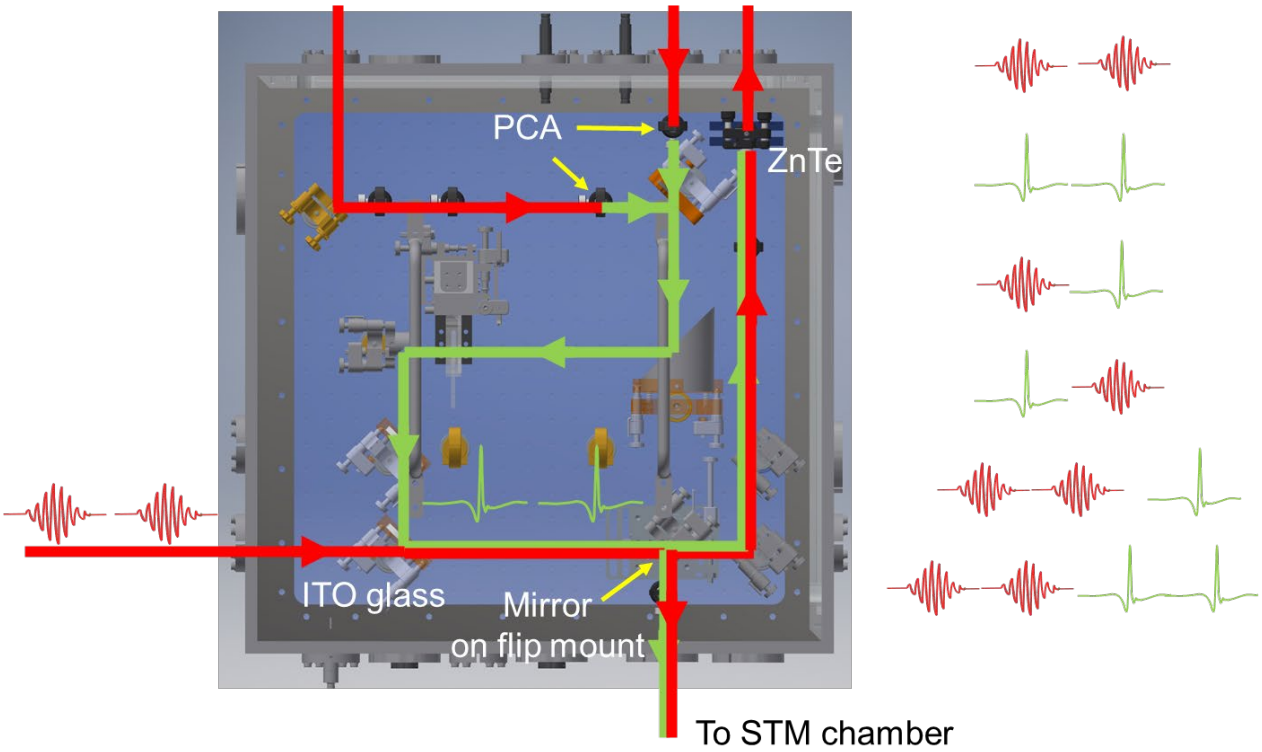
PCA
ZnTe
ITO glass
Mirror
on flip mount
To STM chamber

Figure B.10 Gas absorption measurements in the box.

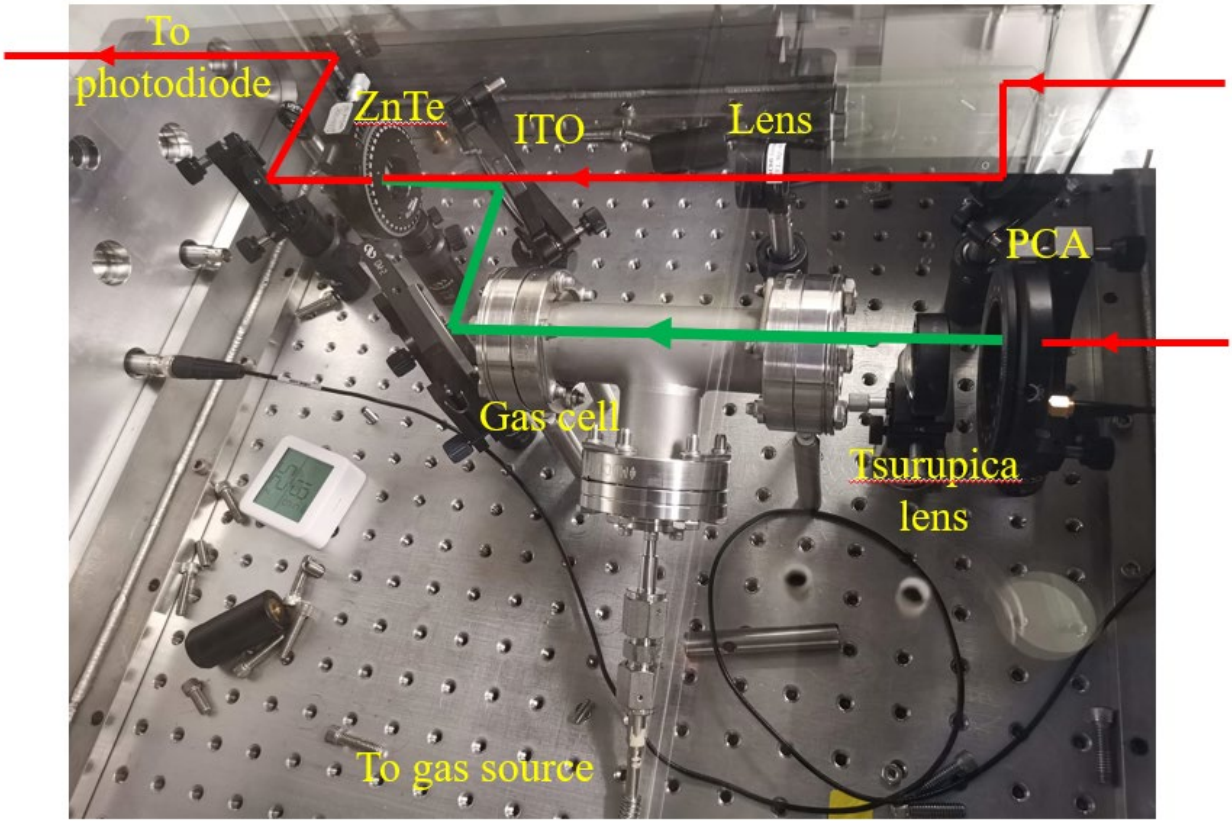
To
photodiode
ZnTe
ITO
Lens
PCA
Gas cell
Tsurupica
lens
To gas source

It was later realized that the large THz box sitting on the optical table introduced a significant drawback. Due to the low beam quality of our generated THz, the beam diverged significantly with a longer propagation length. It took more than 40” from the PCA to the STM junction, making it very difficult to focus the THz into the junction. As a result, the THz power was not high enough to perform the THz rectification spectroscopy.

The large THz box can be converted into a glove box with minimal changes to store some air sensitive molecules such as nickelocene. As shown in Figure B.11, an aluminum plate can be machined with two large ports to hold the two gloves for the glove box. The distance between the two large ports is 12” which is enough to operate with two hands. The 6” diameter of each port also allows a comfortable entrance.

The current design for the glove box is compatible with the ports from Marine and Industrial Plastics in UK. The part number of the circular port is PORT150. With a 150 mm neoprene gasket (203.2 mm OD, 155.6 mm ID) to seal the box, a pair of 150 mm latex gloves from the same company should work well. All the parts have been ordered in our lab. And the webpage for the port with some accessories is https://www.mipltd.co.uk/service/circular-glove-ports/. Table B.1 lists detailed information of all the parts needed to assemble the glove box.

Figure B.11 Dimensions of the side plate modifications.

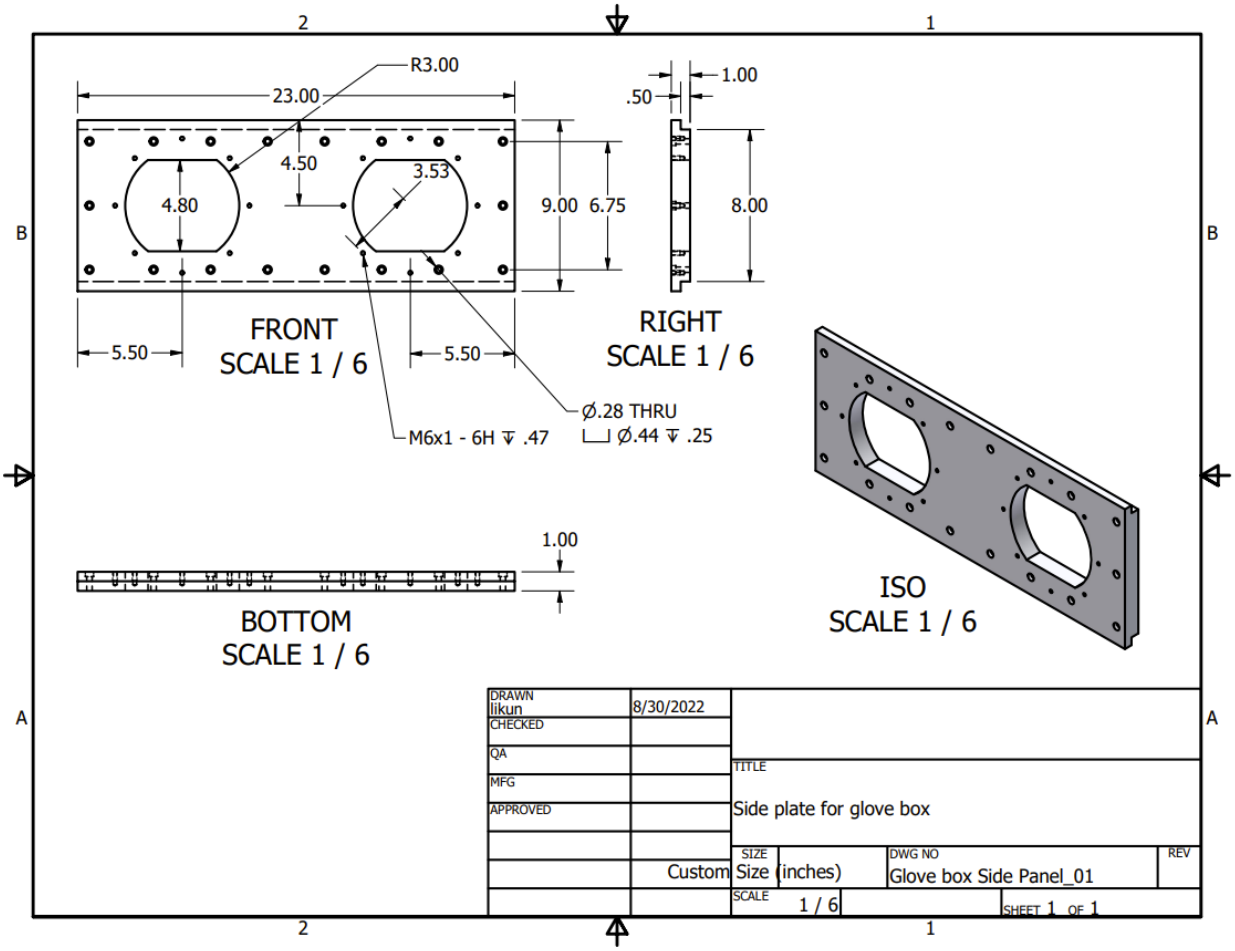
R3.00
23.00
4.50
3.53
4.80
9.00
6.75
5.50
5.50
FRONT
SCALE 1 / 6
1.00
.50
8.00
RIGHT
SCALE 1 / 6
Ø.28 THRU
M6x1 - 6H ↧ .47
⌴ Ø.44 ↧ .25
1.00
BOTTOM
SCALE 1 / 6
ISO
SCALE 1 / 6
DRAWN
likun
8/30/2022
CHECKED
QA
MFG
APPROVED
TITLE
Side plate for glove box
SIZE
Custom
Size (inches)
DWG NO
Glove box Side Panel_01
REV
SCALE
1 / 6
SHEET 1 OF 1

Table B.1 Detailed information of all the parts.

Name	Part number	Manufacturer	Amount	Unit price
Aluminum plate	8975K135	McMASTER-CARR	1	$92.99
Glove ports	PORT150	Marine and Industrial Plastics	2	$53.71
Gasket	GASK150	Marine and Industrial Plastics	1	$15.72
Fixing screws	M6X30S/S	Marine and Industrial Plastics	16	$0.33
Latex gloves	GL150LATSZ10M	Marine and Industrial Plastics	1 pair	$98.25/pair

A more compact design of the THz box requires the box to be as close as possible to the STM junction. The functionality of the box, however, should be similar to the large THz box described above.

As shown in Figure B.12 and Figure B.13, this THz box was made of aluminum and acrylic. The aluminum frame was used to mount fused silica windows and other flanges. The aluminum bottom piece with ¼-20 threaded hole can be used to mount the optics to generate and direct THz and NIR beams. An ITO glass was again used to combine the THz and NIR beams. The Viton O-ring (Part #: V1000-279) from Macro Rubber & Plastics was used to seal the top and bottom plates. This O-ring has a cross section of 0.139" with the inside diameter 12.984" and outside diameter 13.262", which fits to the O-ring grove in Figure B.14 very well.

Similar to the previous large stainless-steel box, this aluminum THz box can also be pumped to vacuum or purged with dry N_2 gas to reach 0% humidity. It is also possible to make combinations of different NIR and THz beams to perform different experiments.

With this setup, the propagation from the PCA to the STM junction is minimized (~ 24.5"), providing us with more THz power and more focused THz beam. Another good thing about this THz box sitting on the STM table is that no further THz alignment is needed once it was aligned initially. Due to the rigid connection with the STM chamber, the THz alignment keeps the same even after a very long time. The only alignment needed is the NIR beam on the PCA, which is easy to do since it is visible.

The lens tube assembly to focus and align the THz beam into the STM junction is shown in Figure B.15 and Figure B.16. The X and Y alignment of THz can be adjusted by the mirror mount, and the Z alignment can be adjusted by rotating the lens tube in this assembly. In this way,

the THz alignment can be adjusted in all X, Y, and Z directions. All the parts in this assembly were from Thorlabs except for the custom-designed Tsurupica lens which was from the Japanese company PHLUXi. The lens tube assembly is connected with the STM chamber viewport via an edge welded bellow coupler (Figure B.17 and Figure B.18). The whole assembly of the THz box, lens tube, and edge welded bellow coupler is shown in Figure B.19.

The detailed drawings of the THz box are shown in Figure B.20-23.

Figure B.12 Picture of the THz box on the STM table.

STM

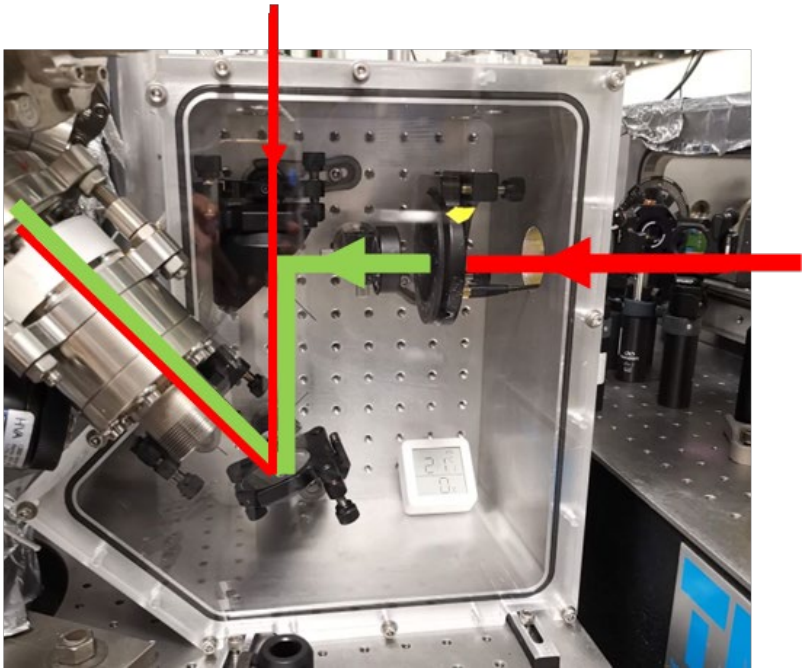

Figure B.13 3D drawing of the THz box.

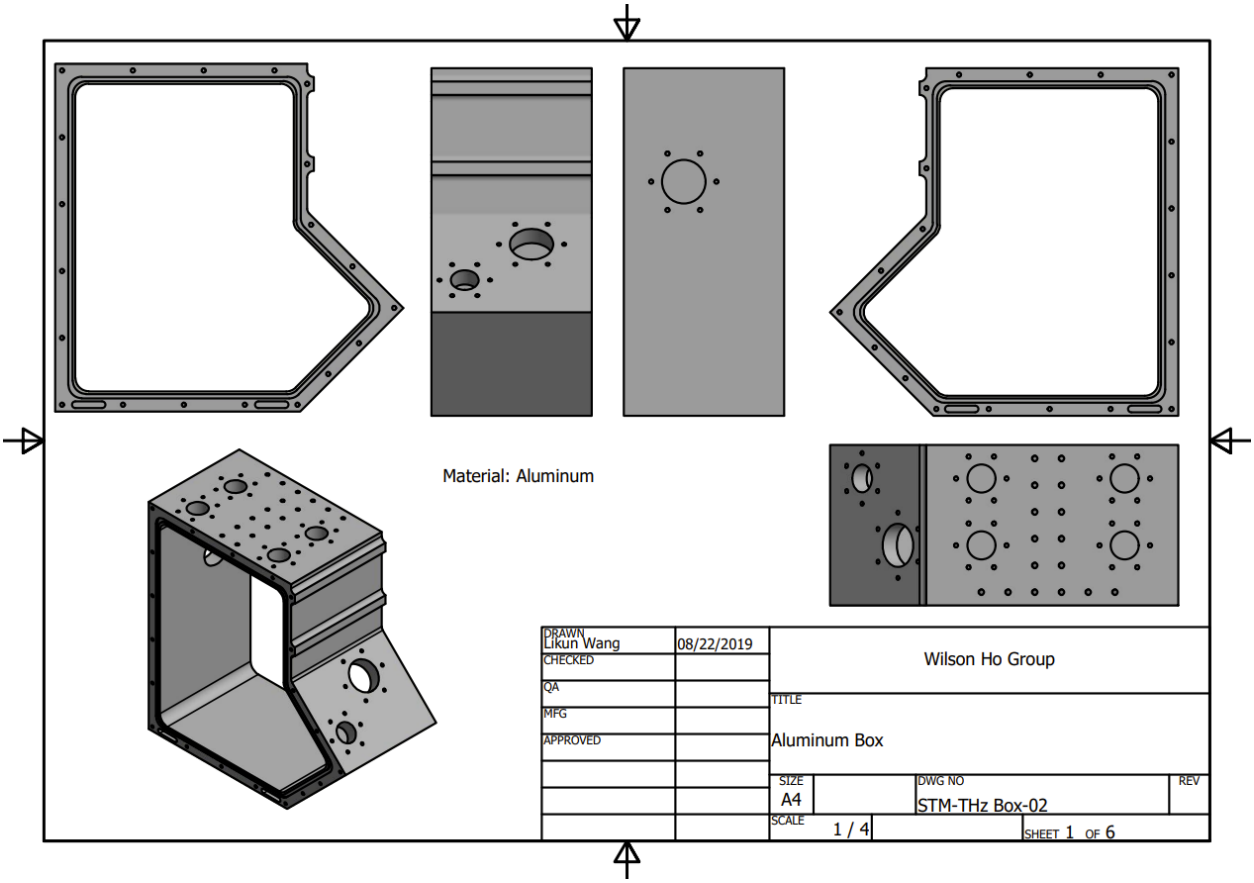
Material: Aluminum
DRAWN
Likun Wang
08/22/2019
CHECKED
QA
MFG
APPROVED
Wilson Ho Group
TITLE
Aluminum Box
SIZE
A4
DWG NO
STM-THz Box-02
REV
SCALE
1 / 4
SHEET 1 OF 6

Figure B.14 2D drawing of the aluminum frame.

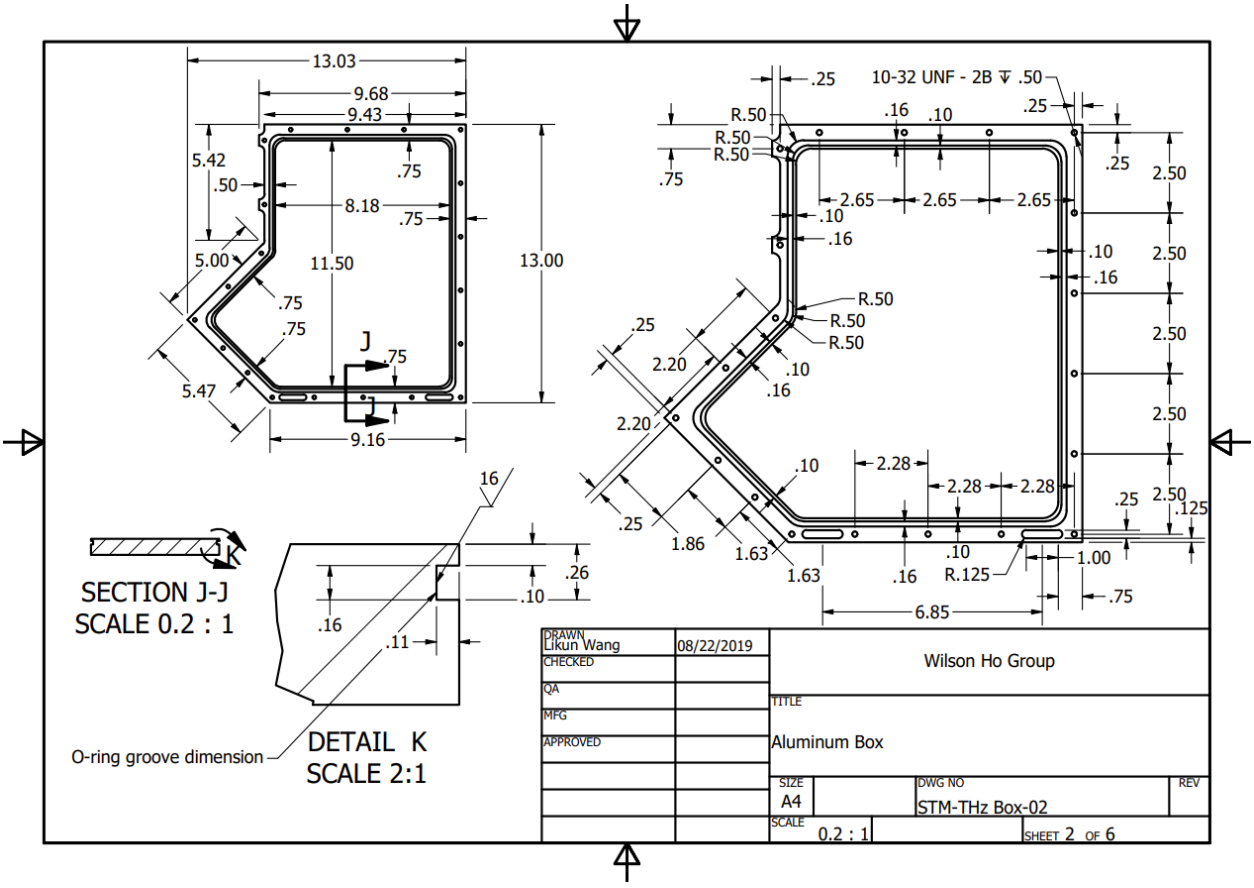
13.03
9.68
9.43
5.42
.50
.75
8.18
.75
5.00
11.50
13.00
.75
.75
J
.75
5.47
9.16
.25
10-32 UNF - 2B ↧ .50
.25
R.50
R.50
R.50
.16
.10
.75
2.65
2.65
2.65
.10
.16
.10
.16
2.50
2.50
2.50
2.50
2.50
.25
.125
R.50
R.50
R.50
.25
2.20
.10
.16
2.20
.10
2.28
2.28
2.28
.25
1.86
1.63
1.63
.10
.16
R.125
1.00
.75
6.85
J
K
SECTION J-J
SCALE 0.2 : 1
16
.26
.10
.16
.11
O-ring groove dimension
DETAIL K
SCALE 2:1
DRAWN Likun Wang 08/22/2019
CHECKED
QA
MFG
APPROVED
Wilson Ho Group
TITLE
Aluminum Box
SIZE A4
DWG NO STM-THz Box-02
REV
SCALE 0.2 : 1
SHEET 2 OF 6

Figure B.15 Drawing of the lens tube assembly.

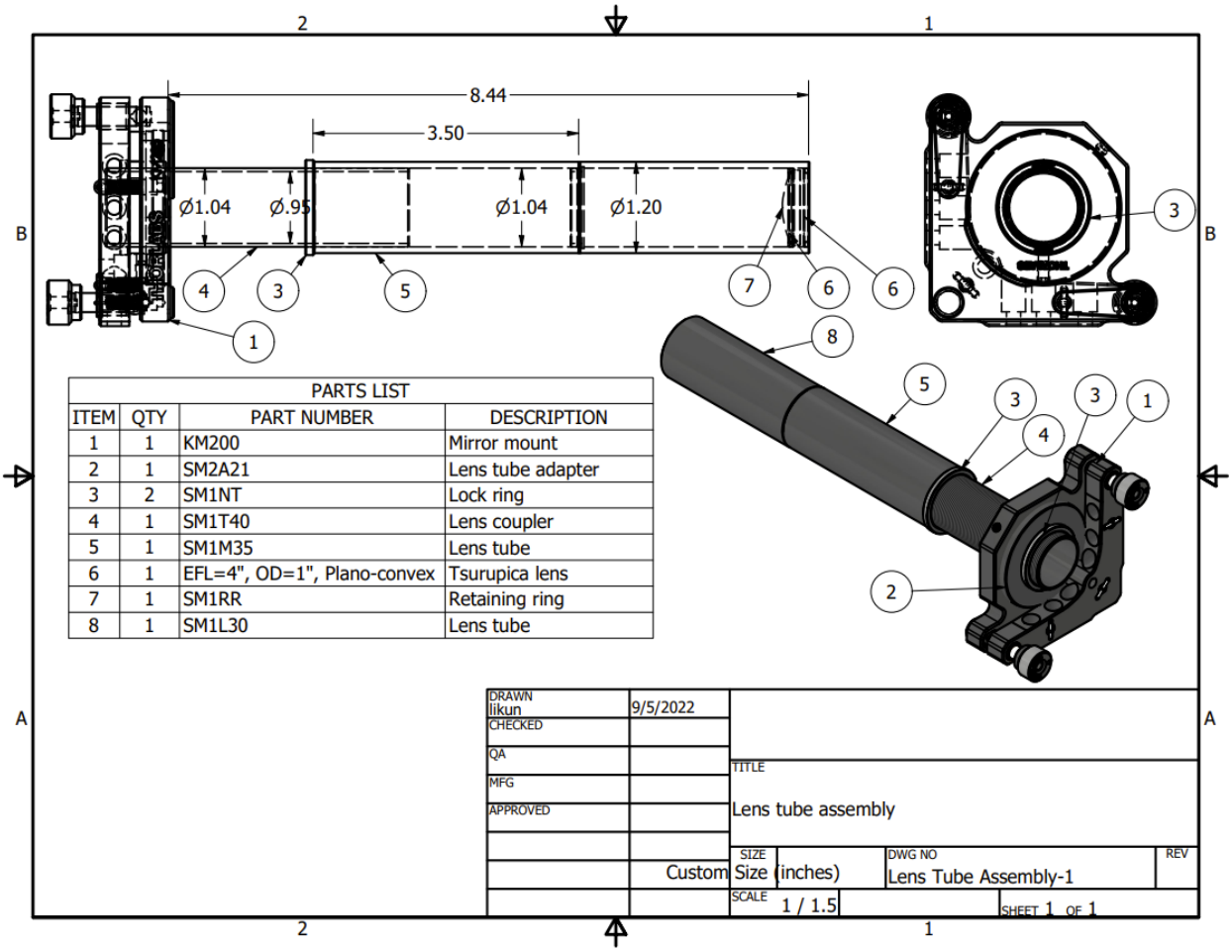

PARTS LIST			
ITEM	QTY	PART NUMBER	DESCRIPTION
1	1	KM200	Mirror mount
2	1	SM2A21	Lens tube adapter
3	2	SM1NT	Lock ring
4	1	SM1T40	Lens coupler
5	1	SM1M35	Lens tube
6	1	EFL=4", OD=1", Plano-convex	Tsurupica lens
7	1	SM1RR	Retaining ring
8	1	SM1L30	Lens tube

DRAWN likun	9/5/2022		
CHECKED			
QA			
MFG		TITLE: Lens tube assembly	
APPROVED			
		SIZE: Custom Size (inches)	DWG NO: Lens Tube Assembly-1 REV
		SCALE: 1 / 1.5	SHEET 1 OF 1

Figure B.16 Picture of the lens tube assembly. The lens tube assembly is attached to the THz box through the mirror mount on the optical post which is bolted down to the aluminum plate with ¼-20 set screw.

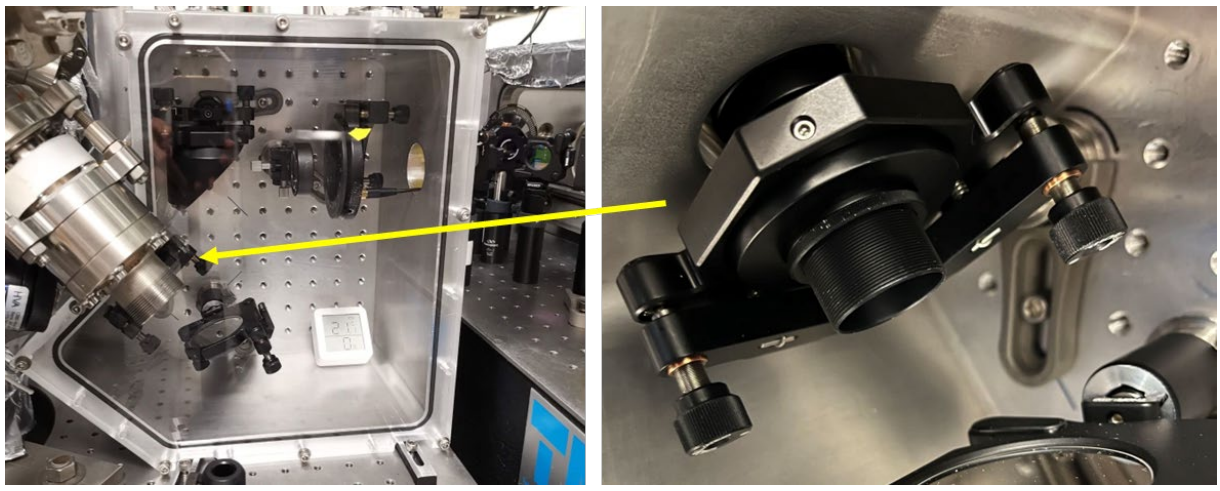

Figure B.17 Drawing of the edge welded bellow coupler. An edge welded bellow was welded with NW40 and NW50 KF flanges to connect the THz box with the STM chamber viewport. The NW40 flange is clamped to the THz box, and the NW50 flange is clamped to the viewport flange.

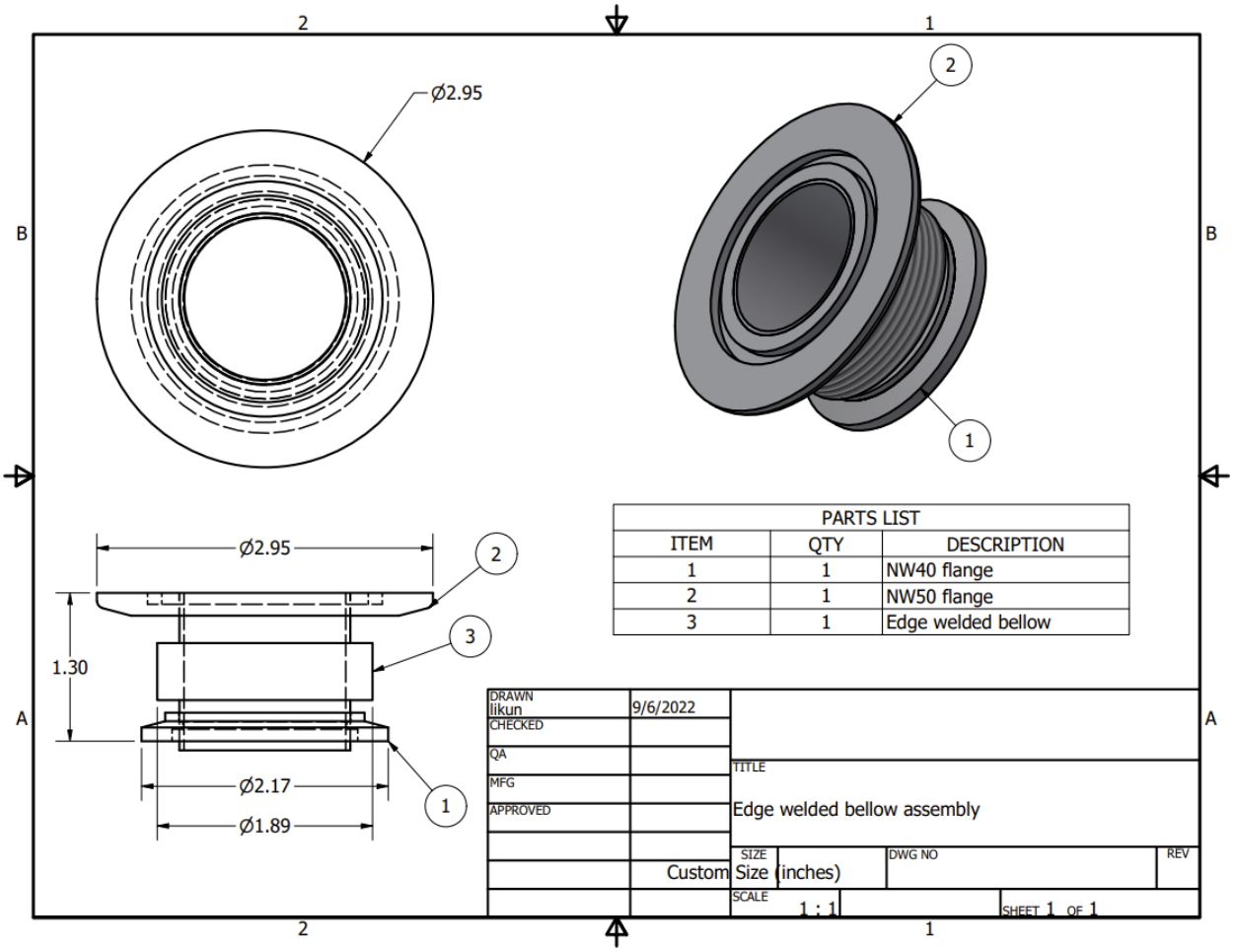
Ø2.95
2
1
Ø2.95
2
3
1.30
Ø2.17
Ø1.89
1
PARTS LIST
ITEM QTY DESCRIPTION
1 1 NW40 flange
2 1 NW50 flange
3 1 Edge welded bellow
DRAWN likun 9/6/2022
CHECKED
QA
MFG
APPROVED
TITLE
Edge welded bellow assembly
SIZE Custom Size (inches)
DWG NO
REV
SCALE 1 : 1
SHEET 1 OF 1

Figure B.18 Photo of the edge welded bellow coupler.

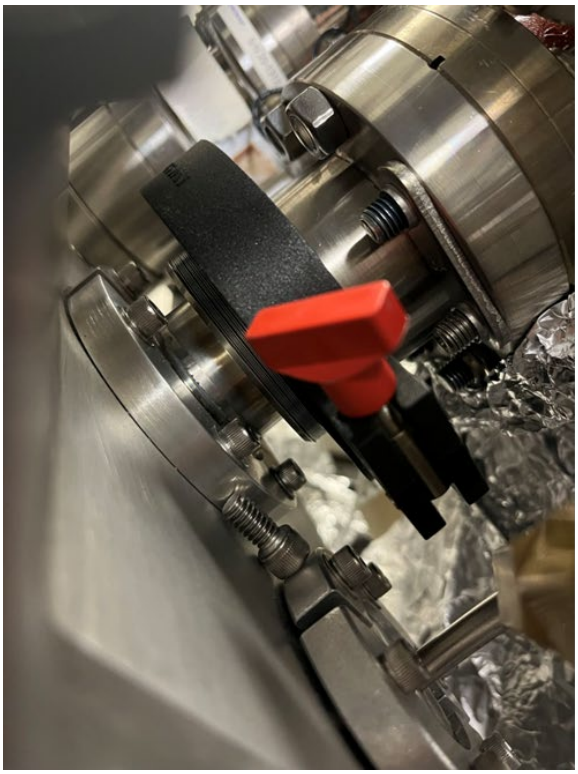

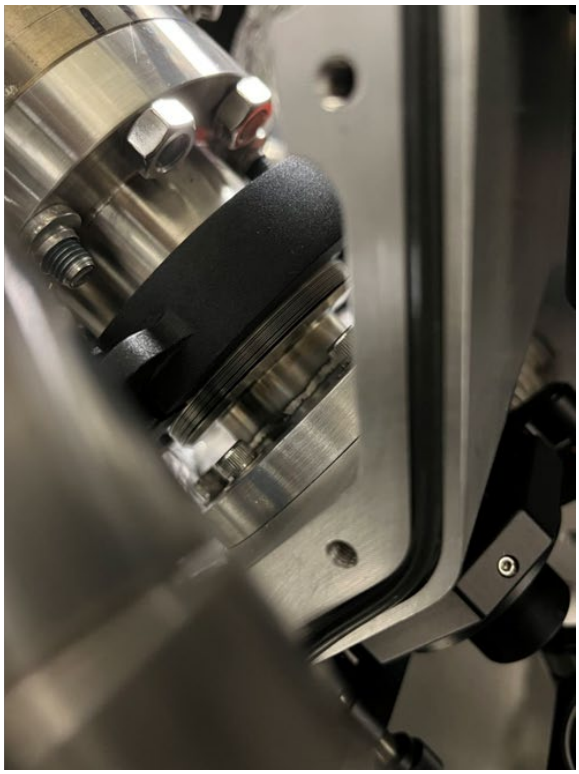

Figure B.19 Drawing of the THz box and lens tube assemblies. The whole assembly is attached to the STM chamber viewport through the edge welded bellow coupler. The tilt angle for adjusting the lens in X and Y directions with the two knobs of the mirror mount is about ±1.5° for each direction. The Z motion of the lens is adjusted by loosening the lock ring (#3 on the mirror mount in Figure B.15) and rotating the lens tube on the mirror mount(#7). The distance range between the end of the lens tube assembly and the viewport window is 0.5”-1.5”. After moving out the mirror mount (#7), there is enough room to take out the lens tube assembly, after which the THz box can be detached with the chamber viewport.

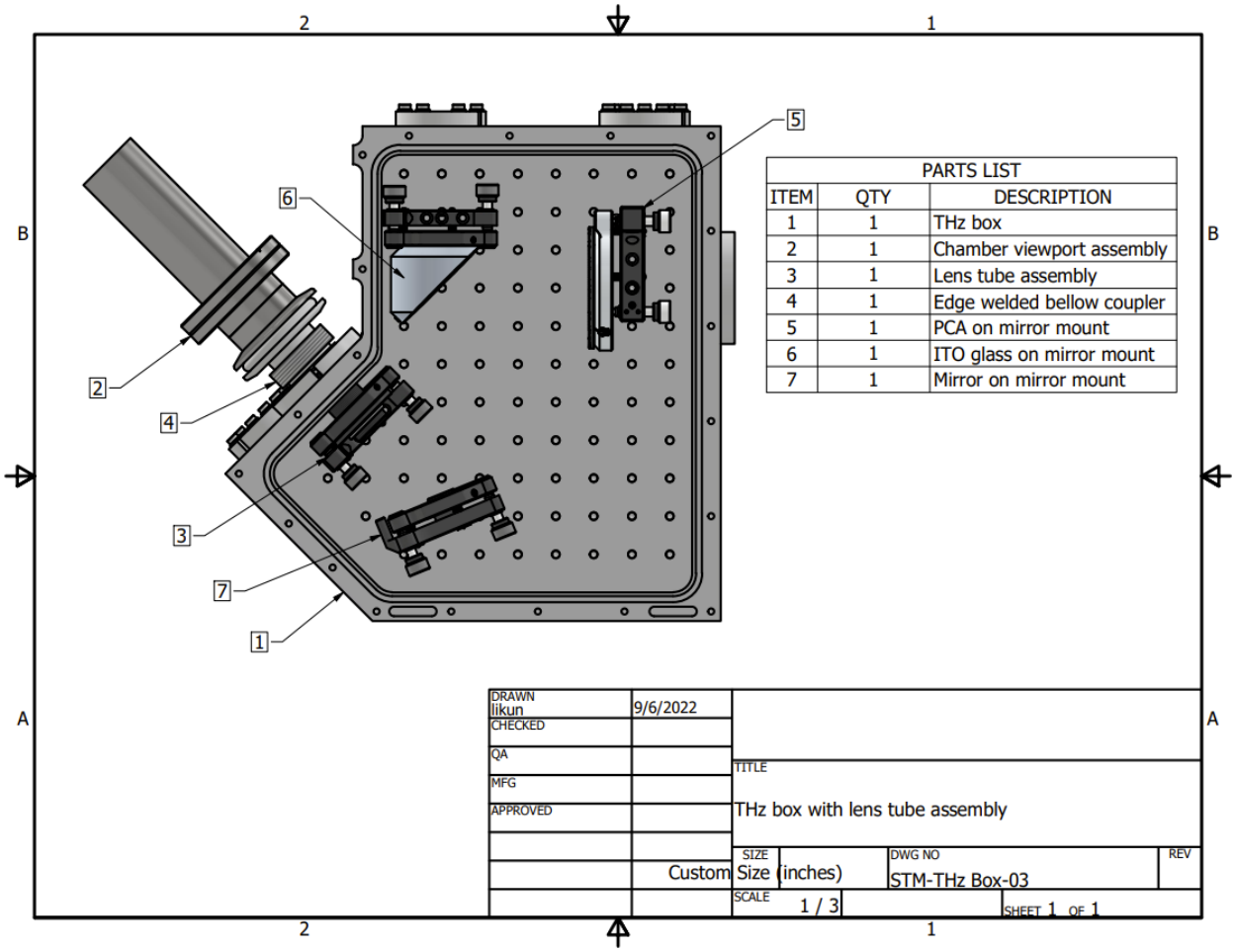

PARTS LIST		
ITEM	QTY	DESCRIPTION
1	1	THz box
2	1	Chamber viewport assembly
3	1	Lens tube assembly
4	1	Edge welded bellow coupler
5	1	PCA on mirror mount
6	1	ITO glass on mirror mount
7	1	Mirror on mirror mount

DRAWN likun	9/6/2022	
CHECKED		
QA		TITLE: THz box with lens tube assembly
MFG		
APPROVED		
	Custom	SIZE: Size (inches) / DWG NO: STM-THz Box-03 / REV
		SCALE: 1 / 3 / SHEET 1 OF 1

Figure B.20 2D drawing of the flange ports on the THz box.

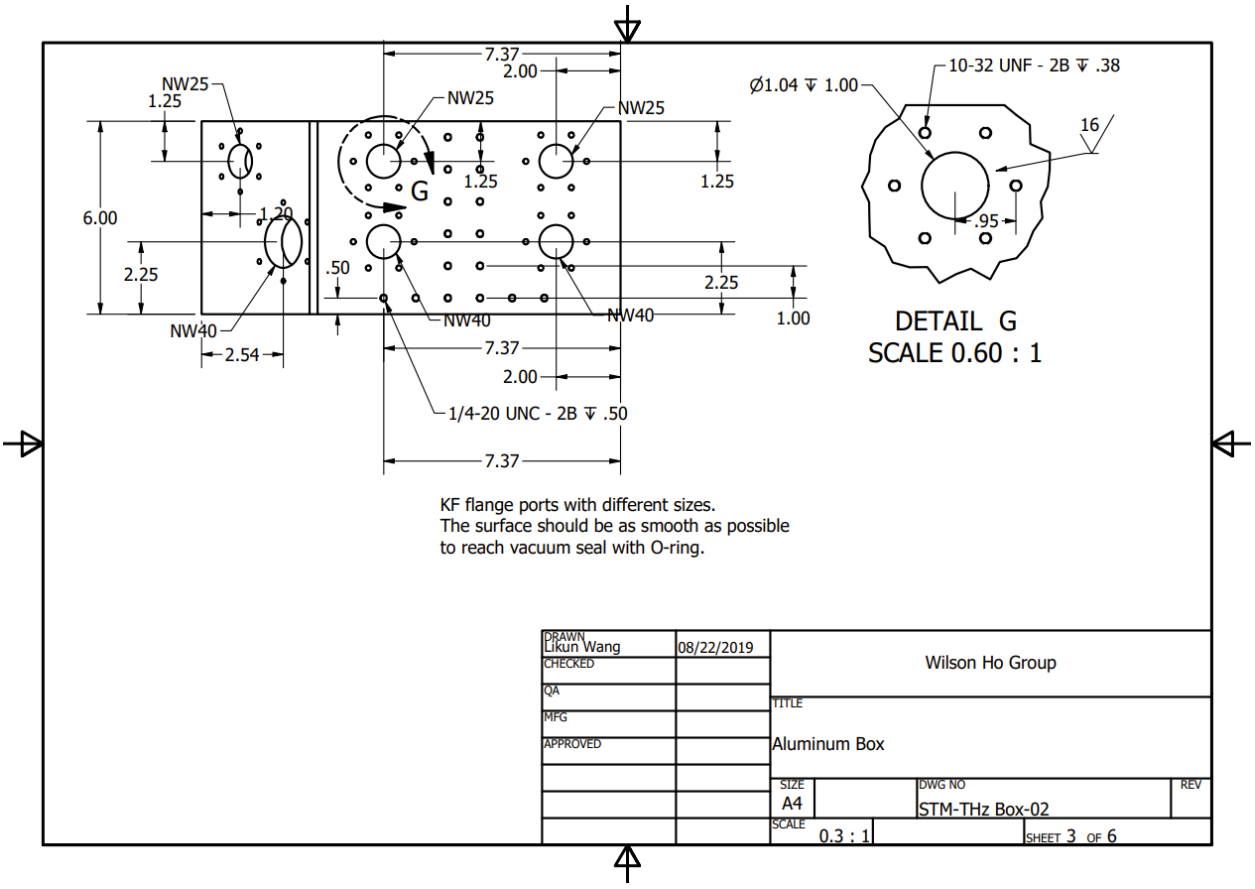
7.37
2.00
NW25
1.25
NW25
NW25
1.25
1.25
G
6.00
1.20
2.25
.50
2.25
1.00
NW40
NW40
NW40
2.54
7.37
2.00
1/4-20 UNC - 2B ↧ .50
7.37
Ø1.04 ↧ 1.00
10-32 UNF - 2B ↧ .38
16
.95
DETAIL G
SCALE 0.60 : 1
KF flange ports with different sizes.
The surface should be as smooth as possible
to reach vacuum seal with O-ring.
DRAWN
Likun Wang
08/22/2019
CHECKED
QA
MFG
APPROVED
Wilson Ho Group
TITLE
Aluminum Box
SIZE
A4
DWG NO
STM-THz Box-02
REV
SCALE
0.3 : 1
SHEET 3 OF 6

Figure B.21 2D drawing of the acrylic cover.

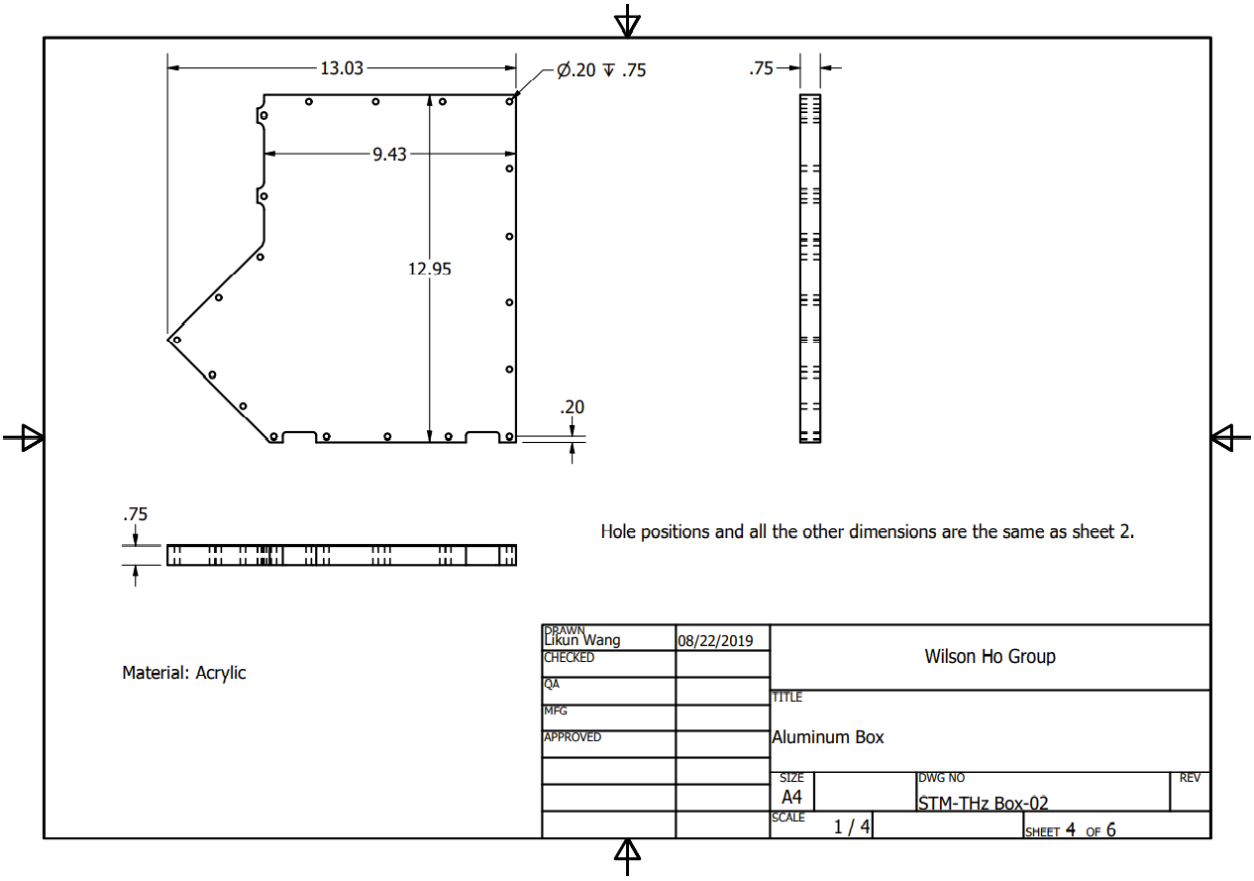
13.03
Ø.20 ⊽ .75
.75
9.43
12.95
.20
.75
Hole positions and all the other dimensions are the same as sheet 2.
Material: Acrylic
DRAWN
Likun Wang
08/22/2019
CHECKED
QA
MFG
APPROVED
Wilson Ho Group
TITLE
Aluminum Box
SIZE
A4
DWG NO
STM-THz Box-02
REV
SCALE
1 / 4
SHEET 4 OF 6

Figure B.22 2D drawing of the aluminum plate with ¼-20 threaded holes.

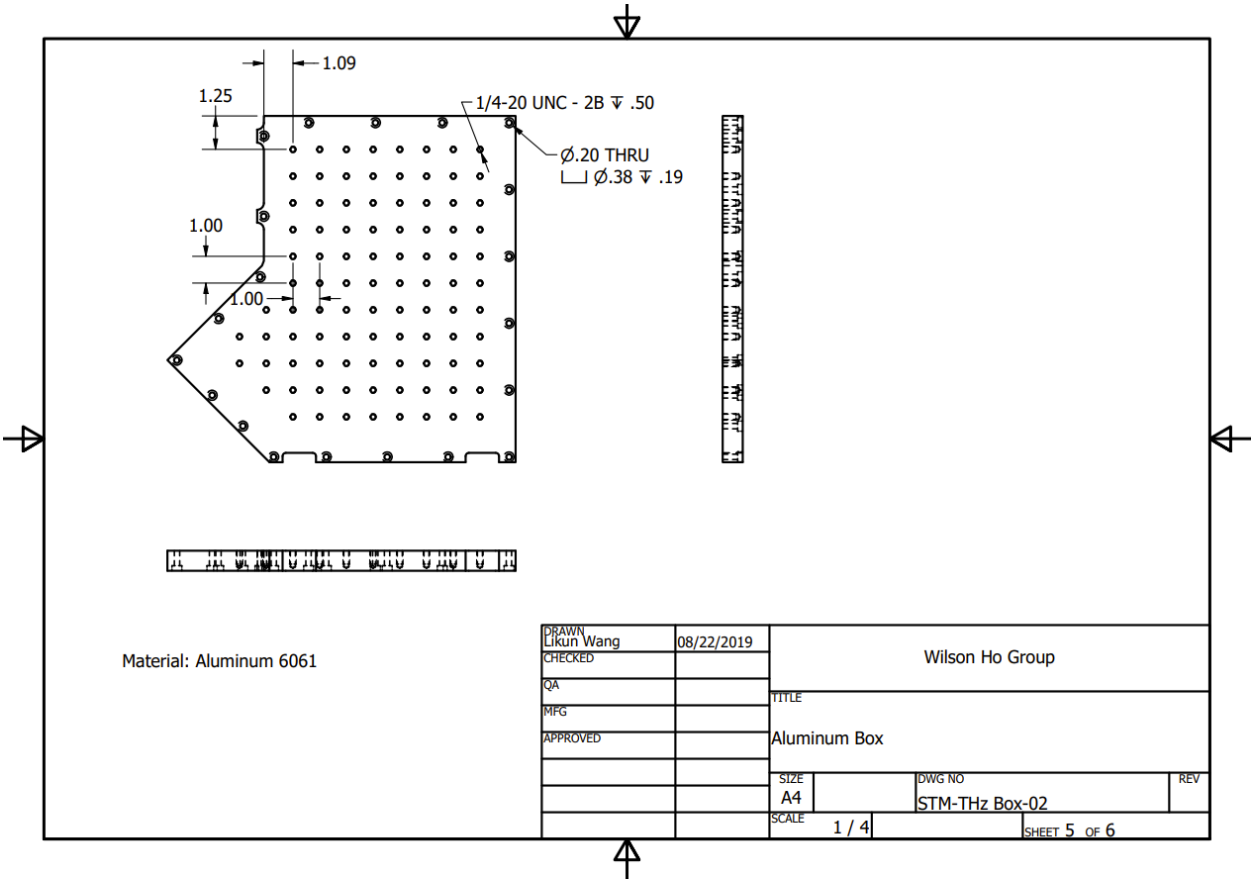
1.09
1.25
1/4-20 UNC - 2B ↧ .50
Ø.20 THRU
⌴ Ø.38 ↧ .19
1.00
1.00
Material: Aluminum 6061
DRAWN
Likun Wang
08/22/2019
CHECKED
QA
MFG
APPROVED
Wilson Ho Group
TITLE
Aluminum Box
SIZE
A4
DWG NO
STM-THz Box-02
REV
SCALE
1 / 4
SHEET 5 OF 6

Figure B.23 2D drawing of the NW40 flange port.

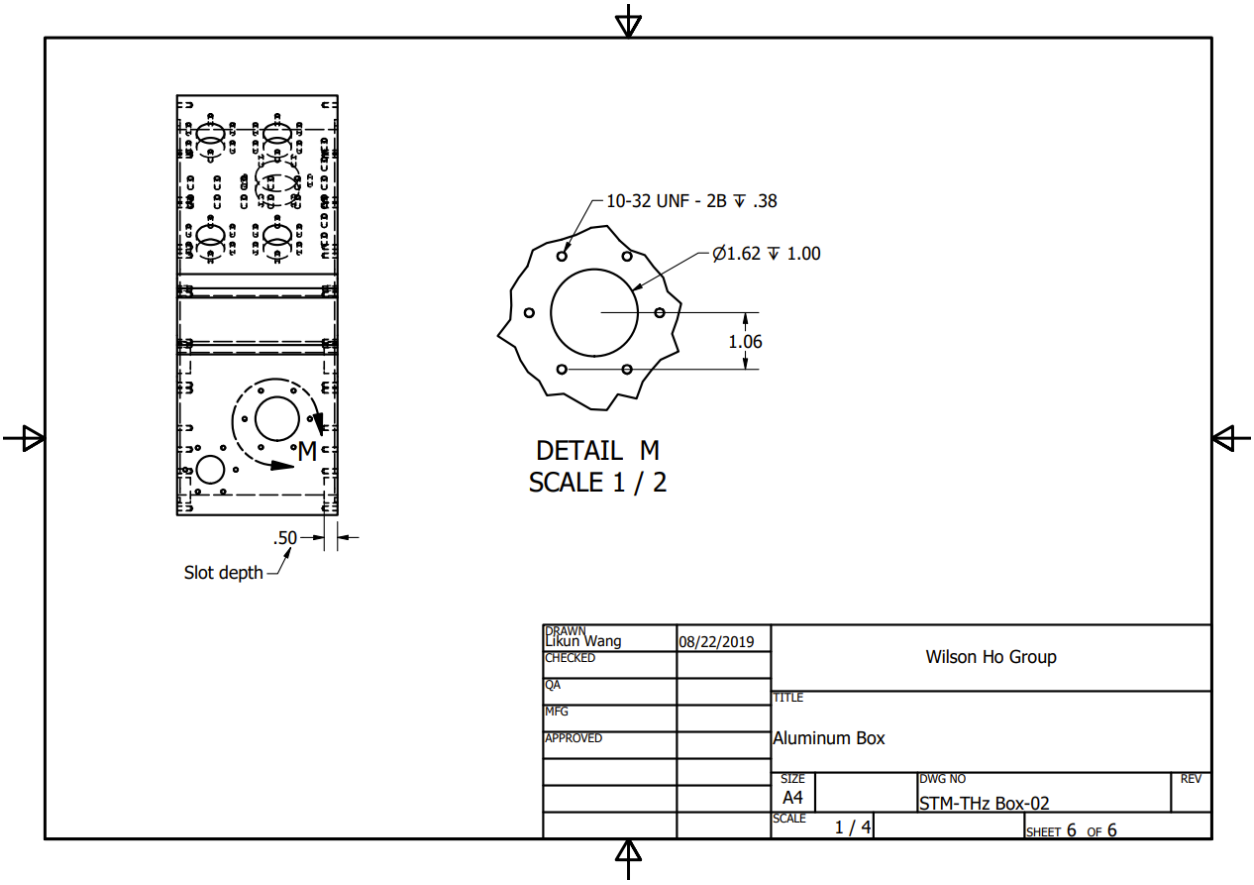
10-32 UNF - 2B ↧ .38
Ø1.62 ↧ 1.00
1.06
M
.50
Slot depth
DETAIL M
SCALE 1 / 2
DRAWN Likun Wang 08/22/2019
CHECKED
QA
MFG
APPROVED
Wilson Ho Group
TITLE
Aluminum Box
SIZE A4
DWG NO STM-THz Box-02
REV
SCALE 1 / 4
SHEET 6 OF 6

APPENDIX C

PCAs Used in STM 2

High power photoconductive antennas (PCA) for THz generation shared the similar design of the interdigital array antennas (Figure C.1) which generated much larger photocurrent than traditional PCAs, emitting higher THz power [1–4]. To generate THz from the PCA, a laser beam is required to be focused on the finger electrodes of the PCA. After applying a voltage across the finger electrodes, hot carriers generated by the laser will be accelerated and the PCA emits THz electromagnetic waves with linear polarization. PCAs are particularly suitable for lasers with high repetition rates, such as the one in STM 2 with 1 GHz rep rate. The emitted THz power can be easily controlled by either adjusting the NIR laser power or the applied voltage on the PCA. The polarization of the THz can be controlled effectively by mounting the PCA onto a rotational mount and control its rotation angle.

There were in total three types of PCAs used in STM 2, namely, Batop PCA (Figure C.2), Laser Quantum PCA (Figure C.3), and UCLA PCA (Figure C.4).

Figure C.1 Schematic diagram of the PCA.

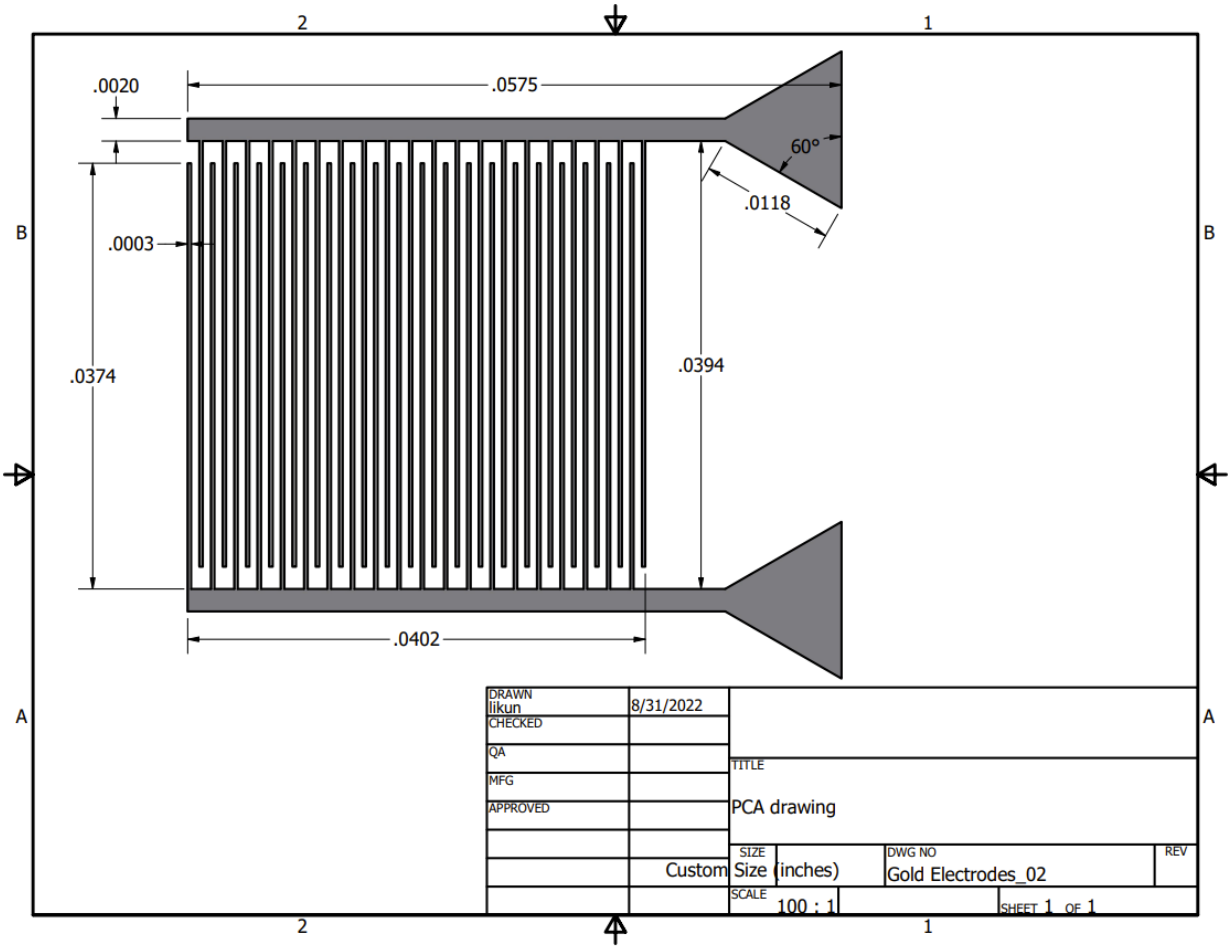
.0020
.0575
60°
.0118
.0003
.0374
.0394
.0402
DRAWN
likun
8/31/2022
CHECKED
QA
MFG
APPROVED
TITLE
PCA drawing
SIZE
Custom
Size (inches)
DWG NO
Gold Electrodes_02
REV
SCALE
100 : 1
SHEET 1 OF 1

Figure C.2 Batop PCA.

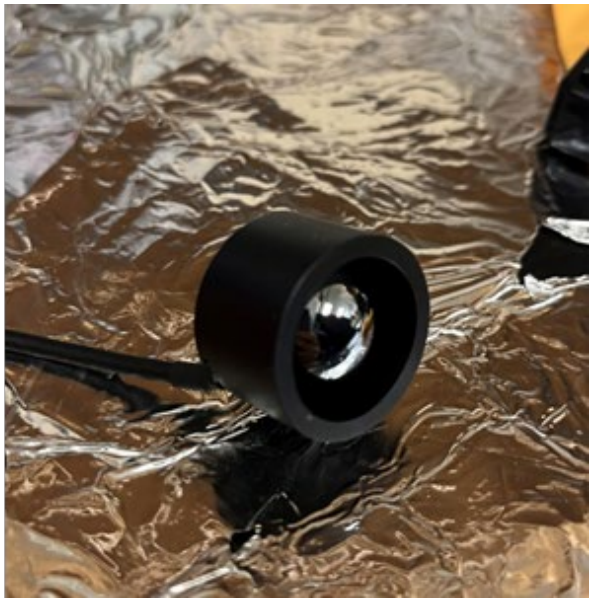

Figure C.3 Laser Quantum PCA.

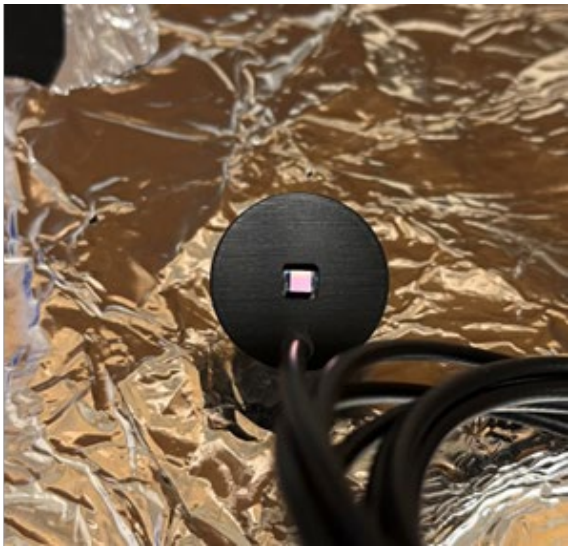

Figure C.4 UCLA PCA.


Ti-D3


0
20
40
60
80
100
120
140
160
180
200
220
240
260
280
300
320
340

The Batop PCA (iPCA-21-05-1000-800) was ordered from BATOP electronics. It was designed for laser wavelength smaller than 800 nm. Due to the micro lens arrays next to the finger electrodes, the input NIR laser beam needs to be collimated. But a lot of NIR power was needed to generate enough THz, and the PCA can be easily damaged by running two NIR beams across the zero delay. The emitted THz was collected and focused by the attached hyper semispherical silicon lens on the PCA to give collimated THz output beam. The generated THz waveform environment and frequency spectrum in vacuum are shown in Figure C.5. Two batches of PCAs from Batop were tested in STM 2 with the second batch emitting much lower THz power. It was found that the GaAs substrate color of the second batch (dark blue) was slightly different from the first one (gray). Unfortunately, the first batch has discontinued due to supply issues according to the company.

The Laser Quantum PCA (Tera-SED3) didn't have micro lens array on the PCA to focus the NIR laser, neither did it have silicon lens to collect and focus the emitted the THz. Thus off-axis parabolic mirrors had to be used to collect the emitted THz, which made it more difficult to operate during the experiment. The emitted THz power was lower than the Batop PCA even though it was designed for the Taccor ultra 8 laser, thus we did not spend much time on testing the PCA. The generated THz waveform and frequency spectrum are shown in Figure C.6. Unfortunately, the waveform data was not saved in the computer at that time, so we did not directly get the frequency spectrum. The frequency spectrum in Figure C.6 was obtained by extracting the data points in the waveform figure and performing the Fourier transform. Note that the data with the Laser Quantum PCA was acquired in the air.

The two PCAs we obtained from the UCLA group [4] showed the best performance with much higher emitted THz power. The UCLA PCAs were plasmonic PCAs with the distance between the finger electrodes in the nm range (~100 nm). Electron beam lithography was thus needed instead of just optical lithography to make the finger electrodes. The PCA can endure as high as 2 W NIR and 13 V voltage. During the experiment, we usually set the voltage to be 10 V to increase the lifetime of the PCA. The UCLA PCA was also the most used during our experiments. The generated THz waveform and frequency spectrum in vacuum are shown in Figure C.7. Almost all the rectification data were acquired with this PCA, including all the hydrogen data showing oscillations.

Figure C.5 THz emission from Batop PCA.

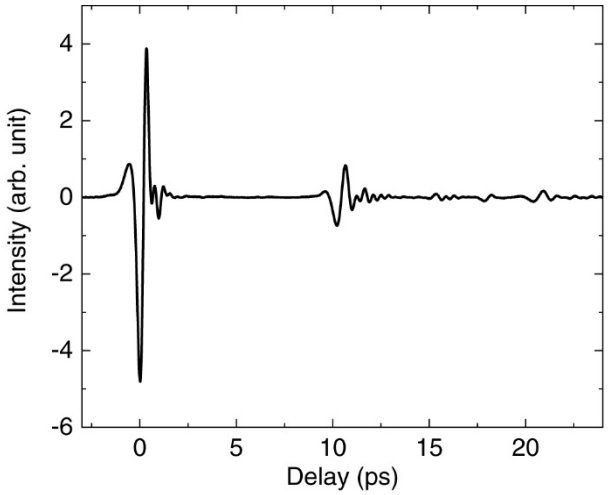
Intensity (arb. unit)
4
2
0
-2
-4
-6
0
5
10
15
20
Delay (ps)

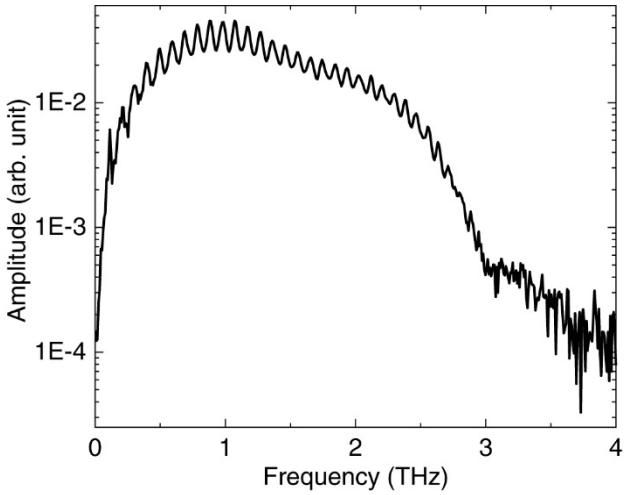
Amplitude (arb. unit)
1E-2
1E-3
1E-4
0
1
2
3
4
Frequency (THz)

Figure C.6 THz emission from Laser Quantum PCA.

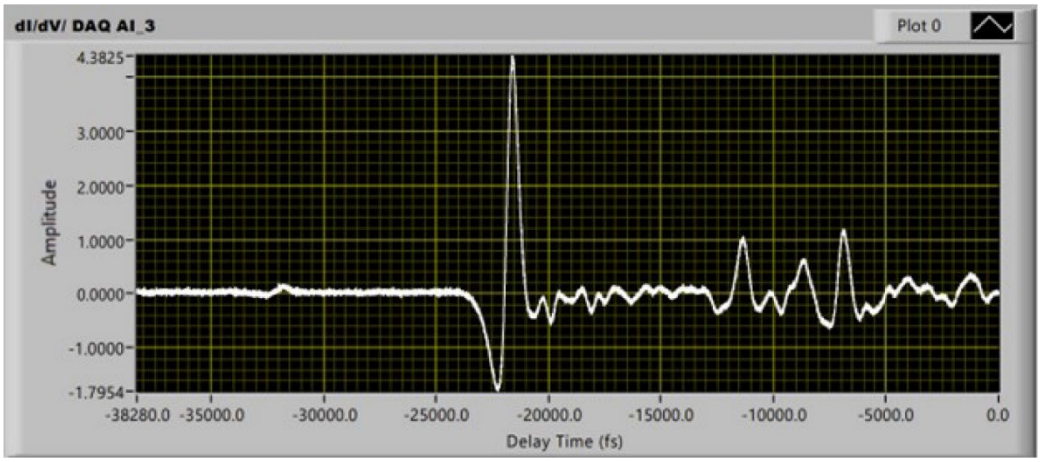
dI/dV/ DAQ AI_3
Plot 0
4.3825
3.0000
2.0000
1.0000
0.0000
-1.0000
-1.7954
Amplitude
-38280.0
-35000.0
-30000.0
-25000.0
-20000.0
-15000.0
-10000.0
-5000.0
0.0
Delay Time (fs)

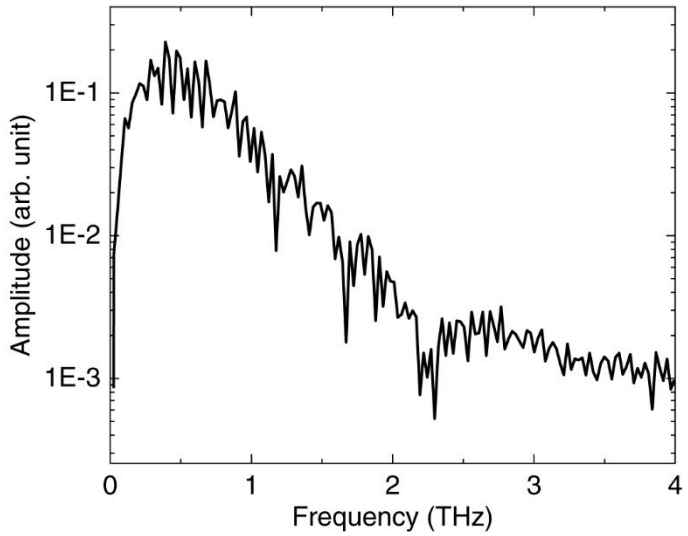
1E-1
1E-2
1E-3
Amplitude (arb. unit)
0
1
2
3
4
Frequency (THz)

Figure C.7 THz emission from UCLA PCA.

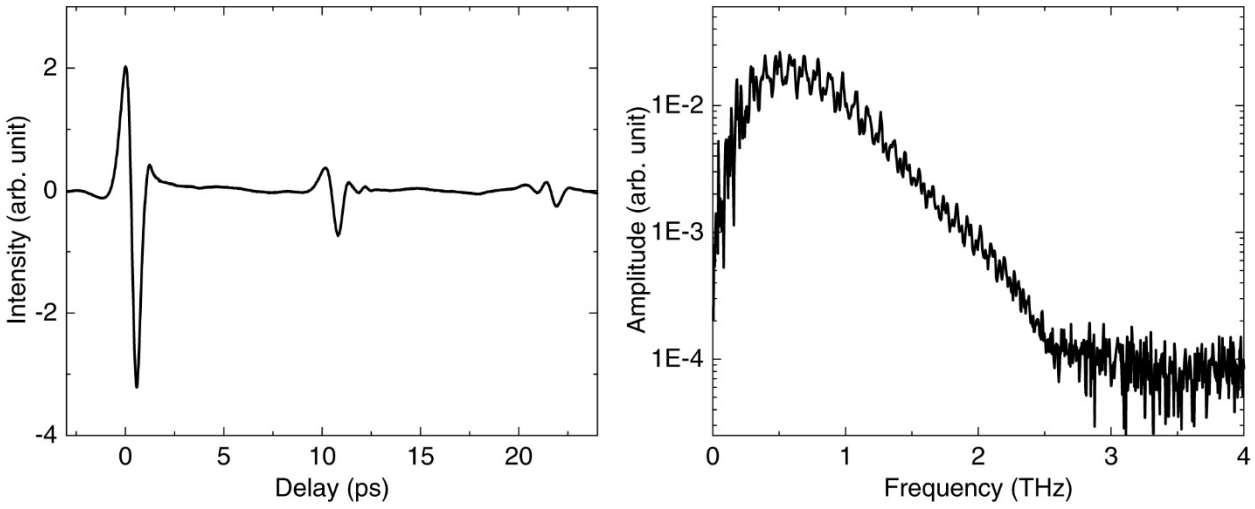
Intensity (arb. unit)
2
0
-2
-4
0
5
10
15
20
Delay (ps)
Amplitude (arb. unit)
1E-2
1E-3
1E-4
0
1
2
3
4
Frequency (THz)

In the future, it would be very beneficial to make our own PCAs to generate THz. The plasmonic type PCA has proven to be very stable and emit high enough power for the experiments. Future students with trained skills from the IMRI and INRF should be able to make such PCAs after some practices. The detailed steps to fabricate the plasmonic PCA is shown in Table C.1. It follows the same procedures as described in the paper from the UCLA group [4]. The necessary instruments included in this table were available in the INRF. Due to limited time the author could spend on the project of the plasmonic PCA fabrication, it was ended at the learning stage. 3D drawing of the many electrodes in nm dimensions was not possible in Inventor. Instead, it can only be done in the e-beam lithography computer in IMRI where a specific software was installed. Future students should follow strictly the PCA design in [4] and try to reproduce their results. The paper was detailed enough to include all the design and fabrication information.

It is possible to move the PCA very close to the vacuum viewport by customizing the PCA mount, which can probably increase the THz power received by the junction. The beam diameter can also be decreased a lot with such a small propagation path from the PCA to the STM junction.

Table C.1 Process steps to fabricate the plasmonic type PCA.

Process steps	Method	Device	Material
Grow LT-GaAs			
Pattern plasmonic contact electrodes	E-beam lithography	FEI SEM / E-Beam Writer	Resist
5/45 nm Ti/Au deposition and liftoff		E-Beam 1 evaporation (Temescal CV-8)	Ti, Au, Acetone
Pattern the bias lines	Optical lithography	Karl Suss MA6 Mask Aligner	Mask, Photoresist
50/550 nm Ti/Au deposition and liftoff		E-Beam 1 evaporation (Temescal CV-8)	Ti, Au, Acetone
350 nm Si_3N_4 deposition	Plasma-enhanced CVD	BMR Low Temp PECVD	SiH_4, N_2
Pattern shadow metals	Optical lithography	Karl Suss MA6 Mask Aligner	Mask, Photoresist
10/90 nm Ti/Au deposition and liftoff		E-Beam 1 evaporation (Temescal CV-8)	Ti, Au, Acetone
Pattern contact vias	Optical lithography	Karl Suss MA6 Mask Aligner	
Etch Si_3N_4 layer to open contact vias	Reactive ion etching (RIE)	Trion ICP/RIE	CHF_3, O_2
Mount prototype on silicon lense			

Bibliography

[1] A. Dreyhaupt, S. Winnerl, T. Dekorsy, and M. Helm, *High-Intensity Terahertz Radiation from a Microstructured Large-Area Photoconductor*, Appl. Phys. Lett. **86**, 121114 (2005).

[2] M. Beck, H. Schäfer, G. Klatt, J. Demsar, S. Winnerl, M. Helm, and T. Dekorsy, *Impulsive Terahertz Radiation with High Electric Fields from an Amplifier-Driven Large-Area Photoconductive Antenna*, Opt. Express, OE **18**, 9251 (2010).

[3] S. Winnerl, *Scalable Microstructured Photoconductive Terahertz Emitters*, J Infrared Milli Terahz Waves **33**, 431 (2012).

[4] N. T. Yardimci, S.-H. Yang, C. W. Berry, and M. Jarrahi, *High-Power Terahertz Generation Using Large-Area Plasmonic Photoconductive Emitters*, IEEE Transactions on Terahertz Science and Technology **5**, 223 (2015).

APPENDIX D

Voltage Amplifier for the PCA

The voltage amplifier was modified from the old existing voltage amplifier in the Ho group. The old amplifier had an output voltage of up to 15 V and a rise time of ~10 microsecond (μs). In order to make it suitable for our PCAs and reach the best performance when taking data, it is necessary to minimize the rise time and increase the output voltage while having a high output current.

The initial design is shown in Figure D.1 where the main part of the voltage amplifier is the OPA551PA op-amp. It is a high voltage (60 V), high current (380 mA), and a high slew rate (15 V/μs) operational amplifier. By using a stable DC power supply (LD28.8 from AAK power supply, ±28 V, 800 mA), the requirement from the PCA can be easily fulfilled. Due to the lack of voltage regulator in the lab by the time it was made, the offset tuning part was not added to the amplifier. And the final design is shown in Figure D.2. As marked by the frames in Figure D.2, 'Vin' is the input voltage from the lock-in amplifier, 'Vout' is the output voltage from this voltage amplifier, and the 'Invert/Non-invert' switch controls the polarity of the output voltage. The amplification is controlled by a combination of 'Gain' and 'Multiplier'. The 'Gain' is a variable resistor with resistances labelled in the diagram and 'Multiplier' represents the potentiometer with a range of 0~10 kΩ. During the operation, the 'Gain' should be firstly switched to the desired value, and then 'Multiplier' can be continuously adjusted to reach an exact voltage required by the PCA. Figure D.3 and Figure D.4 show two pictures of the voltage amplifier. Note that the two holes in Figure D.4 initially designed for offset adjustment (one hole for switch, and the other one for potentiometer) were left for blank.

With this simplified design, the measured rise time (10% to 90%) was about 3 μs from 0 to 10 V. The screenshot of its performance for a 0 to 10 V square wave output are shown in Figure D.5 and Figure D.6. Note that it is always necessary to measure the output voltage with an oscilloscope before connecting it to the PCA. Otherwise, the PCA might be damaged if too high voltage is applied. Usually, we operate in internal reference mode and the square wave output (0 to 5 V) from the back panel of the lock-in amplifier will be the input voltage of the voltage amplifier. Considering the DC power supply in the voltage amplifier can only reach ±28 V and the resistor before the op-amp is 5 kΩ, there is no need to switch the 'Gain' variable resistor above 20 kΩ.

In the future, the current version of the voltage amplifier should be redesigned on a printed circuit board. The initial idea was for amplifiers in one box to have two simultaneous outputs for the two PCAs and the board in Figure D.3 had extra room for the second one. However, the THz system was modified, and we kept using only one PCA from our collaborator. Thus, a more compact design of the voltage amplifier will make it more convenient during operation.

Figure D.1 Schematic diagram of the initial design.

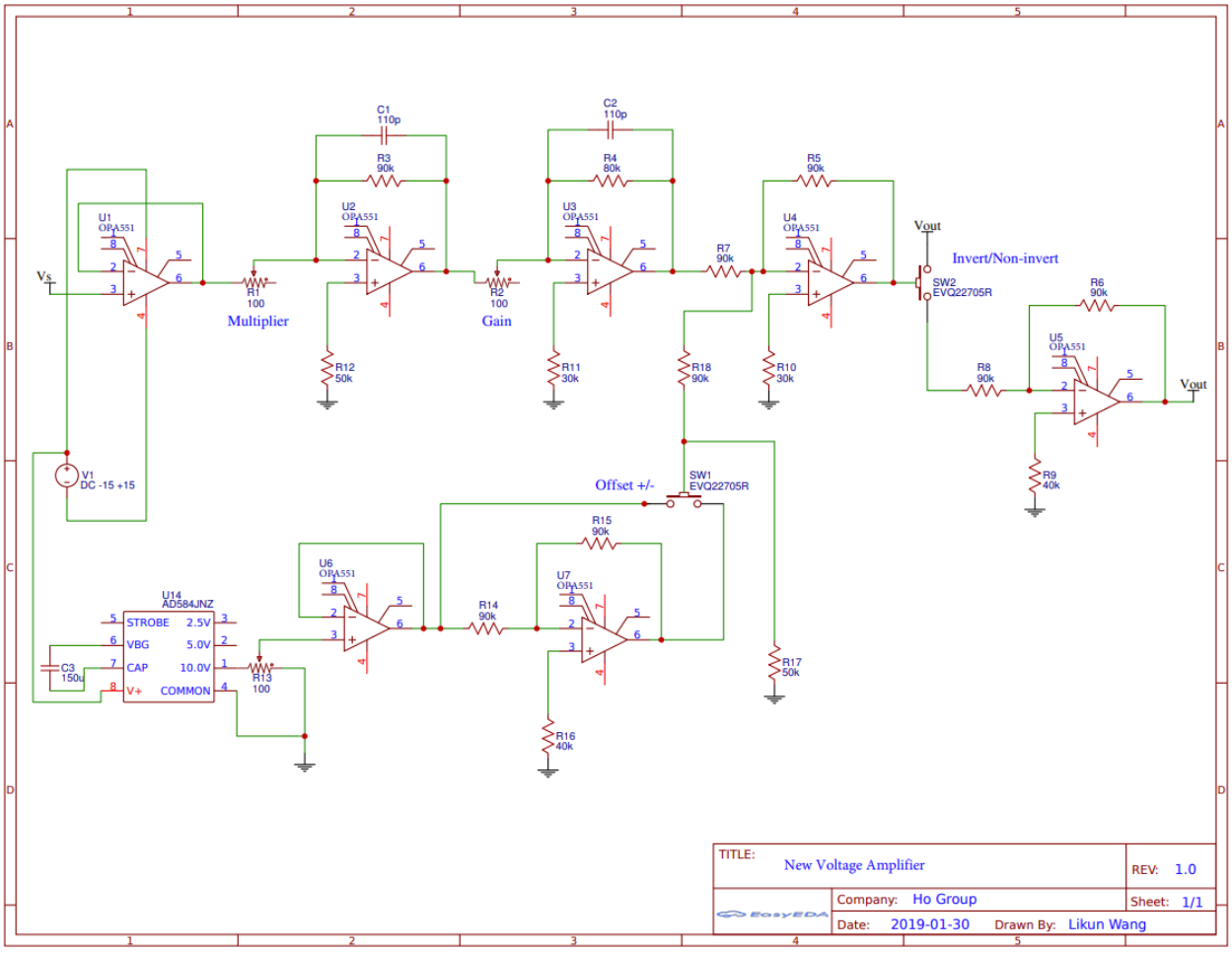
C1
110p
C2
110p
R3
90k
R4
80k
R5
90k
U1
OPA551
U2
OPA551
U3
OPA551
U4
OPA551
Vs
R1
100
Multiplier
R2
100
Gain
R7
90k
Vout
Invert/Non-invert
SW2
EVQ22705R
R6
90k
U5
OPA551
R8
90k
Vout
R12
50k
R11
30k
R18
90k
R10
30k
R9
40k
V1
DC -15 +15
Offset +/-
SW1
EVQ22705R
R15
90k
U6
OPA551
U7
OPA551
U14
AD584JNZ
STROBE
VBG
CAP
V+
2.5V
5.0V
10.0V
COMMON
C3
150u
R13
100
R14
90k
R17
50k
R16
40k
TITLE:
New Voltage Amplifier
REV: 1.0
Company: Ho Group
Sheet: 1/1
Date: 2019-01-30
Drawn By: Likun Wang

Figure D.2 Schematic diagram of the final design.

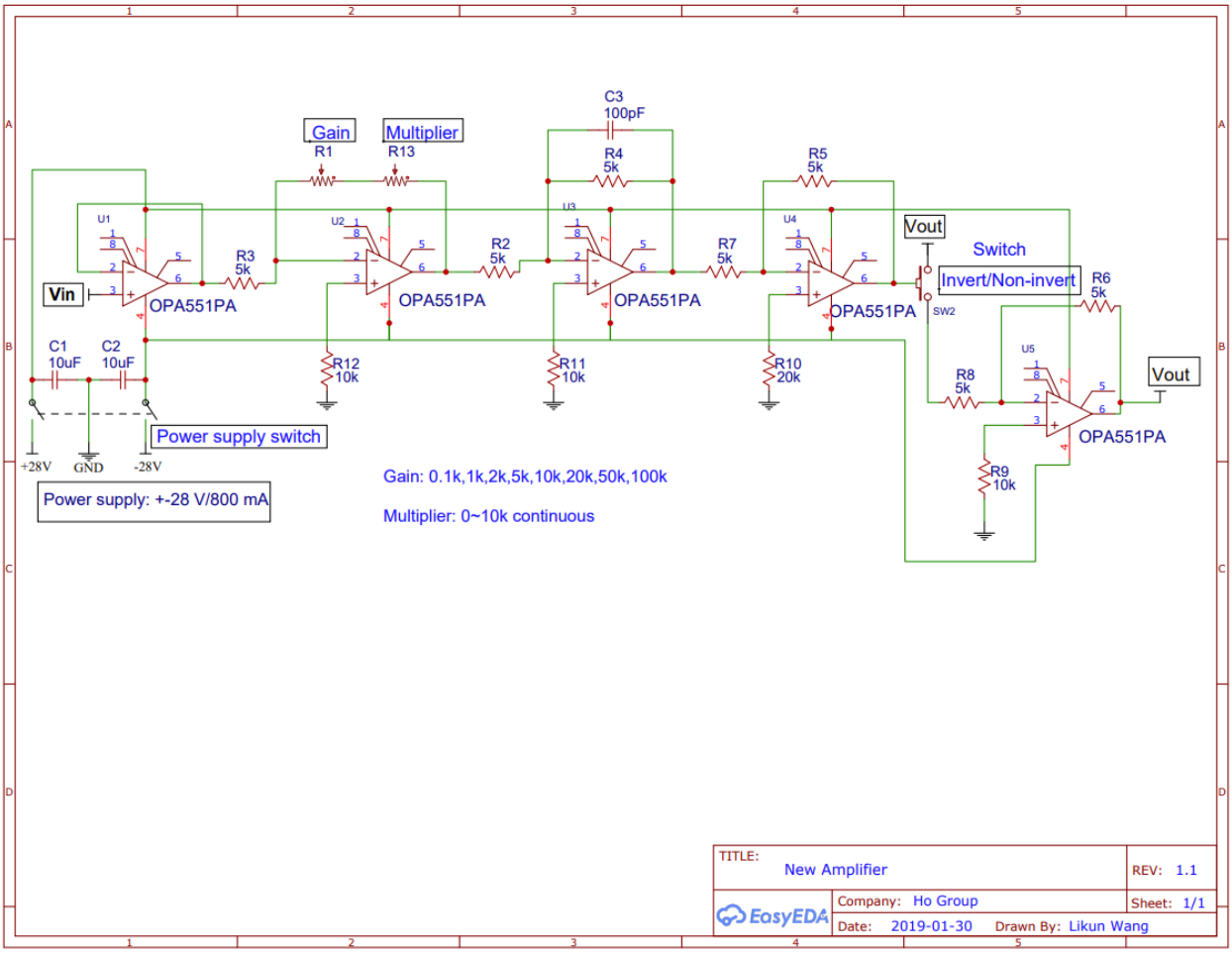
Gain
Multiplier
R1
R13
C3
100pF
R4
5k
R5
5k
Vout
Switch
Invert/Non-invert
R6
5k
Vin
R3
5k
R2
5k
R7
5k
OPA551PA
OPA551PA
OPA551PA
OPA551PA
SW2
C1
10uF
C2
10uF
R12
10k
R11
10k
R10
20k
R8
5k
Vout
Power supply switch
+28V
GND
-28V
R9
10k
Power supply: +-28 V/800 mA
Gain: 0.1k,1k,2k,5k,10k,20k,50k,100k
Multiplier: 0~10k continuous
TITLE:
New Amplifier
REV: 1.1
EasyEDA
Company: Ho Group
Sheet: 1/1
Date: 2019-01-30
Drawn By: Likun Wang

Figure D.3 Picture 1 of the voltage amplifier.

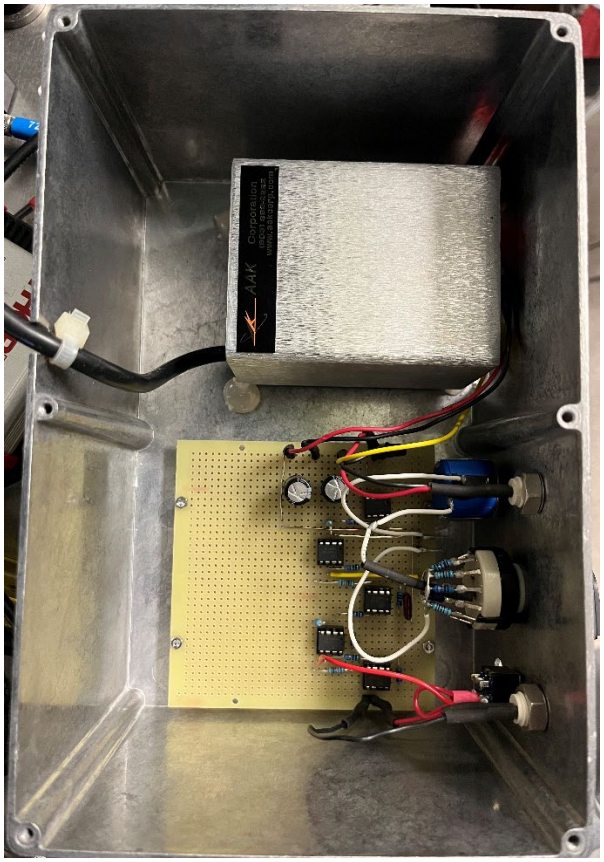

Figure D.4 Picture 2 of the voltage amplifier.

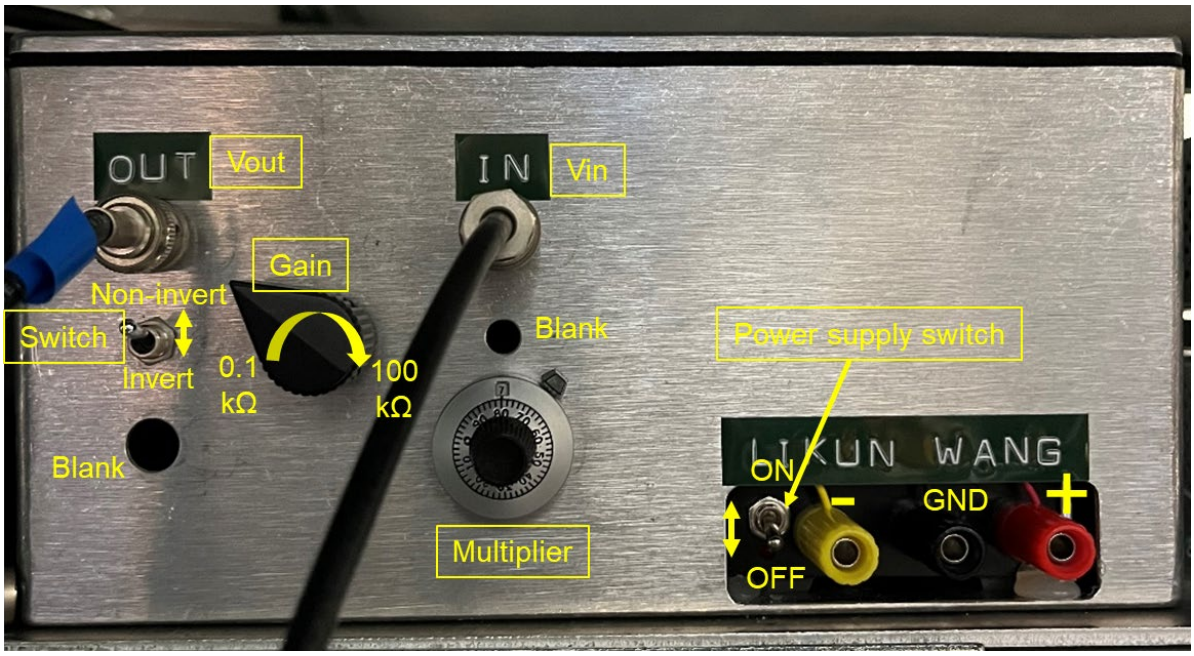
OUT
Vout
IN
Vin
Gain
Non-invert
Switch
Invert
0.1
kΩ
100
kΩ
Blank
Blank
Multiplier
Power supply switch
LIKUN WANG
ON
OFF
GND
-
+

Figure D.5 Performance 1 of the voltage amplifier.

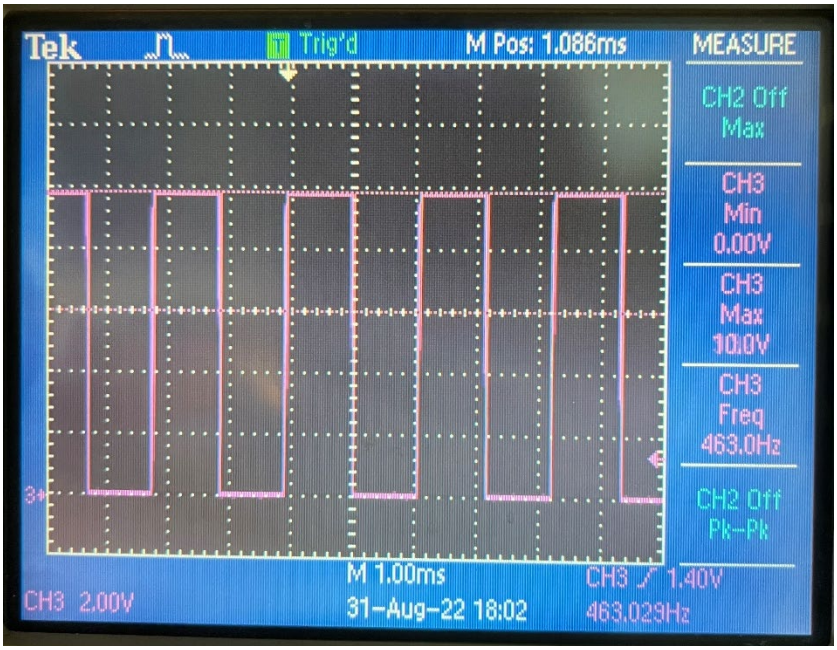
Tek
Trig'd
M Pos: 1.086ms
MEASURE
CH2 Off
Max
CH3
Min
0.00V
CH3
Max
10.0V
CH3
Freq
463.0Hz
CH2 Off
Pk-Pk
M 1.00ms
CH3 2.00V
31-Aug-22 18:02
CH3 ⟋ 1.40V
463.029Hz

Figure D.6 Performance 2 of the voltage amplifier.

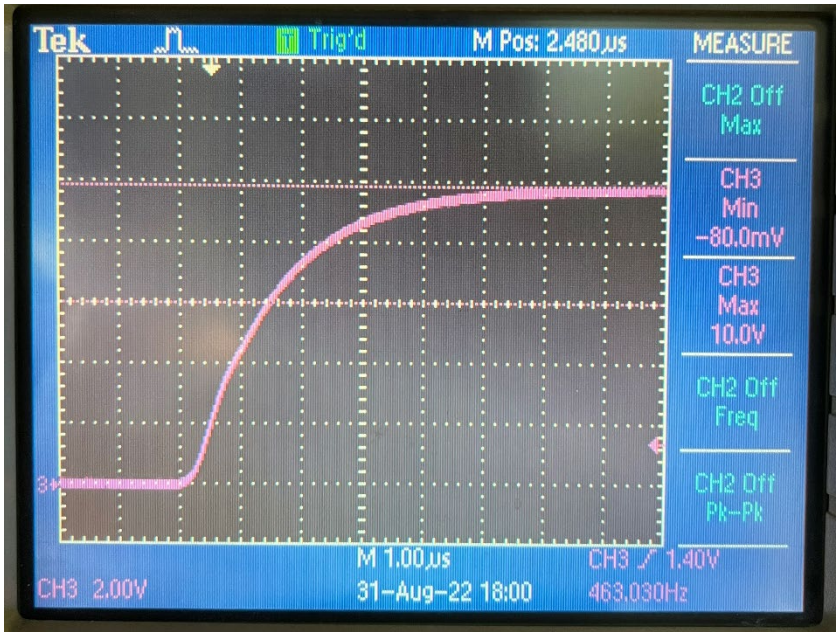
Tek
Trig'd
M Pos: 2.480µs
MEASURE
CH2 Off
Max
CH3
Min
−80.0mV
CH3
Max
10.0V
CH2 Off
Freq
CH2 Off
Pk−Pk
M 1.00µs
CH3 ⁄ 1.40V
CH3 2.00V
31−Aug−22 18:00
463.030Hz

APPENDIX E

Spintronic THz Emitter

Different types of THz sources, including non-linear crystals [1] and photoconductive antennas [2], have been utilized to generate THz for the THz-STM application. However, the generated THz rarely exceeds 3 THz and is further narrowed down to below 2 THz in the STM junction due to the tip induced low-pass filter effect [3]. It is thus not possible to study quantum coherence of atoms and molecules induced by resonant excitation at higher frequencies. Most recently, there have been studies on spintronic THz emitters (STE) to generate ultrabroadband single-cycle THz pulses covering 1-30 THz [4], as shown in Figure E.1. After coupling the ultrabroadband THz into the STM junction, frequencies up to 15 THz can still be characterized [3].

An STE is a nanometer-thick bilayer structure made of a ferromagnetic (FM) layer and a non-magnetic (NM) layer. The FM layer is magnetized in-plane along the y axis by a pair of external magnets. Upon femtosecond NIR laser irradiation, electrons in the metal layers will be excited above the Fermi energy with changed band velocity and scattering rate. A net current J_s along the z axis will then be launched due to different transport properties of the FM and NM layers. More importantly, in the FM layer the mobility of spin-up electrons is much higher than spin-down electrons. Thus, the launched z current is spin-polarized parallel to the sample magnetization. Once entering the NM layers, the spin-up and spin-down electrons will be deflected in opposite directions due to spin-orbit coupling. As a result, the spin current J_s along z direction is converted into an ultrafast transverse charge current J_c along x direction, which generates THz pulse radiation.

During the training in INRF, the author grew a nickel thin film with a thickness of 10 nm on a 500 um silicon substrate. A very weak signal was detected in the THz power meter, as schematically shown in Figure E.2. The signal strength was not saved, but it was about 1/20 of the UCLA PCA with the same input NIR power. Two Neodymium magnets were used to generate a magnetic field of about 20 mT at the center of the thin film. However, later testing of a Fe (2 nm)/Pt (3 nm) thin film on silicon did not show any THz signal. The substrate probably needed to be changed to GaAs and the thin film thickness should be controlled accurately.

By implementing the STE into our THz-STM system to generate ultrabroadband THz pulses, we will be able to study relatively high energy resonant excitations such as the hindered rotation of CO molecule on surface. The simple structure of STE will also enable us to move the THz source closer to the STM junction such that the signal detection sensitivity can be significantly enhanced.

Apart from STE, there are also studies of THz generation from hydrogen bonded single crystal [5]. The generation efficiency is comparable to the nonlinear crystal ZnTe. This THz generation from hydrogen bonded crystal raises the interest of studying temporal evolution of proton transfer in hydrogen bonding.

Figure E.1 Structure of the spintronic emitter.

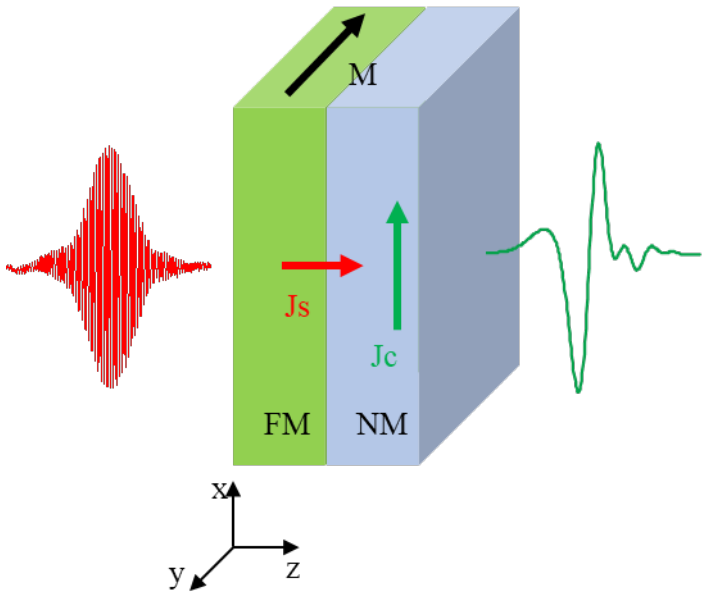
M
Js
Jc
FM
NM
x
y
z

Figure E.2 Schematic of the measurement of THz from spintronic emitter.

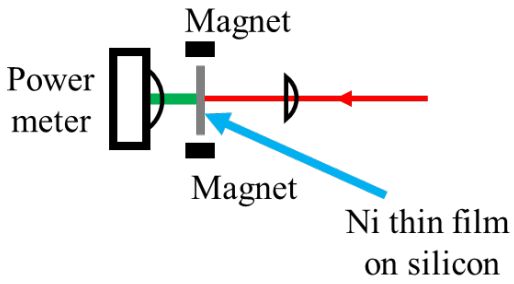
Magnet
Power
meter
Magnet
Ni thin film
on silicon

Bibliography

[1] T. L. Cocker, D. Peller, P. Yu, J. Repp, and R. Huber, *Tracking the Ultrafast Motion of a Single Molecule by Femtosecond Orbital Imaging*, Nature **539**, 263 (2016).

[2] Y. Luo, V. Jelic, G. Chen, P. H. Nguyen, Y. J. R. Liu, J. A. M. Calzada, D. J. Mildenberger, and F. A. Hegmann, *Nanoscale Terahertz STM Imaging of a Metal Surface*, Physical Review B **102**, 205417 (2020).

[3] M. Müller, N. Martín Sabanés, T. Kampfrath, and M. Wolf, *Phase-Resolved Detection of Ultrabroadband THz Pulses inside a Scanning Tunneling Microscope Junction*, ACS Photonics **7**, 2046 (2020).

[4] T. Seifert et al., *Efficient Metallic Spintronic Emitters of Ultrabroadband Terahertz Radiation*, Nature Photonics **10**, 483 (2016).

[5] M. Sotome, T. Ogaki, K. Takimiya, and N. Ogawa, *Highly-Efficient Terahertz Emission from Hydrogen-Bonded Single Molecular Crystal 4-Nitro-2,5-Bis(Phenylethynyl)Aniline*, Optics Express **29**, 10048 (2021).

APPENDIX F

THz Quarter Wave Plate

Recently, much interest have been applied to tuning the power and polarity of the THz pulse to control the effective voltage developed in the STM junction. However, there has been much less studies on the polarization control of THz, particularly the circular polarization control. One main reason is the lack of quarter waveplates due to the ultrabroadband nature of THz electromagnetic waves. Here, we design and machine a THz quarter waveplate following the idea of polarization conversion based on the Fresnel rhomb concept, as shown in Figure F.1. By introducing this broadband quarter wave plate into our THz-STM system, we will be able to continuously control the circular polarization angle of the THz at the STM junction.

The Fresnel rhomb is a prism device that can introduce some phase shift between the s and p components of a linearly polarized light upon total internal reflection inside the prism. By choosing a calculated angle of incidence, it is possible to develop a 45° phase shift for each total internal reflection. In this way, the phase shift will be 90° after two total internal reflections and the output will be a circularly polarized light travelling parallel with the input beam. Since our THz spans from 0.1 THz to 3 THz, it is crucial to choose a material exhibiting constant index of refraction over our THz operating range.

Due to the limited access of placing orders from outside, the author had to choose the high density polyethylene (HDPE) as the material to make the ¼ waveplate. According to its flat refraction index of ~1.54 at the THz range, the drawing is shown in Figure F.2. The most critical

things during the machining process are the angle and parallelism of the Fresnel rhomb. The tested transmission of THz in the air through this single piece ¼ waveplate was around 70%.

Figure F.1 Operation principle of the THz ¼ waveplate.

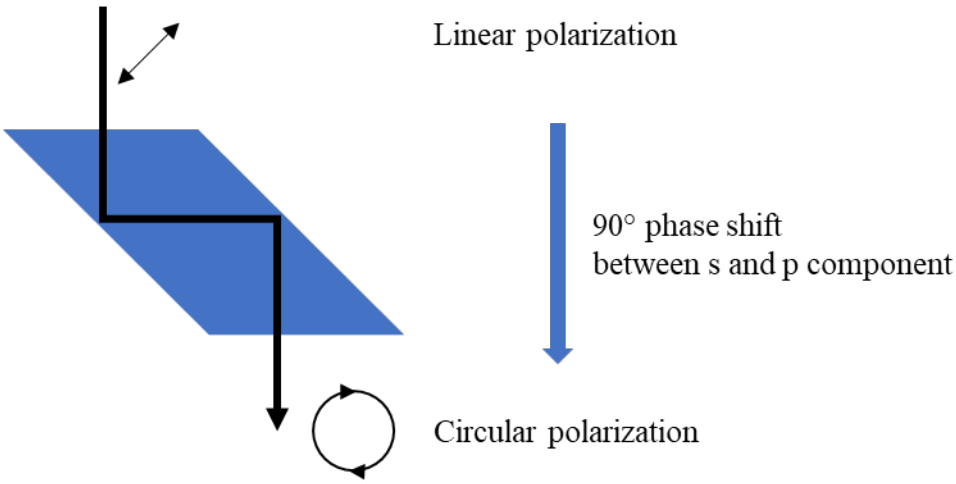
Linear polarization
90° phase shift
between s and p component
Circular polarization

Figure F.2 Drawing of the single piece of HDPE THz ¼ waveplate.

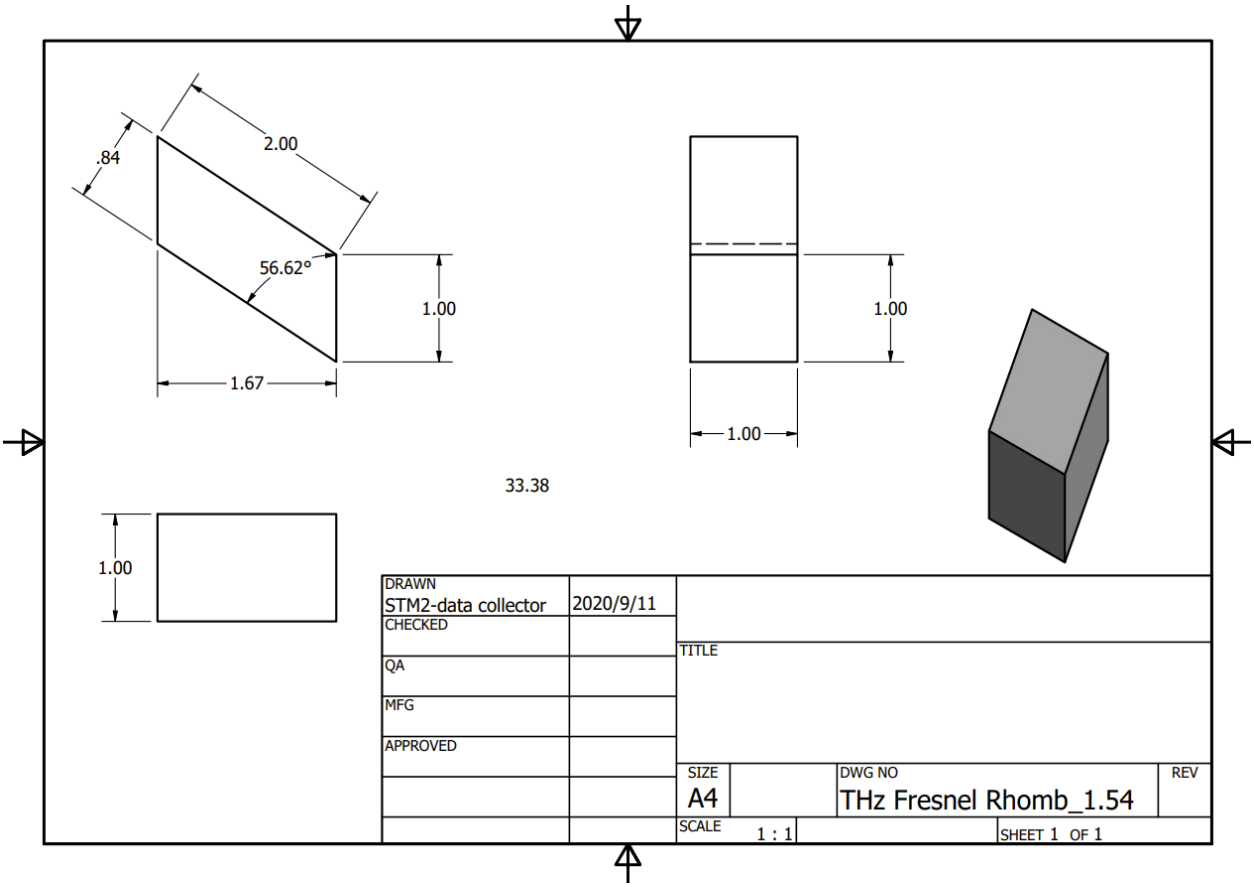
.84
2.00
56.62°
1.00
1.67
1.00
1.00
33.38
1.00
DRAWN
STM2-data collector
2020/9/11
CHECKED
QA
MFG
APPROVED
TITLE
SIZE
A4
DWG NO
THz Fresnel Rhomb_1.54
REV
SCALE
1 : 1
SHEET 1 OF 1

In addition to the single piece ¼ waveplate which is bulky and limited by the large THz beam diameter, multiple Fresnel rhombs (Figure F.3) can be parallel assembled to form an array with 1 mm spacing, as shown in Figure F.4.

The horizontal beam offset induced by the Fresnel rhomb will be minimized to about 8 mm. After inserting this array type of quarter wave plate into our THz beam path, we can convert the linearly polarized THz into circular polarization. The polarization angle can also be controlled by rotating the THz photoconductive antenna in a continuous manner.

This array also showed a similar transmission (about 70% from linear to circular polarization) to the single piece but with a much smaller horizontal beam offset. In the future, an E-O sampling should be run through this THz ¼ waveplate array to characterize the ellipticity of the converted circularly polarized THz.

Figure F.3 Drawing of the single Fresnel rhomb used for the assembly.

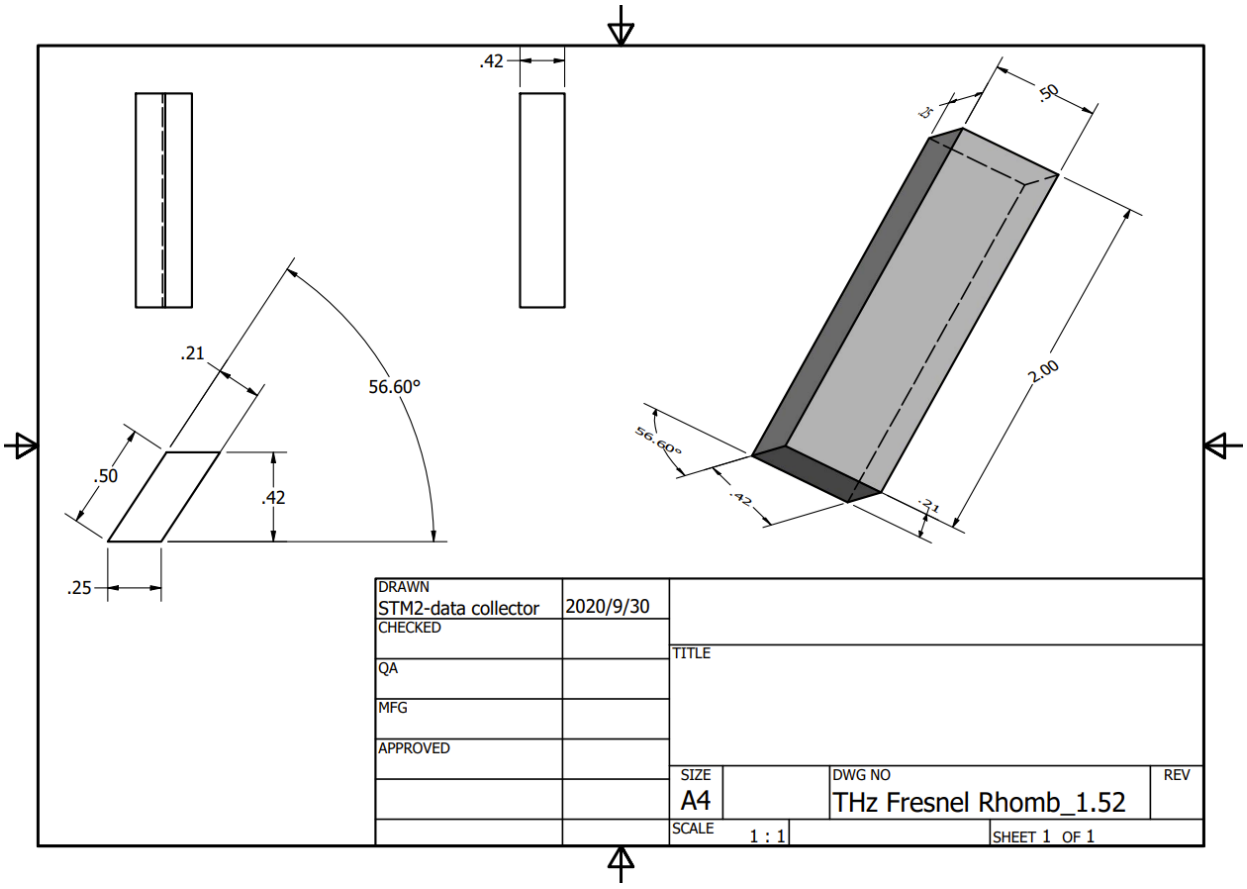
.42
.21
56.60°
.50
.42
.25
.50
2.00
56.60°
.42
.21
DRAWN
STM2-data collector
2020/9/30
CHECKED
QA
MFG
APPROVED
TITLE
SIZE
A4
DWG NO
THz Fresnel Rhomb_1.52
REV
SCALE
1 : 1
SHEET 1 OF 1

Figure F.4 Picture of the ¼ waveplate assembly.

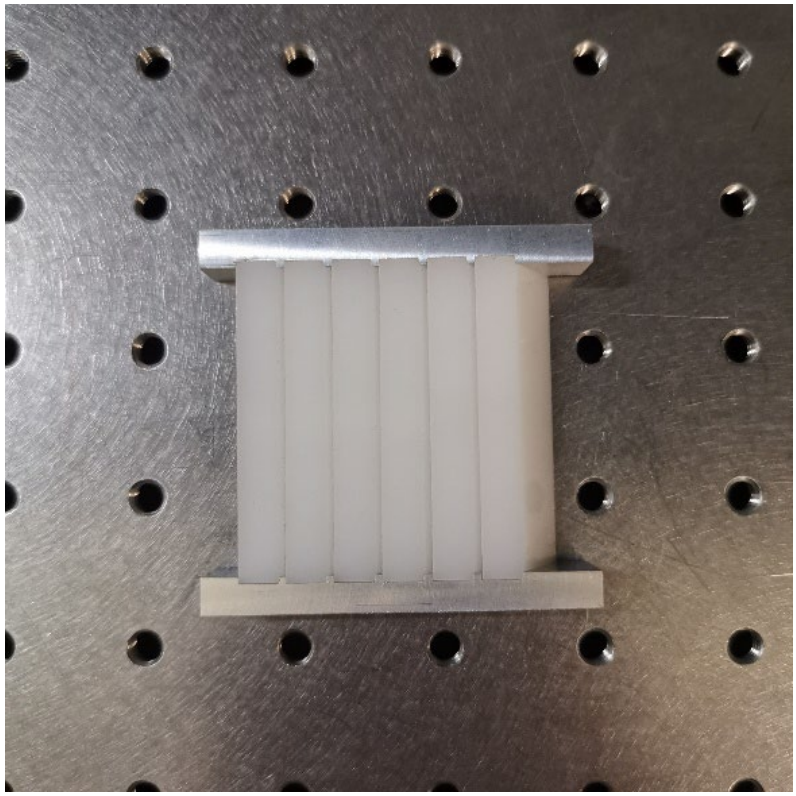

Bibliography

[1] T. L. Cocker, V. Jelic, M. Gupta, S. J. Molesky, J. A. J. Burgess, G. D. L. Reyes, L. V. Titova, Y. Y. Tsui, M. R. Freeman, and F. A. Hegmann, *An Ultrafast Terahertz Scanning Tunnelling Microscope*, Nature Photon **7**, 8 (2013).

[2] V. Jelic, K. Iwaszczuk, P. H. Nguyen, C. Rathje, G. J. Hornig, H. M. Sharum, J. R. Hoffman, M. R. Freeman, and F. A. Hegmann, *Ultrafast Terahertz Control of Extreme Tunnel Currents through Single Atoms on a Silicon Surface*, Nature Phys **13**, 6 (2017).

[3] K. Yoshioka, I. Katayama, Y. Arashida, A. Ban, Y. Kawada, K. Konishi, H. Takahashi, and J. Takeda, *Tailoring Single-Cycle Near Field in a Tunnel Junction with Carrier-Envelope Phase-Controlled Terahertz Electric Fields*, Nano Lett. **18**, 5198 (2018).

[4] Y. Kawada, T. Yasuda, A. Nakanishi, K. Akiyama, K. Hakamata, and H. Takahashi, *Achromatic Prism-Type Wave Plate for Broadband Terahertz Pulses*, Opt. Lett., OL **39**, 2794 (2014).

[5] E. V. Jasper, T. T. Mai, M. T. Warren, R. K. Smith, D. M. Heligman, E. McCormick, Y. S. Ou, M. Sheffield, and R. Valdés Aguilar, *Broadband Circular Polarization Time-Domain Terahertz Spectroscopy*, Phys. Rev. Materials **4**, 013803 (2020).

APPENDIX G

MIIPS Operation

Multiphoton intrapulse interference phase scan (MIIPS) is a technique used for pulse shaping of the ultrafast lasers. It can simultaneously measure and compensate phases of each frequency component by an array of liquid crystals. The liquid crystal arrays were separately controlled by electric voltage such that the nematic liquid crystal can be aligned into required directions. The new MIIPS box in STM 2 is MIIPSBox640 from Biophotonics, which has 640 liquid crystal pixels.

With this pulse shaper, we were able to compress the laser pulse to around 20 fs. Figure G.1 shows a laser spectrum from our Taccor 8 laser. And the autocorrelation after pulse compression is shown in Figure G.2.

During the operation of the MIIPS in STM 2, the author found an interesting usage which was the generation of frequency combs. As shown in Figure G.3, after reflecting a femtosecond laser beam from the grating, the laser is converted from time domain into frequency domain with the frequency components spanning across the liquid crystal arrays. By manually select a set of frequencies and control the corresponding liquid crystal pixels, it is possible to block all other frequencies and transmit only the ones needed. In this manner, the selected frequency will be converted back into time domain after the second reflection from the grating. Then the output laser beam will essentially be a frequency comb with the frequency components as designed. Figure G.4 shows an example of the frequency comb generated from the MIIPS. The energy resolution was

about 4 meV limited by the number of liquid crystal pixels in the MIIPS. The second example in Figure G.5 shows the generation of a laser pulse with two main frequency components.

With such a controlled frequency comb, it will be possible to generate THz with arbitrary frequency. The only limiting parameters will be the MIIPS resolution and the low power of the generated frequency components. It has been demonstrated that the generated frequency components can be further amplified by laser amplifiers to generate enough THz.

Figure G.1 Laser spectrum of Taccor 8.

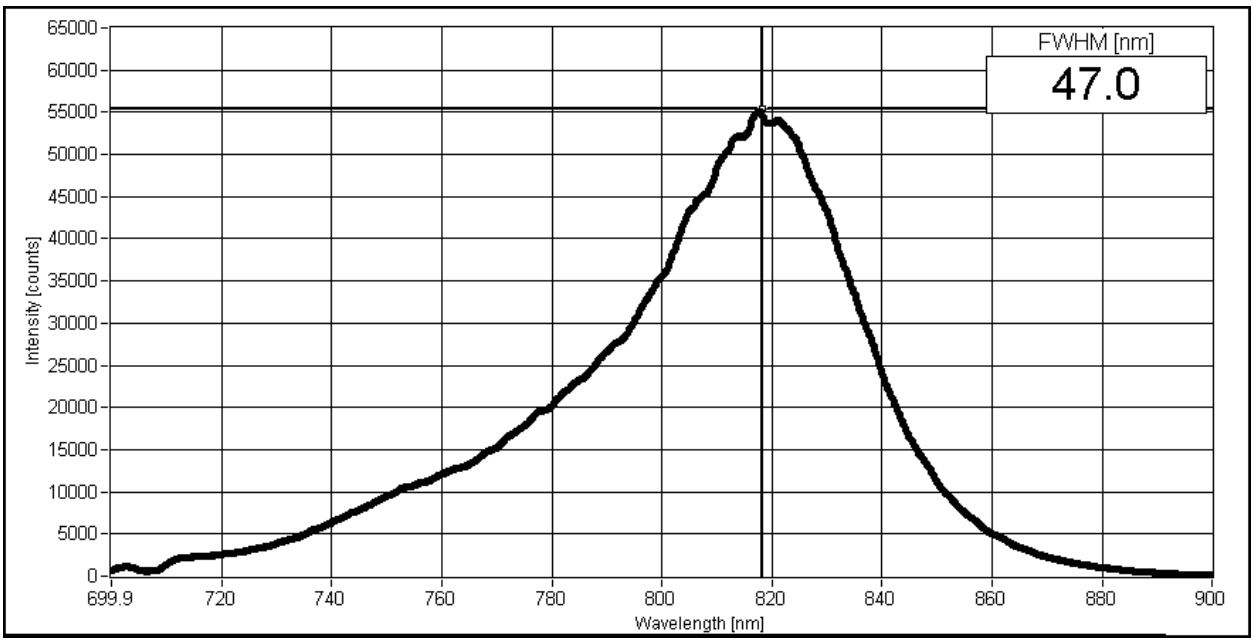
FWHM [nm]
47.0
Intensity [counts]
65000
60000
55000
50000
45000
40000
35000
30000
25000
20000
15000
10000
5000
0
699.9
720
740
760
780
800
820
840
860
880
900
Wavelength [nm]

Figure G.2 Auto-correlation after pulse compression.

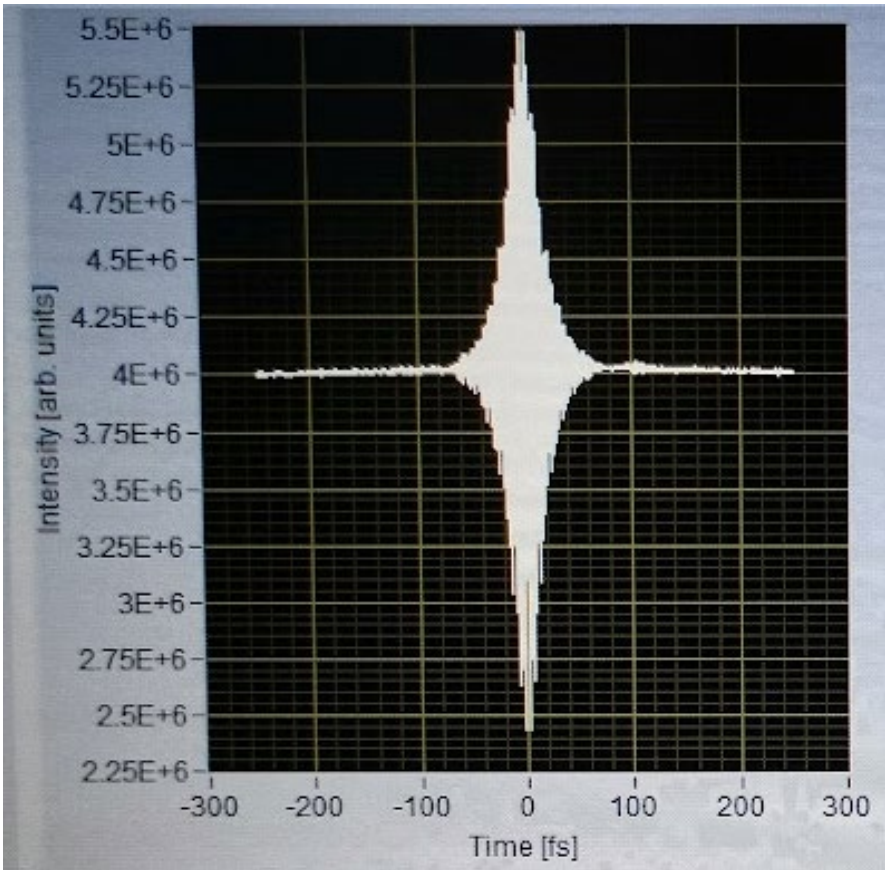
5.5E+6
5.25E+6
5E+6
4.75E+6
4.5E+6
4.25E+6
4E+6
3.75E+6
3.5E+6
3.25E+6
3E+6
2.75E+6
2.5E+6
2.25E+6
Intensity [arb. units]
-300
-200
-100
0
100
200
300
Time [fs]

Figure G.3 Schematic diagram of the frequency comb generation.

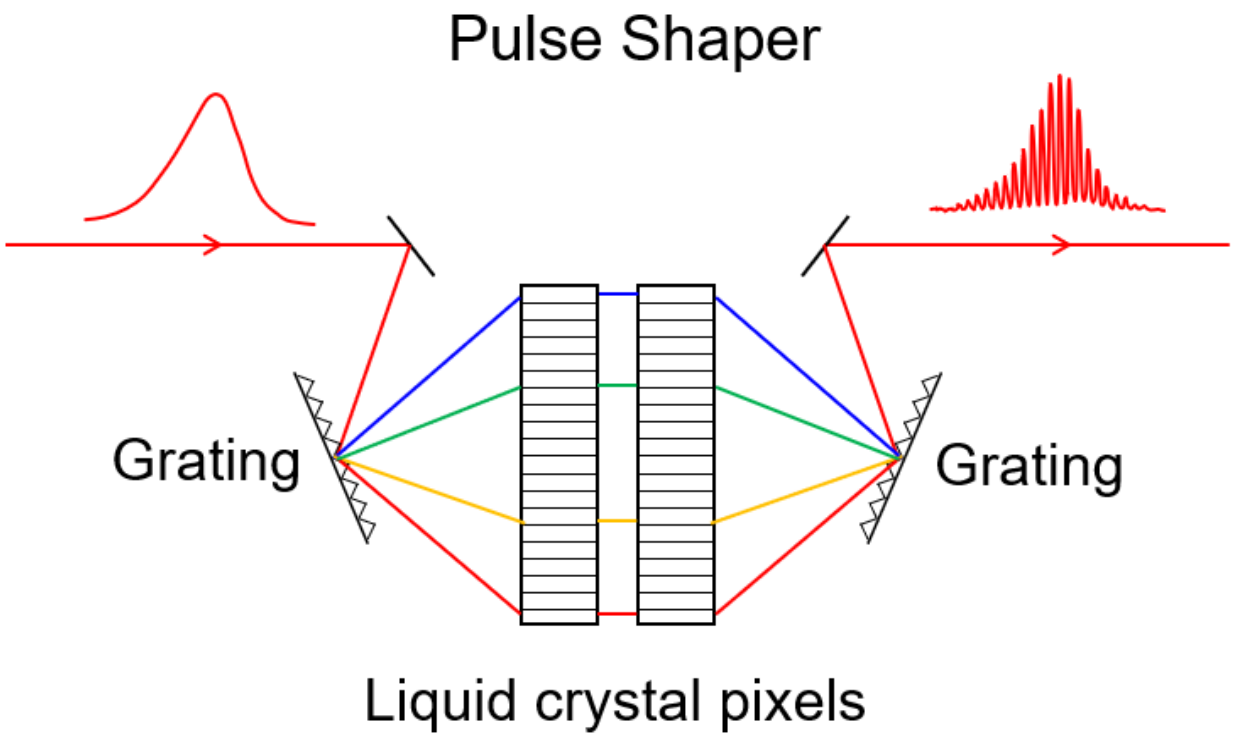
Pulse Shaper
Grating
Grating
Liquid crystal pixels

Figure G.4 Measured frequency comb generation from MIIPS.

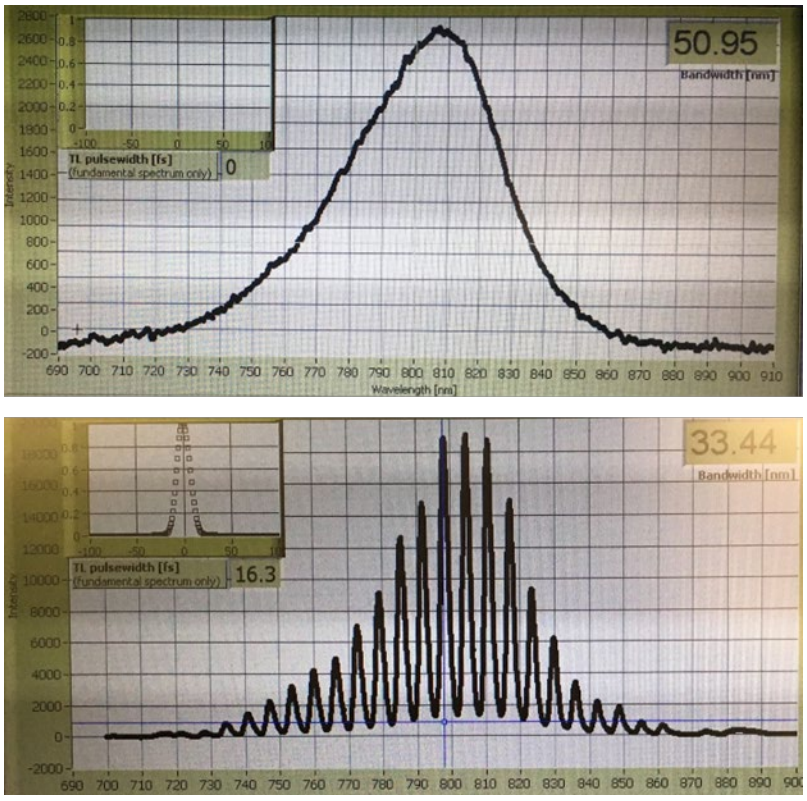
50.95
Bandwidth [nm]
TL pulsewidth [fs]
(fundamental spectrum only)
0
Intensity
Wavelength [nm]
33.44
Bandwidth [nm]
TL pulsewidth [fs]
(fundamental spectrum only)
16.3
Intensity

Figure G.5 Measured two frequency spectrum for photo mixing.

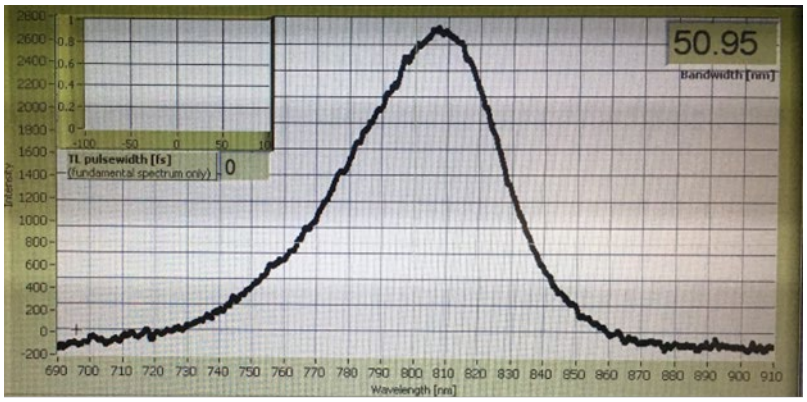
50.95
Bandwidth [nm]
TL pulsewidth [fs]
(fundamental spectrum only)
0
Intensity
Wavelength [nm]

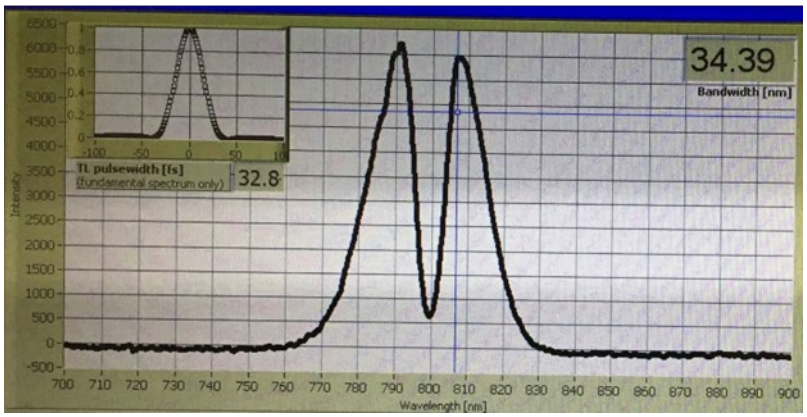
34.39
Bandwidth [nm]
TL pulsewidth [fs]
(fundamental spectrum only)
32.8
Intensity
Wavelength [nm]

APPENDIX H

Welding Operation

Due to the limited access to the machine shop during the pandemic, many machining jobs especially the welding of some parts had to be delayed for a long time. Thus we decided to order a welder and do the welding in the lab.

As shown in Figure H.1, the ordered welder was a tungsten inert gas (TIG) welder from PrimeWeld (TIG225ACDCP), allowing up to 225 A output current with a 240 V input. It is a multi-function welder capable of welding in both the DC and AC modes. Lots of metals can be welded by this TIG welder, such as stainless steel and copper. With a 225 A output current, the thickest material can be welded is ½ inch. The author has successfully employed it to weld three copper wires into one which was later used in the triple cell doser. The welding of the stainless-steel water-cooling tube was another success.

The most important thing during the welding process is the safety of the person operating the welder and other people around it. Welding can be very dangerous if the safety guidelines are not followed. The high voltage, high current, harmful fumes and gases, strong arc flash, and many others can all cause damage.

Below are the welding procedures:

1. Make sure no one else is around the welding space. Due to limited room in the Ho group, we did not have a specific welding room equipped with welding curtains. Nor do we have extra welding mask for the second person to wear. It is thus necessary to

keep everyone else away from the welding space to prevent eye damage from the strong arc flash.

2. Check the ground clamp. The welding parts and the ground clamp have to been in close contact with the underlying metallic working surface which is further connected with the building ground.
3. Check the Argon gas cylinder and regulator. Make sure the Argon cylinder is opened and the flow is enough for welding from the flow meter in Figure H.2.
4. Wear the welding mask (Figure H.3), inflammable lab coat, inflammable gloves, and other PPEs. The welding mask is made of liquid crystal which can automatically adjust the transmission according to the external brightness. It is safe to always wear the mask during welding.
5. Check all the knobs on the front panel of the welder. Make sure they are at the correct settings.
6. Start the welder. Test it by ramping the current. Purge the system with Argon gas.
7. Weld the parts with caution. Usually it takes many times of practice to do a good welding job.
8. After the welding is done, make sure to turn off the welder and close the Argon gas cylinder valve.

With the recent setup of the welding table as shown in Figure H.4, life is much easier while working with the all metal table top on the cart.

Two welding examples made by the author are shown in Figure H.5 and Figure H.6, respectively.

Figure H.1 Picture of the welder.


PrimeWeld
AMP
TIG
MMA
AC
DC
START CURRENT
UP SLOPE
DOWN SLOPE
END CURRENT
2T
4T
TIG225ACDCP
PRE FLOW
BASE CURRENT
PULSE FREQUENCY
PULSE DUTY
POST FLOW
ON
OFF
PrimeWeld

Figure H.2 Different parts of the TIG welder.

Regulator with flow meter

Foot pedal

TIG torch

Figure H.3 Helmet and grounding.

Liquid crystal mask

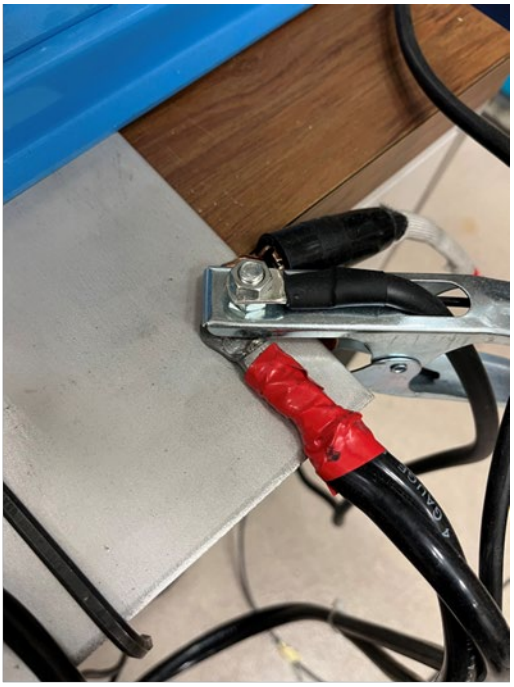

Ground clamp

Figure H.4 Welding working station.


PrimeWeld

Figure H.5 Practice welding with plate nuts.

Figure H.6 Welding of the water cooling doser.